Antiferromagnetic Insulatronics: Control and Manipulation of Magnetic Domains

Dissertation zur Erlangung des Grades
„Doktor der Naturwissenschaften“
am Fachbereich Physik, Mathematik und Informatik der
Johannes Gutenberg-Universität
in Mainz

Hendrik Meer
geb. in Haren (Ems)
Mainz, den 17. Juli 2023

JOHANNES GUTENBERG
UNIVERSITÄT MAINZ

Hendrik Meer
Antiferromagnetic Insulatronics: Control and Manipulation of Magnetic Domains

Date of Oral Defense: 13th September 2023

Reviewer: Removed due to data privacy

Supervisor: Removed due to data privacy

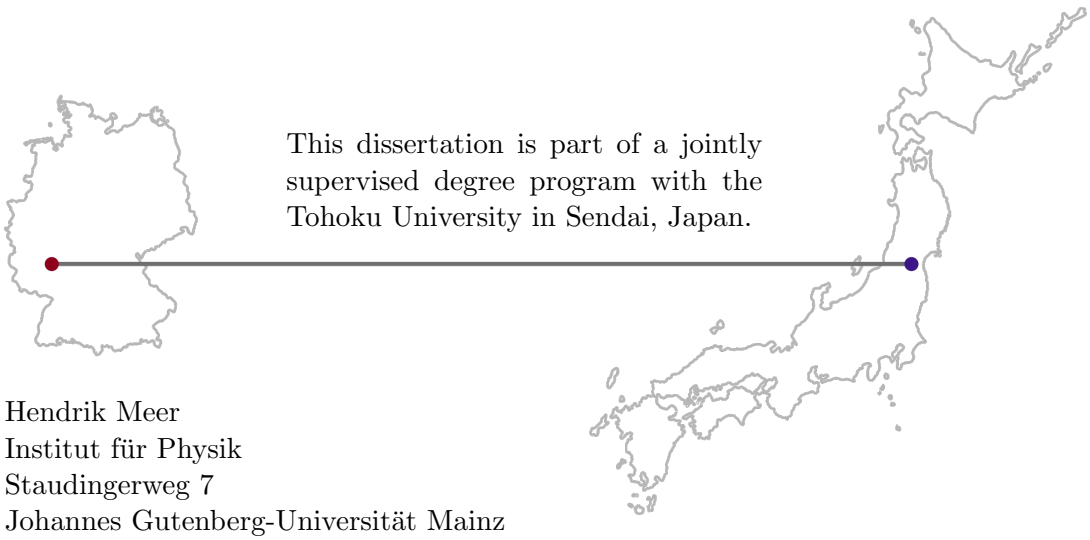

This dissertation is part of a jointly supervised degree program with the Tohoku University in Sendai, Japan.

Hendrik Meer
Institut für Physik
Staudingerweg 7
Johannes Gutenberg-Universität Mainz
D-55099 Mainz
meer@uni-mainz.de

Abstract

The control and manipulation of the antiferromagnetic order in insulating magnetic thin films is of paramount importance for advancing the development of possible high-speed, energy-efficient spintronic devices. The field of antiferromagnetic insulatronics has great potential to overcome the limitations of conventional electronic devices due to the inherent advantages of insulating antiferromagnets. These materials exhibit intrinsic frequencies in the THz range, surpassing ferromagnets, and possess the ability to transport information through pure spin currents. Thus, allowing for the mitigation of Joule heating issues commonly encountered in current devices.
However, the absence of a net magnetic moment poses a significant challenge for writing the antiferromagnetic order, thereby hindering further exploration of their properties and their practical implementation as active elements. Therefore, the aim of this thesis is to investigate and establish mechanisms to control and manipulate the magnetic order in insulating antiferromagnets. Here, we investigate three different mechanisms to manipulate the domain structure in antiferromagnetic NiO and CoO thin films.
First, we explore current-induced switching in bilayers of heavy metals and insulating antiferromagnets. Using birefringence imaging, we optically study the current-induced changes in the domain structure. By examining different device and pulse geometries, we identify a heat- and strain-based switching mechanism, thereby resolving previously conflicting switching interpretations based on spin-orbit torque mechanisms.
Second, we investigate the influence of the patterning geometry on a device. Although shape anisotropy, as it is established in ferromagnets due to dipolar interactions, is not expected, theoretical studies suggest that analogous effects may occur in antiferromagnets due to magnetoelastic coupling. We use the X-ray magnetic linear dichroism effect in photoemission electron microscopy to reveal a strain-induced antiferromagnetic shape anisotropy. Thereby, we enable the tailoring of the antiferromagnetic ground state of a device.
Third, we investigate a contactless switching mechanism. By irradiating our domain structures with pulse trains of laser light with different polarizations and fluences, we observe the creation of antiferromagnetic 180° domain walls and domains. The underlying mechanism is based on laser-induced heating and limited by the inherent strain in our samples.
In summary, this work aims to address the challenges associated with the control and manipulation of antiferromagnetic order in insulating thin films. By exploring current-induced switching, antiferromagnetic shape anisotropy, and laser-induced domain creation, our research contributes to expanding the toolbox of antiferromagnetic insulatronics and reveals the critical role of strain and heat. These findings provide a foundation for the future development of antiferromagnets as active elements in spintronic devices and further exploration of the fascinating properties of insulating antiferromagnets.

Declaration of Authorship

I hereby declare that the thesis submitted is my own unaided work. All direct or indirect sources used are acknowledged as references. The thesis, in whole or in part, has never been submitted to any other examination committee that is able to admit a doctoral degree.

Ich versichere, dass ich meine Dissertation selbstständig verfasst und keine anderen als die angegebenen Quellen und Hilfsmittel benutzt sowie Zitate kenntlich gemacht habe. Die Doktorarbeit ist weder abschnittsweise, noch in der vorliegender Form bei einer anderen Prüfungsbehörde zur Erlangung eines Doktorgrades eingereicht worden.

Mainz, 17th July 2023

Hendrik Meer

Dedicated to

my father, who may be gone
but will never be forgotten.

Table of Contents

Abbreviations

AFM	Antiferromagnet
AI	Artificial intelligence
ANN	Artificial neural network
AOS	All-optical switching
APPLE	Advanced planar polarized light emitter
CCD	Charge-coupled device
fcc	Face-centered cubic
FFT	Fast Fourier-transformation
FM	Ferromagnet
FOV	Field of view
FWHM	Full width at half maximum
GMR	Giant magnetoresistance
HC	Helical coil
HM	Heavy metal
iAFM	Insulating antiferromagnet
ICP MS	Inductively coupled plasma-assisted magnetron sputtering
ID	Insertion devices
LED	Light-emitting diode
LH	Linear horizontal
LINAC	Linear accelerator
LMB	Linear magnetic birefringence
LV	Linear vertical
MS	Magnetron sputtering
PEEM	Photoemission electron microscopy
PM	Paramagnet
RAM	Random access memory
RF	Radio frequency
S-domain	Spin-domain
SOT	Spin-orbit torque
STT	Spin-transfer torque
T-domain	Twin-domain
TMR	Tunnel magnetoresistance
X-PEEM	X-ray photoemission electron microscopy
XAS	X-ray absorption spectroscopy
XMCD	X-ray magnetic circular dichroism
XMLD	X-ray magnetic linear dichroism
XNLD	X-ray natural linear dichroism

1 | Introduction

Progress of our society has always been intertwined with advances in the storage, transport, and processing of information. A historical example is the widespread adoption of Gutenberg's movable-type printing press [1] in Renaissance Europe, which played a critical role in the spread of knowledge, discovery, and literacy. The ease and reduced cost of printing books made them the preferred means of storing information. This facilitated the global exchange of knowledge between different cultures, such as the exchange of books by Dutch sailors in Japan during the Edo period [2].
Today, we no longer rely on ships to transport information[1]. Personal computers and mobile phones grant us unprecedented access to the internet, connecting people around the world. As a result, our digital society is accumulating and processing more information and data than ever before in history [4]. To manage this influx of data, we have turned to artificial intelligence (AI) and machine learning as tools for analyzing and processing our data [5]. Remarkable achievements, such as developing an AI capable of defeating professional human players in games like Go [6] and creating large-scale language models like ChatGPT [7], have been made possible by training artificial neural networks (ANNs) inspired by the neural networks in our own brains [8]. However, ANNs are currently far from being as energy efficient as our own brain [9, 10]. Current technology, based on silicon semiconductors, faces a major challenge: Joule heating [11, 12]. In today's data centers, the largest energy consumption arises not from the computation itself, but from the cooling required to counteract current-induced heating [13]. Thus, there is a need to develop more energy-efficient technologies that minimize Joule heating.
To address this need, the field of spintronics aims at revolutionizing computing and information processing by harnessing not only an electron's charge but also its spin as a means of transporting, storing, and processing information [14]. The potential of spintronics was revealed with the discovery of tunnel magnetoresistance (TMR) [15] and giant magnetoresistance (GMR) [16, 17], laying the basis for the development of modern magnetic hard drives. The recent development of spin-transfer torque-based magnetic tunnel junctions and magnetic random-access memory has solidified the position of spintronics as a key field for the future of information technology [18–21]. While the focus of spintronics has traditionally been on the use of ferromagnets (FMs) as active elements, attention has recently shifted to antiferromagnets (AFMs) [22].

[1] Instead, we now use airplanes to transport 5 petabytes of black hole data [3].

AFMs lack a net magnetic moment due to the cancellation of opposite magnetic moments from different sublattices. Louis Néel, a leading figure in the development of antiferromagnetism, commented upon receiving his Nobel Prize in 1970: AFMs *"are extremely interesting from the theoretical standpoint but do not appear to have any practical applications"* [23]. Today, AFMs are already used as passive elements in exchange bias applications [22, 24], and as active elements they have several potential advantages over their ferromagnetic counterparts [25]. Their absence of a net magnetic moment allows for potentially 100 times smaller bit sizes [26]. In addition, AFMs are insensitive to external fields of up to several Tesla compared to ferromagnets, which are manipulated by mT external fields. Furthermore, the strong inter-sublattice exchange in AFMs leads to intrinsic frequencies in the THz range, exceeding the GHz frequencies of the dynamics of ferromagnets [27].

In order to increase the energy efficiency of spintronic devices, it is necessary to switch from current-based information transport to spin-based information transport, thereby minimizing Joule heating [28]. This feat has been achieved in insulating AFMs, where excited spin currents could be detected after traveling several tens of micrometers in the absence of current flow [29, 30]. The ability to eliminate Joule heating through pure spin transport positions insulating AFMs as a promising material platform for the future of spintronics.

Nevertheless, the origin for several advantages of AFMs, the absence of a net magnetic moment, is also a key issue for reading and writing the antiferromagnetic order. Reading the antiferromagnetic order has recently become more accessible due to the observation of antiferromagnetic domains by birefringence imaging and the discovery of interfacial magnetoresistance effects [31–35]. However, writing the antiferromagnetic order is challenging due to their insensitivity to external fields. The lack of established writing mechanisms limits current research and potential applications for AFMs.

In the work presented in this thesis, we address the challenge of writing the antiferromagnetic order in insulating transition metal oxides by three different mechanisms. Our goal is to establish a set of tools for effectively controlling and manipulating the magnetic order in insulating antiferromagnetic materials. We draw inspiration from established techniques used to control the order of ferromagnets, such as current-induced switching through spin torque, shape anisotropy, and all-optical switching [36–39]. By applying similar methods, we aim to understand and uncover new approaches to control the antiferromagnetic order.

There have been initial reports on the current-induced switching of insulating AFMs by applying current in an adjacent heavy metal (HM) layer [40]. However, there are conflicting reports on the current-induced switching direction and the origin of the switching [40–42]. To address this, we investigate the current-induced switching in different device geometries and aim to reveal the underlying mechanism by imaging the switching of the antiferromagnetic order.

Geometry is not only important in current-induced switching experiments. Due to the absence of a net magnetic moment, AFMs are not expected to exhibit shape anisotropy based on the minimization of dipolar magnetic stray fields. However, magnetoelastic

coupling of AFMs is predicted to lead to shape-dependent domain formation [43, 44]. Here, we experimentally investigate this phenomenon to uncover the shape-induced control of the domain structure in AFMs.
Another method to manipulate the antiferromagnetic order is optical excitation. Previous studies have demonstrated the excitation of the antiferromagnetic order by irradiation with laser light, and there have been reports of polarization dependent excitation of magnons [45–47]. However, the transition from a dynamic modulation of the antiferromagnetic order to a permanent change in the domain structure, similar to the optical switching observed in ferromagnets, remains less explored [47, 48]. Here, we investigate the effects of laser irradiation on antiferromagnetic domain structures and aim to uncover an optically based mechanism for manipulating the domains of antiferromagnetic materials.
This thesis is structured as follows: We first discuss the theoretical background in Chap. 2. After an introduction to AFMs and the magnetic energy terms that define the antiferromagnetic order, the spin structure of the materials studied in this thesis, NiO and CoO, is reviewed. The chapter ends with an overview over current-induced effects that are relevant to the later discussion of the results. Chap. 3 gives an introduction to the main experimental techniques used by the author of this work to fabricate and image the antiferromagnetic thin film samples. Then, in Chap. 4, we discuss the current-induced switching of insulating AFMs and our findings from Ref. [49] on geometry dependent switching and additional current-induced switching experiments. In Chap. 5, we investigate shape-induced effects and present our findings from Ref. [50]. These are complemented by additional observations of patterning induced effects in NiO and shape dependent domain formation in CoO thin films. In Chap. 6, laser irradiation is introduced as a third tool to manipulate the antiferromagnetic domain structure. Our results from Ref. [51] are presented and further investigations on CoO thin films are discussed. Finally, in Chap. 7, we summarize our achievements in establishing new approaches to control the antiferromagnetic order of insulating thin films and give an outlook on possible future research directions.
Through this comprehensive experimental investigation, we aim to contribute to the field of spintronics by advancing the understanding of how we can write the antiferromagnetic order, paving the way for future investigations and novel applications for fast and energy-efficient information processing.

2 | Theoretical Background

This chapter serves as a guide to the theoretical background necessary to understand the experimental results presented in this thesis. First, different classes of magnetism are introduced and an overview of the magnetic free energy and exchange interactions is given. This is followed by an overview of AFMs, the formation of their domains, and the spin structure of the materials used in this thesis. Finally, we provide a brief introduction to several current-induced effects that are relevant for the study of insulating antiferromagnets (iAFMs) and HM bilayers.

2.1 | Classes of Magnetism

We can classify different types of magnetism by comparing the response of a material to an external magnetic field $\boldsymbol{H}$. The induced magnetization of a material $\boldsymbol{M}$ is related to the external field $\boldsymbol{H}$ via the susceptibility $\chi = {}^{\boldsymbol{H}}/_{\boldsymbol{M}}$ [52, 53].
All materials exhibit diamagnetism in which the induced magnetic moment is counteracting the external field, $\chi < 0$. Thus, in an experiment the application of a magnetic field causes a repulsion of a diamagnetic material [54]. The opposite behavior is observed for a material that also exhibits dominating paramagnetism (PM) in addition to diamagnetism. The electronic shells of paramagnetic materials are only partially filled, and their atoms exhibit a net magnetic moment μ. The application of an external field leads to the alignment of these moments parallel to the external field, $\chi > 0$ [53, 55]. The magnetization of both dia- and paramagnets linearly depends on the externally applied field, and is zero once the external field is removed. However, some materials exhibit a collective magnetic ordering in the absence of an external field [52].
One type of collective magnetic order is ferromagnetism, in which the magnetic moments of individual atoms are aligned parallel to each other [52, 56]. FMs exhibit a nonlinear response of their magnetization to an external field. They possess a hysteresis, their magnetic state depends not only on the strength of the external magnetic field, but also on its history [57].
Another more common type of collective ordering is antiferromagnetism [58–60]. One can imagine a simple collinear AFM as a superposition of two opposing ferromagnetic lattices, see Fig. 2.1. Both sublattices individually exhibit a magnetic moment $|\boldsymbol{M}_1| = |\boldsymbol{M}_2| = M_0$. However, when superimposed the net magnetization of an AFM

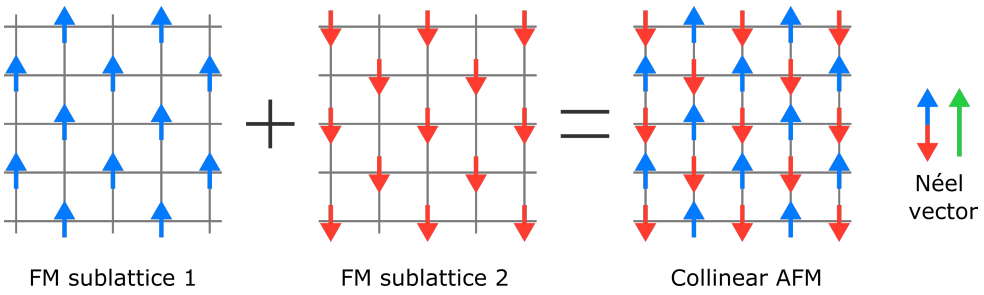

Figure 2.1: Collinear antiferromagnetic ordering can be achieved via the combination of two ferromagnetic sublattices with opposing magnetization. The antiferromagnetic order is characterized by the Néel vector.

vanishes $\boldsymbol{M} = \boldsymbol{M}_1 - \boldsymbol{M}_2 = 0$. While the magnetic order of FMs can be characterized by the magnetization, AFMs are characterized by the direction of the magnetic order, the Néel vector defined as $\boldsymbol{L} = \boldsymbol{M}_1 - \boldsymbol{M}_2$ or normalized to unit length $\boldsymbol{n} = {}^{(\boldsymbol{M}_1 - \boldsymbol{M}_2)}/_{2M_0}$ [61, 62].
A third type of magnetic order is exhibited by ferrimagnets [63]. Ferrimagnets have similarly coupled sublattices as AFMs. However, the sublattices are inequivalent $|\boldsymbol{M}_1| \neq |\boldsymbol{M}_2|$ and they possess a net magnetization. There are other types of collective magnetic ordering [53], however, the work presented in this thesis focuses on AFMs.

2.2 | Magnetic Free Energy

The magnetic ordering of a material is determined by an energy minimization [64]. The total free energy W_{total} of a magnetic system is the sum of different intrinsic and external energy contributions [37, 52, 53]

$$W_{\text{total}} = \int d\boldsymbol{r} \left(w_{\text{ex}} + w_{\text{anis}} + w_{\text{demag}} + w_{\text{zee}} + w_{\text{me}} + w_{\text{elas}} + w_{\text{destr}} \cdots \right). \tag{2.1}$$

Here, we only briefly introduce the different terms, a more detailed discussion follows in the upcoming sections. The exchange energy w_{ex} and the crystalline anisotropy w_{anis} are crucial for the determination of the magnetic ground state. The demagnetization energy w_{demag} and the Zeeman energy w_{Zee} are relevant to understand the domain formation of ferromagnetic domains [37], but can be neglected for the formation of antiferromagnetic domains. The magnetoelastic w_{me} and elastic contributions w_{elas} contribute to the magnetic energy in FMs. However, they are particularly important for the formation of antiferromagnetic domains [37, 43]. This section introduces the exchange interaction as origin of the long range ordering and discusses the relevant energies for the formation of magnetic domains. Several simplifications that are used in the modelling of the free energy of antiferromagnetic thin films are presented [50, 65–67]. However, the discussion of the magnetoelastic energy w_{me}, the elastic energy

w_{elast} and the destressing energy w_{destr} follows in the context of the antiferromagnetic domain formation in Sec. 2.3, after an introduction into AFMs.

2.2.1 Exchange Energy

Exchange interactions are essential for establishing long-range magnetic order and are crucial for the strong antiferromagnetic coupling in AFMs. We first introduce the direct exchange interaction [68–70], following the descriptions in Ref. [52, 53], before discussing the superexchange interaction [71], which can lead to an antiferromagnetic ordering.

2.2.1.1 Direct Exchange Interaction

We can imagine two electrons with overlapping wave functions. The total wave function is a product of the individual states, but in order to obey the Pauli principle, the wave functions must be antisymmetric with respect to the exchange of the electrons. This antisymmetric state minimizes the Coulomb energy due to the spatial separation of the electrons. The exchange energy of neighboring electrons, with dimensionless spin operators $\hat{S}_1, \hat{S}_2$, can be expressed by the Heisenberg Hamiltonian [52, 53]

$$\mathcal{H}_{\text{ex}} = -2\mathcal{J}\hat{S}_1 \cdot \hat{S}_2, \tag{2.2}$$

with the exchange integral $\mathcal{J}$. We can generalize this for a whole lattice by including the sum of all electronic interactions between different electrons i and j. For a whole lattice of different electrons [53]

$$\mathcal{H}_{\text{ex}} = -2\sum_{i>j} \mathcal{J}_{i,j}\hat{S}_i \cdot \hat{S}_j. \tag{2.3}$$

The value of the exchange integral $\mathcal{J}$ determines if a coupling between neighboring atoms is ferromagnetic or antiferromagnetic. If the exchange integral for $\mathcal{J}$ is larger than 0, a parallel alignment of the spins is preferred. If the exchange value is negative an antiferromagnetic coupling between neighboring atoms is preferred [52, 53].
To describe the energy of a complex magnetic system, without considering the atomic structure, we switch to a continuum approximation. Here, the magnetization $\boldsymbol{M}$ is a continuously varying function $\boldsymbol{M}(\boldsymbol{r})$, which only is varying in direction. The magnitude is constant and given by the spontaneous magnetization M_{s} [53]

$$\boldsymbol{m}(\boldsymbol{r}) = \frac{\boldsymbol{M}(\boldsymbol{r})}{M_{\text{s}}} = \begin{pmatrix} \alpha_1 \\ \alpha_2 \\ \alpha_3 \end{pmatrix} = \begin{pmatrix} \cos(\phi)\sin(\theta) \\ \sin(\phi)\sin(\theta) \\ \cos(\theta) \end{pmatrix}, \tag{2.4}$$

we also introduce here the spherical polar coordinates, θ describes the angle between the z axis and $\boldsymbol{m}(\boldsymbol{r})$ and ϕ the angle in the xy-plane. We can use $\boldsymbol{m}(\boldsymbol{r})$ to express the exchange energy as [53]:

$$w_{\text{ex}} = \int A(\nabla \boldsymbol{m}(\boldsymbol{r}))^2 d^3\boldsymbol{r}, \tag{2.5}$$

with the temperature dependent exchange stiffness A. An equivalent form of Eq. 2.5 in spherical coordinates is [53]

$$w_{\text{ex}} = \int A[(\nabla\theta)^2 + \sin^2(\nabla\phi)^2] d^3\boldsymbol{r}. \tag{2.6}$$

In the simplest case of an in-plane magnetization in thin magnetic films (ϕ =constant), the exchange term further simplifies to $A(\nabla\theta)^2$ [53].
The exchange energy increases for abrupt transitions of the magnetization. Thus, exchange favors the creation of large domains. The sign of the exchange constant determines the magnetic ordering. A positive exchange leads to a ferromagnetic ordering and a negative exchange to an antiferromagnetic ordering [53].

2.2.1.2 Superexchange

The magnetic structure of 3d transition metal oxides is often determined by indirect coupling of the magnetic ions. In materials such as NiO or CoO, the wavefunctions of neighboring 3d orbitals have a vanishing overlap and direct exchange between them can be neglected [72]. However, the magnetic ions can interact with each other via non-magnetic intermediate atoms. This interaction is called superexchange, after the long distance the magnetic ions are separated from each other [52, 73, 74].

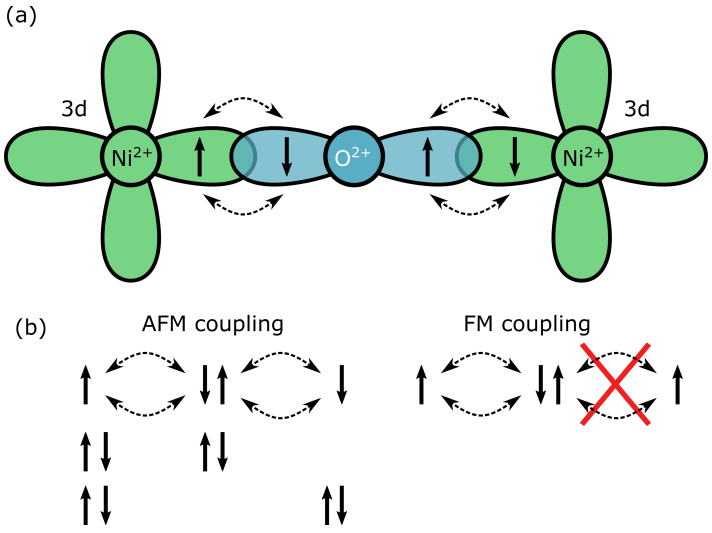

Figure 2.2: (a) The Ni 3d orbitals are indirectly coupled via the hybridization with the oxygen ion. (b) The virtual hopping of the electrons leads to a favourable antiferromagnetic coupling, as the Pauli exclusion principle suppresses the hopping for ferromagnetic coupling.

The basic principle of superexchange is shown for NiO in Fig. 2.2. The 3d Ni electrons cannot directly interact with each other, but they can hybridize with the 2p oxygen orbitals. The virtual exchange of two electrons from the oxygen 2p orbital to the unoccupied 3d Ni orbitals leads to a long-range interaction between the magnetic ions. This hybridization results in an energetically favorable antiparallel alignment of the neighboring Ni atoms [52]. To understand the energetic advantage of the antiferromagnetic coupling, one can compare potential antiferromagnetic and ferromagnetic states, see Fig. 2.2 (b). The antiferromagnetic coupling is preferred because it allows for a higher delocalization of the electrons. For ferromagnetic coupling, hopping between different magnetic ions would be suppressed due to the Pauli principle. The lower kinetic energy of the antiferromagnetic coupling leads to the preferred antiferromagnetic ordering of 3d transition metals such as NiO, CoO and MnO [52, 53, 72].

2.2.2 Magnetocrystalline Anisotropy

Experimentally one can observe a difference in the magnetization for non isotropic magnetic materials if a magnetic field is applied along different axes [53]. This directional dependence of the magnetization originates from the crystal structure and spin-orbit interaction [75, 76]. This so-called magnetocrystalline anisotropy results in an energetically favorable alignment of the magnetic order along the easy axes and an unfavorable alignment along the hard axes [76]. An example for a material with a simple uniaxial anisotropy would be Co. The anisotropy energy E_a depends on the angle θ between the anisotropy axes and the magnetic order [52, 53]:

$$E_\mathrm{a} = K_1 \sin\theta + K_2 \sin(4\theta) + \cdots \tag{2.7}$$

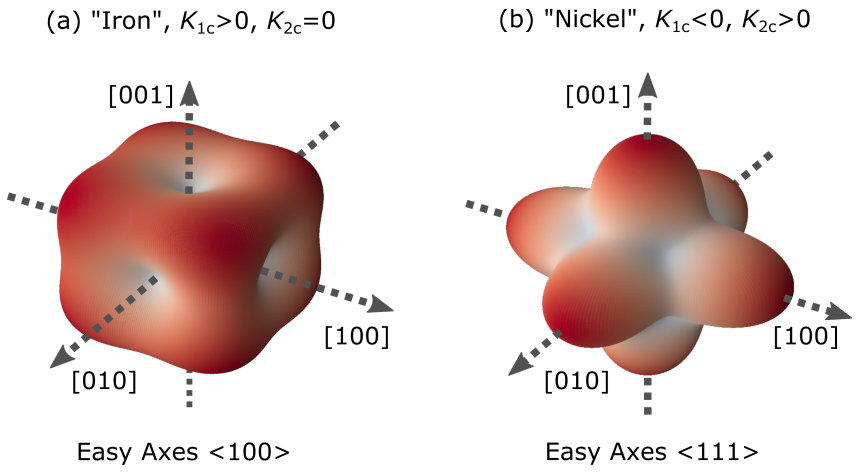

Figure 2.3: Mangetocrystalline anisotropy iso-energy surfaces for iron (a) and nickel (b) like anisotropy constants.

Here K_1 and K_2 are the temperature dependent anisotropy constants, which approach zero near the transition temperature [77]. Other magnetic materials like Ni and Fe exhibit a cubic anisotropy, which can be represented in the following way [53, 78]

$$E_a = K_{1c}(\alpha_1^2\alpha_2^2 + \alpha_2^2\alpha_3^2 + \alpha_3^2\alpha_1^2) + K_{2c}(\alpha_1^2\alpha_2^2\alpha_3^2) + \cdots , \tag{2.8}$$

here α_i are the directional cosines. When the cubic anisotropy constant $K_{1c} > 0$ and $K_{2c} \approx 0$ the directions of the easy axes are parallel to the x, y, z axes, see Fig. 2.3 (a). Thus, a material like Fe has 3 easy axes, along the {100} directions. If the constants are $K_{1c} < 0$ and $K_{2c} > 0$, like in the case of Ni, then there are four different easy axes along the cube diagonals {111} [52], see Fig. 2.3 (b). In magnetic thin films the magnetocrystalline anisotropy can be simplified for magnetic domains which only differ in their in-plane ordering. For a thin film with fourfold in-plane symmetry, the magnetocrystalline anisotropy energy can be expressed as [50, 79]

$$w_{\text{ani}} = -\frac{1}{4}k\cos(4\theta), \tag{2.9}$$

with the anisotropy constant k. The magnetic anisotropy energy depends on the orientation of the magnetization, the angle θ, relative to the easy axes [37].

2.3 | Antiferromagnets

There are a variety of different AFMs, ranging from metallic AFMs over semiconducting AFMs to insulating AFMs [25]. Depending on their crystallographic structure, different types of antiferromagnetic coupling can be observed [52]. In the simplest case of a cubic crystallographic structure an A-type AFM can emerge, see Fig. 2.4 (a).

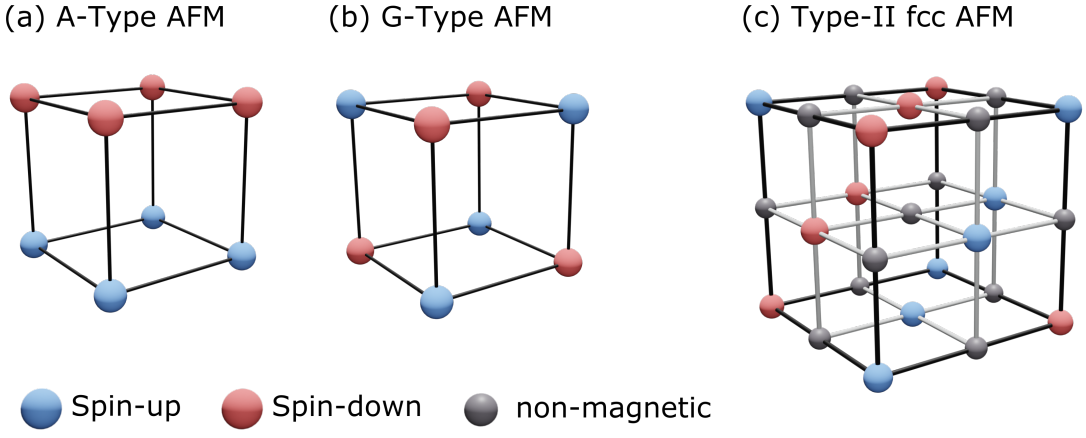

Figure 2.4: Different types of antiferromagnetic ordering for cubic crystals (a,b) and for NaCl-type crystals (c).

The magnetic moments of neighboring atoms within a plane, e.g. (100) plane, are ferromagnetically coupled, but antiferromagnetically coupled between different planes. Hematite is an insulating AFM that can exhibit such ordering [80]. Another possibility is the G-type order shown in Fig. 2.4 (b), as a result of a dominant superexchange interaction between nearest neighbors. Cubic perovskites, such as $LaFeO_3$, typically exhibit G-type antiferromagnetic order [52]. Transition metal oxides, such as NiO and CoO, crystallize in a sodium chloride structure, see Fig. 2.4 (c) [31, 81]. Here the spins are ferromagnetically coupled in the plane and antiferromagnetically coupled between planes due to the dominant superexchange interaction. More details on the antiferromagnetic structure of NiO and CoO are given in Sec. 2.3.3.
All antiferromagnetic structures discussed so far are considered to be collinear. In collinear AFMs, the compensating magnetic moments point in opposite directions but along the same axes. Similar collinear coupling can also be achieved in synthetic AFMs, e.g. a trilayer in which ferromagnetic sheets are antiferromagnetically coupled [25]. However, antiferromagnetic coupling is not limited to collinear structures, as non-collinear structures are also possible, e.g. the triangular structure of $IrMn_3$ [25, 82]. In the following, we focus on the collinear AFMs investigated in this work. We first introduce the Weiss model of antiferromagnetism, before discussing the domain formation of antiferromagnetic domains and the spinstructures of the materials investigated in this work.

2.3.1 Weiss Model of Antiferromagnetism

Louis Néel, a student of Pierre Weiss [60], extended the Weiss model of ferromagnets [56, 83] to systems with two sublattices [58, 84, 85]. The development of such a Weiss model for two sublattice systems with opposing sublattice magnetizations $\boldsymbol{M}_1 = -\boldsymbol{M}_2$ was fundamental for the understanding of AFMs and later ferrimagnets [60]. Here, we present the basic ideas, as outlaid in [52, 53], to derive the antiferromagnetic ordering temperature T_N.
The effective field acting on one sublattice largely depends on the magnetization of the other sublattice [52]

$$\boldsymbol{H}_{M1} = -\iota_{11}\boldsymbol{M}_1 - \iota_{12}\boldsymbol{M}_2, \tag{2.10}$$
$$\boldsymbol{H}_{M2} = -\iota_{21}\boldsymbol{M}_1 - \iota_{22}\boldsymbol{M}_2, \tag{2.11}$$

the proportionality constants ι_{11} and ι_{22} depend on the coupling inside one sublattice. The inter-sublattice exchange is described by ι_{12} and ι_{21}. For sublattices with the same atoms $\iota_{11} = \iota_{22} = \iota_{ii}$ and $\iota_{12} = \iota_{21}$. We can now consider the application of an additional external field $\boldsymbol{H}$ on Eqns. 2.10

$$\boldsymbol{H}_1 = \boldsymbol{H}_{M1} + \boldsymbol{H} = \boldsymbol{H} - (\iota_{11} - \iota_{12})\boldsymbol{M}_1, \tag{2.12}$$
$$\boldsymbol{H}_2 = \boldsymbol{H}_{M2} + \boldsymbol{H} = \boldsymbol{H} - (\iota_{21} - \iota_{22})\boldsymbol{M}_1. \tag{2.13}$$

In thermal equilibrium we can use the Brillouin function B_J to express the magnetization of each sublattice [53]

$$\boldsymbol{M}_{1,2} = \boldsymbol{M}^0_{1,2} B_J(x_{1,2}), \tag{2.14}$$

$$\boldsymbol{M}^0_1 = \boldsymbol{M}^0_2 = (\frac{n}{2}) g \mu_B J \tag{2.15}$$

with $n/2$ as the number of magnetic ions per sublattice, the Bohr magneton μ_B and the Lande factor g. The total number of angular momentum J, includes spin and orbital angular momentum. The Brillouin function B_J for each sublattice depends here on x_i,the ratio of the Zeeman energy and the thermal energy [80]

$$x_{1,2} = \frac{g \mu_\mathrm{B} J \boldsymbol{H}_{1,2}}{k_\mathrm{B} T}, \tag{2.16}$$

with the Boltzman constant k_B and temperature T. Similar to ferromagnets AFMs posses a critical temperature T_N at which their sublattice magnetizations are zero. At a small temperature above T_N we can use the small limit expansion of Brillouin function to derive the susceptibility χ of AFMs above T_N [52, 53]

$$\chi \propto \frac{1}{T + T_\mathrm{N}}. \tag{2.17}$$

In the paramagnetic phase the susceptibility can be expressed as [52]

$$\chi \propto \frac{1}{T - \Theta_\mathrm{P}}, \tag{2.18}$$

The paramagnetic temperature Θ_P is defined by the exchange interactions [53]

$$\Theta_\mathrm{P} = \frac{1}{2} C(\iota_{ii} + \iota_{12}). \tag{2.19}$$

In the case of a $\Theta_\mathrm{P} > 0$ the material is ferromagnetic and Θ_P is equivalent to the Curie temperature T_C. For $\Theta_\mathrm{P} < 0$ the material is antiferromagnetic and in the absence of a magnetic field the Néel temperature can be determined via [53]

$$T_\mathrm{N} = \frac{1}{2} C(\iota_{12} - \iota_{ii}). \tag{2.20}$$

Thus, the Néel temperature depends on the inter-lattice ι_{12} and intra-lattice ι_{ii} exchange. A high Néel temperature should be observed for materials with a strong inter-lattice and weak intra-lattice exchange.

2.3.2 Antiferromagnetic Domain Formation

Magnetically uniform regions, magnetic domains [56], are a result of minimizing the magnetic free energy [64], see Sec. 2.2. We can illustrate the ferromagnetic domain

formation by investigating a small rectangular element, see Fig. 2.5, following the discussion in Ref. [37].
Considering only the exchange energy and the crystalline anisotropy energy, the formation of a large uniform magnetization along the crystalline easy axes would be favorable for a FM, see Fig. 2.5 (a). Such a monodomain state would maximize the demagnetization energy w_{demag} due to the presence of large stray fields. The formation of additional domains along the easy axes, decreases the stray field and demagnetization energy, see Fig. 2.5 (b). However, it also creates a domain wall, a region separating different domains [86, 87], in which the spins change their orientation, increasing the exchange energy. The demagnetization energy can be further minimized by introducing closure domains at the edges of an element, see Fig. 2.5 (c). The creation of large closure domains increases the crystalline anisotropy energy of the system. Such an increase can be minimized by reducing the domain sizes [37], Fig. 2.5 (d).
Depending on the size of an element and the material properties different energy terms dominate the formation of ferromagnetic domains and determine the equilibrium domain structure. For FMs the demagnetization energy allows a tailoring of an elements magnetic properties by changing the size and aspect ratio [52, 53].

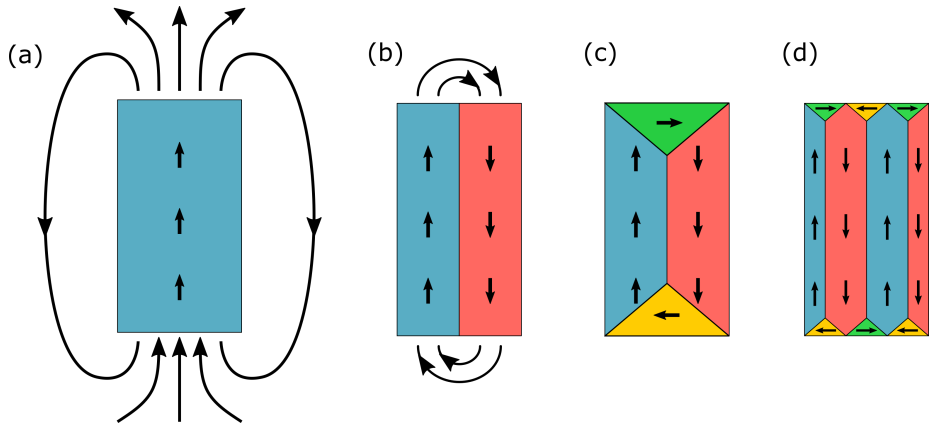

Figure 2.5: Domain structure and magnetic stray field of a single domain (a) and a two domain (b) state. The overall energy can be reduced via introducing closure domains (c) and reducing their size (d).

AFMs do not have a net magnetic moment, and therefore no multidomain structure is expected, due to the absence of the demagnetization energy. However, multidomain states have been observed in a variety of antiferromagnetic materials [31, 88–93]. One idea for the origin of the multidomain structure in AFMs was that the increase in disorder could offset the energy cost of the domain wall, but the change in entropy is typically not sufficient [94, 95]. Some domains are expected to arise from defects or pinning effects [44, 94]. However, annealed antiferromagnetic crystals do not naturally exhibit a single domain [31]. To understand the formation of antiferromagnetic domains, one must consider the effect of the strong magnetoelastic coupling in AFMs

and the influence of strain. The coupling between the strain and the antiferromagnetic domain formation has been investigated theoretically [43, 44, 94, 96], and also observed experimentally [50, 65, 66].
The following section first discusses the magnetoelastic and elastic energy contributions before introducing the basic concept of incompatibility and the influence of the destressing energy on antiferromagnetic domain formation.

2.3.2.1 Elastic and Magnetoelastic Energy

Lattice deformations introduce strain into the system and contribute to the free energy. One has to consider not only the elastic energy, but also magnetoelastic contributions due to the magnetoelastic coupling of the magnetic order to the lattice [44]. The following section first introduces some basic concepts of linear elasticity from Ref. [97] before discussing the elastic and magnetoelastic energy terms. Further information on linear elasticity and the modelling of the energy in antiferromagnetic thin films can be found in Refs. [67, 79, 98].

Linear Elasticity

If the length of an object L is changed by the amount ΔL to the length L', the strain u can be defined as the ratio of both $u = {}^{\Delta L}/_{L}$. In the case of an elongation of the object, the strain is tensile ($u > 0$). For a decreasing length the strain is compressive ($u < 0$). The strain can be assumed to be linearly proportional to the force (stress) σ, for small strains that do not permanently change the object.
We can now transfer this concept to the three dimensional space with the unit vectors $\hat{\boldsymbol{e}}_i$ and introduce a three dimensional strain tensor [97]

$$\begin{bmatrix} L_x' \\ L_y' \\ L_z' \end{bmatrix} = \begin{bmatrix} L_x \\ L_y \\ L_z \end{bmatrix} + \begin{bmatrix} u_{xx} & u_{xy} & u_{zz} \\ u_{yx} & u_{yy} & u_{yz} \\ u_{zx} & u_{zy} & u_{zz} \end{bmatrix} \begin{bmatrix} L_x \\ L_y \\ L_z \end{bmatrix}. \tag{2.21}$$

The strains along the unit vectors u_{xx}, u_{yy}, u_{zz} are here defined as normal strains. To illustrate the role of the strain u_{xy}, we can imagine two vectors, which span up a square area, see Fig. 2.6 (a). The strains $u_{ij,i\neq j}$ are responsible for a perpendicular deformation, see Fig. 2.6 (b) [97]. They are defined as shear strains, with $u_{i,j} = u_{j,i}$. Thus, the deformation can be described by six independent parameters, three normal strains (u_{xx}, u_{yy}, u_{zz}) and three shear strains (u_{yz}, u_{zx}, u_{xy}). The notation u_n can be used to refer to the six independent parameters [97].
The deformation (strain) is related proportionally to the force (stress) via Hookes law. Thus, the stress σ can be expressed as [97]

$$\sigma_n = C_{nm} u_n, \tag{2.22}$$

with the elastic stiffness C_{nm} as a fourth rank tensor. It can be shown that the elastic stiffness tensor reduces to only two independent elastic constants in an isotropic medium [97, 99].

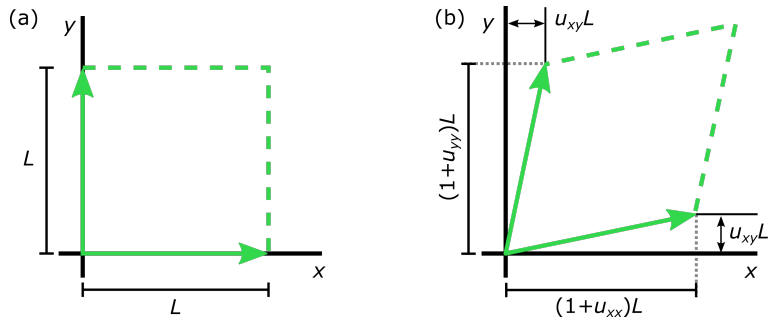

Figure 2.6: Vectors along x and y before (a) and after (b) deformation.

$$\begin{bmatrix}\sigma_1\\ \sigma_2\\ \sigma_3\\ \sigma_4\\ \sigma_5\\ \sigma_6\end{bmatrix} = \begin{bmatrix}C_{11} & C_{12} & C_{12} & 0 & 0 & 0\\ C_{12} & C_{11} & C_{12} & 0 & 0 & 0\\ C_{12} & C_{12} & C_{11} & 0 & 0 & 0\\ 0 & 0 & 0 & C_{44} & 0 & 0\\ 0 & 0 & 0 & 0 & C_{44} & 0\\ 0 & 0 & 0 & 0 & 0 & C_{44}\end{bmatrix} \begin{bmatrix}u_1\\ u_2\\ u_3\\ u_4\\ u_5\\ u_6\end{bmatrix}, \tag{2.23}$$

with $C_{44} = {}^{(C_{11}-C_{12})}/_{2}$. The independent constants C_{11} and C_{12} can be expressed by a set of elastic constants [97]:

$$C_{11} = \frac{2\mu(1-v)}{1-2v}, \qquad C_{12} = \frac{2\mu v}{1-2v}. \tag{2.24}$$

Here, μ is the shear modulus which linearly couples the shear stress to the shear strain and v is the Poisson ratio, the ration between transverse and normal strain $v = |u_{yy}/u_{xx}| = |u_{zz}/u_{xx}|$. Sometimes other elastic constants are also chosen to express C_{ii}, such as the Youngs modulus $E = \mu \cdot (2 + 2v)$ [97].

Elastic Energy

Assuming an isotropic material the elastic energy density w_{elast} can be expressed as [98]

$$\begin{aligned} w_{\text{elast}} = {} & \frac{1}{2}C_{11}[u_{xx}^2 + u_{yy}^2 + u_{zz}^2] + C_{12}[u_{xx}u_{yy} + u_{yy}u_{zz} + u_{zz}u_{xx}] \\ & + 2C_{44}[u_{xy}^2 + u_{yz}^2 + u_{zx}^2]. \end{aligned} \tag{2.25}$$

In the special case of investigating the domain structure in NiO thin films, the out-of-plane strains (u_{zz}, u_{yz}, u_{zx}) and the isotropic strains $(u_{xx} + u_{yy})$ can be neglected, as they are not crucial for the formation of the domain structure [50]

$$w_{\text{elas}} = \frac{1}{2}\mu[(u_{xx} - u_{yy})^2 + 4u_{xy}^2] + \frac{\mu(u_{xx} + u_{yy})^2}{2(1-2v)}. \tag{2.26}$$

Magnetoelastic Energy

The structure of a material is coupled to its magnetic order and can be influenced by external magnetic fields [100, 101]. The magnetoelastic coupling relates the magnetization to mechanical strain. It usually arises from spin-orbit coupling in FMs, with strong additional contributions from exchange coupling in AFMs [75, 81, 102]. In the simple case of a uniaxial FM one can observe either a contraction, see Fig. 2.7 (b) or an elongation, Fig. 2.7 (c), of the material along an externally applied magnetic field, depending on the sign of the magneto elastic constant λ [53].

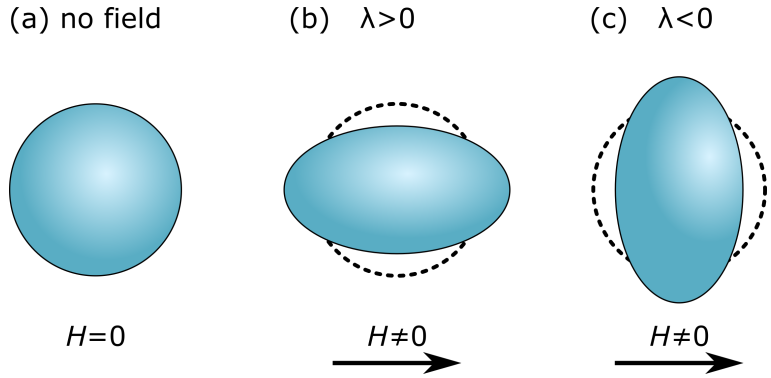

Figure 2.7: Illustration of the linear volume expansion of a magento-elastic material (a) upon the application of an external field $\boldsymbol{H}$ in the case of a positive (b) and negative (c) magnetoelastic coupling constant [53].

The magnetoelastic coupling is not only relevant for FMs in the case of external fields, but the coupling between the magnetic ordering and the strain also contributes to domain formation [64]. This is particularly relevant for AFMs. Due to the magnetoelastic coupling, a redistribution of domains is accompanied by a redistribution of strain [31]. The magnetostriction depends on the direction of the magnetization (or Néel vector) with respect to the crystallographic axes. However, it does not depend on the direction along an axis ($\lambda_{100} = \lambda_{\bar{1}00}$) [53]. Magnetostriction contributes to the magnetic free energy and can phenomenologically be described for a collinear AFM by [67]:

$$w_{\mathrm{me}} = \lambda_{ijkl} u_{ij} n_k n_l, \tag{2.27}$$

the magnetoelastic coupling constant λ_{ijkl} is here a tensor relating the strain to the antiferromagnetic order parameter $\boldsymbol{n}$. For modelling the domain structure of our antiferromagnetic thin films, one can again assume an isotropic crystal and neglect contributions from n_z [67]

$$w_{\mathrm{me}} = \lambda[(u_{xx} - u_{yy})(n_x^2 - n_y^2) + 4 n_x n_y u_{xy}]. \tag{2.28}$$

We can express the magnetoelastic energy as a function of the angle ϕ between the magnetic order parameter and the crystallographic axes [50, 79]:

$$w_{\mathrm{me}} = \lambda_{\mathrm{me}} M_{\mathrm{s}}^2 [\cos(2\phi)(u_{xx} - u_{yy}) + 2\sin(2\phi)u_{xy}], \tag{2.29}$$

$M_{\mathrm{s}}/2$ is here the saturation magnetization of a magnetic sublattice.

2.3.2.2 Incompatibility of Antiferromagnetic Domains

To illustrate the concept of incompatibility, we can imagine an antiferromagnetic thin film on a substrate. Initially there is no incompatibility, upon cooling through the Néel temperature the magnetic ordering of the thin film leads to strain and a deformation of the magnetic thin film [94]. However, the requirement of an interface with the substrate creates an incompatibility $\eta \neq 0$.

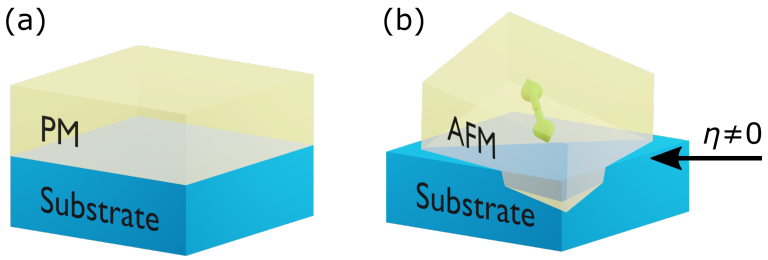

Figure 2.8: Illustration of the incompatibility of a magnetic thin film above (a) and below (b) the Néel temperature.

It has been observed that several insulating AFMs, such as NiO and CoO, exhibit strong magnetoelastic coupling and that their antiferromagnetic domains are associated with different lattice distortions [31, 94]. Different domains can therefore be treated as deformation twins [44]. This connection between the antiferromagnetic order and the lattice can be used to understand the formation of a multidomain state in AFMs. To minimize the strain inside an antiferromagnetic crystal, Slack proposed that AFMs exhibiting deformation twins could form special domain structures [103], as shown in Fig. 2.9 (a). In these domain configurations, lattice contractions of one type of domain are counteracted by the presence of a domain exhibiting an opposite strain, which reduces the overall strain of a crystal. While this concept can explain the preferential formation of only two different types of domains in annealed antiferromagnetic crystals [31], it does neglect the conditions at the surfaces and interfaces. At surfaces and interfaces, AFMs naturally exhibit differences in their elastic properties due to changes in their environment [94]. Depending on the domain termination, the interface of an AFM can exhibit an incompatibility, as shown in Fig. 2.9 (b) [94]. Such incompatibilities can be the source of additional strain, which contributes to the magnetic free energy via the so-called destressing energy [43, 44].

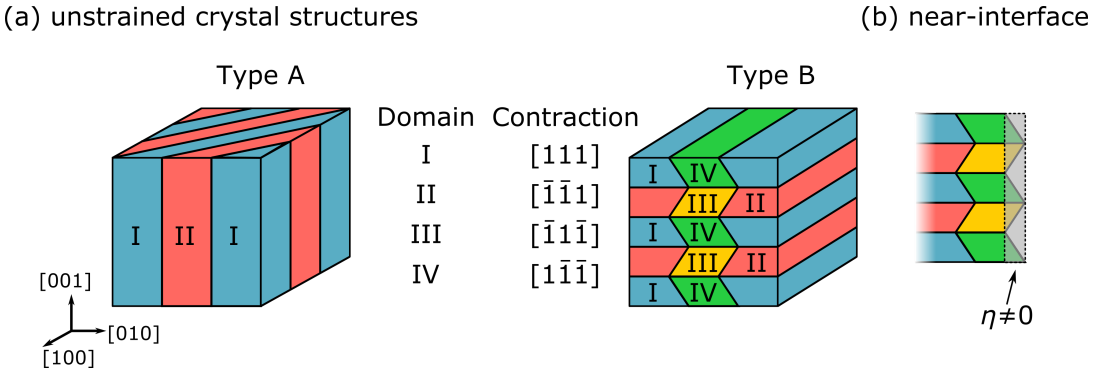

Figure 2.9: (a) Domain structure configurations that have been proposed by Slack to minimize the strain inside an antiferromagnetic crystal with magnetoelastic coupling [103]. At interfaces incompatibilities (b) can arise $\eta \neq 0$ when cooling through the Néel temperature.

2.3.2.3 Destressing Energy

The destressing energy w_{destr} is the result of the coupling between an antiferromagnetic thin film and a non-magnetic substrate and needs to be considered in addition to the magnetic free energy [43, 44]. It originates from the requirement of compatibility at the interface between the AFM and the substrate, which leads to additional strain [65].

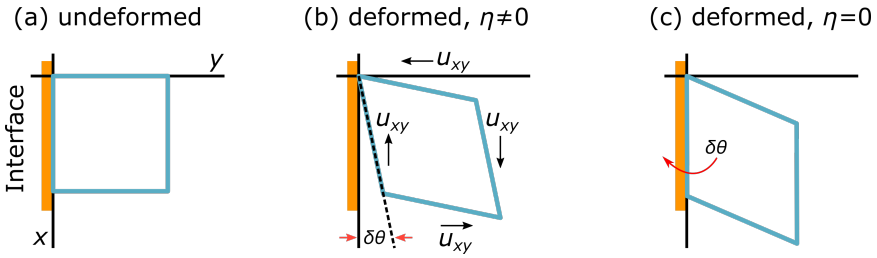

Figure 2.10: Deformation of a square (a) upon application of strain (b). The requirement for compatibility at the interface leads to additional strain (c).

To understand how incompatibility at the interface can lead to additional strain, we can consider a square element [97], see Fig. 2.10 (a), located at an interface. By applying a u_{xy} strain, the square element is deformed, see Fig. 2.10 (b), and compatibility with the interface is no longer ensured ($\eta \neq 0$), as $\delta\theta(u_{xy}) > 0$. However, the compatibility needs to be preserved. Thus, the incompatibility causes another strain u_{comp} that counteracts the incompatibility created by the original u_{xy} strain $\delta\theta(u_{xy}) = -\delta\theta(u_{\text{comp}})$, restoring the overall compatibility ($\eta = 0$), see Fig. 2.10 (c) [97].

A similar situation occurs in antiferromagnetic thin films due to substrate clamping. The magnetoelastic coupling induces spontaneous strains $\hat{u}_0^{\text{spon}}$ which are coupled to the magnetic order parameter. Additional elastic strains $\hat{u}^{\text{elast}}$ originate from the requirement of compatibility at the interface between the substrate and the thin film. Thus, the total strain $\hat{u}^{\text{tot}}$ tensor in the AFM layer can be represented as the sum of both $\hat{u}^{\text{tot}} = \hat{u}_0^{\text{spon}} + \hat{u}^{\text{elast}}$ [50]. The spontaneous strains can be determined from minimizing the equations for the elastic and magnetoelastic energies of a system and the elastic strains can be calculated from the compatibility equations [50], as the total strain should satisfy

$$\varepsilon_{ijk}\varepsilon_{lmn}\partial_j\partial_m u_{kn}^{\text{tot}} = \eta_{il} = 0, \tag{2.30}$$

ε_{ijk} is the antisymmetric Levi-Civita tensor. Thus, one can determine first the incompatibility caused by the spontaneous strains

$$\varepsilon_{ijk}\varepsilon_{lmn}\partial_j\partial_m u_{kn}^{\text{elast}} = \eta_{il}, \tag{2.31}$$

and in a second step, we search for a solution for the elastic strains. The destressing energy can then be calculated by inserting the additional elastic strains $\hat{u}^{\text{elast}}$ into Eqs. 2.26 and Eqs. 2.29 and is added to the total free energy of the system. The domain structure can then be determined via an energy minimization. However, one has to consider the boundary conditions [43]. In the case of a patterned device, changes in the chemical composition and symmetry at the edges of the device might lead to preferential formation of a certain domain at the boundary [104]. Such edge effects can be parameterized by an additional surface energy W_{surf}, which contributes to the boundary conditions. If one now minimizes the total energy of the system under consideration of the boundary conditions, one can determine the domain structure [50]. Here, only the general idea of determining the destressing energy for a system is presented, equations for different antiferromagnetic systems can be found in Refs. [50, 65, 66, 99].
The influence of the incompatibility induced strain from the substrate clamping has been observed for several AFMs [65, 66] and plays a crucial role in the formation of the antiferromagnetic domain structure. Our experimental investigations of shape-induced domain structures in NiO are presented in Sec. 5.1.

2.3.3 Spinstructure of Insulating AFMs

Among the insulating AFMs, the transition metal oxides NiO and CoO have received considerable attention because their spin structure is well understood, they have an accessible Néel temperature, and can be grown in thin films with high quality [42, 105]. In the following section, both materials are introduced and an overview of their antiferromagnetic spin structure is given.[1]

[1] *The following Sec. 2.3.3.1 and Sec. 2.3.3.2 were transcribed from Ref. [106] with the first author of this reference being the author of this thesis.*

2.3.3.1 NiO

NiO has possibly been the first material in which antiferromagnetic domains could be observed directly [31, 107]. The high Néel temperature of $T_N = 523\,K$ [108] in the bulk and its inert surface [109] make NiO an attractive candidate for investigating antiferromagnetic domain structures and antiferromagnetic spintronics. Below its Néel temperature, NiO adopts a type-II antiferromagnetic order: the spins are antiferromagnetically coupled between the {111} planes due to superexchange [74] and ferromagnetically coupled inside the {111} planes [110] as shown in Fig. 2.11.

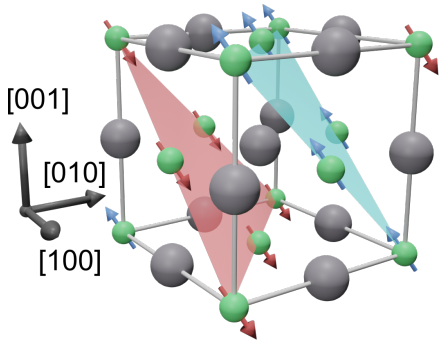

Figure 2.11: Spin structure of NiO. The spins are coupled ferromagnetically inside the {111} planes and antiferromagnetically between them, adapted with permission from Ref. [106].

The exchange striction between the antiferromagnetically coupled planes leads to a contraction between the {111} planes and a temperature dependent [111, 112] rhombohedral distortion of the cubic crystal [72, 113–115]. The symmetry of the original face-centered cubic (fcc) lattice allows four possible combinations of antiferromagnetically coupled {111} planes, which are each associated with a different strain. These domains are considered to be twin domains (T-domain) [31]. An additional smaller anisotropy due to dipolar interactions leads to a threefold set of preferential spin orientations within the ferromagnetic planes along the [112] directions, the so-called spin domains (S-domains) [31, 116–118]. Thus, there are a total of 12 different Néel vector orientations possible in the bulk NiO crystal. If one additionally considers 180° domains, see Fig. 2.12, bulk NiO exhibits a total of 24 possible domain configurations. The impact of strain on the antiferromagnetic domain structure has been studied extensively in NiO [31, 103, 107, 116, 118–124]. In particular, external strain such as strain during cleaving, polishing, sample glue, or handling with tweezers that exert pressure can easily manipulate the antiferromagnetic domains [116, 125–128].
Furthermore, the domain structure of both, bulk and thin film NiO samples is influenced by the growth conditions such as growth temperatures [129, 130], oxygen pressure [131], and film thickness [109]. Importantly, the strain resulting from the lattice mismatch with the substrate plays a significant role for the anisotropy [130, 132].

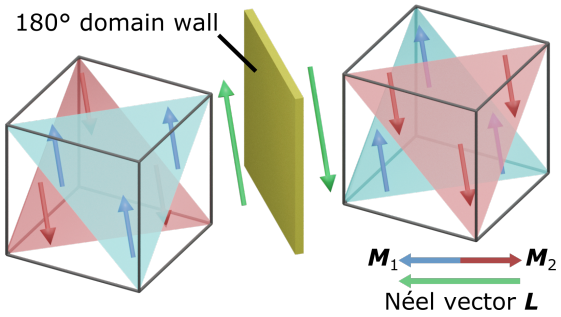

Figure 2.12: Depiction of 180° domains in which the magnetization of the sublattices (red and blue) is interchanged and the Néel vector (green) points along the opposite direction, adapted with permission from Ref. [106].

Compressive strain in NiO grown on MgO leads to an out-of-plane alignment [109, 133] and tensile strain in NiO grown on Ag [129] leads to a preferential in-plane alignment of the Néel vector [134, 135]. Large domain sizes can be achieved by annealing [107, 136]. As a result, it is crucial to study the domain structure of NiO thin films by imaging, before modulating the domain structure by currents, patterning or optical irradiation [137, 138].

2.3.3.2 CoO

First neutron diffraction data has indicated a similar magnetic structure for CoO as for NiO [72]. However, the spin structure of CoO differs from NiO [71, 72, 139]. Investigations of the crystallographic structure of CoO have revealed a tetragonal distortion of the fcc lattice below the Néel temperature (290 K) in contrast to the rhombohedral distortion in NiO or MnO [140–142].
Neutron diffraction measurements could not provide clear information on the spin structure of CoO and different models have been proposed [143]. Initially, a collinear spin structure has been assumed in which the spins are ferromagnetically coupled inside the {111} planes [72, 144–146]. However, the tetragonal symmetry of the crystal has led to the proposal of a noncollinear spin structure in a multi-spin-axis model [146–148]. Further studies have revealed that the tetragonal deformation can occur in a collinear spin alignment and is additionally accompanied by a monoclinic deformation [71, 149, 150]. After the experimental observation of the additional monoclinic distortion, the magnetic structure of CoO is widely accepted to be collinear [143, 150, 150–154]. However, we note that recent studies have again proposed a noncollinear structure for CoO [155–157]. In the collinear structure, the spins of CoO are coupled ferromagnetically inside the {111} planes and antiferromagnetically between the planes. The tetragonal distortion of CoO along one of the three cubic axes leads to the possible formation of three different twin domains, compared to four different twin domains in NiO [92].

Large domains in CoO crystals can be obtained by annealing the crystals above the Néel temperature [150, 152, 158, 159] and the application of external strain can lead to the preferential stabilization of certain domains [152]. The magnetoelastic coupling can be observed in birefringence measurements [153] and can be utilized to image the domains of CoO crystals in X-ray diffraction measurements [150].
Similar to NiO, the magnetic structure of CoO depends on the growth parameters and on the substrate-induced strain [92, 160]. In thin films, compressive strain favors an in-plane alignment of the magnetic moments [161, 162] and tensile strain leads to an out-of-plane alignment [161, 162]. For CoO grown on MgO(001) the spins align in the plane of the film [163] and two in-plane magnetic easy axes along [110] or [$\bar{1}$10] are present [105, 164]. Birefringence imaging can be used to image the domains of thin-films [165, 166] and second-order magneto-optical effects can also be used to study the magnetization dynamics of CoO thin films [167].
CoO is often considered to be similar to NiO, however, it differs in its crystallographic structure, magnetic properties [168], and electrical properties [169].

2.4 | Current-Induced Effects

In this section, we briefly describe several current-induced effects relevant to the study of the current-induced switching of insulating AFM and HM bilayers. First, we introduce the creation of spin accumulations at the interface. We then discuss their use for reading the antiferromagnetic order and how the antiferromagnetic order can be switched. Finally, we conclude this section by discussing heating effects resulting from the high current densities used in switching experiments.

2.4.1 Spin Hall Effect

The classical Hall effect refers to the deflection of charge carriers inside a magnetic field [170, 171]. The spin Hall effect (SHE) refers to the spin dependent deflection of electrons inside a material [172], a comprehensive review is given in Ref. [35].
In materials with large spin-orbit coupling, like HMs, an electrical current generates a transverse spin current which is polarized perpendicular to the plane [35], see also Fig. 2.13 (a). The SHE can originate either from intrinsic contributions [173] or extrinsic contributions [174], similar to the anomalous Hall effect [175]. The efficiency of the SHE in a material is often defined by the spin Hall angle $\Theta_{\mathrm{SH}} = j_{\mathrm{S}}/j_{\mathrm{C}}$, the ratio between the applied charge current j_{C} and the generated spin current j_{S} [25].
A common material for spin current generation is Pt as it exhibits a large spin Hall angle [35]. However, one has to be careful when using Pt due to possible proximity effects [33]. Due to reciprocity also the inverse spin Hall effect (iSHE) exists, which describes the conversion of a spin current into a charge current [176]. For the interpretation of experimental results which include the SHE or iSHE it can be advantageous to use materials with negative and positive spin Hall angle to differentiate between spin and temperature dependent effects.

2.4.2 Spin Hall Magnetoresistance

The above-mentioned SHE can be used to measure the magnetic orientation in bilayers of HMs and magnetic insulators. Spin Hall magnetoresistance (SMR) refers to the magnetization dependent resistance changes in the HM layer depending on the magnetization of the adjacent insulator [33, 177]. The current flow in the HM layer leads to a spin accumulation σ at the interface due to the SHE. In a simple picture, the spin accumulation can either be absorbed or reflected at the interface, see Fig. 2.13, depending on the magnetic ordering of the insulator.

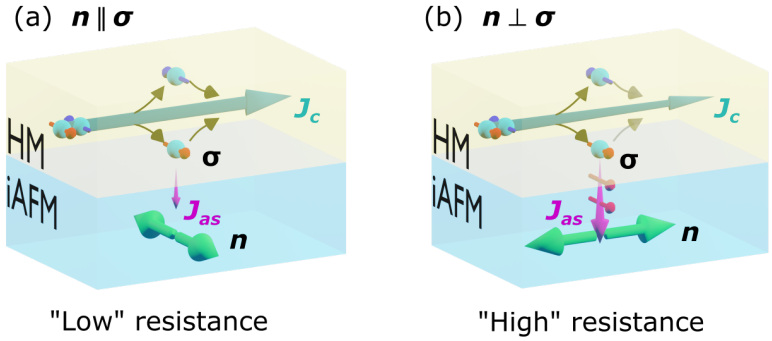

Figure 2.13: Charge current flow $\boldsymbol{J_c}$ through a HM layer generates a spin current via the SHE, which creates a spin accumulation σ at the interface. Depending on the orientation of the Néel vector $\boldsymbol{n}$ in an adjacent insulating antiferromagnet (iAFM), the spin current can be mostly reflected or absorbed $\boldsymbol{J_a}$. Leading to a "low" (a) and "high" resistance state (b).

In the case the magnetic ordering is perpendicular (parallel) to the current direction the resistance decreases (increases) [33]. The theoretical model developed for FMs [33, 178] can be transferred to AFMs [179, 180].
In bilayers of insulating AFMs and HMs the resistance variation $\Delta R/\bar{R}$ depends on the orientation of the Néel vector $\boldsymbol{n}$ with respect to the current direction $\boldsymbol{j}$. The longitudinal ($\parallel j_x$) and transverse ($\perp j_x$) SMR can be modeled as [180]

$$\frac{\Delta R_{xx}}{\bar{R}} \propto \frac{\Delta\rho}{\rho}\langle n_y^2\rangle, \tag{2.32}$$

$$\frac{\Delta R_{xy}}{\bar{R}} \propto \frac{\Delta\rho}{\rho}\langle n_x n_y\rangle, \tag{2.33}$$

here the current flows along x and y is perpendicular to x in the sample plane, $\langle\cdots\rangle$ denotes the averaging over the domain structure. Both SMR signals are dependent on the SMR coefficient $\Delta\rho/\rho$, which is material dependent with the resistivity ρ. Due to the dependence on n_x and n_y the transverse SMR is used in current-induced switching experiments to determine the reorientation of the Néel vector in AFM/HM bilayers [181, 182].

2.4.3 Spin Torques

The field of spintronics aims to use the spin of an electron to transport information. In magnetic tunnel junctions, spin-transfer torques (STTs) are currently used to switch the magnetic order in STT-RAM (random access memory) [19, 21, 36, 183]. Current passing through a magnetic layer can be spin polarized and can exert a torque on the local magnetic moments in an adjacent layer [184, 185]. However, STTs require conductive materials. Spin-orbit torques (SOTs) are currently being explored as a more energy efficient way to switch the magnetic order [25, 186–188]. SOTs can potentially arise from different effects. In magnetic systems lacking inversion symmetry, the inverse spin Galvanic effect can lead to a spin accumulation at the interface [189]. Alternatively, the SHE of materials with large spin-orbit coupling can be used to generate a spin accumulation. In the following, we discuss how SOTs generated at the interface between an insulating AFM and a HM layer can induce a switching of the magnetic order [25].

Spin-Orbit Torque Based Switching of AFMs

SOTs can generally be separated into two parts: A field like torque, acting similar as in the case of an applied external field, and an antidamping-like torque, see Fig. 2.10 (a). If the torque acts differently on the different sublattices one refers to a staggered torque. Staggered bulk torques are crucial for the rotation of the Néel vector in metallic AFMs with broken inversion symmetry [190–192]. However, due to the lack of inversion symmetry breaking and the insulating nature of NiO and CoO, we focus on non-staggered interfacial torques. We can formulate the SOT acting on one sublattice with magnetization M_1 [25]:

$$T = T_{\parallel} \boldsymbol{M}_1 \times (\boldsymbol{P} \times \boldsymbol{M}_1) + T_{\perp} \boldsymbol{M}_1 \times \boldsymbol{P}, \tag{2.34}$$

the vector $\boldsymbol{P}$ depends on the symmetry of the system and $T_{\parallel}(T_{\perp})$ is the magnitude of the torque component in (out-of) the $(\boldsymbol{M}_1, \boldsymbol{P})$ plane [25].
To understand how one can manipulate AFMs, one can consider the effect of the different torques on the antiferromagnetic ordering as outlaid in Ref. [25]. For a field-like torque acting on both sublattices we can imagine a field applied perpendicular to the Néel vector, see Fig. 2.10 (b). The field would induce a canting of the antiferromagnetic order and opposite torques T_{H} on each sublattice. However, these torques are compensated by the exchange torques T_{Ex}, which originate from the strong antiferromagnetic exchange interaction. Thus, the torques compensate each other and no reorientation of the magnetic order is expected from a field-like torque [25]. In the case of an antidamping-like torque, the magnetic moments are canted, and the exchange torque T_{Ex} acts on the individual sublattices. However, the exchange torque is not compensated and thus a rotation of the antiferromagnetic order around $\boldsymbol{P}$ is allowed [25].
Interfacial spin-orbit torques are predicted to possibly reorient the Néel vector in insulating AFM/HM bilayers [193], here we briefly introduce a few results from Ref. [193].

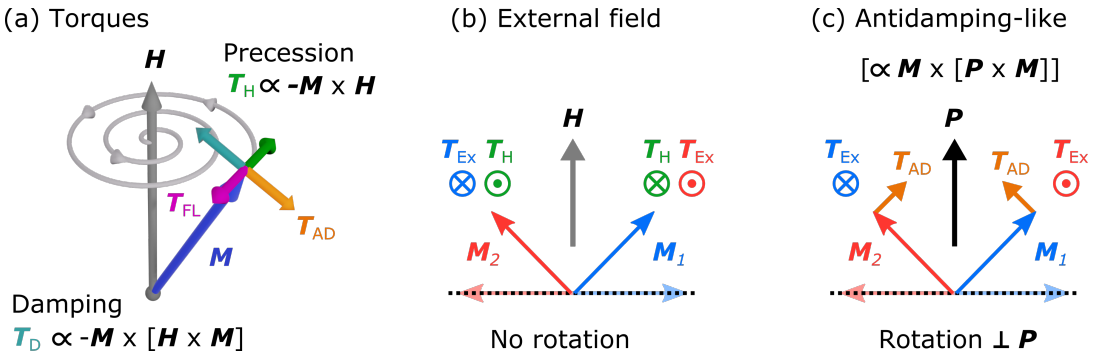

Figure 2.14: (a) Depiction of different possible torques acting upon a magnetic moment $\boldsymbol{M}$ in an external field $\boldsymbol{H}$. (b) Field-like torque and (c) antidamping-like torque acting on a collinear AFM with magnetic moments $\boldsymbol{M_1}$ and $\boldsymbol{M_2}$.

As mentioned in Sec. 2.4.1, the flow of a charge current j_C through a HM layer can lead to spin accumulation at the AFM/HM interface via the SHE. Interfacial spin-orbit torques can act on the domain wall in the AFM. The interfacial antidamping torques can then lead to an antiferromagnetic domain wall motion that can exceed the velocity v of a ferromagnetic domain wall. The ferromagnetic domain wall velocity v_F is usually limited by the Walker breakdown, which induces a precessional motion of the domain wall and reduces its velocity [25, 194]. However, this phenomenon is absent for antiferromagnetic domain walls [193, 195]. The velocity of an antiferromagnetic domain wall v_{AFM} is predicted to increase linearly with the applied current j_C and the effective spin Hall angle Θ_{SH} of the HM [193]

$$v_{AFM} \propto \frac{j_C \cdot \Theta_{SH}}{d_{AFM}\alpha_d} \tag{2.35}$$

However, the velocity is inversely proportional to the thickness of the antiferromagnetic layer d_{AFM} and the damping coefficient α_d of the material. Consequently, AFMs with low damping, such as NiO or CoO [196, 197], are excellent candidates for achieving high domain wall velocities [193]. Model calculations suggest that v_{AFM} could reach velocities of 1-10 $\mathrm{km\,s^{-1}}$ for current densities of $10^7\,\mathrm{A\,cm^{-2}}$, making them faster and more energy efficient than FMs [25]. However, the speed of antiferromagnetic domain wall motion is also limited due to a predicted Lorentz contraction of the domain walls at high speeds, resulting in the emission of THz radiation [193]. Thus, the combination of AFM/HM bilayers could potentially be used as a source of current-driven THz radiation [193]. Current driven THz radiation would be desirable for applications such as the development of artificial neurons [198], but is still experimentally challenging [199].
The current-induced switching of iAFMs with Pt capping layer was observed experimentally, but the underlying switching mechanism is still debated [40–42, 193, 200]. Different mechanisms based on interfacial antidamping-like torques have been put

forward in which the switching is achieved by either a coherent rotation of $\boldsymbol{n}$ or an induced domain wall motion [41, 42, 193, 200]. Mechanisms based on domain wall chirality dependent switching are now questioned, as high resolution imaging could not reveal chiral domainwalls [42, 201]. In addition, it became clear, that in order to determined the underlying mechanism in iAFM/HM bilayers also non-magnetic heating effects need to be considered in the interpretation of measurement signals [202].

2.4.4 Joule Heating Effects

The electrical switching of AFMs requires high current densities to achieve sufficient torque to reorient the magnetic order [203]. High current densities on the order of $j \approx 10^{12}\,\mathrm{Am}^{-2}$ lead to a significant heating of the devices due to the Joule heating $\Delta T \propto j^2$ [204]. Such current-induced heating can assist the electrical switching of AFMs in overcoming anisotropy barriers between different magnetic states [205]. However, high currents can also lead to a permanent damage of the device through current-induced electromigration, a diffusion of material [203, 206]. These non-magnetic effects can significantly influence the resistance and thus the measured SMR signals in electrical switching experiments, an analysis of non-magnetic contributions to the SMR can be found in Refs. [203, 207].

Separating Magnetic SMR and Non-Magnetic Transport Signals

In electrical switching measurements via transverse SMR, two different types of signals can be distinguished. The first type is a triangular or sawtooth-like signal, where the resistance continues to change after applying multiple pulses along the same current direction [42, 202, 207, 208]. The second type is a step-like signal, where the resistance changes significantly for the first pulse along a new current direction, but then reaches a plateau after applying multiple pulses [42, 182, 208].
For our NiO(10 nm)/Pt(2 nm) thin films, Felix Schreiber conducted a careful comparison of the electrical SMR signal with optically observed changes in the domain structure [209]. The results are presented in Fig. 2.15, where in Fig. 2.15 (a) the pulsing direction is changed after the application of 5 pulses and kept constant in Fig. 2.15 (b). The optically observed changes in the domain structure (represented by orange triangles) exhibit a plateau after the application of the first few pulses. Therefore, any further changes in the electrical signal (represented by blue dots), after the domain structure changes have reached a plateau, can be attributed to non-magnetic contributions to the electrical switching signal. These non-magnetic contributions arise from the aforementioned electromigration and device damage. In our thin films, the non-magnetic signal contribution to the SMR signal shows a roughly linear dependence on the number of applied pulses. By subtracting this linear contribution from the SMR signal, the electrical switching signal can be correlated with the optically observed switching.

It should be noted that such a linear subtraction is a simplification of the underlying processes and may not hold for high current densities near the device limit [182]. Furthermore, the applicability of this procedure to other material systems is not clear since a step-like signal can also originate from a non-magnetic background [203] and a sawtooth shaped signal can originate from a magnetic switching [210].

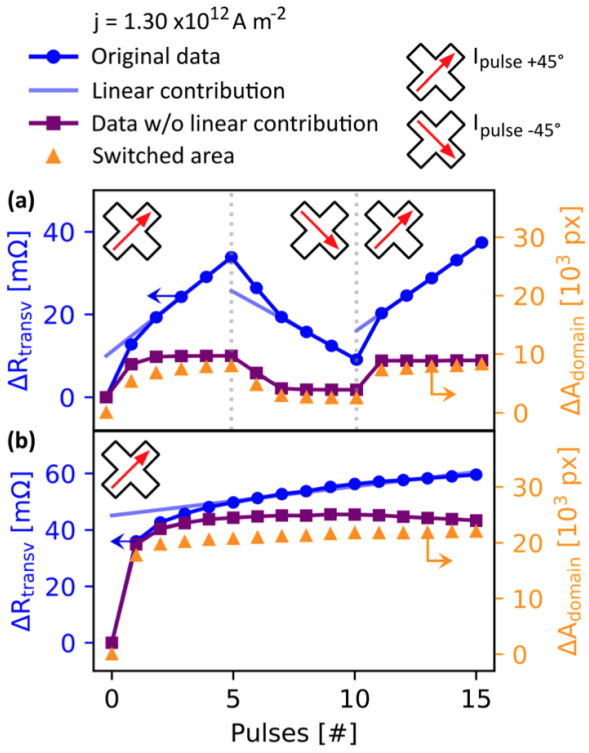

Figure 2.15: Comparison between the electrically measured switching signal (blue) and optically observed switching (orange) of an MgO(001)/NiO(10 nm)/Pt(2 nm) thin film. The current direction is switched after five consecutive pulses ($\Delta T = 0.1$ ms) (a), or kept constant (b). The non-magnetic contribution to the transport signal can be removed by linear subtraction (violet). Reprinted from [182], with the permission of AIP Publishing.

Thermomagnetoelastic Switching

The application of high current densities not only results in Joule heating of a device, but also leads to inhomogeneous heating, causing strain gradients within the device [204]. This strain depends on the device and the pulse geometry [105, 204]. Antiferromagnetic insulators such as NiO or CoO are known for their magnetoelastic coupling, and strain can be used to manipulate their antiferromagnetic order [162, 211]. It has been suggested that the switching behavior of AFM/HM bilayers is not only influenced by the intrinsic strain of the samples [200], but may even originate from a heat and strain based switching mechanism [105, 204].
Thus, the switching direction of a device would depend not only on the current direction, as for SOT-based mechanisms, but also on the distribution of current-induced heat and strain [105]. Therefore, current-induced switching in one region of a device could be different from that in other regions. A study of different device geometries via SMR is limited by averaging over the underlying domain structure [180].
Consequently, to uncover the origin of current-induced switching in AFM/HM bilayers, it is necessary to image the current-induced switching [182]. In the next Chap. 3 we discuss how to image the antiferromagnetic domain structure in our thin films, which allows us to reveal the origin of current-induced switching in MgO(001)/NiO(10 nm)/Pt(2 nm) thin films in Chap. 4.

3 | Methods

For the investigation of the control and manipulation of antiferromagnetic domains high quality thin films and advanced imaging techniques are required. This chapter first introduces the sample fabrication before discussing the imaging of antiferromagnetic domains via birefringence and X-ray based microscopy.

3.1 | Sample Fabrication

The following sections give an overview of the growth of the antiferromagnetic thin films and how they can be patterned into the devices used in this work.

3.1.1 Thin Film Deposition

Sputtering [212–214] is a common technique for growing high quality thin films in a research or industry environment, due to its high deposition rate [214–216]. The high-quality growth of the antiferromagnetic thin films is essential for the observation and manipulation of large antiferromagnetic domains, which can exhibit a strong dependence on the growth conditions [42, 217].
The NiO and CoO thin films used in this work have been grown via an automated magnetron sputtering system in the group of Prof. Dr. Eiji Saitoh at the Tohoku University, based on a recipe that has been developed by Dr. Rafael Ramos. Prior to this work, NiO and CoO samples have been grown at the Tohoku University by Christin Schmitt, Adithya Rajan and Dr. Lorenzo Baldrati. The samples grown by Christin Schmitt have been primarily used for the experiments presented in this work. Additional samples have been grown by Dr. Takashi Kikkawa and the author after the relocation of the sputtering machine to the University of Tokyo. These samples have not been used in the work presented in this thesis, but are being investigated in ongoing projects.
Due to the importance of high sample quality, this section first provides an overview of basic sputtering techniques and then introduces the experimental setup that has been used for the deposition of the antiferromagnetic thin films used in this work.

3.1.1.1 Sputtering Fundamentals

The fundamental principle of a sputtering machine is the ablation of a material from a target and the subsequent deposition of the target material onto a substrate [215, 216]. To increase the quality of the grown films, the entire process is performed in a vacuum chamber. A simple DC sputtering system is depicted in Fig. 3.1 (a). For the sputtering a noble gas is introduced into the chamber. The noble gas of choice is often argon because it is an inert gas with a high sputtering yield [218]. By applying a high DC voltage between the target cathode and the chamber and substrate anode, electrons are accelerated away from the cathode and randomly collide with Ar atoms, ionizing them in the process. The ionization is accompanied by the emission of photons, resulting in the formation of a plasma that can be observed visually [219].
The Ar^+ ions are accelerated towards the target (cathode) due to their positive charge. They cause a collision cascade at the surface of the target, resulting in the ejection of target atoms [220, 221]. The target atoms are radially distributed in the surrounding space and accumulate on the substrate. The rate at which material is removed from the target is defined as the sputter yield S [221]:

$$S = \frac{\text{Atoms removed}}{\text{Incident ions}} \tag{3.1}$$

A disadvantage of DC sputtering is a low sputter yield and possible charging effects at the surface of insulating targets. Both can be overcome by replacing the DC voltage with an AC voltage [216]. This type of sputtering is called radio frequency (RF) sputtering, due to the common usage of an AC current with a radio frequency of 13.56 MHz [216, 222]. In RF sputtering the electrons oscillate near the target material due to the oscillating electric field, which increases the collision rate of the electrons with the Ar atoms. Thus, the ionization rate increases, the key to a higher sputter yield. The higher ionization rate increases the emission of target atoms and allows the operation of the sputter chamber at lower gas pressures [223].
The sputtering rate can be increased further by trapping electrons near the target by magnetic fields in so-called magnetron sputtering (MS) [215, 216], see Fig. 3.1 (b). Permanent magnets create a magnetic field orthogonal to the electric field. The magnetic field traps the electrons in a circular orbit over the target, further increasing their collision rate [215]. A disadvantage of MS is the increased target ablation along the electron path [215], leading to an inhomogeneous ablation of the target. In addition, magnetic targets can interfere with the magnetic field and reduce the effectiveness of the MS. One way to minimize these issues can be to use more complex magnet geometries [222].
Another option is to further increase the sputter yield by using an additional coil above the target in so-called inductively coupled plasma-assisted magnetron sputtering (ICP MS). Reviews on this technique can be found in Ref. [223] and Ref. [224]. The coil is driven by an RF frequency, creating an oscillating magnetic field, which leads to an additional oscillating electron motion and further increases the sputter rate. Due to the high plasma density in ICP MS, an increased ionization rate of the target

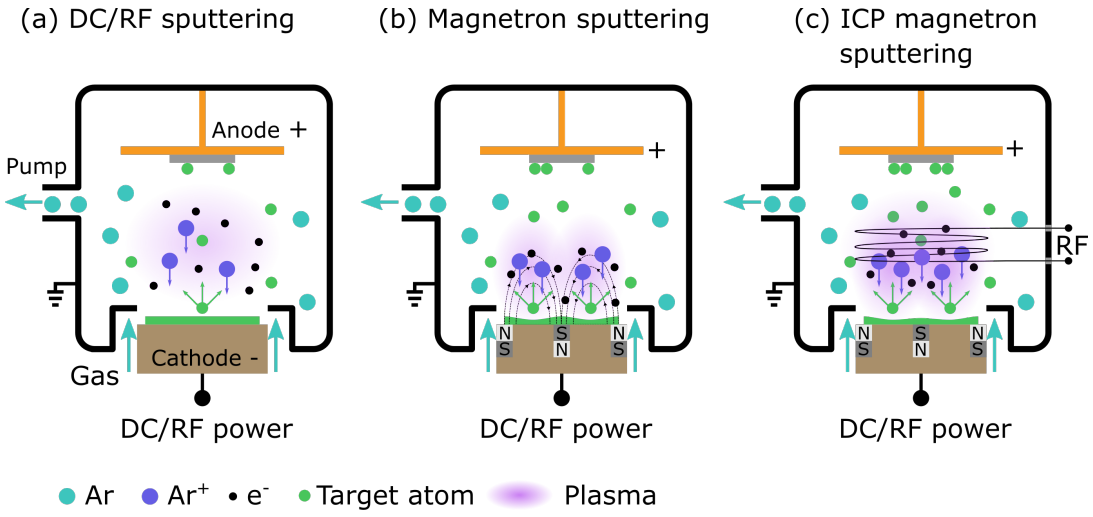

Figure 3.1: Schematic representation of different sputtering modes. (a) A basic sputtering system in which DC or RF voltages can be applied to the target cathode. (b) In a magnetron sputtering system the magnetic field of permanent magnets confines the electrons, leading to an increased sputter yield, and increases the deposition of target atoms on the substrate (orange). (c) Magnetron sputtering can be combined with an inductive coil in ICP MS.

atoms has been observed for metallic and magnetic materials [224–227]. The higher ionization rate of the target atoms in ICP MS sputtering can lead to significant changes in the crystal structure, texture and oxygen incorporation for the growth of thin films [223, 228]. However, material buildup on the coils can be an issue, making ICP MS with an immersed coil an impractical technique for industrial applications. ICP MS is still a powerful sputtering technique for producing high quality thin films in a research laboratory and has been used to deposit the NiO thin films used in this work [223, 224].

3.1.1.2 Growth of NiO and CoO Thin Films

The growth of the insulating NiO and CoO thin films is performed in a customized version of the QAM4 sputtering system from ULVAC [229] at the Saitoh Laboratory. In addition to Ar as sputtering gas, oxygen gas is introduced into the chamber for a reactive sputtering of Ni and Co targets [230].
In reactive sputtering, the oxygen reacts with the Ni and Co atoms to form NiO and CoO respectively. The oxidization reaction occurs on the cathode surface and the substrate during the deposition [215, 222, 231]. The pressure of the oxygen gas is a critical handle to control the growth of a film, influencing the adatom diffusivity and the film structure [131, 228, 230].

A schematic of the sputtering chamber used to grow the samples is depicted in Fig. 3.2. The substrates are placed upside down in a rotating copper holder above the sputtering targets. The targets are positioned at an oblique angle below the target, allowing the placement of up to four targets. The oblique angle reduces the surface roughness of the sputtered films [232]. The target holders are suitable for MS and can be operated with either DC or RF voltage. Some cathodes, such as the Ni cathode, are additionally equipped with a single turn helical coil (HC), which enables ICP MS. Deposition times can be electrically controlled via shutters above the targets, or via a linear shutter that can be inserted in front of non-rotating substrate. The sample holder can be heated for high temperature depositions. The sputtering chamber is connected via a transfer chamber to a similar sputtering chamber for the subsequent deposition of Pt or other non-magnetic materials. Exact process details and growth recipes are given in the Appendix A.1.

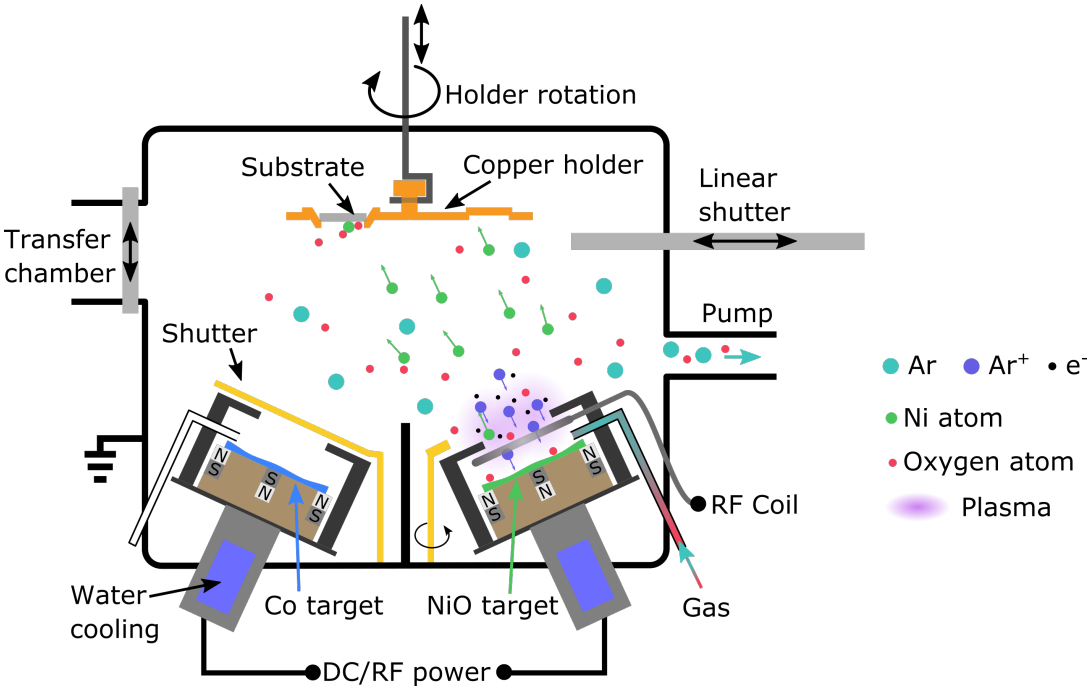

Figure 3.2: Sketch of one of the chambers of the ULVAC sputtering system in the Saitoh Laboratory. The Ni target is equipped with a helical coil, enabling ICP MS.

3.1.2 Structuring of Thin Films

For the research presented in this work, sputtered AFM/HM bilayers have been patterned into various device geometries: cross-like devices to control the current flow in our samples, different geometric elements to observe shape-induced changes in the domain structures and grids and markers for optical switching experiments. In the following, the basic patterning steps are outlined, as discussed in Ref. [233].
The structuring of thin films can be achieved by means of optical or electron beam lithography in a four-step process, as shown in Fig. 3.3. In the first step, see Fig. 3.3 (a), a radiation-sensitive polymer layer, a so-called photoresist, is applied to the surface of the bilayer. The samples are cleaned in a multistep cleaning process to remove any surface contamination from the sample surface. After depositing a few drops of photoresist on the cleaned surface, the sample is rotated in a spin-coater to ensure a flat and uniform distribution of the photoresist. After the photoresist is applied, the sample is placed on a hot plate to aid the evaporation of additional solvents in the photoresist liquid.
In the second step, see Fig. 3.3 (b), a pattern is imprinted on the polymer by partially illuminating the photoresist. In optical lithography, a structured glass plate with Cr patterns is placed slightly above or in contact with the resist on top of the sample. Illumination with a Mercury-vapor lamp causes a chemical reaction of the exposed areas of the photoresist. In electron beam lithography, exposure is performed by a focused electron beam that scans the surface along defined patterns.
In the third step, the patterned films are developed by immersing them in a developer solution, see Fig. 3.3 (c). There are usually two types of photoresist. A “positive” photoresist causes a weakening of the polymer chain in the exposed areas, which is removed by the developer. This reproduces the unexposed mask pattern, the Cr pattern. For a “negative” photoresist the exposure leads to a strengthening of the polymer chains and development removes the unexposed areas, reproducing the exposed pattern.
In the final step, the patterned photoresist is used to structure the thin films, see Fig. 3.3 (d). An inert gas plasma, such as Ar ions, can be used to remove the patterned material in an etching process, similar to the ablation of target material in the sputtering process described in Sec. 3.1.1. Alternatively, additional material, such as markers, can be deposited in the patterned areas before the resist is removed by immersion of the sample in acetone in a lift-off process. This allows for a wide variety of thin film structures, as well as the combination of etching and deposition of material. The lithography recipes for the resist handling are in the Appendix A.2.

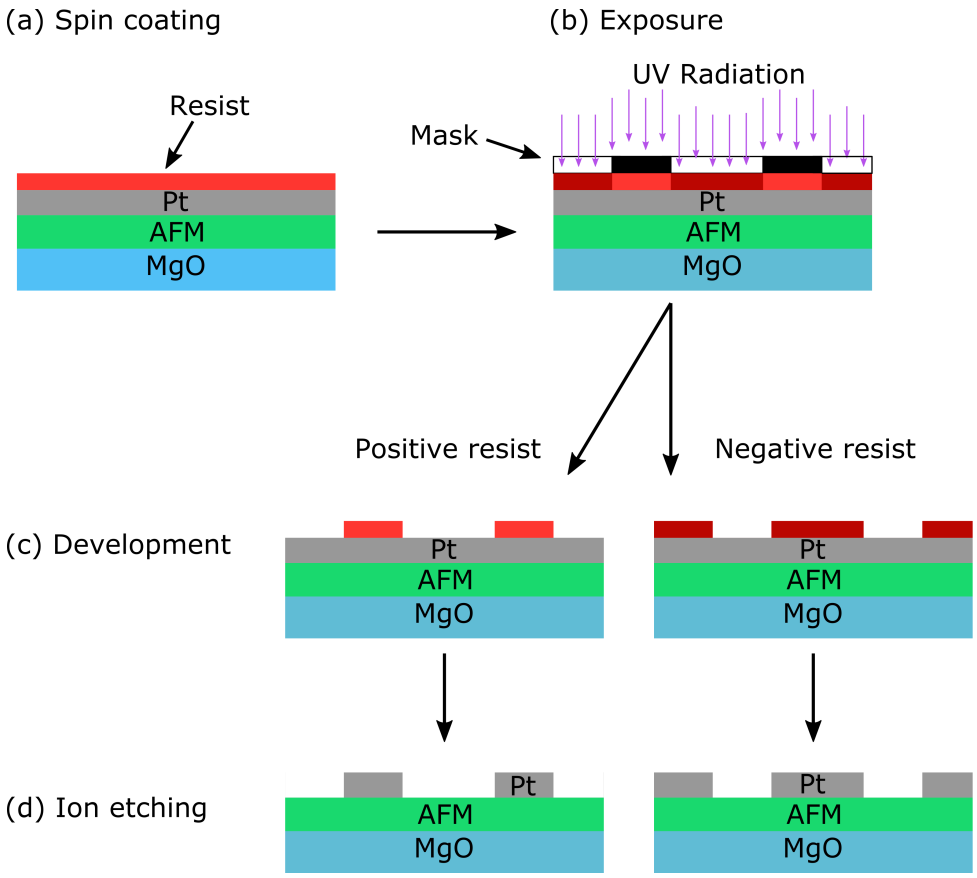

Figure 3.3: Different steps of the patterning process are depicted. After the application (a) and exposure (b) of the photoresist, the resist is developed (c). Depending on the type of the resist, negative or positive, different final structures can be produced by ion beam etching (d).

3.2 | Birefringence Imaging of Antiferromagnetic Domains

A primary obstacle in the development of antiferromagnetic devices is the ability to read the antiferromagnetic ordering. Unlike their ferromagnetic counterparts, AFMs do not possess any net magnetic moments or stray fields. Thus, it is more challenging to detect their magnetic order [47, 106, 234].
One way to image the antiferromagnetic domain structure is by birefringence imaging [32]. Birefringence refers to the dependence of the refractive indices of a material on the polarization and propagation direction of light. The first observations of linear magnetic birefringence (LMB) were made on garnets by Dillon [235], who used the dependence of the birefringence on the magnetic ordering to visualize magnetic domain structures. Such a coupling between the magnetic order and the birefringence is usually considered to originate either directly from magneto-optical effects or indirectly from lattice distortions due to the magnetoelastic coupling [236]. The magnetic birefringence of various systems has been intensely studied and reviewed after its discovery [236–240].
The following section gives a brief overview over magnetically induced birefringence, reviews the development of birefringence imaging in transition metal oxides, with a focus on NiO, and describes the experimental setup that was used for the birefringence imaging in this work.

3.2.1 Birefringence

Polarized visible light is a common tool for the study of ferromagnetic domain structures. The magneto-optical Kerr effect induces a change in the polarization and ellipticity of linearly polarized light upon reflection [241]. Similarly, the magneto optical Faraday effect acts on transmitted light [242]. The effective change in the polarization and ellipticity of the light depends in both cases linearly on the magnetization $\boldsymbol{M} = \boldsymbol{M}_1 + \boldsymbol{M}_2$, with $\boldsymbol{M}_1, \boldsymbol{M}_2$ as sublattice magnetizations. AFMs with a canted magnetic moment or potentially also non-collinear AFMs can be investigated with such first-order magneto-optical effects [243]. However, collinear compensated antiferromagnetic systems, such as NiO or CoO, do not exhibit any net magnetic moment because their opposite sublattice magnetizations $\boldsymbol{M}_1 = -\boldsymbol{M}_2$ cancel each other out. Thus, first-order magneto-optical effects, which depend linearly on m, are expected to cancel each other out [47].
In addition, there are second order magneto-optical effects, proportional to M^2, L^2, which can lead to a difference in the refractive index for polarized light parallel or perpendicular to the magnetization of a material (Cotton-Mouton or Voigt effect) [45, 244]. The polarization rotation is here dependent on the birefringence, the difference Δn in the refractive indices parallel $n_\parallel$ and perpendicular $n_\perp$ to the optical axes: $\Delta n = n_\parallel - n_\perp$. This rotation is proportional to the Néel vector $\boldsymbol{L}^2 = (\boldsymbol{M}_1 - \boldsymbol{M}_2)^2$ and does not vanish for compensated AFMs [47, 245].

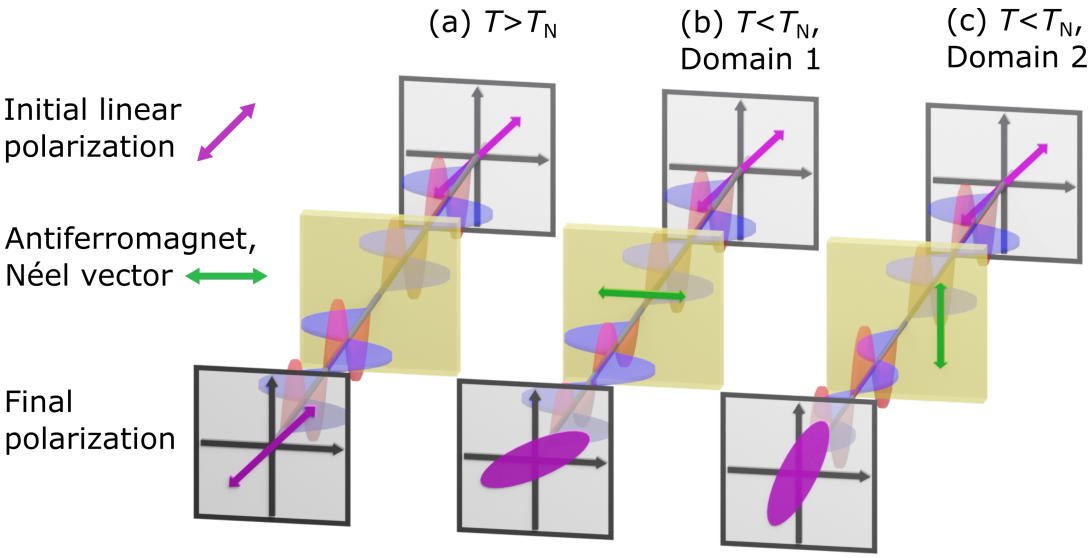

Figure 3.4: The magnetic birefringence of an antiferromagnetic material vanishes above the Néel temperature (a). Below the Néel temperature the different refractive indices for the direction parallel (blue) and perpendicular (red) to the propagation direction lead to a rotation and change of ellipticity (b), which depends on the orientation of the Néel vector and can vary between domains (c).

Birefringence can arise not only from magneto-optical effects, but also from changes in the crystallographic structure due to magnetoelastic coupling [240, 246]. In materials with strong magnetoelastic coupling, such as NiO or CoO, strain in the lattice also contributes to magnetic birefringence [236, 240, 247]. It can be difficult to distinguish direct magneto-optical contributions to the birefringence from lattice contributions, since the lattice strain is directly coupled to the magnetic order [240].
In both cases, however, birefringence originates from the magnetic ordering and can thus be used to study antiferromagnetic domain structures, as shown in Fig. 3.4. When investigating magnetic birefringence above the Néel temperature, there is no expected difference in the refractive index for light travelling parallel (blue) or perpendicular (red) to the optical axes, see Fig. 3.4 (a). However, below the Néel temperature, initially linear polarized light (purple) can experience changes in polarization and ellipticity when passing through an antiferromagnet, see Fig. 3.4 (b). These changes in the rotation of the polarization and ellipticity depend on the orientation of the Néel vector, see Fig. 3.4 (a-c), and can vary between different magnetic domains. Thus, the magnetic birefringence can be used to image antiferromagnetic domains. The development of birefringence imaging of antiferromagnetic domains in transition metal oxides is reviewed in the next section, with a focus on NiO.

3.2.2 Birefringence Imaging in Transition Metal Oxides

The first studies of AFMs which utilized birefringence imaging were carried out by Roth on NiO single crystals in combination with neutron diffraction studies to directly image the spin system [31, 107]. He observed different T-domains and T-domain walls in annealed NiO crystals [31]. The birefringence contrast was attributed to the rhombohedral lattice distortion between different T-domains, which were also observed by imaging the crystallographic structure with X-ray micrography [136, 248]. These first studies were mostly limited to the observations of T-domain walls [31, 103, 136]. In comparison to the distortion of T-domains, which leads to birefringence of the order of $\Delta n_{\mathrm{T}} = 6 \cdot 10^{-3}$, the distortion of S-domains is smaller $\Delta n_{\mathrm{S}} = 1 \cdot 10^{-4}$, making it more challenging to observe them experimentally [116, 240]. However, by improving the annealing procedure [249], increasing the size of the S-domains and improvements in the imaging techniques later studies were able to utilize birefringence imaging to observe new patterns in addition to the T-domains [116, 250]. In combination with X-ray diffraction studies of the lattice deformation and theoretical studies, these additional patterns could be identified to originate from S-domains [118–120]. Thus, birefringence imaging theoretically allows one to fully investigate the antiferromagnetic domain structure in NiO T- and S-domains. However, in the experiment the geometry and contrast of a setup can limit the detectable domains.
The study of antiferromagnetic birefringence was expanded to other transition metal oxides, such as CoO [153], MnO [251], hematite [252], and other AFMs [253]. The origin of the birefringence in these materials could not easily be attributed to magneto-optical effects or to lattice distortions, as both contribute to the birefringence [246].
After studying the temperature dependent birefringence in transition metal oxides (NiO [254], CoO [153]) it was concluded that the birefringence in NiO and CoO is likely to be dominated by the distortion of the lattice and not by second order magneto-optical effects [236, 247]. However, this does not imply a total absence of second order magneto-optical effects. It was later demonstrated that quadratic X-ray magneto-optical effects [255], based on the Schäfer Hubert effect (or sometimes called Voigt effect in reflection), can be observed in the transition metals and transition metal oxides [45, 256, 257]. Previously mentioned studies have focused on antiferromagnetic bulk crystals. Recently, the domain structures of CoO [165, 166] and NiO [32, 182] thin films were studied by birefringence imaging.
Birefringence imaging is a powerful and easy technique to investigate transparent, insulating AFMs [258]. In the rapidly growing field of antiferromagnetic opto-spintronics [47], birefringence imaging is a convenient tool to investigate AFMs, as it can be easily combined in the laboratory with other techniques like the application of magnetic fields [166], pump-probe schemes [45] or current-induced switching experiments [49, 182, 209]. The experimental setup used in this work is described in the following section.

3.2.3 Experimental Setup

Birefringence imaging of antiferromagnetic thin films can be performed with a polarizing microscope [32]. The images presented in this work were obtained using a commercial magneto-optical Kerr microscope from Evico Magnetics, details on the microscope can be found in Ref. [259, 260]. The Kerr microscope was operated as a polarizing microscope. Thus, no external fields are applied during the imaging. Light, emitted by a light source consisting of an array of light-emitting diodes (LEDs), see Fig. 3.5 (a), is guided by fiber optics to the microscope. The light path inside the microscope is depicted in Fig. 3.5 (b). A polarizer linearly polarizes the light before the light is guided onto a sample. Depending on the properties of the sample, the reflected light is rotated and elliptically polarized due to the birefringence of the material, as illustrated in Fig. 3.4. The reflected light passes through a compensator, which can be adjusted to convert the elliptically polarized light to linearly polarized light. The subsequent analyzer is in the extinction position, at 90-degrees to the polarizer. This allows only the rotated light to pass through the analyzer and to be observed by a charge coupled device (CCD) camera.

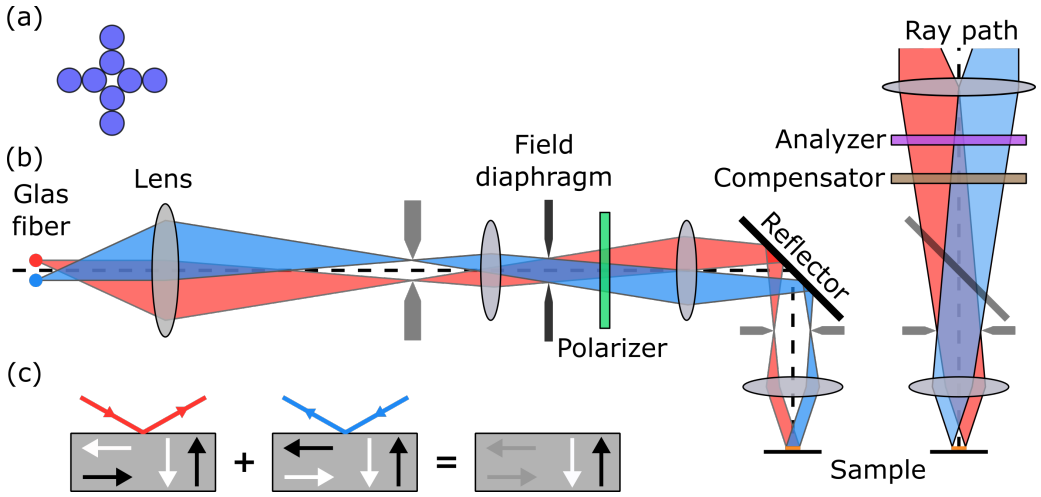

Figure 3.5: (a) LED array with white or blue LEDs, (b) light path inside the microscope. (c) Sketch of the polar operation mode of the microscope.

Operating only one arm of the light path, e.g. the blue light path in Fig. 3.5 (b) of the LED array, results in an oblique incidence angle on the sample. However, two opposing arms (blue and red light paths) can be operated together in a so-called polar operation mode of the microscope. Polar refers here to the polar Kerr effect. For ferromagnetic materials investigated by the Kerr effect, the sum of both light paths leads to a vanishing in-plane sensitivity and a strong out-of-plane (polar) sensitivity, see Fig. 3.5 (c) [259, 260]. The nomenclature cannot be transferred to the imaging of AFMs. However, the birefringence images depicted in this work were obtained in

the polar operation mode of the microscope, as previous investigations on our films observed a strong antiferromagnetic contrast in polar operation mode [182, 217]. Contrast for antiferromagnetic domains can be obtained when the orientation of the Néel vector induces birefringence. The resulting difference in the refractive indices parallel $r_{\parallel}$ and perpendicular $r_{\perp}$ to the Néel vector leads to an observable rotation of the light polarization by θ_v. This difference depends on the angle ϕ between the orientation of the light polarization and the Néel vector [32]:

$$\theta_v = \frac{r_{\parallel} - r_{\perp}}{r_{\parallel} + r_{\perp}} \sin(2\phi). \tag{3.2}$$

The sinusoidal dependence is characteristic for birefringence contrast [32, 165, 240]. Domains with different Néel vector orientations and different birefringence lead to different rotations of the polarization. This creates contrast between different domains. Due to the mostly in-plane polarized light, the birefringence imaging is limited to antiferromagnetic contrast between domains with different in-plane components of the Néel vector, as shown in Fig. 3.6. Domains with the same in-plane component have a similar birefringence and no contrast is expected [32].

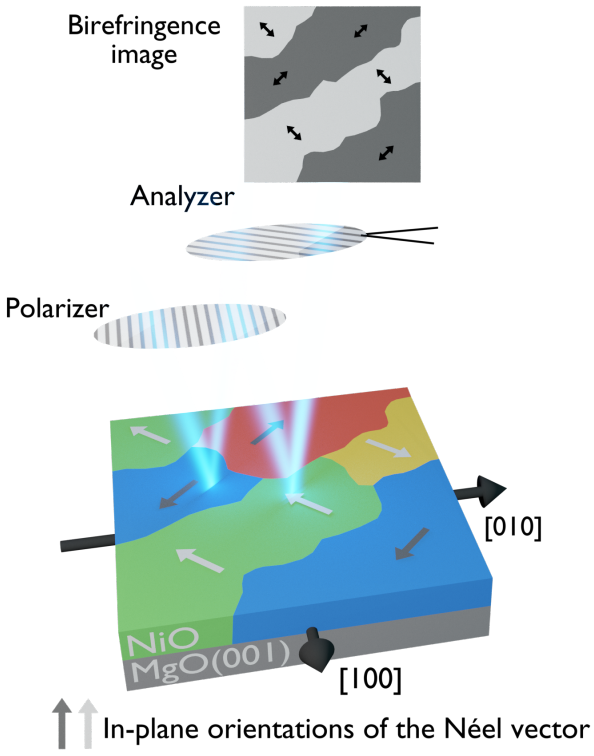

Figure 3.6: Birefringence imaging of our antiferromagnetic thin films yields contrast between domains with different in-plane orientations of the Néel vector.

The best contrast between domains with 90° difference in-plane projection of the Néel vector can be achieved if the polarization of the light is at $\phi = 45°$ to the orientation of the Néel vector. One can now conduct imaging by setting the analyzer to a small offset angle θ, such that one domain appears brighter. The inversion of the analyzer offset direction inverses the domain contrast. The contrast of the birefringence image can be enhanced by taking the difference image between these two analyzer positions [32, 217]. The offset angle for the analyzer was here chosen to be $\theta = 10°$ which offers good contrast and is experimentally easily reproducible, as it is the maximum possible offset for the analyzer at the used microscope. More details on the operation procedure can be found in Ref. [217].
The contrast can be further improved by increasing the film thickness or by reducing the temperature of the sample [32, 165]. The temperature dependence originates from the proportionality between the birefringence and the magnetic moments [240]. The temperature can be reduced either by using a Peltier element or by a custom-made helium flow cryostat for the Kerr microscope. In addition, the contrast depends on the light source. Currently, two different light sources are available, consisting of an array of either blue (central wavelength 460 nm) or white (400-700 nm) LEDs [260]. Interestingly, a strong wavelength dependence of the birefringence contrast can be observed for both transition metal oxides [32, 165]. For both NiO and CoO, the contrast is higher when a blue light source is used [165]. In particular, for the imaging of CoO thin films in this work, the blue light source and cooling were required to observe the antiferromagnetic domain structures.

3.3 | X-ray Imaging of Antiferromagnetic Domains

The discovery of X-rays by Röntgen [261] has led to significant advances in imaging techniques. Compared to techniques based on visible light, X-ray imaging offers several advantages, such as non-invasiveness and elemental sensitivity. The resolution of a microscope is usually limited by the wavelength of the light source [262]. Thus, optical microscopes have a limited spatial resolution of about 200 nm. X-ray based microscopes are not limited by wavelength and have been reported to resolve structures as small as 5 nm [263, 264]. In addition, imaging with polarized monochromatic X-rays offers magnetic sensitivity, as their absorption depends on the orientation of the magnetization of a material.
The first part of this section focuses on the absorption of X-rays and their sensitivity to antiferromagnetic ordering. The second part examines how polarized X-rays can be generated and used to image antiferromagnetic domains.

3.3.1 X-ray Absorption Spectroscopy

X-ray absorption spectroscopy (XAS) is a powerful tool in materials science for the determination of material properties. The energy-dependent absorption of monochromatic X-rays by a sample can provide information about electronic structure, oxidation state, and magnetic ordering [265]. One way to measure the energy-dependent X-ray

absorption cross-section σ is to measure the photons transmitted through a sample of thickness d. The initial intensity I_0 of the X-rays is reduced during transmission [265]

$$I = I_0 \cdot \exp(-\rho\sigma d),$$

with the resulting I as X-ray intensity and ρ as atomic density. Thus, transmission-based techniques, such as scanning transmission X-ray microscopy, require the preparation or growth of very thin samples, typically in the range of a few hundred nm [266]. However, the X-ray absorption of thicker layers and single crystals can be studied by measuring the electrons emitted from the sample after X-ray irradiation, the total electron yield [265].
In a simple picture, the irradiation with photons excites core level electrons into empty valence states, as shown, in Fig. 3.7 (a). Upon recombination of these excited electrons with core holes, Fig. 3.7 (b), an electron can be excited above the vacuum energy E_F and ejected from the atom (Auger electron). The inelastic scattering of the Auger electrons, Fig. 3.7 (c), drives the emission of secondary electrons from the sample, which can then be measured [265, 267], see Sec. 3.3.2.3.

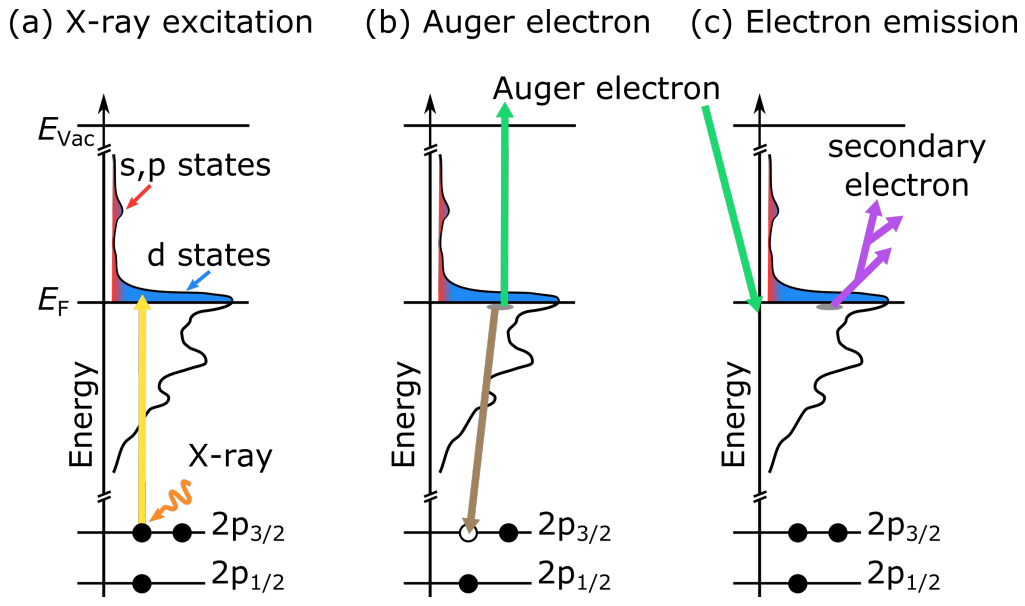

Figure 3.7: (a) The absorption of photons leads to an excitation of core electrons from core p states into empty d states near the Fermi energy E_F (b). The relaxation of these excited electrons can lead to the excitation of electrons above the vacuum energy E_{Vac} and subsequent ejection from the atom (Auger electrons). (c) The inelastic scattering of the Auger electrons leads to the emission of secondary electrons [267, 268].

If the sample layer is thinner than the X-ray penetration depth, the measured intensity of the electrons I_e is limited by the secondary-electron escape distance [130, 269]

$$I_e = I_{e,0} \cdot [1 - \exp(-\frac{d}{z})]. \tag{3.3}$$

The phenomenological parameter z describes the secondary electron escape distance at which the initial electron intensity $I_{e,0}$ has fallen to about 37 % of its original intensity. Typical values for this parameter are $z_{Fe} = 1.7\,nm$, $z_{Co} = 2.5\,nm$, $z_{Ni} = 2.5\,nm$ [269] and $z_{NiO} = 5.5\,nm$ [130]. It is estimated that one can still observe the absorption of layers in up to 3 times the electron escape distance [270].
Element sensitivity can be achieved by tuning the photon energies to the absorption edges of a material. For 3d metals the XAS at the L-edge characteristically exhibits two peaks, the L_3 and L_2 absorption edges, as illustrated in Fig. 3.8 (a). The two peaks arise from the splitting of the core level into $2p_{1/2}$ and $2p_{3/2}$ states. While transitions from the core level to s and p states also occur, the double peak shape of XAS spectra for 3d metals is dominated by 2p to 3d transitions (blue segments in Fig. 3.7) [265, 271]. The shape of the XAS varies depending on the chemical composition. Features like a double peak at the Ni L_2 edge can be used to identify oxidized layers [272].

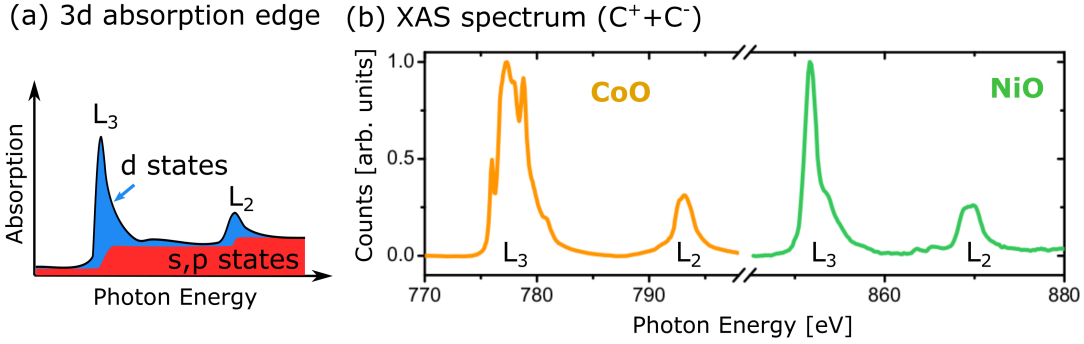

Figure 3.8: The characteristic double peak for the absorption at the L-edge of transition metals is sketched in (a). The peak structure is dominated by the excitation of core electrons into empty d states (blue) [268]. (b) Example of a XAS spectrum for 10 nm thick CoO and NiO thin films. The XAS has been calculated by the summation of two XAS with circularly left and circularly right polarized X-rays. The individual material data sets are obtained at different facilities, the background is subtracted and normed individually to the L_3 peaks.[2]

[2]The CoO data has been measured on an MgO(001)/CoO(10 nm)/Pt(2 nm) sample by Felix Fuhrmann, Christin Schmitt and the author during a beamtime at the ALBA synchrotron. The NiO data has been measured on an MgO(001)/NiO(10 nm)/Pt(2 nm) sample during remote beamtime at BESSY by the beamline scientists under the guidance of the author.

XAS obtained with different X-ray polarization can vary significantly due to dichroism. Dichroism refers to the polarization dependent absorption of light due to polarization dependent absorption coefficients. Depending on the X-ray polarization four different types of dichroism can be distinguished for X-rays:

- X-ray natural linear dichroism [265, 273],
- X-ray magnetic linear dichroism [274, 275],
- X-ray natural circular dichroism [276],
- X-ray magnetic circular dichroism [277],

natural refers here to the intrinsic (non-magnetic) component of the dichroism [265, 278]. For ferromagnetic materials, X-ray magnetic circular dichroism (XMCD) [277] is used to investigate the magnetic ordering. Circular polarized phonons carry angular momentum and are thus sensitive to the magnetic ordering [265]. Compensated AFMs, such as NiO and CoO investigated in this work, do not exhibit any net magnetic moment and no XMCD. However, the orientation of their magnetic order can be investigated using linearly polarized X-rays, which are sensitive to the orientation, not the direction, of the magnetic moments. For linearly polarized X-ray studies, it is important to distinguish between non-magnetic and magnetic origins of the linear dichroism, which are discussed in the following sections.

3.3.1.1 X-ray Natural Linear Dichroism

The X-ray natural linear dichroism (XNLD) is a polarization dependent absorption of linearly polarized X-rays that can occur intrinsically in magnetic and non-magnetic materials [273]. In contrast to circularly polarized X-rays, linearly polarized X-rays do not carry any angular moment. The XNLD originates from charge anisotropies. The symmetry breaking often results from the surrounding crystal field [279]. For a non-magnetic cubic system without charge anisotropy the XNLD vanishes and no difference between different degrees of linearly polarized X-rays can be observed [265]. The coupling between the X-rays and the electronic states depends on the polarization direction (e.g. in-plane or out-of-plane) of the X-rays. To visualize this effect, one can imagine the electric field of the X-rays as a searchlight. The absorption of photons depends on the number of valence states in the direction of the electric field $\boldsymbol{E}$ [265]. For an uniaxially aligned system the intensity of the XNLD depends on the angle β of the electric field $\boldsymbol{E}$ with the symmetry axes [265]

$$I(\beta) = I_{\parallel} \cos^2 \beta, \tag{3.4}$$

with $I_{\parallel}$ as intensity for $\beta = 0$. One example for such an uniaxially aligned system is a thin film for which the substrate mismatch leads to strain and symmetry breaking [137]. Especially in thinner films ($d_{\mathrm{NiO}} < 5\,\mathrm{nm}$ [130]), XNLD, due to crystal field effects, contributes significantly to the observed dichroism [130]. These non-magnetic

contributions can manifest as a small shift in the L_3 and L_2 peaks between linear horizontally and vertically polarized X-rays [280]. In addition, they can induce a dichroism of opposite sign and lead to misinterpretations of the magnetic order based on the XAS alone [130, 281, 282]. Thus, XNLD needs to be considered when interpreting polarization dependent X-ray absorption of thin films.

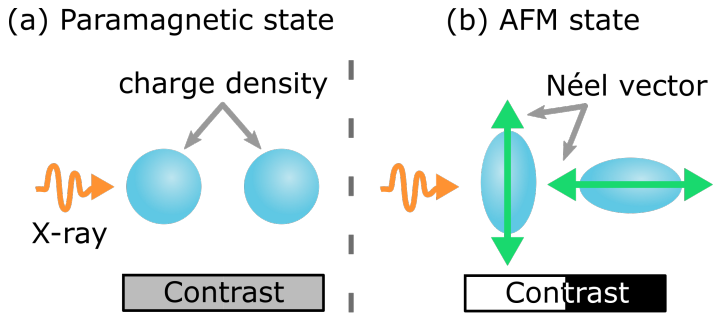

Figure 3.9: Sketch of contrast changes for a spherically symmetric charge density (blue) of an AFM in the paramagnetic state (a) in contrast to the distorted charge density in the antiferromagnetic state (b).

3.3.1.2 X-ray Magnetic Linear Dichroism

The X-ray magnetic linear dichroism (XMLD) can be used to study the magnetic ordering of collinear AFMs [275, 283] and ordered ferromagnets [284]. XMLD arises from spin-orbit coupling and depends on the magnetic ordering [278], as illustrated in Fig. 3.9.
XMLD leads to a difference in the absorption for different domains and different X-ray polarizations. The XMLD signal can be obtained from the difference in absorption between light polarized in the plane, linear horizontal (LH), and out-of-plane, linear vertical (LV), of the sample.
For collinear AFMs large differences between the absorption of LH and LV polarized X-rays can be observed, as can be seen in Fig. 3.10 for CoO (a) and NiO (b) thin films. A detailed discussion of the XMLD in NiO can be found in Ref. [279] and [265]. The dependence of the XMLD signal on the polarization of the beam can be used to determine the orientation of the magnetic ordering of the sample [268, 285, 286], for details see also Appendix B.2.1.
To distinguish magnetic from non-magnetic dichroism one can heat up a sample above the magnetic ordering temperature, without a magnetic order the remaining dichroism originates from non-magnetic effects [280]. Such investigations can be performed for AFMs which have a cubic symmetry in the paramagnetic state, such as NiO or CoO, since their cubic symmetry leads to a vanishing of the XNLD above the Néel temperature [180].

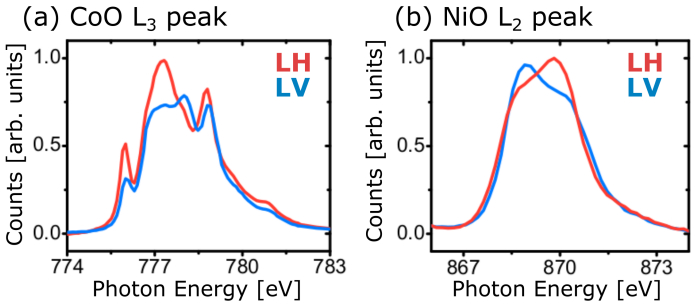

Figure 3.10: X-ray absorption of linear vertically (blue) and linear horizontally (red) polarized X-rays at the Co L_3 peak for CoO (a) and at the Ni L_2 peak for NiO (b).[4]

3.3.2 Polarized X-ray Radiation

The dichroism of polarized X-rays can be a powerful tool to investigate the magnetic properties of a material. However, to measure XMCD and XMLD effects monochromatic X-rays with variable polarization are required. A synchrotron facility can produce such X-rays [264]. When electrons are deflected from their path by a magnetic field, they emit radiation. While this radiation was initially considered a waste of energy, the high brilliance (photon flux emitted per unit source area per radiation opening angle) of the emitted photons makes the radiation from modern synchrotrons an important tool for X-ray studies [264, 265].
The following section discusses the basic principles of a synchrotron facility, the generation of polarized X-ray radiation by undulators and the basic principles of a photoemission electron microscope.

3.3.2.1 Synchrotron Sources

A synchrotron facility consists of several key elements [264], as shown in Fig. 3.11. Electrons are first emitted from an electron gun and then accelerated by a linear accelerator (LINAC) into a booster ring for further acceleration. From the booster ring, electrons are injected into the main storage ring. Depending on the synchrotron and the operating mode, electron bunches with electron energies of several GeV move at near the speed of light along a circular path. Despite the ultra-high vacuum of the storage ring, the electron bunches can still collide with residual gas particles. In modern synchrotron facilities, the main ring is therefore operated in a *top-up* mode, in which the lost electron bunches are constantly replaced. The actual shape of the storage ring is not circular, but resembles a polygon [264].

[4]The CoO data has been measured on an MgO(001)/CoO(10 nm)/Pt(2 nm) sample by Felix Fuhrmann, Christin Schmitt and the author during a beamtime at the ALBA synchrotron. The NiO data has been measured on an MgO(001)/NiO(10 nm)/Pt(2 nm) sample during remote beamtime at BESSY by the beamline scientists under the guidance of the author.

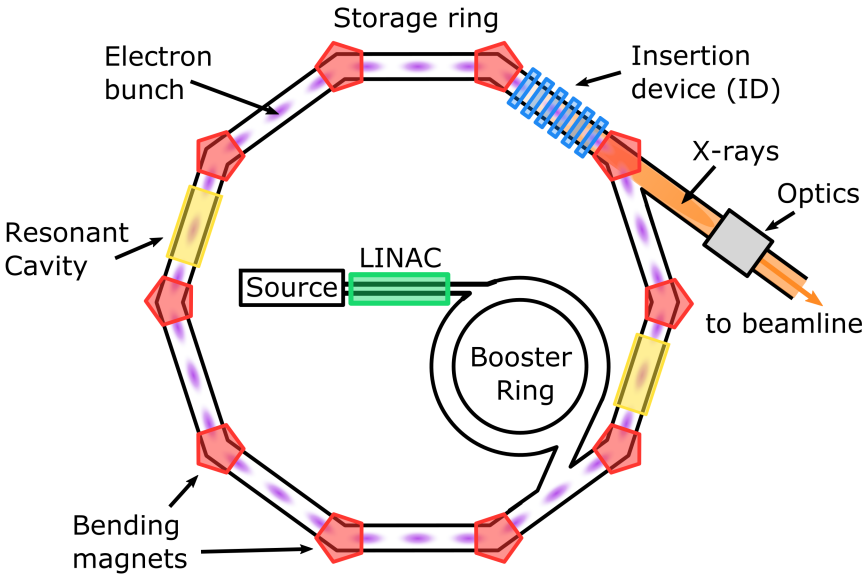

Figure 3.11: Depiction of a synchrotron storage ring and its key elements.

At the corners of the polygon, bending magnets deflect the electrons along the new trajectory. During this deflection the electrons loose energy and synchrotron radiation is emitted [264]. The energy of the electrons is replenished by radio-frequency emitters along the linear sections. Additional insertion devices (IDs), such as wigglers or undulators, can be inserted to produce photons of higher brilliance. These photons can then be directed through X-ray optics to the individual beamlines and experimental setups [264, 287].

3.3.2.2 Undulator Devices

Undulators such as the APPLE II (Advanced Planar Polarized Light Emitter) undulator are used at several synchrotron facilities in Europe (such as BESSY[5], SLS[6] and ALBA[7]). In addition to a high brilliance, they offer a full polarization control of the emitted X-rays [288, 289]. APPLE II undulators consist of 4 rows (A-D) of permanent magnets with periodic alignment over the length λ, as illustrated in Fig. 3.12.
The properties of the magnetic field of the undulator depend on the distance (the gap) between the upper and lower rows of the undulator and on the shift between the different rows of the undulator. The electrons are not deflected after passing

[5]Berlin Electron Storage Ring Society for Synchrotron Radiation operated by Helmholtz-Zentrum Berlin, Germany.
[6]Synchrotron Light Source Switzerland operated by the Paul Scherrer Institute, Switzerland.
[7]Synchrotron Light Source near Barcelona operated by the Consortium for the Exploitation of the Synchrotron Light Laboratory, Spain.

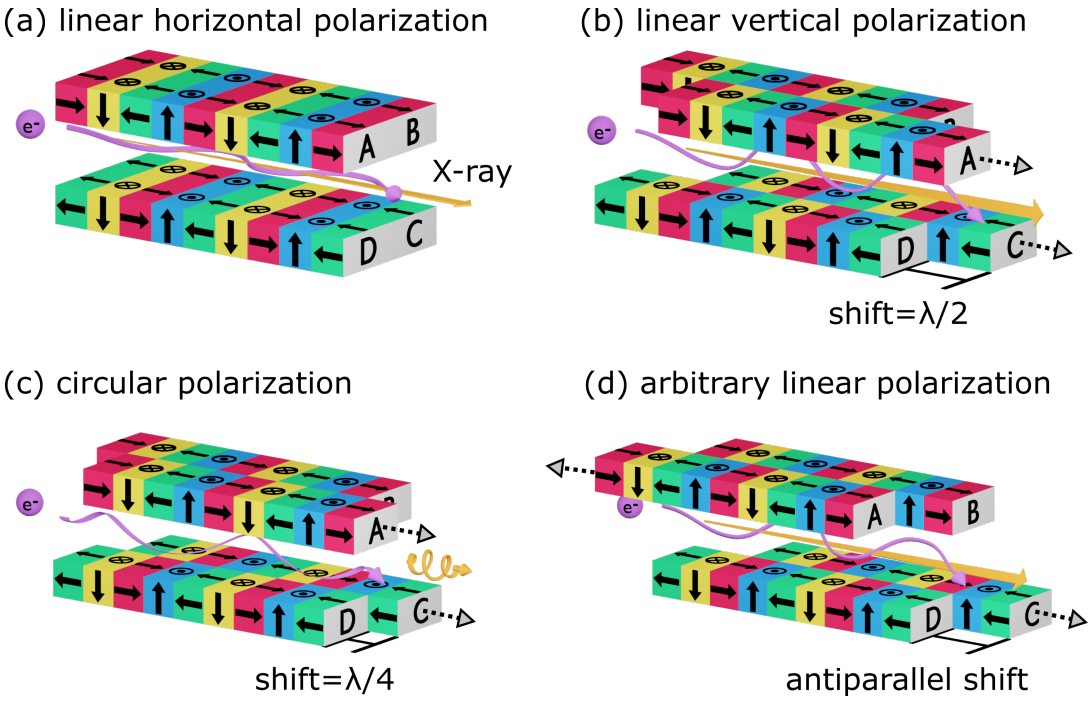

Figure 3.12: Operational principles of an APPLE II undulator. The APPLE II undulator consists of four different rows of permanent magnets, here named A,B,C,D. By shifting rows A and C parallel or antiparallel to each other, one can control the polarization of the created X-ray radiation (orange) between linear horizontal (a), linear vertical (b), circular (c) and arbitrary linear polarization (d).

through the undulator, but the periodic modulation of their path inside the undulator leads to the emission of X-rays. Altering the path of the electron also affects the polarization of the emitted photons due to the conservation of angular momentum. By shifting the arrays B and D in a parallel fashion one can switch between linear horizontally polarized X-ray radiation (Fig. 3.12 (a), shift = 0), linear vertical polarization (Fig. 3.12 (b), shift=$\lambda/2$) and circularly polarized X-ray radiation (Fig. 3.12 (c), shift$\approx \lambda/4$) [264]. Linear vertical and linear horizontal here always refers to the plane of the synchrotron and not to the plane of incidence on the sample at the end stations, which can vary across setups. The undulator arrays can also be used in an antiparallel mode, see Fig. 3.12 (d), to create arbitrary linearly polarized light. This is particularly useful for the investigation of antiferromagnetic domains, as arbitrary linear X-ray polarization allows for a precise analysis of the domain orientation of antiferromagnetic domains [264, 288, 289].

3.3.2.3 X-ray Photoemission Electron Microscope

Photoemission electron microscopy (PEEM) allows the spatial mapping of electrons emitted from a sample surface [290]. If these electrons are emitted due to illumination by an X-ray beam, one refers to X-ray photoemission electron microscopy (X-PEEM). In this work, several different PEEM setups have been used at different synchrotron facilities in Europe: ALBA [291], BESSY [292], SLS [293, 294]. Thus, the following section only gives an overview over the basic PEEM principles, more details can be found in [295] and [270].
In PEEM, not the incoming photons are observed, but the secondary electrons, that are emitted due to the Auger scattering, see Fig. 3.7. Essential for PEEM imaging are a conductive sample surface and suitable photon wavelengths to excite the core electrons of the material [267]. A typical X-PEEM setup is depicted in Fig. 3.13. The X-rays impinge on the sample surface at an incidence angle of 16° with respect to the sample surface. An electric field of 10-20 kV between the sample surface and the objective accelerates the secondary electrons emitted from the sample surface. These electrons are focused by the objective lens and pass through an array of magnetic lenses before entering an energy analyzer. After passing through an energy slit, they can then be focused by projective lenses onto a detector.

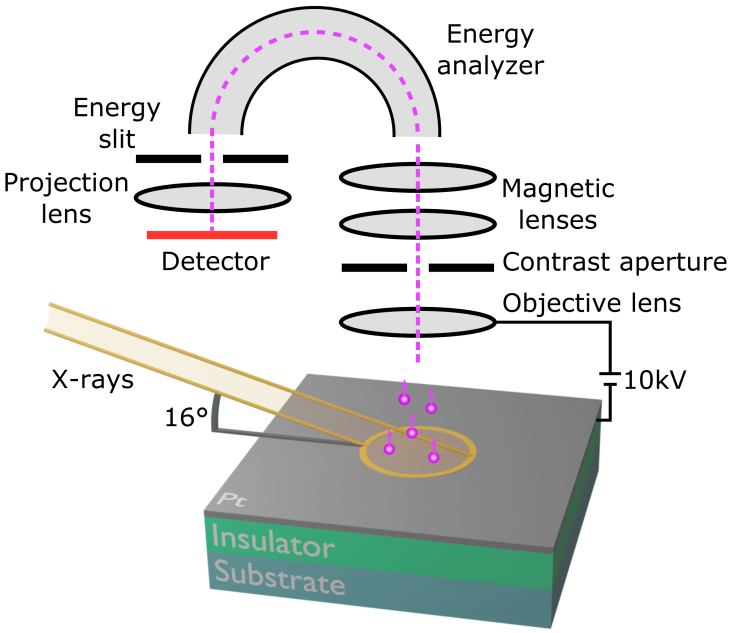

Figure 3.13: Schematic depiction of a PEEM setup. Emitted electrons (purple) are accelerated by an electric field towards the optical column and are focused by an objective lens. Depending on the setup, the electrons pass several magnetic lenses and an energy analyzer before they are projected onto a detector.

The resolution of X-PEEM is not limited by the wavelength of the X-rays because electrons are used for the imaging. However, the spatial resolution is limited by the electron optics in the X-PEEM to usually 20 nm, due to spherical aberration, chromatic aberration, and diffraction [264, 270].
PEEM itself is very sensitive to the surface of the sample, as defects on the sample surface distort the electrical field and thus influence the trajectories of the emitted electrons. In grazing incidence geometry defects that are elongated perpendicular to the incoming X-ray radiation absorb more photons and thus appear brighter [270]. However, PEEM does not only provide surface sensitivity, but by exploiting the XMCD and XMLD effect, X-PEEM can also image the magnetic domain structure of a sample. This magnetic imaging is sometimes referred to as XMCD-PEEM or XMLD-PEEM. An XMLD-PEEM image can also be obtained by using energy dependent XMLD-PEEM imaging [124, 296, 297]. The XMLD-PEEM images in this work have been obtained by subtracting the images at the energies (E_1 and E_2) from each other [42, 265]:

$$\mathrm{XMLD}_{\mathrm{Images}} = \frac{I(E_1) - I(E_2)}{I(E_1) + I(E_2)}. \tag{3.5}$$

By normalizing with the sum of the images obtained at the different energies, non-magnetic contributions (e.g. surface roughness) to the XMLD-PEEM image are minimized. The XMLD-PEEM images presented in this work were obtained by energy dependent imaging at the L_2 edge for NiO and at the L_3 edge for CoO.

4 | Current-Induced Switching

The ability to manipulate and write the antiferromagnetic order is crucial to the development of spintronic devices with AFMs as active elements [25]. In ferromagnetic devices, current-induced switching of the magnetic order is a common tool for controlling the ferromagnetic state [183, 298, 299]. The current-induced switching of AFMs is still in its infancy, and the underlying mechanisms are part of ongoing investigations. After the first observations of current-induced switching in particular metallic AFMs [191, 192], current-induced switching has been extended to insulating AFMs capped by a HM layer. Several experiments have demonstrated the experimental switching of antiferromagnetic order in thin NiO, CoO and hematite layers by applying current pulses through the HM layer [40, 42, 105, 168, 300–302]. Initial observations suggested an interfacial non-staggered spin-orbit torque (SOT) based switching mechanisms, based on a spin accumulation at the interface between the HM and AFM [40–42, 193].
However, switching based on current-induced heating and strain has been proposed as an alternative mechanism to switch the domains in AFM/HM bilayers [105, 204]. The basic idea of such thermomagnetoelastic switching is illustrated in Fig. 4.1. The Joule heating induced by the current pulse leads to an inhomogeneous heating and strain. In a material with magnetoelastic coupling, inhomogeneous strain can remove the degeneracy between two antiferromagnetic states and switching can occur.

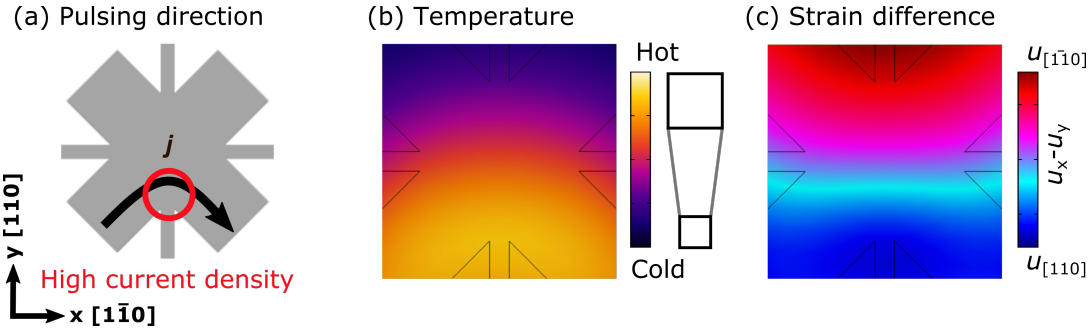

Figure 4.1: Depending on the pulse geometry (a) high current densities in a device lead to an inhomogeneous Joule heating (b) and thus an inhomogeneous distribution of strain (c) inside a device.

The dominant switching mechanism in MgO(001)/NiO(10 nm)/Pt(2 nm) thin films has been investigated as the first author in Ref. [49]. This work is reproduced/partly adapted in Sec. 4.1. Further work extending the investigation of electrically induced switching to pulse length dependent studies is presented in Sec. 4.2. The origin of the difference in the electrical readout sensitivity for different geometries is briefly discussed in Sec. 4.3. The last part of this section, Sec. 4.4, summarizes our results and discusses the impact of our research on the electrical switching of AFMs.

4.1 | Electrical Switching in NiO/Pt Thin Films

4.1.1 Introduction

In view of applications, it is of paramount importance to be able to perform the read-out and write operations of AFMs fast and efficiently and to understand the underlying switching mechanism. In collinear AFMs, magnetic information can be stored in the orientation of the Néel vector $\boldsymbol{n}$. In AFM/HM bilayers the orientation of the Néel order can be read electrically via the spin Hall magnetoresistance (SMR) [34, 181]. However, some reports have interpreted the electrically detected SMR signals after current pulses as mere results of electrical heating and electromigration of the platinum wire [207, 303] or a combination with resistive switching and torques due to thermomagnetoelastic effects [204]. Imaging of the magnetic domains, however, allows to unambiguously determine the existence of magnetic switching [42, 182].
In the metallic AFMs CuMnAs [304] and Mn_2Au [192] magnetic switching, due to current pulses inducing spin torques, relies on the special crystal symmetries of these materials, leading to current-induced bulk Néel spin orbit torques. In insulating AFMs the underlying switching mechanism is highly debated. So far, different final states of the Néel vector $\boldsymbol{n}$ with respect to the current direction $\boldsymbol{j}$ have been reported in different collinear AFMs ($\boldsymbol{n} \parallel \boldsymbol{j}$) for NiO [42], ($\boldsymbol{n} \perp \boldsymbol{j}$) for CoO [105] and for different device and pulsing geometries in NiO ($\boldsymbol{n} \parallel \boldsymbol{j}$ [41, 42] and $\boldsymbol{n} \perp \boldsymbol{j}$ [40]), thus different switching mechanisms have been put forward as the origin. Most authors proposed mechanisms related to non-staggered antidamping-like SOTs to explain the observed electrical switching in insulating AFM/HM bilayers: the torques have been considered acting on the uncompensated moments focusing on one sublattice [40], as well as SOTs related to both sublattices [41] or acting on the domain walls [42].

[1] *The following Sec. 4.1 and its subsections were transcribed from Ref. [49] and its supplementary information, with the first author of this reference being the author of this thesis. Individual contributions are detailed in Appendix C.1.*

We unravel the origin of current-induced magnetic switching of insulating AFM/HM systems. We utilize concurrent transport and magneto-optical measurements to image the switching of antiferromagnetic domains in specially engineered devices of NiO/Pt bilayers. Different electrical pulsing and device geometries reveal different final states of the switching with respect to the current direction. We can explain these final states through simulations of the temperature induced strain and we identify the thermomagnetoelastic switching mechanism combined with thermal excitations as the origin, in which the final state is defined by the strain distributions and heat is required to switch the antiferromagnetic domains. We show that such a potentially very versatile non-contact mechanism can explain the previously reported contradicting observations of the switching final state, which have often been attributed to spin-orbit torque mechanisms.

To understand the origin of these different reports, primarily based on electrical readout, one needs to directly image the magnetic switching. NiO is an ideal material system to investigate the switching mechanism of insulating AFMs. Due to its high Néel temperature of 523 K in the bulk [31], its insulating collinear antiferromagnetic phase and the magnetoelastic coupling [305] that allows one to image the AFM domain structure with birefringence microscopy [32, 182]. This lab-based imaging approach can be combined with concurrent electrical readout to reliably identify a magnetic switching of NiO/Pt bilayers [182].

Additionally, the samples need to allow one to be able to disentangle the effects of SOTs, directly generated by the current, and the thermomagnetoelastic torques, generated by the current-induced temperature gradients. This can be achieved by engineering the device geometry, e.g. one can generate temperature gradients in regions where no current is flowing. This is necessary due to the similar linear functional dependency of the effective fields from SOTs and from thermomagnetoelastic effects on the current density $|\boldsymbol{j}|$ [105], while other heat induced torques depend quadratically on $|\boldsymbol{j}|$ [42, 204, 205].

Here, by combining electrical measurements, table-top direct imaging of the magnetic domains and simulations of the thermally-induced strain in specially engineered device geometries, we find that the final state of the switching does not solely depend on the direction of $\boldsymbol{j}$, but rather also on the device geometry. We show that the switching is enabled by a combination of strain and heat, while the current flow through the device is not necessary to induce the switching. We explain these findings by a thermomagnetoelastic switching mechanism of the Néel order in NiO/Pt thin films. Finally, we discuss how this mechanism can explain the different switching final states previously reported for the NiO/Pt system, based on the different geometries used.

4.1.2 Results

To investigate the contribution of current-induced SOTs, heat and thermomagnetoelastic effects, we have grown NiO(10 nm)/Pt(2 nm) bilayers on MgO(100) and have patterned different device geometries by Ion beam etching. We have characterized similar grown NiO thin films previously and demonstrated using XMLD based mi-

croscopy the presence of antiferromagnetic T-domains with a spin orientation along $[\pm 5 \pm 5\,19]$, mostly out-of-plane, different from bulk NiO where {111} planes harbor the Néel vector orientation [137].

Device and Pulsing Geometry Dependent Switching

Note that, according to the SOT mechanism, the final state of the switching depends only on the direction of the current $\boldsymbol{j}$, while in the case of the thermomagnetoelastic switching it is determined by the distribution and orientation of the temperature gradients [105, 204]. To disentangle the two mechanisms, we employ two devices, patterned with different orientation on the same sample, aiming to obtain orthogonal strain while using the same direction of the pulse current density $\boldsymbol{j}$ in the center of the device. The devices are 8 terminal star-shaped devices that have four 10 µm wide arms and four 2 µm wide arms, as depicted in Fig. 4.2 (a, d). In the first device, the wide arms are aligned parallel (0°) to the easy axis, along $[1\bar{1}0]$ and [110], see Fig. 4.2 (a-c).

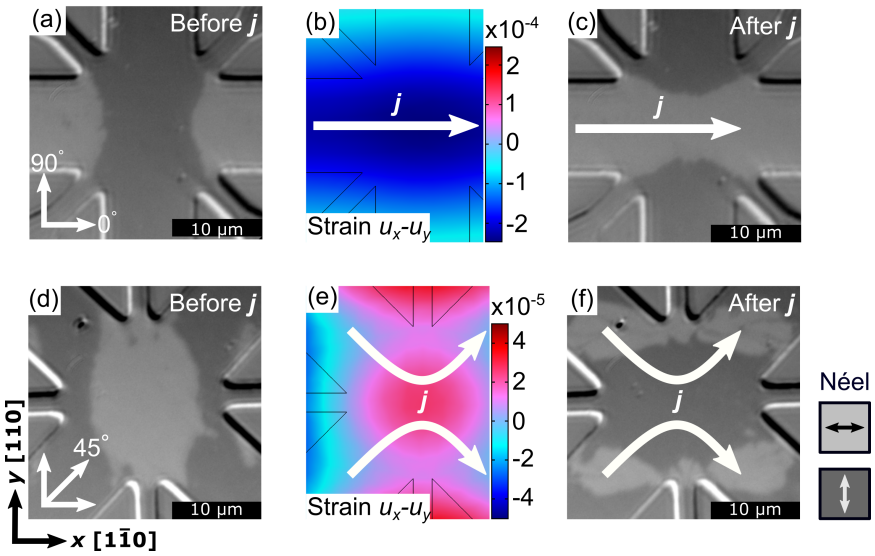

Figure 4.2: Comparison of the switching between different device geometries in MgO(001)/NiO(10 nm)/Pt(2 nm) thin films. Initial domain structure in the [110] star device (a) and [100] star device (d). Simulations of the current induced strain u differences between the easy axes ($u_{[1\bar{1}0]} - u_{[110]}$) for a straight pulse along $[1\bar{1}0]$ in the [110] star device (b) and for X-shaped pulses along $[1\bar{1}0]$ in the [100] star device (e). Domain structure in the [110] star device (c) and [100] star device (f) after applying five pulses in the directions indicated in (b) and (e). We can conclude from the electrical measurements depicted in Fig. 4.6, that the dark (light) contrast in the images corresponds to $\boldsymbol{n} \parallel [110]$ ($[1\bar{1}0]$). Adapted with permission from Ref. [49]. Copyright 2020 American Chemical Society.

In the second device, the wide arms are along [100] and [010], at an angle of 45° to the easy axis, see Fig. 4.2 (d-f). We simulate the current-induced heat and resulting strain for different pulse configurations in our geometries using the COMSOL Multiphysics software, more details in Appendix B.1.1. For the [110] star device, we simulate a straight current pulse ($j = 1.35 \cdot 10^{12}\,\mathrm{A/m^2}$, $\Delta t = 0.1\,\mathrm{ms}$) along the $[1\bar{1}0]$ direction, see white arrow in Fig. 4.2 (b). To effectively achieve the same direction of $\boldsymbol{j}$ in the center of the [100] star device, we use an X-shaped current pulse ($j = 1.95 \cdot 10^{12}\,\mathrm{A/m^2}$, $\Delta t = 0.1\,\mathrm{ms}$) through four arms, white arrows in Fig. 4.2 (e). We plot the difference between the strain along the two easy axes $u_{[1\bar{1}0]} - u_{[110]}$ at the surface of the NiO layer. Thus, a positive strain difference (red) corresponds to a larger expansion of the NiO along $[1\bar{1}0]$ in contrast to [110], while a negative strain difference (blue) indicates orthogonal strain. One can see from the simulations that, even if the orientation of $\boldsymbol{j}$ with respect to the crystallographic axis in the center of the cross is the same in the two devices (along $[1\bar{1}0]$), the strain difference induced by the current pulses is opposite in the center of the devices. We have performed this experiment in the laboratory, imaging the initial domain states for both devices shown in Fig. 4.2 (a, d) and the current-induced switched states after pulsing in Fig. 4.2 (c, f). For both devices we find reproducible switching, e.g. a subsequent pulse in a direction rotated by 90° switches the AFM order back to the initial state.
First, we note that we observe two different final states at the center of the devices depending on the dominant strain direction and not on the direction of $\boldsymbol{j}$. This is consistent with a thermomagnetoelastic mechanism that leads to opposite final states based on the dominating strain. The current induced heating of the NiO layer results in a subsequent inhomogeneous expansion of the lattice, generating stresses compensated by shear strains, making the lattice expand differently along the $[1\bar{1}0]$ and the [100] directions. These strains remove the degeneracy between the two easy axes and facilitate the switching [105]. Second, one can see in Fig. 4.2 (f), that X-shaped current pulses switch the AFM domains in the arms of the cross in opposite directions with respect to the center, regardless of the direction of $\boldsymbol{j}$ in the arms. This can only be explained by differences in dominant strain between the center and the region in the arms and not by a SOT dominated mechanism, which would instead induce switching towards a final state depending on the direction of $\boldsymbol{j}$. Combining our results shows that the final state in our NiO/Pt samples is determined by the thermally induced strain.

Activated Switching

Next, we investigate whether strain alone is sufficient to switch the orientation of the Néel order and the role that current and temperature play. We consider a [100] star device and use only two arms to send a current pulse ($j = 0.925 \cdot 10^{12}\,\mathrm{A/m^2}$, $\Delta t = 0.1\,\mathrm{ms}$) at a right angle across our device, as depicted in Fig. 4.3 (a) (white arrow).

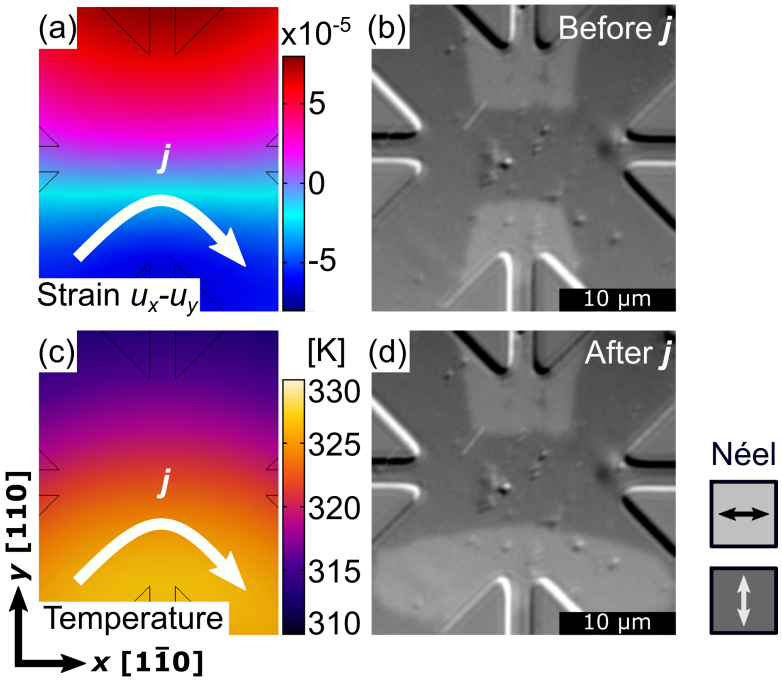

Figure 4.3: Switching of a star-shaped device with a right angle pulse in MgO(001)/NiO(10 nm)/Pt(2 nm) thin films. Simulations of the current-induced strain differences between the easy axes ($u_{[1\bar{1}0]} - u_{[110]}$) for an edge pulse along [1$\bar{1}$0] in the [100] star device (a) and the corresponding heat profile (c). The domain structure has been imaged before (b) and after pulse injection (d). Adapted with permission from Ref. [49]. Copyright 2020 American Chemical Society.

From our simulation of the induced strains, Fig. 4.3 (a), we would expect to observe switching in the area of the current pulse and an opposite switching final state on the other side of the device. However, if we compare the imaged initial state in Fig. 4.3 (b) with the final state in Fig. 4.3 (d) we can only detect a switching in the wide arms, where the current flows and thus the temperature is increased due to the higher current density, see Fig. 4.3 (c). The simulated strain difference on the opposite side of the device is of similar magnitude as in the switched region, see Fig. 4.3 (a), however, no switching is observed.
We conclude that, in this case, strain alone is not sufficient to reorient the Néel vector, and an additional contribution by the current flow is needed either generating SOTs or heat. However, we cannot disentangle purely temperature related effects from other possible influences of the current pulse (such as SOTs) from this device geometry, due to their similar spatial distribution.

Switching of an Electrically Isolated Dot

To make the distinction between temperature and SOT-induced effects, we have designed a cross-shaped device with a central NiO/Pt dot, that is electrically insulated (2 µm wide and 5-6 nm deep gap) from the arms where the current flows, see Fig. 4.4. The dot is subject to high heat and strain contributions, Fig. 4.4 (d,e), but it is not influenced by current-induced SOTs. The NiO layer below the inner circle is still affected by the electrically-induced temperature and thermomagnetoelastic strain changes, as shown by simulations of this device for a current pulse ($j = 1.7{\cdot}10^{12}$ A/m^2, $\Delta t = 0.1$ ms) along the [1$\bar{1}$0] direction, as depicted in Fig. 4.4 (f).

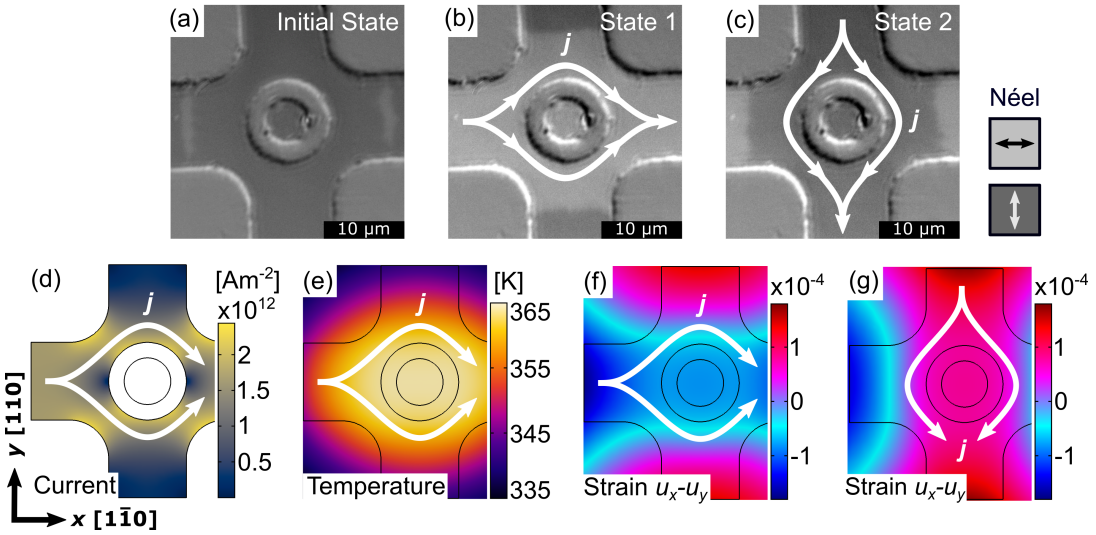

Figure 4.4: Switching of a device with an electrically isolated area in MgO(001)/NiO(10 nm)/Pt(2 nm) thin films. The domain structure of the device has been imaged via birefringence before the pulse application along [1$\bar{1}$0] (a) and after (b). Domain structure after a second pulse along [110] (c). The corresponding current and temperature profiles are depicted in (d) and (e). (f, g) Simulations of the current-induced strain differences between the easy axis ($u_{[1\bar{1}0]} - u_{[110]}$) for a straight pulse along [1$\bar{1}$0] in the cross shaped device with an inner Pt circle. Adapted with permission from Ref. [49]. Copyright 2020 American Chemical Society.

First, we image the initial domains depicted in Fig. 4.4 (a) and then pulse with a current density of $1.7 \cdot 10^{12}$ A/m^2. This single pulse is sufficient to fully switch the device, including the NiO in the region below the center dot, as can be seen in Fig. 4.4 (b). Secondly, we probe the reversibility of the switching by pulsing along the [110] direction. This change in pulsing direction results in a strain difference opposite to the first pulse, see Fig. 4.4 (f, g).
Therefore, the domains, as shown in Fig. 4.4 (c), are switched back to their initial state. We can observe a homogeneous switching at the center of our device, including

the electrically insulated dot in the center of the cross, which indicates that the current itself is not necessary to achieve switching. Moreover, in the case of a current-assisted switching mechanism, we would expect an inhomogeneous switching pattern around the etched ring due to the inhomogeneous current distribution shown in Fig. 4.4 (d), that we do not see here. Therefore, we conclude that the observed switching is enabled by the combination of heating and strain, where strain breaks the degeneracy and defines the final state, while heating is necessary to assist the switching and overcome the anisotropy barrier.

Switching with an MgO Interlayer

As a further direct demonstration of the thermomagnetoelastic switching mechanism, we have conducted experiments with an additional 3 nm MgO interlayer between the NiO and platinum layer, to suppress any possible SOT effects from the platinum. The MgO interlayer is sufficiently thick to prevent any significant spin current transport, as demonstrated from spin-pumping in Fe/MgO/Pt layers, where a signal has only been reported for MgO < 2 nm [306]. We used a 10 nm NiO film that has been fabricated similar to the one used for the other devices (but coming from a different batch and grown with a different oxygen flow leading to slightly smaller domains). We have used a liftoff technique to pattern the MgO(3 nm)/Pt(3 nm) structures on top.
Although possible SOT based effects are now suppressed, we can still observe a switching as can be seen in Fig. 4.5 (a). We used $\Delta t = 0.1$ ms pulses with a current density of $j = 1.6 \cdot 10^{12}$ A/m^2 to switch our device. The pulsing direction is switched between the [110] and [1$\bar{1}$0] direction, and we can observe the same switching behavior as in Fig. 4.2, with pulses along [110]([1$\bar{1}$0]) switching the center region to a dark (bright) contrast. The switched domains that we observe in this film are smaller, and the contrast is reduced due to the different stack used. However, the switched domains can be identified using the difference image. The lines visible in the images along the [100] crystallographic directions are likely dislocations from the substrate.
In particular, we now observe not only the switching in the center of the device, we can also observe a switching of the bare NiO between the arms, where no MgO or Pt has been deposited. This can be seen for example in the orange area which is closer depicted in Fig. 4.5 (b). The white domains shrink after applying a pulse along the [110] direction and increase after pulsing along the [1$\bar{1}$0] direction. Thus, we have observed switching in devices with an additional MgO interlayer that suppresses spin current transport [306] and even for adjacent areas of the NiO with no capping and where thus no SOTs can be exerted.

Comparing Electrical and Optical Readout

In addition to imaging, we conducted SMR measurements to read out the orientation of the Néel vector in the different star-shape device pulsing geometries. Our results are consistent with the imaging and explain why, in the existing literature, different switching mechanisms have been proposed based on electrical SMR measurements.

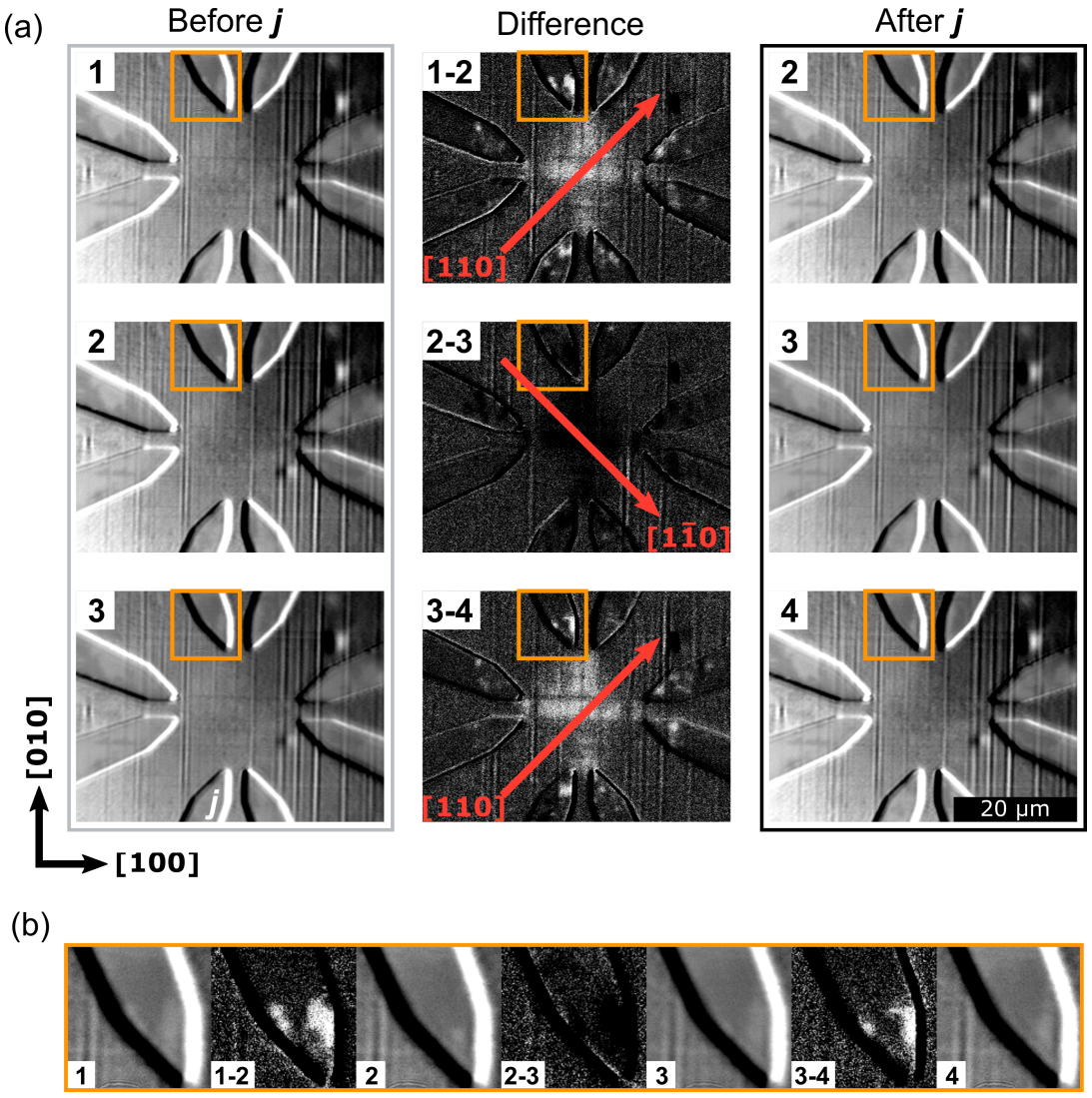

Figure 4.5: Switching of NiO domains in a NiO(10 nm)/MgO(3 nm)/Pt(3 nm) [110] star device. (a) We image the changes in the domains structure of our NiO thin film that occurred during 3 consecutive pulses via birefringence imaging. On the left side the image before the application of the pulse is shown and on the right the image after the pulse application, in the middle the difference picture (Initial-Final) and the pulsing direction is depicted. (b) The orange area in between the pulsing arms is magnified to aid the comparison between the 4 different imaged states. Dark and bright contrast indicates orthogonal Néel vector projections. Adapted with permission from the supplementary of Ref. [49].

We apply the pulses in the wide arms (10 µm) and read out the transverse resistance in the arms along the [010] direction, the contact scheme is depicted in Fig. 4.6 (a). Since the direction of the current at the center of star-shaped devices is comparable to cross-shaped devices, we can compare the different switching behaviors to previous reports on crosses. The differences in the SMR sensitivity of the different geometries is explored in Sec. 4.3.

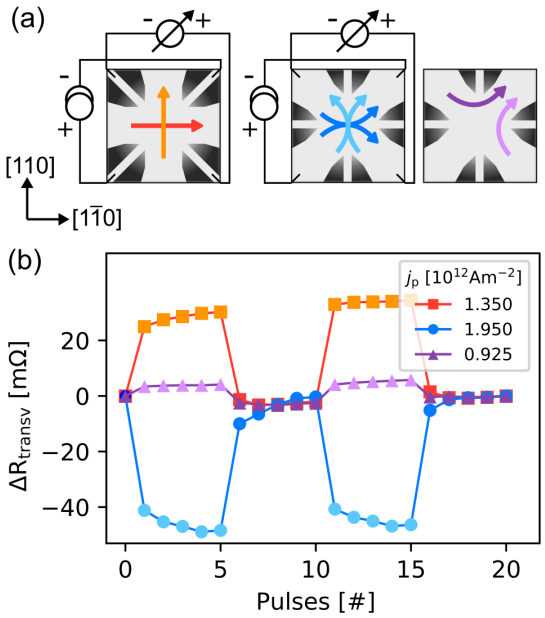

Figure 4.6: Comparison of electrical measurements in different device and pulsing configurations in MgO(001)/NiO(10 nm)/Pt(2 nm) thin films. (a) Device geometries and SMR measurement scheme with respect to the crystallographic axis. The arrows indicate the current pulse directions with light and dark color for effective [110] and [1$\bar{1}$0] pulses, respectively. (b) Corresponding electrical measurements for alternating pulse directions after subtraction of a nonmagnetic component. The magnetic origin of the shown electrical signal is confirmed by the optical imaging of the domain switching. Adapted with permission from Ref. [49]. Copyright 2020 American Chemical Society.

To single-out the resistance changes of magnetic origin from the total resistance variation featuring also contributions of non-magnetic effects, we use the subtraction procedure described in Ref. [182], see Sec. 2.4.4. We use a series of 5 pulses each, first along the [110] direction and then along the [1$\bar{1}$0] direction. In the case of straight pulses in a [110] cross geometry, see orange color in Fig. 4.6 (b), the transverse resistance increases after pulsing along [110] and decreases after pulses along [1$\bar{1}$0]. This indicates a final state of the Néel vector parallel to the current direction ($\boldsymbol{n} \parallel \boldsymbol{j}$), consistent with the report by Chen et al. for NiO/Pt grown on STO [41].

The same switching behavior can be observed, with lower magnitude, for the switching with right angle pulses in [100] crosses (Fig. 4.6 (b), purple), as has been previously reported in NiO/Pt Hall cross devices grown on MgO [42]. Moreover, as expected from the data shown in Fig. 4.2, we observe compared to the straight pulse (Fig. 4.6 (a), orange) an opposite final state of the switching for X-shaped pulses (Fig. 4.6 (b), blue), where the resistance decreases after pulse application along the [110] direction and increases after pulsing along $[1\bar{1}0]$ direction. This data indicates a final state ($\boldsymbol{j} \perp \boldsymbol{n}$), in line with the report of Moriyama et al. for Pt/NiO/Pt trilayers [40]. We note that different orientations of the final states with respect to the current direction in different devices have led to the proposal of several different mechanisms in the literature, which is necessary if one assumes that a SOT-based mechanism dominates. By taking into account a thermomagnetoelastic switching mechanism, we can now reconcile these previous findings.

4.1.3 Discussion

Based on four different device and pulsing geometries, we identify the thermomagnetoelastic mechanism in combination with thermal excitations to be responsible for the observed current-induced switching in our NiO/Pt bilayers and NiO/MgO/Pt trilayers, where SOT effects are thus suppressed, and show how previously observed contradicting reports on the final switching state of NiO/Pt can be unified by considering a thermomagnetoelastic switching mechanism and different geometries. With these robust findings, we suggest that the thermomagnetoelastic switching mechanism is not solely limited to NiO thin films. There is evidence that the thermomagnetoelastic mechanism can dominate over SOTs also in other AFMs with large magnetoelastic coupling such as hematite [204] and CoO [105] and might also contribute to some recent data obtained in ferrimagnetic insulators [307]. As a key point, we find that additionally the heating of the AFM is an essential component to enable the thermomagnetoelastic AFM switching and thus not only the strain but also the temperature profile has to be considered. In addition, we note that the final state of the observed switching in NiO/Pt with straight pulses ($\boldsymbol{n} \parallel \boldsymbol{j}$) is opposite to the recently reported switching in CoO/Pt ($\boldsymbol{n} \perp \boldsymbol{j}$) [105]. These differences between materials can be traced back to an opposite sign of the magnetoelastic coupling, resulting in different preferred orientations of the Néel vector [105]. Future investigations on current-induced switching of the Néel vector have to take these findings into account in order to differentiate between switching due to SOTs or thermomagnetoelastic effects in heated areas. While multiple mechanism can coexist, SOT based switching might dominate in thinner layers or materials with lower magnetostriction. Here, we identified that strain alone is not sufficient to switch our NiO thin film, but heat is additionally required. Since both strain and heat can be generated in a non-contact manner, the discovery of a thermally assisted thermomagnetoelastic switching mechanism establishes an alternative writing scheme for insulating AFMs with strong magnetoelastic coupling.

4.2 | Pulse Length Dependent Switching

Heat and strain based switching dominates the observed antiferromagnetic switching of the MgO(001)/NiO(10 nm)/Pt(2 nm) thin films presented in the previous section. However, under certain conditions, one expects that a SOT based switching mechanism could dominate over the thermomagnetoelastic switching, e.g. lead to a change of the switching direction for certain geometries.
Another popular material for the investigation of SOT-based electrical switching is the antiferromagnetic insulator $\alpha-Fe_2O_3$. Investigations of the pulse length-dependent switching have led to contradicting conclusions regarding the underlying mechanism. One study reports the absence of switching for sub 1 µs pulses [308], interpreted as a dominant thermomagnetoelastic switching mechanism. Another study reports switching at ultrashort pulse length of 0.3 ns, the fast timescale indicates here the presence of a SOT based switching [309]. While thermomagnetoelastic switching should be limited by the thermal heating, SOT based switching is expected to possibly occur at (ps) and (ns) timescales [309]. Both mechanisms seem to be present in $\alpha-Fe_2O_3$ and can be revealed through harmonic measurements [310, 311]. More detailed information on the electrical switching of $\alpha-Fe_2O_3$/Pt bilayers can be found in Ref. [312]. Thus, the question arises if SOT based switching can also be observed in our NiO thin films.

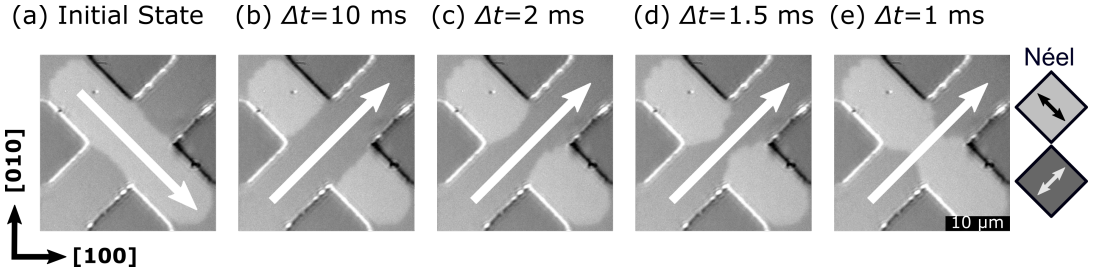

Figure 4.7: Birefringence imaging of the domain structure in a pulse length dependent study of the thermomagnetoelastic switching in MgO(001)/NiO(10 nm)/Pt(2 nm) thin films. An initial 10 ms long pulse (white) has been used to create an initial state and subsequent pulses with varying lengths along the [110] direction have been used to observe a pulse length dependent switching of the central area of the device.

To investigate the pulse length dependent switching we first use the same setup and sample environment, MgO(001)/NiO(10 nm)/Pt(2 nm), described in Sec. 4.1. We initialize a state by a 10 ms pulse along the $[1\bar{1}0]$ direction, see Fig. 4.7 (a). We then use the same current density, but different pulse lengths ($\Delta t = 10, 2, 1.5, 1$ ms) to pulse along the [110] direction, imaging the final state, see Fig. 4.7 (b-e), and re-initializing the state every time in the same manner. One can observe a pulse length dependency, longer pulses with the same current density can switch a larger area.

For the investigation of current-induced switching with shorter pulse lengths (< 1 ms) a different pulsing setup has been implemented and a different sample with additional gold contact pads has been used to enable the switching with shorter pulses. This investigation has been carried out by Merle Schwager as part of her Bachelor thesis [313], assisted by the author. She studied the changes in the switched area ΔA as a function of the current-density and the pulse lengths. The key results of her investigation are presented in Fig. 4.8. One can observe, a dependence of the switched area on the length of the current pulse. For longer current pulses of 500 µs, lower current densities are required than for shorter current pulses of 10 µs. The experimental data could also be fitted to a heat based activation model for the switching, see Ref. [205], which indicates the dominance of a heat assisted switching mechanism. Important to note here is that the minimum pulse length of 10 µs has been a limit of the experimental setup and not of the switching mechanism. For more details, the reader is referred to her thesis [313].

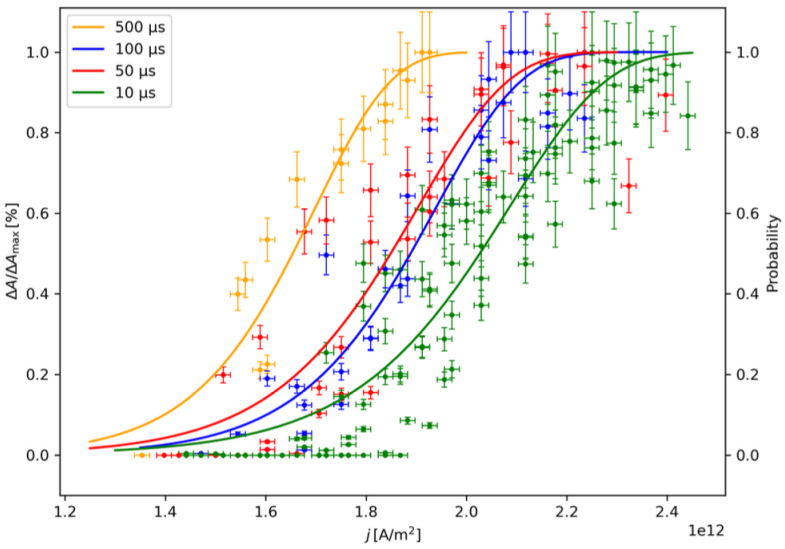

Figure 4.8: The ratio of switched domain area in dependency of the current density for 10 µs, 50 µs, 100 µs and 500 µs. For straight pulses in a 10 µm cross device on a MgO(001)/NiO(10 nm)/Pt(2 nm) thin film with gold contact pads. Reprinted with permission from Ref. [313].

4.3 | Sensitivity of the Electrical Readout

Another option to investigate possible contributions of SOT-based mechanisms to antiferromagnetic domain switching is to study thinner films. The basic idea behind investigating switching in thinner films is that SOT-based switching should scale with $1/d$, where d is the film thickness [42, 201]. Thus, in thinner films, SOT-based switching

may dominate over thermomagnetoelastic switching. However, a challenge for studying the switching of antiferromagnetic thin films is the reduced imaging contrast for techniques such as XMLD-PEEM or birefringence imaging for ultra-thin ($d < 4\,\mathrm{nm}$) antiferromagnetic films [130, 165].
Readout of the antiferromagnetic state in such ultra-thin films can be achieved by electrical readout via SMR measurements. However, relying solely on the electrical measurement of current-induced switching can be misleading. There are several effects such as electromigration and heating [314] that can lead to similar electrical signatures after pulse application [207, 303], as demonstrated for magnetic MgO/NiO/Pt and non-magnetic MgO/Pt thin films [203]. For our NiO thin films, direct comparison between the imaged switched areas and the switched regions allows identification of the magnetic part of the electrical switching signal, manifesting as a step-like electrical signal [182, 209, 217]. However, this cannot be generally assumed for AFMs, since a step-like signal can also originate from a non-magnetic background, like electromigration, [203] and a sawtooth shaped signal can originate from a magnetic switching [210]. One way to combat such an ambiguity is to conduct measurements under magnetic fields [301] or below and above the Néel temperature. Such investigations have allowed for the demonstration of current-induced switching of the antiferromagnetic order in CoO/HM bilayers [105, 168, 302]. Relying on electrical measurements alone to identify the underlying mechanism can be challenging due to the potential non-magnetic signals and limited sensitivity of the electrical readout.
For our NiO/Pt thin films we can separate magnetic and non-magnetic contributions in the electrical signal [182, 217], see Sec. 2.4.4. However, we additionally need to consider the sensitivity distribution of the electrical readout on different regions, as the SMR signal depends on the average domain structure of the measured area [180]. For different pulse geometries, thermomagnetoelastic switching can lead to multiple switching directions within a device after the application of a current pulse [49]. To ensure a correct interpretation of a purely electrical signal in ultra-thin films, the sensitivity of the total resistivity changes to local changes in the domain structure (e.g. changes in the arms or the center of a device) need to be considered.
Felix Schreiber investigated the magnetic sensitivity distribution of Hall devices in antiferromagnetic switching experiments as part of his master thesis [217] and published the results in Ref. [209]. His research has been supported by the author of this work and the main results are briefly presented here.
The two electrical measurement geometries used in the previous Sec. 4.1 are compared in Fig. 4.9. In Fig. 4.9 (a), the SMR measurements are performed along the wide channels of the star device, as would be the case for a device along the [100] direction that uses edge or X-shaped pulses for switching of our NiO(001) thin films. In the second device in (b), the large arms are aligned along the [110] directions. The SMR measurements of the transverse resistance are performed along the small channels, see Fig. 4.9 (a).
The current density distributions can be calculated using COMSOL and are shown in Fig. 4.9 (c) and Fig. 4.9 (d). By simulating a local excitation with a magnetic field for different parts of the devices and plotting the intensity of the measured change

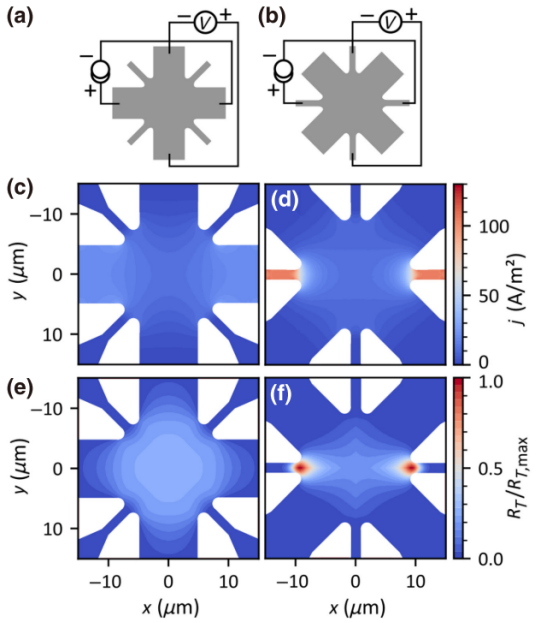

Figure 4.9: (a), (b) Sketch of the measurement geometries. (c), (d) Respective current-density distributions of the resistance read-out to local magnetic signals. Simulations are for a $I = 210\,\mu A$ reading current in a 2 nm thick Pt layer. (e),(f) Sensitivity of transverse-resistance carried out using COMSOL Multiphysics, reprinted with permission from Ref. [209] © 2021 American Physical Society.

in the Hall voltage, one can generate sensitivity maps for the different devices as shown in Fig. 4.9 (e) and Fig. 4.9 (f). As shown in Fig. [209], these distributions can be used to directly correlate the switched regions with the observed changes in the electrical switching signal, and the different signal intensities for the different switching directions in Fig. 4.6 can be reproduced [209], demonstrating the feasibility and validity of the electrical switching readout. The device and pulse geometry not only affect the switching direction, but can also significantly influence the electrical readout. In particular, the inhomogeneous readout sensitivity when using the small readout channels could lead to misinterpretation of the electrical switching signal in thin AFMs. For more details, the reader is referred to Refs. [209, 217].

4.4 | Conclusion

The electrical switching of AFMs is a key step for the development of the writing of antiferromagnetic devices [315]. The possibility of electrically manipulating antiferromagnetic thin films has been demonstrated in recent years in a wide range of materials, from metallic AFMs with special crystal symmetries [191, 192], to bilayers of insulating AFMs and HMs [40–42], and noncollinear AFMs [210, 316]. While

there have been several experimental reports on current-induced switching of NiO/Pt bilayers, the question of the underlying switching mechanism remained open, with most discussions focusing on different types of spin-orbit torques [40–42]. By combining simultaneous electrical measurements and imaging of the magnetic order for different device geometries, we have been able to demonstrate the presence and dominance of a thermomagnetoelastic switching mechanism in Ref. [49], Sec. 4.1, for our MgO(001)/NiO(10 nm)/Pt(2 nm) thin films. A switching mechanism based on heat and strain is able to explain and unify previously conflicting observations of the switching direction in NiO/Pt thin films, which has originated from different device geometries [40–42, 49]. Crucial for the determination of the underlying mechanism is the ability to directly image the switched domains via XMLD or birefringence microscopy [182].

The thermomagnetoelastic switching that dominates in our thin films is not limited to NiO/Pt bilayers [105, 204]. The imaging of the switching of domains outside the current path, as in $\alpha-Fe_2O_3$ [308, 317], CoO [201] can now be explained by a heat and strain based switching, independent of SOTs. In a recent study that has been led by Christin Schmitt and supported by the author, we observe a dominating thermomagnetoelastic switching for thicker ($4 >$ nm) CoO thin films. For thinner films we observe the presence of a second domain pattern that could result from an SOT based mechanism [201]. Demonstrating the possibility of a dominating SOT based switching in thin bilayers of insulating AFMs and HMs. We have attempted to identify such an SOT based switching in our NiO/Pt bilayers by conducting pulse length dependent studies, similar to previous studies on $\alpha-Fe_2O_3$ [309]. For the investigated pulse length range $\Delta t = 10-500$ µs, we have observed temperature assisted switching. Overall, both SOT and thermomagnetoelastic switching are present in antiferromagnetic insulators [201, 310], but the thermomagnetoelastic switching dominates in our MgO(001)/NiO(10 nm)/Pt(2 nm) thin films.

The impact of our results is not limited to the field of insulating spintronics. The observation of a thermomagnetoelastic switching has also resulted in a critical reevaluation of the electrical switching in the metallic AFMs CuMnAs and Mn_2Au. Both materials also exhibit magnetoelastic coupling [66, 297, 318], and there have been reports of a heat activated switching [205]. While a thermomagnetoelastic mechanism might contribute to the switching, it has recently been demonstrated that the observed switching in Mn_2Au depends on the current polarity [319]. Thus, the Néel spin orbit torque dominates over possible heat and strain based switching [319]. However, previous observations of current-induced switching in AFMs need to be critically evaluated for possible non-magnetic contributions and the role of a potential heat and strain-induced switching.

Although strain has long been a common tool to manipulate antiferromagnetic bulk crystals [31] the effect of current-induced strain has previously often been neglected in the switching of AFMs [320]. Our results contributed to putting strain back on the map as a tool for the manipulation of antiferromagnetic domains. Strain is not only relevant for the current-induced switching of AFMs, but also for patterning, see Chap. 5, and optically induced effects on the domain structure of iAFMs, see Chap. 6.

5 | Antiferromagnetic Shape Anisotropy

A common way to manipulate the anisotropy of a ferromagnetic device is to change the shape of the device [37]. In the absence of an external field, the ferromagnetic domain structure of a thin film often adopts a multi-domain state that depends on the exchange interaction, dipolar interaction, anisotropy, and the magnetic stray field. For devices below a certain size, the stray field can lead to a shape dependent domain formation, the ferromagnetic shape anisotropy [53]. Collinear compensated AFMs have no net magnetic moment and thus no stray field. However, multidomain states can still be observed in a wide range of antiferromagnetic materials [31, 88, 91, 92]. In antiferromagnetic oxides, magnetoelastic interactions must be considered in domain formation [43, 44]. In addition, patterning induced changes in the surface anisotropy can also influence domain formation and lead to preferential stabilization of certain domains at the edges of a device [104].

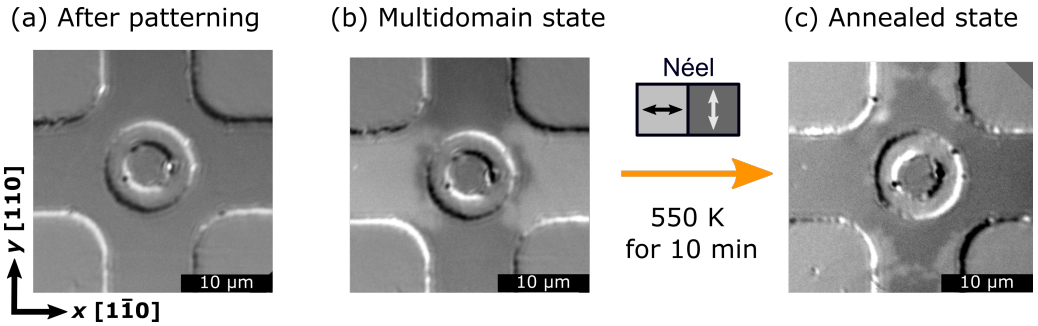

Figure 5.1: Birefringence image of the antiferromagnetic domain structure of a MgO(001)/NiO(10 nm)/Pt(2 nm) bilayer before (a) and after pulse application (b). (c) Domain structure after annealing the device in vacuum at 550 K above the Néel temperature for 10 minutes.

To motivate our exploration of patterning and shape-induced effects, we investigate a device whose initial almost monodomain structure, see Fig. 5.1 (a), is electrically switched into a multidomain state, see Fig. 5.1 (b). If we anneal the device above

its Néel temperature, in vacuum, without a magnetic field, one expects the device to switch back to the initial near monodomain state. However, in Fig. 5.1 (c) we observe the formation of additional domains near the edge of the device, which might seem counter-intuitive. To better understand these effects, differently shaped geometric elements have been investigated as the first author in Ref. [50]. This work is reproduced in Sec. 5.1 with a focus on the experimental work. More details on the theoretical modeling by Olena Gomonay can be found in the Appendix of Ref. [50] and Refs. [65, 66]. Further work extending the investigation to different patterning methods is presented in Sec. 5.2. The observed effects are not unique to NiO and similar effects for CoO thin films are presented in Sec. 5.3. The implications of our work and recent advances in antiferromagnetic shape anisotropy are discussed in Sec. 5.4.

5.1 | Strain-Induced Shape Anisotropy in Antiferromagnetic Structures

5.1.1 Introduction

For the implementation of AFMs as active spintronic devices is the control of the antiferromagnetic order is crucial. In recent years, it has been established that current pulses through an adjacent heavy metal layer can induce a reorientation of the antiferromagnetic ordering in insulating AFMs [40–42]. For iAFMs with strong magnetostriction, the reorientation of the Néel vector is dominated by a thermomagnetoelastic switching and strongly depends on the device geometry [49, 105, 321].
For FMs the device geometry and shape-induced control of the domains is a key tool for tailoring functional device properties. In AFMs, conventional shape anisotropy caused by the magnetic dipolar interactions is not present, due to the absence of a demagnetization field. However, theoretical work on shape-induced phenomena in finite size AFMs predicts an ordering of the antiferromagnetic domains, with long-range strain fields leading to the formation of shape-dependent domain structures [44, 322]. Initial studies of patterning-induced effects in antiferromagnetic $LaFeO_3$ could not observe any changes in the domain structure, after patterning different elements with etching [323]. However, later studies patterned elements via an Ar^+ ion implantation-based patterning technique, which resulted in antiferromagnetic structures embedded in a non-magnetic layer [104, 324]. This technique led to the observation of changes in the antiferromagnetic ordering near the patterning edge for $LaFeO_3$ [104, 325, 326] and more recently $La_{0.7}Sr_{0.3}FeO_3$ [324], interpreted as an edge effect near the edge for

[1] *The following Sec. 5.1 and its subsections were transcribed from Ref. [50] with the first author of this reference being the author of this thesis. Individual contributions are detailed in Appendix C.1.*

elements patterned along the easy axis. Further studies have suggested the exploitation of this effect in exchange bias applications of AFM/FM heterostructures [327]. However, these previous investigations of patterning-induced modulations of the AFM order have been focused on the passive application of AFMs in AFM/FM bilayers. Considering the potential of AFMs as active elements in spintronic devices, it is important to investigate patterning- and shape-induced effects and in particular the control of the domain configuration in AFMs without an adjacent FM layer. It is crucial to not only understand patterning-induced effects near the edge, but also the influence of shape-dependent strain on the domain structure inside a structured antiferromagnetic device. This effect would be most suitable to tailor domain configurations by the shape.
The prototypical collinear antiferromagnet NiO has been considered to be a promising candidate for an active element in spintronic applications, due to the possibility of electrically controlling and reading the AFM order [34, 40, 179, 180] and recent observations of ultrafast currents in the THz regime in NiO/Pt bilayers [27, 328]. In addition, NiO exhibits a high Néel temperature of 523 K in the bulk [31] and strong magneto-elastic coupling [305]. The latter has been used extensively to manipulate the AFM order of NiO by growth-induced strain [109, 134, 329], piezoelectric substrates exerting strain [211] and indirectly via current-induced heating leading to strain [49]. However, the effect of shape-dependent strain on the domain structure of NiO thin films has not been explored. Considering the application of AFMs with strong magnetostriction like NiO or CoO in active spintronic devices, it is important to investigate how the geometry influences the antiferromagnetic domain configuration and how one could use different geometries to control the antiferromagnetic order.
Here, we demonstrate the tailoring of the AFM ground state domain configuration of NiO by shape-dependent strain. We study the Néel vector orientation in patterned elements by PEEM exploiting the XMLD effect for magnetic contrast. We first identify and compare the shape-induced domain structure of elements oriented along different axes before we theoretically explore how shape-induced effects can manipulate the antiferromagnetic ordering in different element geometries. Finally, we demonstrate how the modification of the shape-dependent strain by variation of the aspect ratio of our elements can be used to control the antiferromagnetic domain configuration, demonstrating thus a tool for the shape-induced control of future AFM devices.

5.1.2 Results

To investigate shape-induced effects on the antiferromagnetic domain structure, we have grown an epitaxial NiO(10 nm)/Pt(2 nm) bilayer on an MgO(001) substrate and used Ar ion beam etching to pattern various elements with different orientations. Similarly prepared bilayers of NiO and Pt are currently extensively used for current-induced switching [40–42, 49, 200, 321] and THz radiation experiments [330]. As depicted in Fig. 5.2 (a), we have etched trenches with a width of around 1 µm and a depth of about 20 nm around the desired elements. Additionally, we deposited about 1.4 nm of conducting ruthenium inside the trenches

to reduce the possibility of discharges during PEEM imaging [331]. To allow for a reconfiguration of the AFM domains, the sample has been annealed after pattering above its Néel temperature for 10 minutes at 550 K under vacuum. Measurements have been carried out at the UE49-PGM/SPEEM at the BESSY II electron storage ring operated by the Helmholtz-Zentrum Berlin für Materialien und Energie [332].

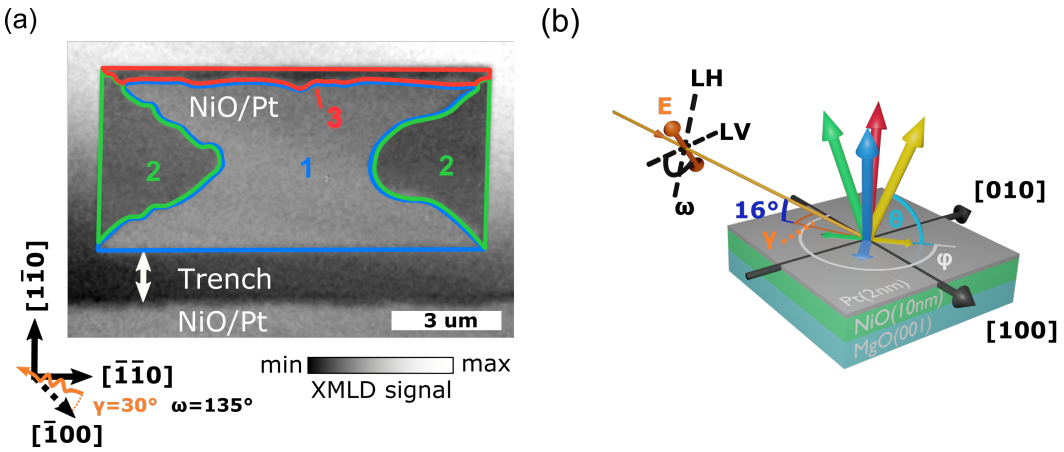

Figure 5.2: (a) XMLD-PEEM image of shape-induced NiO domains inside a rectangular shaped element, MgO(001)/NiO(10 nm)/Pt(2 nm), with its edges oriented along the in-plane projection of the easy axis. (b) Sketch of the experimental setup and orientation of the observed different Néel vector directions [$\pm 5 \pm 5$ 19] with respect to the polarization vector. An orientation along [5 5 19] (yellow) is equally possible, but has not been observed in this particular element. Adapted with permission from Ref. [50]. Copyright 2022 American Physical Society.

We have first measured polarization-dependent absorption spectra around the Ni L_3 and L_2 edge, see Appendix B.2.1, to verify the antiferromagnetic order of our films at room temperature. The XMLD contrast is proportional to the orientation of the Néel vector. By studying the XMLD contrast dependence on the azimuthal angle γ and angle of the beam-polarization ω (Appendix B.2.1) we can identify in Fig. 5.2 (a) four antiferromagnetic domains present in a rectangular element of 10 µm $\times$ 5 µm whose long axis is oriented along the [110] direction. Three different levels of XMLD contrast are observed inside our element, indicating three types of domains, a larger domain in the center (domain 1 - blue), two originating from the short edges (domain 2 - green) and one narrow at the long edge (domain 3 - red). The directions of the Néel vector in the different domains are depicted in Fig. 5.2 (b). We can observe that the in-plane projection of the Néel vector in all domains is oriented orthogonal to the edges of the element along [110] and [1$\bar{1}$0]. The formation of domain 3 (red) along the edge can be attributed to localized changes of the anisotropy near the edge of the element, related to patterning-induced material property changes. However, the shape

of domains 2 (green) and 1 (blue) in the center of the element can not be understood by local changes of the anisotropy at the edge of the element and we need to model long-range magnetoelastic interactions to understand the domain configuration.
NiO is known for its strong magnetoelastic coupling, which is responsible for the creation of internal (magnetoelastic) stresses in a magnetically ordered state. In a free-standing homogeneously magnetically ordered sample, these stresses induce a pronounced spontaneous strain ($u_0 \propto 10^{-4} - 3 \cdot 10^{-3}$ [333]) characterized by the strain tensor $\hat{u}_0^{\text{spon}}$ whose components are related with the components of the Néel vector $\boldsymbol{n}$.
In a multilayer system the internal magnetoelastic stresses are complemented by the external stresses due to the clamping of the antiferromagnetic layer by a nonmagnetic substrate [94]. In this case the resulting strain field can be split into two parts, spontaneous (or plastic) strains $\hat{u}_0^{\text{spon}}[\boldsymbol{n}(\boldsymbol{r})]$ associated with the distribution of the Néel vector (as in the absence of a substrate) and additional, elastic strains $\hat{u}^{\text{elast}}$: $\hat{u}^{\text{tot}} = \hat{u}_0^{\text{spon}} + \hat{u}^{\text{elast}}$.
To calculate the elastic strain, we use an approach of elasticity theory with continuously distributed defects [334, 335]. In particular, we assume that in magnetic multilayers the defects originate from the incompatibility between the spontaneous strain $\hat{u}_0^{\text{spon}}$ and the non-deformed (reference) state of a non-magnetic substrate at the NiO/substrate interface, or from incompatibility between spontaneous strain in neighboring domains. From the compatibility condition for the total strain $\varepsilon_{ijk}\varepsilon_{lmn}\partial_j\partial_m u_{kn}^{\text{tot}} = 0$ (where ε_{ijk} is an antisymmetric Levi-Civita tensor) we obtain a set of equations for the elastic strains

$$\varepsilon_{ijk}\varepsilon_{lmn}\partial_j\partial_m u_{kn}^{\text{elast}} = \eta_{il}, \tag{5.1}$$

in which the incompatibility tensor $\eta_{il} \equiv -\varepsilon_{ijk}\varepsilon_{lmn}\partial_j\partial_m u_{kn}^{\text{spon}}[\mathbf{n}(\mathbf{r})]$ is calculated for a given distribution of the Néel vector. Equation (5.1) is similar to equations of electrostatics, in which the incompatibility $\hat{\eta}$ plays the role of the elastic or magnetoelastic charges and the elastic strains $\hat{u}^{\text{elast}}$ correspond to the potentials [336]. Moreover, similar to the electric and magnetostatic stray fields, the field of the corresponding elastic strains is long-range and therefore can stabilize an inhomogeneous distribution of the magnetic vectors. The similarity with the equations of electrostatics and magnetostatics allows for a qualitative interpretation of the magnetoelastic effects in terms of magnetoelastic charge distributions.
Here, we consider some of the effects that reinforce our intuitive reasoning through modelling. The theoretical description of magnetic textures is based on minimizing the total energy of a sample with respect to magnetic and elastic variables. The bulk energy of the NiO film,

$$W_{\text{bulk}} = \int d\mathbf{r}(w_{\text{mag}} + w_{\text{me}} + w_{\text{elas}}) \tag{5.2}$$

includes magnetic, w_{mag}, magnetoelastic, w_{me}, and elastic, w_{elas} contributions. The magnetic structure of NiO is described by the Néel vector $\mathbf{n}(\mathbf{r})$ ($|\mathbf{n}| = 1$), which is generally parameterized with two angles, ϕ and θ, as shown in Fig. 5.2 (b).

We distinguish in our thin NiO films four types of T-domains with the Néel vector oriented along $[\pm 5 \pm 5\ 19]$ [137]. The pairs with opposite orientation of projection on the film plane have the same in-plane components of spontaneous strain and will be treated in the further discussion as the same domain. Since the out-of-plane component of the Néel vector is the same in all domains, we consider the in-plane angle φ as the only magnetic variable. We also neglect the magnetic homogeneity throughout the thickness of the NiO layer and consider the distribution of the Néel vector to be within the film plane (xy).
We start with a discussion of the origin of the domain structure in thin films and patterned elements. A single-domain continuous film of NiO is charged (elastically) due to incompatibility strain charges homogeneously distributed at the interface with the non-magnetic substrate. The charge density depends on the elastic and magnetoelastic properties of the interface and is localized in a thin layer of the order of the exchange length (characteristic length scale at which the Néel vector decays inside the nonmagnetic region). These magnetoelastic charges create additional homogeneous strain $\hat{u}^{\text{elast}}$ and their non-negative contribution to the energy of the NiO layer is proportional to the volume of the NiO.

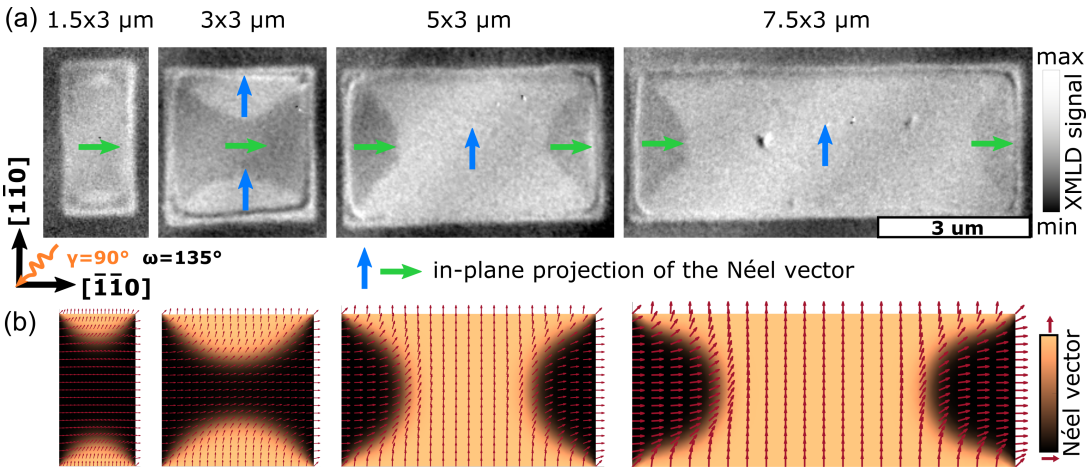

Figure 5.3: (a) XMLD images of different MgO(001)/NiO(10 nm)/Pt(2 nm) rectangular devices with varying aspect ratio. The edges of the devices are oriented along the in-plane projection of the easy axes. The arrows show the in-plane projection of the Néel vector determined from the grayscale contrast. (b) Final equilibrium state of the magnetic texture after considering magneto-elastic interactions to simulate the domain distribution in different aspect ratios. The color code indicates the direction of the Néel vector. Reproduced with permission from Ref. [50]. Copyright 2022 American Physical Society.

In a multidomain sample with equally distributed domains of all types, the average strain incompatibility and average charge density vanish. The local elastic charge density is still non-zero and contributes to the energy of the sample. However, this

contribution is proportional to the average domain volume. Hence, a small-scale multidomain structure is energetically favorable, with the domain size being limited by the positive energy contribution of the domain walls (similar to the Kittel model in ferromagnets [337]). However, the formation of a new domain inside a single-domain region is blocked by a high energy barrier associated with the coherent rotation of a large number of magnetic moments in the two sublattices. The energy barrier can be much lower at the sample surfaces and edges due to the additional contributions from surface energy and incompatibility charges at the element corners [94].
First, we consider the role of the surface magnetic anisotropy present in thin film NiO continuous films and patterned elements, which in our case favors alignment of the Néel vector perpendicular to the surface. For this we studied the evolution of the magnetic structure in the patterned elements with different aspect ratio cut parallel to the in-plane projection of the easy magnetic axis, see Fig. 5.3 (a).
In this geometry the surface anisotropy induces the formation of the dark domains along $[1\bar{1}0]$ edges and bright domains along [110] edges. The final texture includes two closure domains localized at the short edges and a large orthogonal domain that spreads between the two long edges. The closure domains grow from the edges due to magnetoelastic forces that act to diminish the average magnetoelastic charge of the sample. This growth is limited by an increase of the energy of the domain walls. The size of the closure domains is of the order of the size of the short edge and depends on the aspect ratio of the sample, see Fig. 5.3 (b). It should be noted that in the absence of magnetoelastic coupling, the closure domains would be localized in the vicinity of the short edge within a distance of several magnetic domain wall widths, see Fig. 5.4, independent of the aspect ratio of the device.

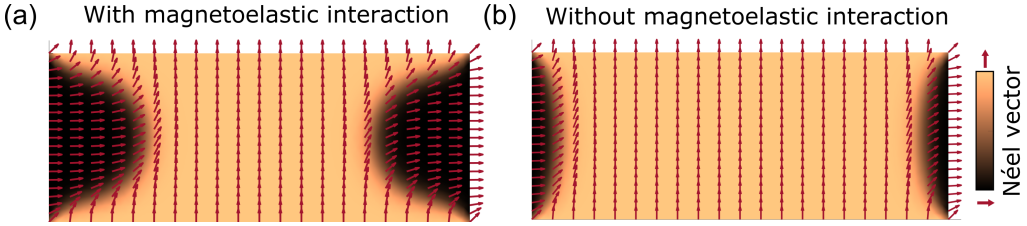

Figure 5.4: Comparison of the simulated domain structures between equilibrium states with (a) and without (b) consideration of magnetoelastic coupling. Adapted with permission from Ref. [50]. Copyright 2022 American Physical Society.

Our simulations also show that the closure domains can be localized along the longer edges of the samples as well, as could be experimentally observed for larger patterned devices. However, both configurations (the one with the closure domains along the short and the other along the long edges) are observed in a finite range of aspect ratios (between 1/3 and 3) for which their energies have comparable values. In this case the structure of the final state depends on the initial configuration and kinetics of the domain growth.

To better illustrate the effect of strain, we next investigate elements oriented along the [100] and [010] axes, where even more conspicuous effects are expected. For elements oriented along the projection of the hard axes the domains do not align along the edges of the element, but instead are centered around the corners of the elements, see Fig. 5.5 (a). Inside the element, we can observe a large green domain (indicated by the green arrow) and two blue domains, which are located near the top left and bottom right corner. Outside the element, we observe a domain (green arrows) and two additional domains (blue arrows) located at the top right and bottom left corner, opposite to the domains in the inner corners. In the case that the domain formation is dominated by an alignment along certain crystallographic axes one would expect the same domains to be present at the inside and outside edge of the element. However, this is not the case and we therefore need to consider shape-dependent strain, in particular the role of incompatibility charges in the corners of the elements, to understand the origin of the domain structure.

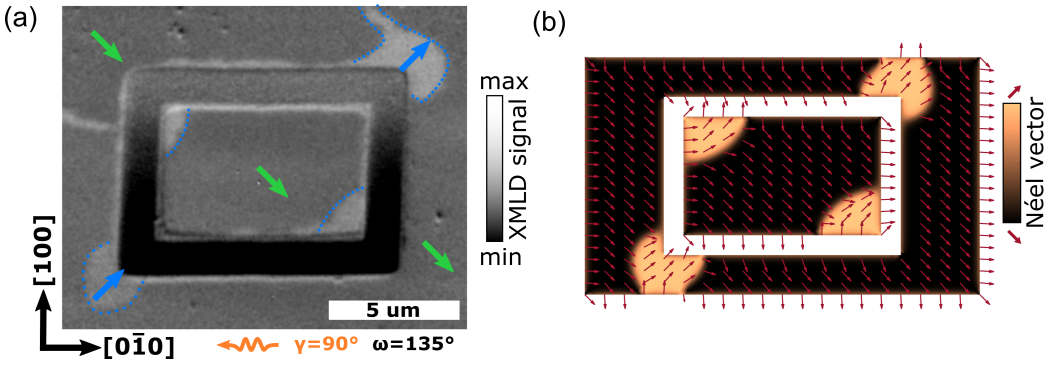

Figure 5.5: (a) Antiferromagnetic domain structure of a rectangular shaped element oriented along the in-plane projections of the hard axes in a MgO(001)/NiO(10 nm)/Pt(2 nm) bilayer. (b) Simulated equilibrium state of the magnetic texture. The color code and the arrows indicate the direction of the Néel vector. Adapted with permission from Ref. [50]. Copyright 2022 American Physical Society.

For elements cut along the in-plane projection of the hard magnetic axis, the surface anisotropy favors an orientation of the Néel vector along a hard magnetic axis and does not set a preferable domain type. However, the surface anisotropy sets orthogonal easy directions at neighboring edges and favors the formation of vortex-like textures of the Néel vectors in the vicinity of the sample corners. Such a rotation of the Néel vector through 90° is associated with an inhomogeneous rotation of the spontaneous strain $\hat{u}_0^{\text{spon}}$ and creates an elastic vortex structure, so-called disclinations [335, 338], localized in the corners. Each disclination is characterized by elastic incompatibility charges which have opposite sign in neighboring corners, see Fig. 5.6. These charges create a radially distributed field of elastic strain $\hat{u}^{\text{elast}}$ [335] that via magnetoelastic coupling sets preferentially directions for the Néel vector along the diagonals of the

element. For the elements cut along the easy magnetic axis, this strain couples with the orientation of the Néel vector in the center of the domain walls and splits the energy of the domain walls pinned to the neighboring corners. For the elements cut along the hard magnetic axis, it removes the degeneracy between the bright and dark domains and facilitates a formation of the domain of a certain type. In other words, the elastic strains lower the energy barrier for a closure domain. Here, the closure domain starts to grow from the opposite corners, which have the same sign of rotation, as shown in Fig. 5.5 (b). Interestingly, such magnetoelastic disclinations appear not only at the inner corners of the rectangular elements, but also at the corners of the outer part of the element, where the spontaneous strain rotates in the opposite direction [339].

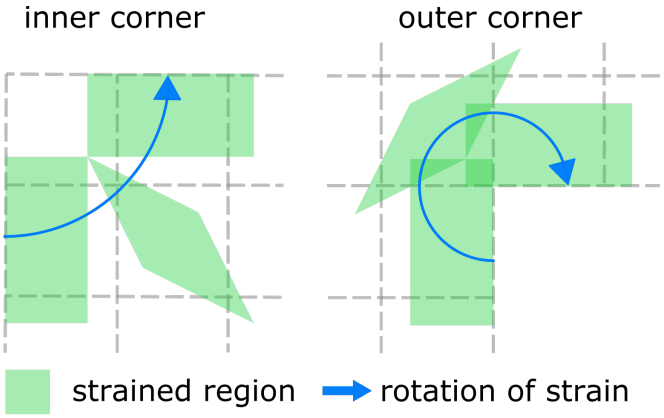

Figure 5.6: Sketch of the different direction of the rotation for strain at inner and outer corners. Adapted with permission from Ref. [50]. Copyright 2022 American Physical Society.

Hence, internal and external strain charges of the same corner have opposite signs. As a result, the closure domains of the same type start to grow along the different diagonals in the internal and external regions, see Fig. 5.5 (a) and (b). Magnetoelastic disclinations (corner charges) are also present in the elements cut along the easy magnetic axes. In this case, corresponding elastic strains set a preferable direction of the Néel vector inside the domain walls near the corners.
In addition, different antiferromagnetic domains are accompanied by the deformation of the crystallographic structure. Due to the need for mechanical equilibrium, the creation of antiferromagnetic domains is accompanied by destressing effects [43, 44]. The total energy of a patterned element is here complemented by the destressing energy W_{destr}, which describes the coupling with the nonmagnetic substrate and edge effects, and the surface energy W_{surf} of the patterned edges. The surface energy is modelled in a way to favor an orientation of the Néel vector parallel to the normal $\mathbf{N}$ with respect to the patterned edge:

$$W_{\mathrm{surf}} = -K_{\mathrm{surf}} \oint (\mathbf{n} \cdot \mathbf{N})^2 d\ell. \tag{5.3}$$

Here, the constant $K_{\text{surf}} > 0$ parameterizes the surface energy and ℓ is the coordinate along the sample edge. The destressing energy, W_{destr}, is treated as an additional contribution of the elastic strains $\hat{u}^{\text{elast}}$, which maintains the strain compatibility of the sample at the interface with nonmagnetic substrate.
To demonstrate the role of incompatibility and the destressing effects in the formation and stabilization of the domain structure, we have calculated the evolution of the domain structure for elements along the in-plane projection of the easy axes, see Fig. 5.7, starting from the almost homogeneous state (domain 2, green) with small domains (domain 1, blue) localized at the long edges of the sample using different values of the damping parameter (different rates of the energy losses). At the initial stage, the closure domains (at the long edge), being pinned in the corners, grow in size trying to reduce the average incompatibility of the sample.

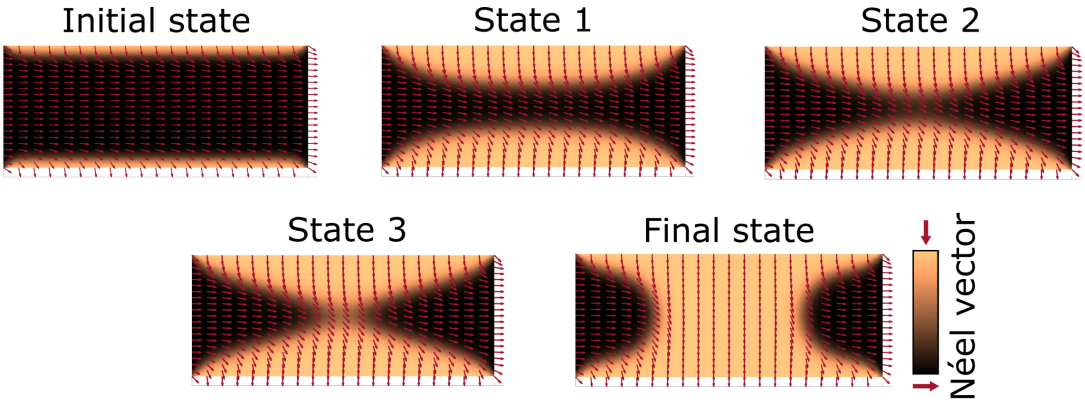

Figure 5.7: Simulated evolution of the domain structure from the initial state to the final equilibrium state. The different states are snapshots of the domain formation during the non-equilibrium. Adapted with permission from Ref. [50]. Copyright 2022 American Physical Society.

In case of slow (quasistatic) relaxation (effectively large damping) the system evolves into a state with the closure domains 1 along the long edges separated by domain 2. In the opposite case of small damping the closure domains merge and the final state corresponds to the closure domains of the type 2 localized at the short edges.

5.1.3 Discussion

We identify long-range strain to govern the shape-dependent formation of antiferromagnetic domains by investigating elements with different orientations and aspect ratios etched into NiO/Pt bilayers. We observe a preferential orientation of the Néel vector perpendicular to the edge of our devices due to patterning effects. Consistent with previous observations, the lattice mismatch between the MgO substrate and the NiO layer leads to a stabilization of different T-domains with only the S-domain

with the largest out-of-plane components, due to the strain in the out-of-plane direction [137]. We investigate the domain structures of elements oriented along the projection of the easy and hard axes and can identify shape-dependent strain to be responsible for the observed domain structures. We can reproduce our experimental observations by magnetoelastic modelling that accounts for the spontaneous strain, due to the distribution of the Néel vector, and elastic strain due to contributions from the substrate and the patterning. In previous studies, the substrate-induced strain has been the same for the different T-domains [137]. Here, however, the shear strain due to the domain formation varies for the different domains across the different geometries. The strain that dominates the formation of the domain structure does not arise from patterning induced strain, but from the strain that is associated with the formation of each T-domain. The interactions between these strains are responsible for the formation and stabilization of the equilibrium domain structure.
Analogous to shape-anisotropy in ferromagnets, magnetoelastic interactions in AFMs are long-range and can be used to tailor the antiferromagnetic ground state of antiferromagnetic devices. For example, by choosing the right size, aspect ratio and orientation one could use shape-induced strain to control the antiferromagnetic ground state in antiferromagnetic THz emitters to tailor and optimize their response [330]. In addition, the strain from the patterned device itself could be used in electrical switching of AFMs to support or hinder the reorientation of the Néel vector independent of the underlying switching mechanism.
Finally, we note that long range magnetoelastic interactions in AFMs could also be a challenge for the development of antiferromagnetic data storage as reorienting the Néel order to switch bits will lead to a change in strain and affect neighboring bits. However, by considering physical separation as in established bit-patterned media [340], the non-interacting nature of AFMs can be fully taken advantage of due to the absence of magnetic stray fields.
In summary, we identify how shape-dependent strain can be used to control the antiferromagnetic ground state in NiO. Since magnetoelastic coupling is significant for several other AFMs such as CoO and hematite, shape-induced strain can be considered to be the antiferromagnetic equivalent of conventional shape-induced anisotropy in ferromagnets and provides a unique means to control AFMs.

5.2 | Patterning Induced Changes in the Surface Anisotropy

Crucial to the observation of antiferromagnetic shape anisotropy in the previous Sec. 5.1 is the change in surface anisotropy at the edges of the geometric elements due to patterning. In the annealed elements, a preferential stabilization of different T-domains occurs near the patterning edges. We observe the preferential formation of three different T-domains in devices patterned along the easy in-plane axes of our NiO thin films. However, considering the fourfold symmetry of NiO, see Sec. 2.3.3, one would expect the formation of four different T-domains at the edges of the de-

vice [137]. Therefore, we here take a closer look at the patterning induced effect on the domain structure after patterning and before annealing our samples.
First, we use the same procedure described in the previous Sec. 5.1 to pattern a geometric element. Using electron beam lithography and subsequent etching, we remove a 1 µm wide trench around the desired shape of our device and deposit a thin 1 nm layer of Ru inside the trench. The antiferromagnetic domain structure of our device is imaged by XMLD-PEEM in Fig. 5.8 (a). We can distinguish three different types of domains. The domains near the long edge have the same in-plane orientation but opposite out-of-plane orientation, as observed for the annealed samples. Along the short edge, only one domain type (domain 2) is present.

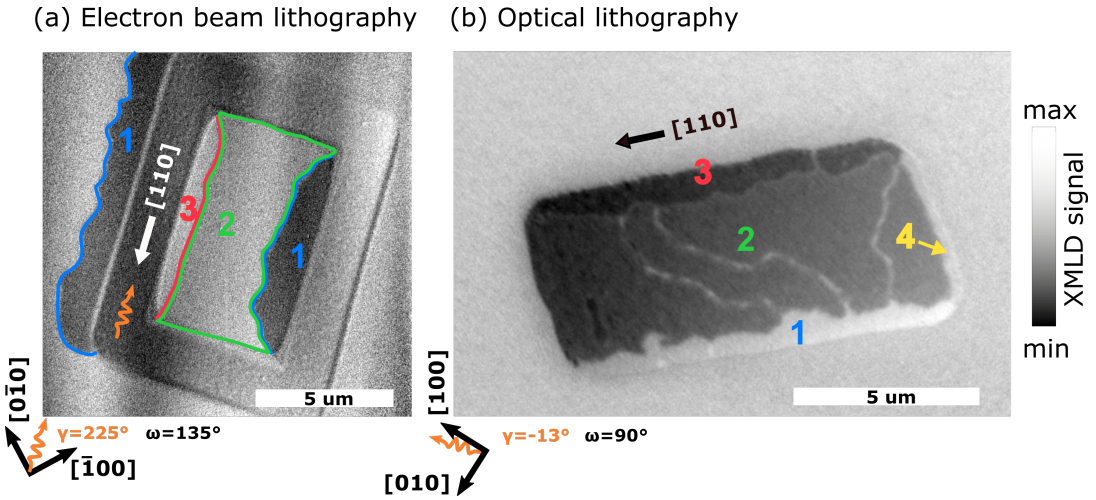

Figure 5.8: XMLD image of the domain structure of a geometrical element in MgO(001)/NiO(10 nm)/Pt(2 nm) bilayers that has been defined by either (a) removing a small trench around the device or (b) being a free standing element. The images have been obtained on different pieces of the same sample at different synchrotron facilities. The [001] axes has been chosen in away that the Néel vector in the central domain points along the same direction.

On a second piece of the same sample we use an optical mask to pattern similar geometrical elements via optical lithography. After etching the NiO/Pt bilayers, the geometric element is freestanding with no surrounding NiO/Pt layer. The nearest other device is 4 µm away. The patterning-induced domain structure of an element, see Fig. 5.8 (b), shows the preferential formation of two different domains at the long edge. This is similar to the element in Fig. 5.8 (a). However, we can observe an additional domain along the short edges, which has the same in-plane orientation but the opposite out-of-plane orientation as the central domain. Thus, all four different possible T-domains [$\pm 5 \pm 5\,19$] can be observed in our thin films [137]. Interestingly, the fourth domain is not present in the geometric elements whose pattern is defined by removing material in a trench around the device, Fig. 5.8 (a). It should be noted, that the patterns in Fig. 5.8 (b) have been etched 60 s longer (approx. 5 nm more

MgO removed) than in Fig. 5.8 (a). However, additional patterning depth dependent studies have not revealed a significant influence of the depth.
The favorable formation of domain 2 and suppression of domain 4 originates likely from a small growth-induced uniaxial anisotropy of our NiO thin films. By removing the surrounding material around the device, we modify the anisotropy of our device. Removing the NiO layer from the MgO substrates could allow for a better relaxation of the strain by the MgO layer, which in turn influences the NiO domain structure due to surface clamping [50, 65]. These changes in anisotropy enable the patterning induced changes in the surface anisotropy to overcome the small uniaxial anisotropy of our thin films, and a fourth domain is formed near the short edge.
The origin of the observed uniaxial anisotropy is the growth of NiO on MgO substrates. The distribution of the four different types of T-domains in NiO crystals was previously studied by Roth [31]. For a cleaved crystal, the four different T-domains of NiO were roughly evenly distributed. However, for a NiO crystal grown on MgO (001), the preferential formation of one type of T-domain (72.3 % coverage) was observed. The domain with the same in-plane but different out-of-plane component was present in only 1.2 % of the sample [31]. His observation is similar to our observation of a dominant domain 2 and a suppressed domain 4. Thus, the growth of NiO on MgO substrates is likely responsible for the observed superimposed uniaxial anisotropy.
We can conclude that patterning induced changes in surface anisotropy can lead to the preferential formation of up to four different types of T-domains in our NiO thin films. In further studies of antiferromagnetic domain formation, it is important to understand that, in contrast to ferromagnetic shape anisotropy, not only the shape of the device defines the antiferromagnetic state. The region surrounding the device can also influence the domain formation due to the coupling of the long-range magnetoelastic interactions with the substrate.

5.3 | Antiferromagnetic Shape Anisotropy in CoO Thin Films

Antiferromagnetic shape anisotropy is expected to be a common phenomenon in AFMs with significant magnetoelastic coupling, and not limited to NiO [43, 44, 50]. Another AFM with strong magnetoelastic coupling is CoO, see Sec. 2.3.3.2. Thus, here we investigate the influence of geometric patterns on MgO/CoO(10 nm)/Pt(2 nm) thin films. First, we identify the domain structure of our 10 nm thick CoO thin films, before investigating the effect of patterning different shapes.

5.3.1 Domain Structure of MgO/CoO/Pt Thin Films

Similar to NiO thin films, the domain structure of CoO thin films is influenced by the substrate-induced strain [161, 162]. The CoO(10 nm)/Pt(2 nm) bilayers investigated here are grown on MgO(001) substrates by reactive magnetron sputtering in an oxygen gas atmosphere. Similarly grown films have been previously characterized in [105].

The lattice mismatch (1.1 %) between the CoO and the MgO leads to compressive strain, which results in a preferential in-plane orientation of the Néel vector in CoO thin films [163].
We image the domain structure of CoO/Pt bilayers by energy-dependent XMLD-PEEM imaging at the L_3 Co edge, as part of current-induced switching studies. A typical image of the domain structure inside a patterned 10 µm cross before pulse application is shown in Fig. 5.9 (a).

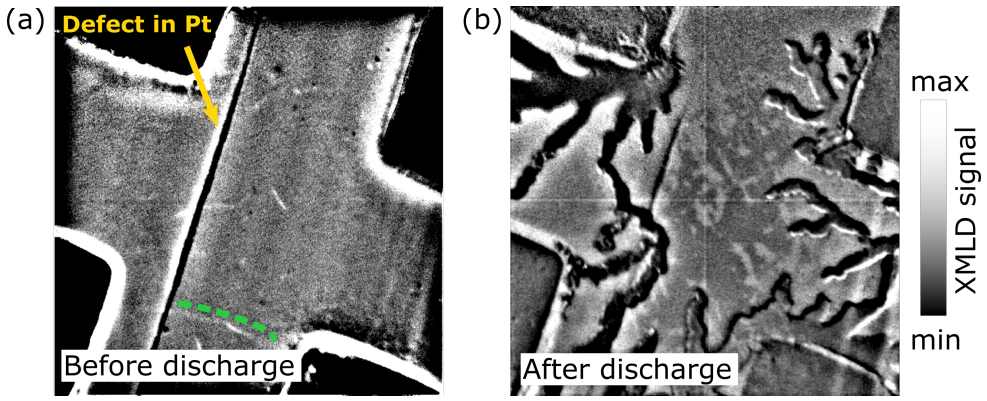

Figure 5.9: XMLD-PEEM image of the antiferromagnetic domain structure in MgO(001)/CoO(10 nm)/Pt(2 nm) bilayers (a). The green line indicates a slightly visible domain wall. In (b) a multidomain structure is visible after an electrical discharge. The contrast near structures includes non-magnetic artifacts from contrast enhancement, see Appendix B.3.4.

The sample exhibits a XMLD signal in the XAS, but most of the sample does not exhibit a clearly visible domain structure. In XMLD-PEEM areas with the same contrast indicate domains in which the Néel vector has the same projection on the X-ray polarization. If the contrast remains identical for multiple variations of the azimuthal angel and beam polarization for two domains, their Néel vector is pointing along the same axes, but not necessarily the same direction [51, 124]. The presence of partially visible narrow domain walls in Fig. 5.9 (a) indicates a possible domain structure which is dominated by 180° domains in the patterned films. In the case of 180° domains the contrast between both domains is identical as they only differ in the orientation of the sublattice moments, but not in the axes of the Néel vector [51, 124]. Before the pulsing experiments an electrical discharge has destroyed the pulsing cross. However, the discharge has also created a multi-domain structure, as shown in Fig. 5.9 (b). Two different types of contrast, indicating the presence of two domains with different Néel vector orientation, can be observed. Such a domain structure is not a unique result of the electrical discharge. A similar multi-domain structure can be observed in an arrow-shaped structure in which the Pt layer has been removed by etching, as seen in Fig. 5.10.

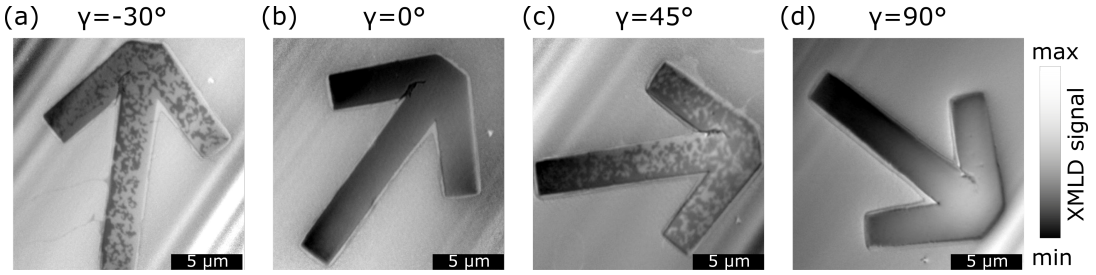

Figure 5.10: XMLD-PEEM image of the antiferromagnetic domain structure in MgO(001)/CoO(10 nm)/Pt(2 nm) bilayers in an etched arrow for multiple azimuthal angles $\gamma = -30°, 0°, 45°, 90°$ (a-d). The edges of the arrow are parallel to the [100] axes. The images have been taken by energy dependent XMLD-PEEM imaging with in-plane polarization. Dark and bright contrast corresponds to domains with 90° differences in in-plane Néel vector orientations. The easy axis is along [110] and $[1\bar{1}0]$.

The multidomain structure is only visible when the X-ray polarization is mostly in the plane of the sample and no contrast can be observed with out-of-plane polarization, indicating an in-plane orientation of the Néel vector. By rotating the sample and obtaining images with different $\gamma = -30°, 0°, 45°, 90°$ azimuthal angle, we can observe a disappearance of the contrast when the direction of the X-ray beam is parallel to the [100] or [010] axes ($\gamma = 0°, 90°$) and a contrast maximum at 45°. Thus, we can identify the orientation of the Néel vector in our thin films to be in-plane with [110] and $[1\bar{1}0]$ as easy axes, leading to the formation of two different types of domains with orthogonal in-plane component of the Néel vector. The fourfold symmetry and in-plane alignment is consistent with previous studies of CoO grown on MgO [161, 162] and previous electrical observations on our MgO/CoO/Pt thin films [105]. In addition, we observe a growth-induced uniaxial anisotropy superimposing the cubic anisotropy leading to the preferential formation of one domain type, similar to our MgO(001)/NiO(10 nm)/Pt(2 nm) thin films, see Sec. 5.2, and observation of a superimposed uniaxial anisotropy in 2 nm CoO thin films, see Appendix of Ref. [201], which may hinder the formation of a multidomain state.

5.3.2 Patterning Induced Effects in CoO/Pt Thin Films

To investigate strain-induced antiferromagnetic shape anisotropy in CoO, we pattern our MgO(001)/CoO(10 nm)/Pt(2 nm) samples with similar geometric patterns as our NiO samples, see Sec. 5.1. The bilayers are patterned by electron beam lithography and then etched with Ar ions before ruthenium (1 nm) has been deposited in the trenches to minimize the risk of electrical discharges during XMLD-PEEM imaging. The domain structure of the thin films has been first imaged after the patterning process, see Fig. 5.11 (a), before the CoO thin film was heated in-situ at an X-PEEM station above its Néel temperature to 370 K. The annealed domain structure is shown in Fig. 5.11 (b).

It can be observed that the domain structure of our CoO thin films has not formed a shape-dependent multidomain state as in the NiO thin films. However, we can still observe changes in the domain structure. The narrow 180° domain walls that have previously been present in the thin films have realigned in several sections to align themselves between the patterned elements, see green lines in Fig. 5.11. By aligning along the shortest path between different elements, the domain walls minimize their energy. Thus, patterning can be used to control the domain walls. Similar antiferromagnetic shape anisotropy effects as in NiO seem to be suppressed due to the growth-induced superimposed uniaxial anisotropy of the thin film.

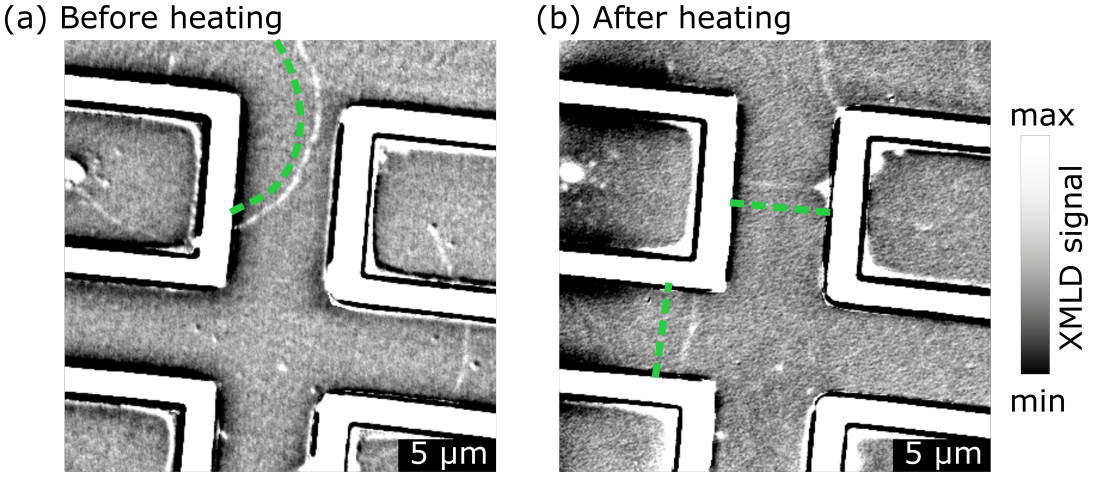

Figure 5.11: XMLD-PEEM image of the antiferromagnetic domain structure in MgO(001)/CoO(10 nm)/Pt(2 nm) bilayers. We can observe a realignment of domain walls (green lines) when comparing the state after patterning (a) and after heating the sample to 370 K (b). The contrast near structures includes non-magnetic artifacts from contrast enhancement, see Appendix B.3.4.

To overcome this limitation, we have carefully applied external pressure to split the sample into two pieces. This introduced dislocations and additional strain into the system, leading to the formation of a multidomain structure in parts of the sample. The sample now exhibits a transition from what appears to be an almost monodomain (or single domain type) state to a multidomain state, which we can image with birefringence imaging, see Fig. 5.12. In the more monodomain region in Fig. 5.12 (a), bright domains are preferred. In other parts of the sample, however, the domain structure transitions from a clear multidomain state Fig. 5.12 (b) to a state dominated by dark domains Fig. 5.12 (c).

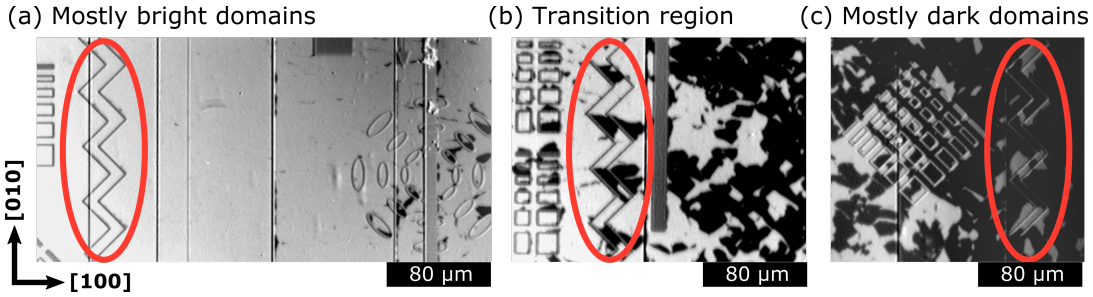

Figure 5.12: Birefringence image of the antiferromagnetic domain structure in MgO(001)/CoO(10 nm)/Pt(2 nm) bilayers after splitting the sample into two pieces. In one piece of the sample a change in the domain structure can be observed from a monodomain bright state (a), via a transition region (b) to a mostly dark state (c). Patterning dependent changes in the domain structure can be observed in the red ellipse. Dark and bright contrast corresponds to domains with 90° differences in in-plane Néel vector orientations.

While the patterning of the geometric elements has no visible influence on the domain structure in the monodomain bright region of the sample, one can observe an influence of the patterning in the transition and dark dominated region. If we focus on the zigzag pattern, see red ellipse in Fig. 5.12, we can observe a preferential formation of white domains when the walls of the pattern are along the [110] direction and a preferential formation of dark domains when the direction is along the $[1\bar{1}0]$ direction. We have observed a similar pattern in studies of antiferromagnetic shape anisotropy in NiO thin films, see Appendix B.3.2. Similar to the shape anisotropy in NiO, the patterning seems to lead to preferential stabilization of different domains at different edges, as the edges with the surface normal pointing along $[1\bar{1}0]$ seem to favor the formation of a dark domain. Similar edge effects can also be identified in the previously imaged arrow structure in Fig. 5.10 and originate from patterning induced changes in the surface anisotropy at the edge of an element, see Sec. 5.2.
Our results on patterning and shape-induced effects in CoO indicate the presence of an antiferromagnetic shape anisotropy similar to NiO. We observe the preferential formation of domains along certain patterning edges and are able to control the domain structure by patterning along the different easy axes. However, the domain structure of our CoO thin films differs from NiO in that only two different types of domains are observed instead due to the in-plane orientation of the Néel vector of up to four, which significantly alters the shape of the observed domain structures. The strong uniaxial anisotropy in our CoO(10 nm) sample superimposes the cubic anisotropy and needs to be overcome to utilize shape anisotropy to tailor the domain structure of CoO. While we have observed preliminary evidence for patterning and shape-induced effects in CoO, more detailed investigations on different samples with a weaker superimposed uniaxial anisotropy are needed to investigate the underlying effects.

5.4 | Conclusion

The antiferromagnetic domain structure is influenced by the patterning and the shape of a device. Patterning of antiferromagnetic thin films leads to a change in the surface anisotropy near the edge of the pattern. Changes in surface anisotropy near the edge can lead to short-range modulations of the antiferromagnetic domain structure, as has previously been observed in $LaFeO_3$ [104, 341]. For our NiO/Pt bilayers we have observed the preferential formation of up to four different T-domains near the edges of a pattern, see Sec. 5.2. The introduction of additional domains by patterning can influence the ground state of the AFM, as can be seen by studying annealed samples, see Sec. 5.1. To understand the equilibrium structure of the annealed state, long-range magnetoelastic interactions must be considered. These arise from the domains created by the patterning, as each T-domain in NiO is associated with a different strain [43, 44]. By controlling the shape of the patterned elements, we demonstrate the control of the antiferromagnetic ground state of our devices.
The strain induced antiferromagnetic shape anisotropy is not restricted to NiO. We have also observed similar effects in CoO thin films, see Sec. 5.3. In the CoO thin films, the domain structure is different from NiO and thus the observed domain structures are different. However, we can observe that patterning along the different easy axes of CoO thin films can modulate the local anisotropy and lead to the preferential formation of a certain domain type. This patterning-induced control of antiferromagnetic domains in CoO indicates that antiferromagnetic shape anisotropy can be expected to be a general phenomenon present in insulating AFMs with strong magnetoelastic coupling [43]. This is supported by a recent report on the domain structure of α-Fe_2O_3, which observed an influence of magnetoelastic coupling on the preferential Néel vector orientations in adjacent domains [65].
Furthermore, it has recently been reported that antiferromagnetic strain anisotropy is not restricted to insulating AFMs with strong magnetoelastic coupling. Similar patterning induced effects as we observed in NiO and CoO have now been demonstrated in the metallic AFMs CuMnAs and Mn_2Au [66]. Thus, strain induced shape anisotropy can be considered to be a general effect in AFMs with magnetoelastic coupling.
The long-range magnetoelastic interactions can hinder the fabrication of antiferromagnetic bits by requiring bit patterning of the media [340], which reduces the potential density of antiferromagnetic bits. However, the antiferromagnetic shape anisotropy is also an advantage. It can be used to tailor the antiferromagnetic ground state of a device. This is particularly interesting for the potential use of AFMs in THz emitters, which exhibit Néel vector dependent signals [342, 343].

6 | Optical Domain Creation

To take full advantage of the potentially ultrafast switching of AFMs, one needs to transition from current- or shape-induced control of the antiferromagnetic order to optically induced switching. AFMs allow potentially faster switching than ferromagnets due to their intrinsic frequencies in the THz range [27]. In the case of NiO, two different magnon modes can be optically excited, see Fig. 6.1. In the low frequency mode, with a frequency around 130 GHz (at 77 K, optical excitation) [45, 99, 344], the Néel vector oscillates in the easy magnetic plane, see Fig. 6.1(a) [99, 344]. In the high frequency mode, with a frequency around 1.07 THz (at 77 K, optical excitation) [45, 99, 344], the Néel vector oscillates out of the magnetic plane [98, 99].

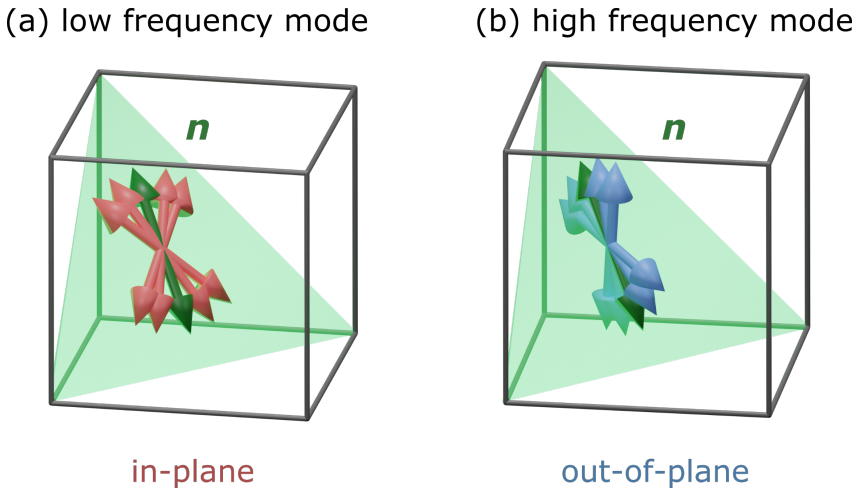

Figure 6.1: In-plane (a) and out-of-plane (b) dynamics of the Néel vector in NiO.

Both modes can be excited by optical irradiation with laser pulses in bulk NiO crystals, and we have observed these features in our MgO(001)/NiO(10 nm)/Pt(2 nm) bilayers together with our collaborators. The low frequency magnon mode could be excited in experiments on the optically induced ultrafast reduction of the sublattice magnetization [345]. In addition, the high-frequency mode could be detected via THz emission from the Pt layer, originating from optically induced magnetoelastic effects [343].

Thus, laser irradiation can be used to excite the antiferromagnetic order [47]. We go beyond the dynamic modulation of the antiferromagnetic order and investigate the creation of antiferromagnetic domains in NiO/Pt bilayers by irradiation with laser pulses with the author of this work as first author in Ref. [51]. This work is reproduced/partly adapted in Sec. 6.1. In addition, results on the optical manipulation of CoO domains are presented in Sec. 6.2 before concluding this section on the optically induced manipulation of antiferromagnetic domains.

6.1 | Optical Domain Creation in NiO

6.1.1 Introduction

A key advantage of AFMs is their potential for ultrafast applications due to their inherent dynamics with resonant frequencies in the THz range [27]. Recently, the electrical switching of AFMs has been intensely investigated [40, 191, 192]. However, to achieve switching on an ultrashort timescale, we must transition from electrical to optical control of the antiferromagnetic order.

In ferri- and ferromagnetic material systems, fs-laser-induced all-optical switching (AOS) has been intensively studied [38, 346–348]. Thermally induced switching has been observed in ferrimagnetic GdFeCo alloys [38, 349] and all-optical helicity-dependent switching based on the inverse Faraday effect has been observed in a wide range of ferri- and ferromagnetic materials [39]. For antiferromagnetic materials, studies on the all-optical switching have focused on the excitation of magnon modes [45–48]. There are experimental reports of large-scale optical switching of antiferromagnetic order in the tilted antiferromagnet $TbMnO_3$ [350]. However, the underlying mechanism relies on the electric polarization and cannot be easily transferred to other AFM systems. Theoretical studies predict possible optically induced switching in antiferromagnetic NiO [351, 352], NiO/FM bilayers [353] and other collinear antiferromagnets [354]. Recently, first experimental evidence for light-induced manipulation of antiferromagnetic domains in NiO crystals has been reported [355].

NiO is a prototypical collinear insulating antiferromagnetic system exhibiting promising features for future potential spintronic devices: current-induced switching of the antiferromagnetic order [40, 49], electrical readout [34], antiferromagnetic shape anisotropy [50], and ultrafast spin dynamics in the THz range [27, 342, 343, 356]. The magnetic order of NiO thin films can be transiently modulated by irradiation with ultrafast laser pulses [345], and several studies have reported helicity-dependent excitation of coherent magnons in NiO [45, 344]. NiO exhibits a strong magnetoelastic

[1] *The following section and its subsections have been transcribed from Ref. [51] and its supplementary, with the first author of this reference being the author of this thesis. Individual contributions are detailed in Appendix C.1.*

coupling [305] and thus the above-mentioned optical manipulation of antiferromagnetic domains [355] has been attributed to a particular phononic mechanism [357]. While several mechanisms have theoretically proposed optically induced switching of NiO, there are no experimental reports on the light-induced domain switching of the antiferromagnetic order in NiO thin films.
Here, we investigate the domain structure of NiO/Pt bilayers that have been irradiated by circularly and linearly polarized laser light using X-PEEM with magnetic linear dichroism as the contrast mechanism. We observe optically induced changes of the domain structure. In contrast to often considered switching between different Néel vector axes, we observe the creation of 180° domains and domain walls, independent of the laser polarization. Variation of the irradiation parameters allows us to identify a thermal origin of the optically induced antiferromagnetic order. We demonstrate the possibility to optically create antiferromagnetic domains in a prototypical antiferromagnetic system.

6.1.2 Results

We have prepared 10 nm thick NiO(001) thin films that are epitaxially grown on MgO(001) substrates by reactive magnetron sputtering. The films are additionally capped with a 2 nm thick platinum layer to allow for imaging with XMLD-PEEM. We have previously characterized and investigated similarly grown NiO(001) thin films and observed that the strain from the substrate mismatch leads to preferential out-of-plane alignment of the Néel vector in these thin films, stabilizing only one type of S-domain [42, 109, 134, 137]. Therefore, only four different T-domains are present in our films, each accompanied by a strong rhombohedral distortion. Similar to our previous studies on 10 nm NiO thin films [137], we observe a domain structure in our field of view (FOV) which predominantly consists of one T-domain. To study the effect of laser-irradiation on NiO/Pt bilayers, we use an ultrafast amplified laser system with a central wavelength of 800 nm and with a pulse repetition rate of 1 kHz, more information in Appendix B.3.1. We have irradiated our samples ex-situ with pulse trains of different pulse duration, pulse fluences, illumination time, and polarization. We imaged the domain structure of the laser irradiated regions using energy dependent XMLD-PEEM at the double peak of the Ni L_2 edge [331]. Fig. 6.2 shows the domain structure of a region irradiated with circular right polarized laser light.
Several narrow domain walls (bright lines) can be observed around a central area where the platinum layer has been structurally changed by the accumulated heat (dark spot). The structural changes in the capping layer are visible due to the high surface sensitivity of X-PEEM and overlay with the magnetic XMLD contrast of the NiO layer in the center.
The XMLD contrast depends on the orientation of the incoming electric field and the orientation of the Néel vector. We have varied the polarization of the incoming X-ray ($\omega = 90°, 112.5°, 135°, 157.5°, 0°$) and the azimuthal angle ($\gamma = 90°, 120°, 135°, 150°, 165°, 180°$) of the sample with respect to the incoming beam. We utilize the same angle definitions for the incoming X-ray and polarization as in

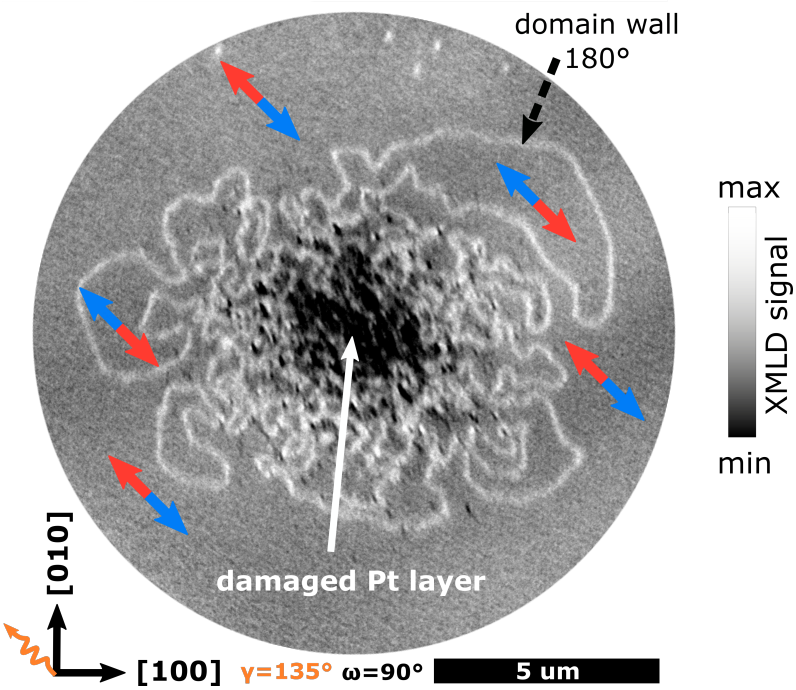

Figure 6.2: XMLD-PEEM image of the AFM domain structure of a MgO(001)/NiO(10 nm)/Pt(2 nm) bilayer in an area that has been illuminated with 2000 pulses with circular right polarized laser light with a pulse length of 6.7 ps and a fluence of 12±2 mJ/cm^2. The incoming X-ray is at an angle of 135° with respect to the [100] axis and the X-ray polarization is vertical to the sample plane with a 16° incidence angle. The blue arrows indicate the direction of the in-plane projection of the Néel vector, the different colors correspond to the different sublattices. Adapted with permission from the supplementary of Ref. [51].

Ref. [50, 137] and the previous Sec. 5.1, as depicted in Fig. 6.3 (a). For all combinations of ω and γ we observe no difference in contrast between the domains inside and outside the domain walls. The absence of contrast changes indicates that the projection of the Néel vector in these domains onto the X-ray polarization is identical for all angles of ω and γ and points along the same directions [268]. Thus, the domain wall between them can be identified as a 180° domain wall between two domains with 180° different orientation of the Néel vector [123]. The orientation of the Néel vector is identical on both sides of the wall, but the spins in the antiferromagnetically coupled sublattices are interchanged, as indicated by the differently colored arrows in Fig. 6.2. Thus, the domains inside and outside the domain walls are in the same T-domain, are accompanied by the same distortion, and their S-domains have the same out-of-plane components. But their sublattices are interchanged, making them 180° differently oriented domains.

For different combinations of ω and γ we observe variation and inversion of the contrast between the domain wall and the surrounding domains, see Fig. 6.3 (b) and (c), confirming the magnetic origin of the contrast. The contrast of the domain wall appears uniform, as previously reported in our recent study on domain walls between T-domains in NiO thin films [138].

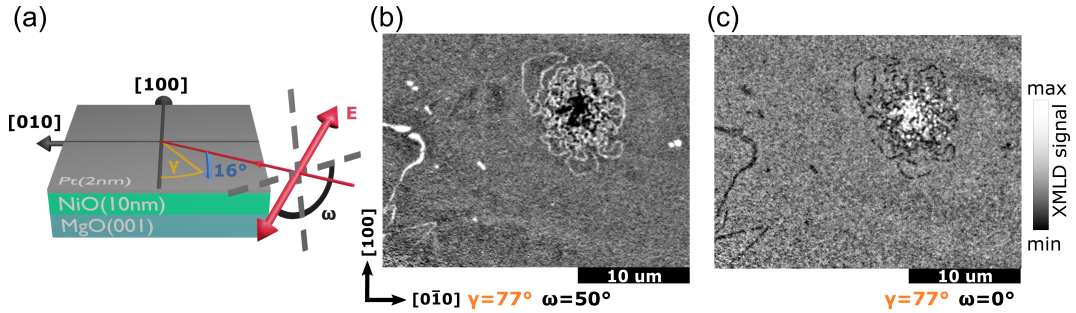

Figure 6.3: (a) Sketch of the experimental setup and angle definitions. (b,c) XMLD-PEEM image of a MgO(001)/NiO(10 nm)/Pt(2 nm) thin film, of an area that has been illuminated with 2000 pulses with circular right polarized laser light with a pulse length of 6.7 ps and a fluence of 12±2 mJ/cm^2. An inversion of the domain wall contrast can be observed when varying the polarization of the X-ray beam between $\omega = 50°$ (b) and $\omega = 0°$ (c). Adapted with permission from the supplementary of Ref. [51] with enhanced contrast, see Appendix B.3.4.

Width of the Domain Wall

In order to estimate the width of the optically created domain wall, we determine the spatial resolution of the microscope. We investigate the line profile of the smallest visible defect and fit a Gaussian function to its peak in the line profile [138]. The full width at half maximum gives us for the resolution minimum an upper limit of $\Delta = 44$ nm, with a 5 nm fit error. We then fit the intensity profile of the domain wall shown in Fig. 6.4 with a Lorentz function convolved with a Gaussian function with the resolution limit as the full width at half maximum (FWHM) to account for the spatial resolution of the microscope [138]. We can estimate the width of the domain wall at the FWHM to be about 100 nm, with an uncertainty of about ±30 nm from the fit and pixel size.

Underlying Mechanism

By irradiation with a laser, we are able to observe the creation of 180° domain walls (bright lines in Fig. 6.2), which indicate the creation of domains with 180° different orientation of the Néel vector. The creation of 180° domains is independent of the polarization of the laser and can also be achieved with linearly polarized laser light, see Fig. 6.5 (a).

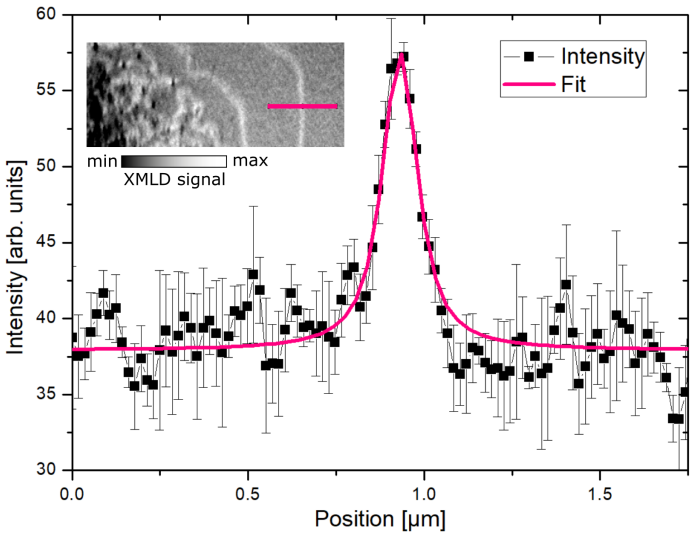

Figure 6.4: The measured intensity of the domain wall profile after averaging over six line scans. The inset shows the area of the line scans from the laser-induced domain structure of a MgO(001)/NiO(10 nm)/Pt(2 nm) thin film, see Fig. 6.2. The width of the domain wall at FWHM can be estimated from fitting a Lorentz function convolved with a Gaussian function to be 100 nm, with an uncertainty of about ±30 nm. Adapted with permission from the supplementary of Ref. [51].

To verify the antiferromagnetic nature of the laser-induced domains, we have annealed our film in vacuum for 10 minutes without magnetic field above Néel temperature, at 550 K, see Appendix B.3.2. This has changed the domain structure and we can observe a disappearance of the 180° domain walls in Fig. 6.5 (b).
After annealing, we have investigated the changes in the domain structure of our sample at another synchrotron facility with a different experimental geometry. To ensure that our contrast and resolution are still sufficient to resolve the antiferromagnetic 180° domain walls, we have checked our contrast at the same position as in Fig. 6.2. The direct comparison between the domain structure before Fig. 6.6 (a) and after annealing Fig. 6.6 (b-d) shows that the domain structure has significantly changed. Most of the previous 180° domain walls have disappeared. However, we can still observe one 180° domain wall and contrast changes by varying the polarization, see Fig. 6.6 (b-d). To image the absence of the 180° domain walls in Fig. 6.5 (b), we chose a polarization of 135° for good contrast and averaged four times more images than for the image depicted in Fig. 6.6 (c).
As mentioned above, the laser-induced 180° domains in Fig. 6.5 (b) have disappeared. However, the domains near the structural defect have not been significantly altered by the heating. In NiO, strain or changes in the surface anisotropy that are introduced by patterning or defects can lead to the preferential stabilization of domains [50]. The

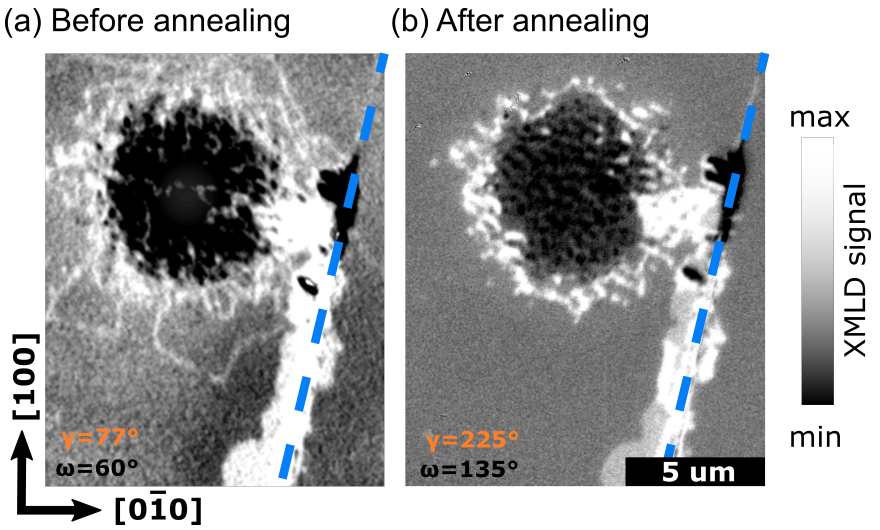

Figure 6.5: (a) XMLD-PEEM image of an area on a MgO(001)/NiO(10 nm)/Pt(2 nm) thin film that has been illuminated for 2 s with linearly polarized laser light with a pulse length of 6.7 ps, 2000 pulses and a fluence of 16±2 mJ/cm^2. (b) Domain structure of the same area after annealing above the Néel temperature. The blue line indicates a structural defect at which domains are stabilized. Adapted with permission from Ref. [51] with enhanced contrast in (a), see Appendix B.3.4.

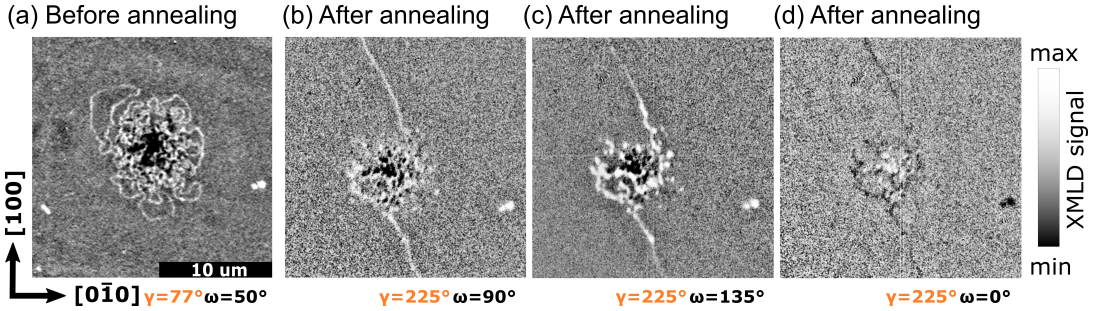

Figure 6.6: XMLD-PEEM image of the laser-induced domain structure of a MgO(001)/NiO(10 nm)/Pt(2 nm) thin film before (a) and after annealing in vacuum at 550 K above the Néel temperature for 10 minutes (b). By changing the beam polarization, we can observe an inversion of the contrast (c) and (d). Adapted with permission from the supplementary of Ref. [51] with enhanced contrast, see Appendix B.3.4.

optically induced 180° domains can be manipulated. Thus, the laser-induced domains are not generated by irreversible ablation-induced defects, which introduce strain or change the surface anisotropy, but originate from a fast heating and cooling of the NiO system. The laser-induced domain creation is dominated by thermal processes, as we

can observe polarization independent creation, which occurs close to the threshold for structural changes. Only the accumulated heating and threshold for structural changes differ slightly between different laser polarizations [358]. For linear polarized light under the same conditions as in Fig. 6.5 (a), but with a lower fluence of 12±2 mJ/cm^2, we could not observe a visible structural change or the creation of 180° domain walls, indicating that the accumulated heat has not been sufficient to allow a reorientation of the spins. We can estimate the temperature increase during irradiation by considering the melting temperature of Pt as a lower boundary for the temperature increase near the ablated area. The temperature of the NiO near ablated areas can be estimated to be around 520 K, which is slightly below the bulk NiO Néel temperature, but above the reduced Néel temperature in our thin film ($T_{\mathrm{N,thin}}$ = 400 K-460 K), see Appendix B.3.3. Thus, the laser-induced heating near the threshold for structural changes can be assumed to be sufficient to allow a reconfiguration of the domain structure. In the case that the laser-induced domain creation is of thermal origin, it can be achieved without structurally affecting the Pt layer. To create domains

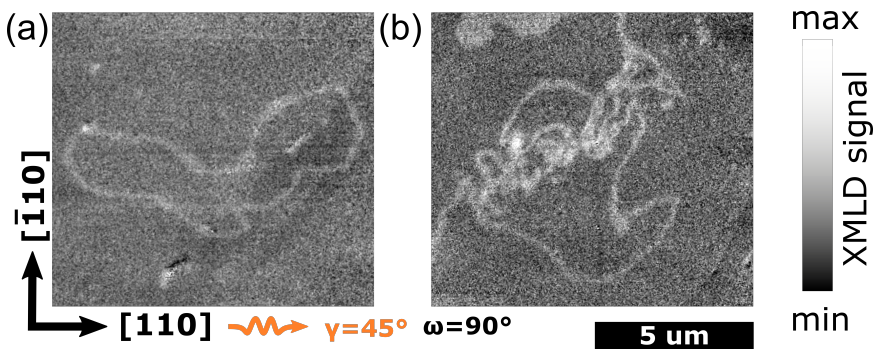

Figure 6.7: XMLD-PEEM image of two areas on a MgO(001)/NiO(10 nm)/Pt(2 nm) thin film that have been illuminated for 0.5 s with linearly polarized laser light with a pulse length of 45 fs and a fluence of 8±1 mJ/cm^2 (a) or 7.2±0.9 mJ/cm^2 (b). Adapted with permission from Ref. [51].

without damaging the Pt layer, we next investigate different laser pulse parameters. We patterned grids of markers onto the sample and irradiated the sample in the center of the grids. This allows us to identify the laser irradiated region in the X-PEEM even if there is no structural change to the Pt layer. We could observe the creation of domains without discernible structural changes to the Pt layer using 45 fs pulses and irradiation with 500 pulses over 0.5 seconds. The characteristic formation of 180° domain walls could be observed, as shown in Fig. 6.7 (a) and Fig. 6.7 (b), for irradiation with linearly polarized light. The threshold fluence for the formation of 180° domain walls under these irradiation conditions is found to be 7.2±0.9 mJ/cm^2. Thus, we can optically create antiferromagnetic 180° domains and domain walls without damaging the NiO or the Pt capping layer.

6.1.3 Discussion

We have observed the optically induced formation of 180° domain walls in NiO, indicating the creation of 180° domains. We observe a polarization-independent creation of the antiferromagnetic domains. The underlying mechanism is not based on a polarization dependent effect but on heat-induced domain formation, since the nucleation of the 180 ° domains is independent of the polarization of the exciting light.
The basic idea behind the mechanism is sketched in Fig. 6.8. Irradiation with the laser light heats up the NiO and its spin system. The lattice system around the heated area is still strained, as illustrated in Fig. 6.8 (b), exerting strain on the system that is heated up. During cooling of the irradiated region, the formation of multiple domains is theoretically possible, see Fig. 6.8 (c), the green arrow denotes the Néel vector. However, not all possible configurations are energetically favorable, the strain leads to a preferential alignment of the spins into the previous T-domain after irradiation, see Fig. 6.8 (d).

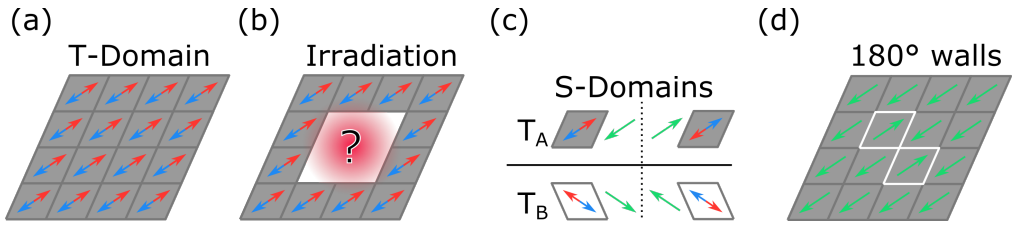

Figure 6.8: Sketch of the mechanism for the optical creation of antiferromagnetic domains. A large antiferromagnetic domain before (a) irradiation and during (b) the irradiation. Multiple domains are possible upon cooling (c). However, the distortion of the surrounding domains leads to a preferential stabilization of the same T-domain (d).

The heated disordered spins settle into one of the two energetically degenerate states, with spins in the different sublattices pointing in opposite directions. Thus, 180° domains and 180° domain walls are formed. The situation is different when the whole sample is annealed, as shown in Fig. 6.5 (b). As the creation of 180° domain walls requires additional energy, it is energetically unfavorable. In the slow cooling process of the annealing, (3.0±0.2 K/min, see Appendix B.3.2), the domain wall formation is avoided, and their size is minimized. These results are consistent with observations on bulk NiO: it was observed that a fast cooling through the Néel temperature (opening the furnace door) can lead to a multidomain state, while annealing with slow cooling (5 K/min) leads to crystals with only few domains [359]. The size of the optically induced domains is not necessarily linear with fluence, as can be seen in Fig. 6.7 (a) and Fig. 6.7 (b), but depends strongly on the local anisotropy landscape of the irradiated area. However, by tuning the timescale of the laser heating pulse, one can potentially switch reversibly between different magnetic states.
The observed width of the antiferromagnetic 180° domain wall of 100 ± 30 nm is comparable to previous observations of 140 nm and 192 nm wide 180° degree walls in

bulk NiO [123]. The determination of the Néel vector orientation inside the domain wall is challenging, due to the single-domain background in our angle dependent study. However, the higher XMLD intensity of the domain wall for out-of-plane polarization ($\omega = 90°$) under all investigated azimuthal angles ($\gamma = 77° - 180°$) indicates a larger out-of-plane component of the Néel vector inside the domain wall compared to the background domains. Previous experiments based on current-induced switching have allowed for the controlled switching between different T-domains [137]. The laser-induced domain creation offers the exciting possibility to additionally create and study 180° domain walls, which have recently been reported to be rather narrow and even atomically sharp in AFMs [360]. Further, domain walls themselves can play a crucial role in the magnon coupling of the NiO modes [98, 99]. By controlled irradiation of a device, one could artificially introduce additional domain walls into the system, decreasing the size of the individual domains. In this way, laser-induced domain creation can be used to locally lower the potential switching energy for a device or to manipulate magnon transport inside a device.

While all-optical creation of 180° domains itself offers exciting opportunities, we believe that the demonstration of optically induced creation of large domains in NiO is an important step for the investigation of AOS in AFMs. The pulse duration is found to be a crucial parameter in this process, since the underlying mechanism is based on the heating and the subsequent cooling of the system. Therefore, there is potential to push the writing speed to faster regimes by optimizing this optical parameter, while simultaneously tailoring the material parameters of the sample. Additionally, the variation of irradiation parameters could provide a tool for the realization of reversible switching. Different heat cycles could be used to switch between multi- and mono-domain states, similar to phase-change memory [361].

It should be emphasized that our observation of a heat-induced optical domain formation does not imply the absence of other optical switching mechanisms in AFMs or NiO. In the experiment presented here, we have observed 180° domain creation inside one T-domain, due to the preferential stabilization of only one S-domain, in our NiO(001) thin films [137]. In other systems the optically induced domain formation might not be as constrained. To investigate the all optical switching in AFMs one has to therefore carefully choose the material platform, a promising candidate might be NiO(111) [353]. In NiO (111) three different S-domains and a total of six different magnetic states per T-domain are present. Thus, NiO (111) could be the ideal platform to explore the theoretically proposed optical switching mechanisms, as the spins could switch between multiple S-domains [353]. We believe that the mechanism found here can also be achieved in other antiferromagnetic systems with strong magnetoelastic coupling, such as CoO or hematite. The optically induced creation of 180° domains and domain walls thus provides an additional handle to manipulate antiferromagnetic domain structures.

6.2 | Optical Domain Creation in CoO

Here, we examine the effect of laser irradiation on CoO thin films. To conduct our investigation, we utilized a piece of the same MgO(001)/CoO(10 nm)/Pt(2 nm) sample that we previously used to study shape-induced patterning effects in CoO, see Sec. 5.3. We present the results of the irradiation of our CoO/Pt thin films, which have been imaged via birefringence imaging and XMLD-PEEM.

6.2.1 Birefringence Imaging

We have used the same 800 nm laser with 1 kHz repetition rate as in the previous Sec. 6.1 to irradiate our MgO(001)/CoO(10 nm)/Pt(2 nm) thin films. The band gap of CoO is estimated to be about 2.5 eV [169], which is larger than the 1.55 eV of the used laser. For the irradiation we used an exposure time of 2 seconds and a pulse length of 45 fs. We varied the polarization of the laser light and the fluence in the illumination of the samples at room temperature. After irradiation, we use birefringence imaging of the illuminated areas to reveal the domain structure [165], as shown in Fig. 6.9.

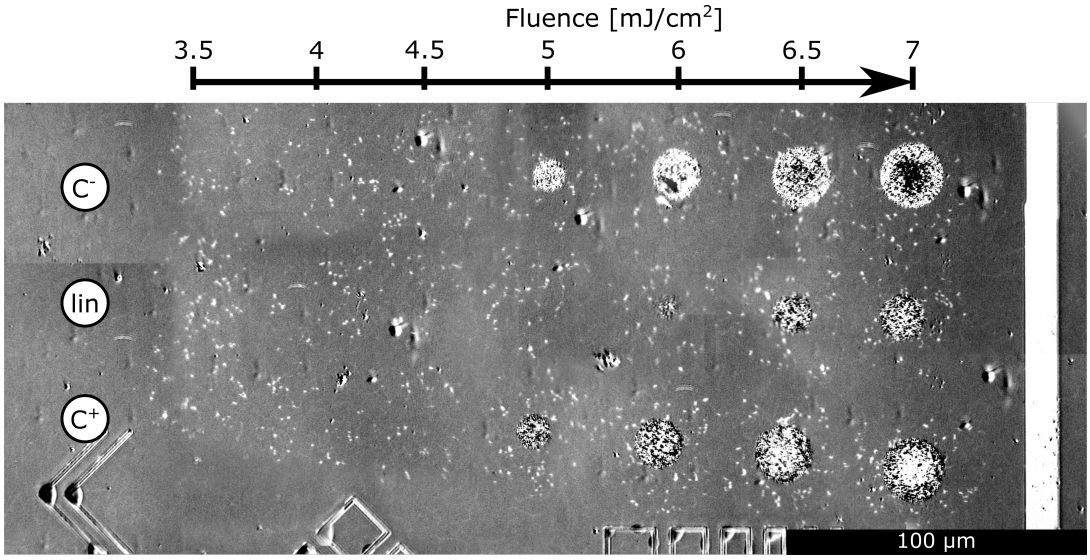

Figure 6.9: Birefringence image of the antiferromagnetic domain structure of MgO(001)/CoO(10 nm)/Pt(2 nm) after irradiation with 45 fs laser pulses, 2000 pulses. The polarization of the laser light has been varied from circular left (c−), linear (lin) to circular right (c+) from the top row to the bottom row. The fluence increases in the columns from left to right. The inhomogeneous background results from the overlay of individual birefringence images. The bright dots indicate the laser-induced creation of domains with 90° different in-plane projection of the Néel vector compared to the background domain. The fluences have an error of $\pm 1 \, ^{\mathrm{mJ}}/_{\mathrm{cm}^2}$.

In the irradiated areas (800 nm laser, 45 fs pulses, illumination time 2 s) a high density of small (white) domains can be observed, which are absent outside the laser irradiated areas. These small domains follow the expected contrast variation of domains with an in-plane Néel vector orthogonal to the surrounding (dark) domains [165]. These small white domains are present regardless of the polarization of the laser light (rows) and can be observed for all applied fluences (columns). For higher fluences ($> 5\,\mathrm{mJ/cm^2}$), additional damage and ablation of the Pt layer can be observed. Similar to our NiO/Pt thin films, the ablation threshold is different for the different polarizations [358]. The polarization independent creation of antiferromagnetic domains in combination with the low Néel temperature of our CoO thin films, around 330 K [105], indicates a possible thermal origin of the observed optically induced domain creation.

6.2.2 XMLD-PEEM Imaging

To confirm the magnetic origin of the laser-induced domains observed by birefringence, we examined the irradiated samples using XMLD-PEEM imaging. During the mounting and focusing, the sample has been split and experienced an electrical discharge. Thus, potentially altering its domain structure. We used energy-dependent XMLD-PEEM imaging at the Co L_3 edge to visualize the antiferromagnetic domains, to compare them to the birefringence images and validate their magnetic nature by analyzing angle and polarization-dependent contrast inversions. The observed domain structure is depicted in Fig. 6.10.

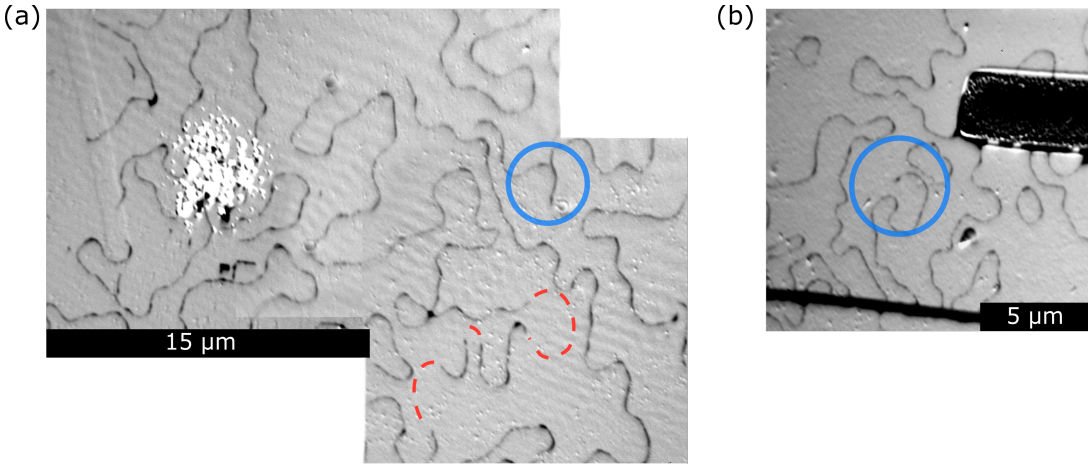

Figure 6.10: XMLD-PEEM images of the domain structure near laser irradiated spots on an MgO(001)/CoO(10 nm)/Pt(2 nm) sample (a). Domain structure several tens of microns away, still exhibiting the same structure (b). The XMLD contrast here has been obtained by dividing images taken with LV and LH polarization at a fixed energy.

For different polarization angles and different azimuthal angles, we can observe a contrast variation only for the dark lines visible in Fig. 6.10. Thus, the Néel vector in the bright domains always points along the same crystallographic axes. This is consistent with our previous observation of superimposed uniaxial anisotropy in our CoO thin films, see Sec. 5.3.1. The presence of a uniform background domain together with domain wall like stripes is reminiscent of the previous observations on the optical creation of domain walls in NiO, see Sec. 6.1. However, the distribution of domain walls is not centered or restricted to the laser spot. We even find the same pattern in a region several tens of microns away from the irradiated area, see Fig. 6.10 (b). In addition, we do not observe the circular arrangement of additional domains around the laser spots as we observed in the birefringence imaging before, see Fig. 6.9.
After performing the XMLD-PEEM measurements, we could not reproduce the birefringence measurements from Fig. 6.9 and the laser-induced domains disappeared. The disappearance of the domains visible in birefringence and the observation of the same pattern further away from the irradiated area in XMLD-PEEM lead us to conclude that the domain structure of the sample has been altered before the first XMLD-PEEM images have been taken. Thus, the domain structure investigated in Fig. 6.10 is not a result of the laser irradiation. While the XMLD-PEEM images do not provide insight into the optical creation of CoO domains, they do provide insight into the domain structure of CoO. At several locations in Fig. 6.10, the visible dark lines appear to have an open end, which would not be expected for domain walls. In some regions, open ends can be connected and explained by potentially very narrow domain walls, indicated by the red lines in Fig. 6.10 (a) [360]. However, in other regions of the sample they appear to have an open end or to split into two different lines (blue circles). This may indicate that the dark lines are not necessarily 180° domain walls. Not only the shape of the observed domain walls is intriguing, but also the thickness and contrast variations of the domain wall. However, care must be taken when interpreting the data. The image in Fig. 6.10 (a) has been taken close to a fracture of the sample edge. The ripples visible in the background are pronounced in this region near the broken edge and could originate from strain effects. More data and higher resolution images are required to understand the domains of our CoO thin films.

6.3 | Conclusion

To fully exploit the THz switching speeds of AFMs and to develop THz electronics, we need to transition from electrical contact to non-contact-based writing schemes [362], such as light-induced switching. The switching speeds for current-induced switching of AFMs investigated in the previous chapter are limited by the experimental setups used. Wire-bonded pulse setups are typically limited to pulse lengths of $\Delta T = 100\,\mathrm{ps}$ [362]. One way to overcome this limitation is to use non-contact THz irradiation to generate THz currents, as recently demonstrated for metallic AFMs [362, 363]. Another possibility is to move from electrical manipulation of AFMs to optical manipulation, similar to the development of AOS in FMs [38, 349].

Optical light has already been shown to excite the spin system of NiO, exciting both the low-frequency and the high-frequency magnon modes [342, 343, 345]. Here, we demonstrate that laser irradiation can be used not only to manipulate the domain structure, but also to create 180° domains and domain walls [51]. Previous studies have shown that domain walls play a crucial role in the coupling of the low and high frequency magnon modes [99]. Thus, our laser-induced domain walls could be used to modify the coupling between such modes.
Our optical domain creation is based on heat and the inherent strain of our MgO(001)/NiO(10 nm)/Pt(2 nm) sample, which limits the switching to 180° domains. However, by applying external strain during the irradiation, one can potentially control the switching direction, as has been demonstrated for the metallic AFM Mn_2Au [363]. It should be noted that the choice of sample orientation, NiO(001), can also limit the observed switching mechanisms. In the observation of laser-induced THz irradiation, our collaborators studied both NiO(001) and NiO(111) samples. While in the NiO(001) samples the THz emission has been generated by strain wave induced torques, in the NiO(111) samples the THz emission originated from optical spin torques [343, 364]. Thus, the NiO(111) system might be more promising for future optical switching experiments.
Changing the sample system to CoO could also have advantages. First investigations of optically induced switching of CoO thin films showed the optical creation of domains with 90° different Néel vector orientation, see Sec. 6.2. Further X-PEEM experiments by Christin Schmitt have now confirmed the antiferromagnetic nature of the optically induced domains. CoO is an attractive candidate for future investigations. The lower Néel temperature around room temperature allows the study of thermally induced switching further away from the melting point of the platinum capping [105]. In addition, CoO exhibits higher THz frequencies (4.4, 6.6 and 8.9 THz) than NiO and thus potentially faster switching [365, 366].
In summary, we have established that optical irradiation with laser light can be used to manipulate the antiferromagnetic domain structure via heat-based switching. The temporal limits of this mechanism remain to be explored. However, the optical manipulation of antiferromagnetic domains is a first step towards non-contact writing of spintronic devices.

7 | Conclusion and Outlook

Conclusion

The field of spintronics has rapidly developed in recent years, and AFMs have moved to the forefront of research due to their unique properties [25]. AFMs are now considered not only as passive elements in exchange bias applications [24], but also as active elements in future information transport, magnetic memory and logic devices [24, 367]. Part of their unique potential for energy efficient, compact, robust, and fast devices stems from their lack of a net magnetic moment. However, this lack of a net magnetic moment makes it difficult to control their domain structure, specifically to write the state of an AFM. Here, we have developed three different tools to control and manipulate the antiferromagnetic domain structure in insulating AFMs.

First, we have used electrical currents in an adjacent heavy metal layer to switch the antiferromagnetic order of NiO thin films. We unravel the origin of the underlying switching mechanism by imaging the switching of specially designed devices and simulating the current-induced strain distributions. We show that current-induced switching in our NiO/Pt bilayers is dominated by heat- and strain-induced switching, with possible contributions from SOT-based switching not playing a dominating role [49].

Second, we have shown that the geometry of a device can also have a direct effect on the antiferromagnetic ground state due to the patterning shape. By studying differently shaped and oriented geometric elements, we observe a shape-dependent formation of antiferromagnetic domain structures. Comparing the domain structure in different devices and additional magnetoelastic simulations allow us to identify long-range magnetoelastic interactions as the origin of the observed shape anisotropy [50].

Third, we have investigated the influence of strong laser irradiation on antiferromagnetic domain structures, going beyond the dynamical manipulation of the spin system. By varying the irradiation parameters and carefully analyzing the imaged domain structure, we reveal a polarization independent optical creation of 180° domains. The underlying switching mechanism is based on the laser-induced heating and the inherent strain of our samples [51].

The underlying mechanisms of all three tools (current-induced switching, patterning-induced switching, optical domain creation) can be traced back to the joint influence of heat and strain on the antiferromagnetic order. It has long been known that heat and

strain can be used to manipulate the antiferromagnetic order of bulk crystals [31, 103]. However, with the exciting prediction and discovery of Néel spin-orbit torques in the metallic AFMs CuMnAs and Mn_2Au [190–192], the focus in current-induced switching of AFM/HM thin films has been on SOT-based mechanisms [40–42] and potential strain effects have initially been neglected [320]. Our results on heat- and strain-based switching have contributed to put strain back on the map as a tool for manipulating antiferromagnetic domains [49, 105, 204]. This development has led to a re-evaluation of current-induced switching experiments in insulating AFM/heavy metal bilayers and in metallic AFMs [319]. Currently, it is still unclear under which conditions SOTs dominate in our iAFM/HM bilayers, but there has been first evidence for the presence of both, SOTs and thermomagnetoelastic switching in similar systems [201, 310]. The dominance of thermomagnetoelastic switching in NiO/Pt bilayers allows us to reconcile previously conflicting reports on current-induced switching resulting from the use of different device geometries [40–42]. Thus, illustrating the importance of the device geometry and strain in controlling the antiferromagnetic order.

However, the device geometry and patterning plays a role not only in the current-induced switching, but also in determining the magnetic ground state of an antiferromagnetic device. We can use the shape of a NiO device to tailor its properties via a strain-induced antiferromagnetic shape anisotropy. Similar effects have now been observed in other AFMs such as CoO, see Sec. 5.3, hematite [65], and metallic AFMs [66]. Although strain-induced shape anisotropy can be a general tool to manipulate antiferromagnetic domain structures, it also requires high quality epitaxial films with large domain structures and low pinning. Furthermore, the observed long-range magnetoelastic interactions challenge the promise of small antiferromagnetic bits that are stable against external perturbations [26]. While the absence of a stray field might make AFMs less susceptible to external magnetic fields, their magnetoelastic coupling limits their stability under the influence of strain. In addition, neighboring antiferromagnetic bits could influence each other due to the magnetoelastic coupling when bits are encoded in a continuous film. These potential limitations need to be considered in the development of future AFM spintronic devices.

Further, the heat- and strain-induced switching of insulating AFMs, such as NiO and CoO, may limit their upon integration into today's CMOS technology, which suffers from significant Joule heating [11, 12]. However, their strong magnetoelastic coupling makes insulating AFMs, like NiO and CoO, perfect candidates for exploring energy efficient devices in the developing field of straintronics [368, 369]. In addition, heat and strain based switching also enables a non-contact based manipulation of the spin structure [49].

Together with our collaborators, we have observed THz emission from NiO(001)/Pt bilayers, which originates from a strain wave, caused by the optical irradiation and ultrafast heating of the Pt layer [343]. Here, we demonstrate that laser-irradiation of AFM/HM bilayers is not limited to magnon excitation [343, 345], but can be used to create domains and domain walls in NiO and CoO platinum bilayers. Currently, the optical domain creation is achieved via laser-induced heating with pulse trains [51]. However, the temporal limitations of our laser-induced domain creation

are not explored and thermally based switching in ferrimagnets can be achieved via 60 fs pulses [349].
The optical creation of 180° domain walls and domains in NiO and CoO complements current-induced switching and antiferromagnetic shape anisotropy in controlling the domain structure. For instance, shape- and patterning induced effects allow us to tailor the ground state of a device, while irradiation with laser light enables the local creation of additional domains and domain walls. Such optically induced changes can subsequently be removed via the current-induced switching of large areas. Having control over the domain structure enables a more comprehensive study of its influence on the properties of AFMs.
Overall, we have demonstrated and investigated three different ways to control the magnetic order in insulating AFMs: current-induced switching, patterning-induced effects, and manipulation by laser irradiation. We have contributed to expanding the toolbox of antiferromagnetic spintronics with the establishment of three valuable approaches to control and manipulate the domain structure of insulating AFMs. The next challenge is to combine and exploit these tools for the further exploration of antiferromagnetic insulatronics and the development of future spintronic devices.

Outlook

The tools developed in the course of this work can be used in future investigations of insulating AFMs. In this section, we highlight two potential areas of fundamental research that aim to advance the development of energy-efficient and ultrafast devices based on antiferromagnetic insulators. The first area focuses on the development of low-power magnon devices, that transport information by pure spin currents. The second area centers around exploiting optical control and THz emission of insulating AFMs for the development of ultrafast devices. In addition, we provide a broader perspective on the role of NiO and CoO in future devices and highlight currently developing research areas with high potential for AFMs.
Insulating AFMs offer a key advantage over their metallic counterparts: the potential for energy-efficient devices through long-distance spin transport [28]. Information transport by spin currents, without charge transport, has been achieved over distances of several µm in other insulating AFMs, such as $\alpha-Fe_2O_3$ [29] and $YFeO_3$ [30]. Considering the existing reports on spin transport in insulating AFMs [28, 199, 370, 371], significant lateral spin transport can also be expected in NiO/Pt and CoO/Pt bilayers [372, 373]. Once the lateral spin transport in NiO(CoO)/Pt bilayers is established, we can investigate the impact of different domain states on magnon transport by current- or shape-induced control of the domain structure. Previous investigations on hematite have revealed that the spin transport length in films with large domains is increased compared to smaller domains, due to possible spin dependent scattering of magnons at domain walls [374]. In the case of a multi-domain sample, current-induced switching could be used to create large domains, thereby increasing the spin transport length, creating an “On” state. To reduce the spin transport length, the optical creation of

additional domains and domain walls could be used to increase magnon scattering, creating an "Off" state. Thus, the combination of spin transport and control over the domain structure could advance the development of spin-logic devices [374, 375], which are a key element for energy efficient magnon transport devices.
Another promising research area for insulating AFMs is the exploitation of ultrafast frequencies of AFMs via optically induced switching or THz emission. A potential material for optically induced switching investigations could be CoO. The observation of laser-induced domain creation is particularly interesting for CoO thin films, due to the creation of domains with 90° different in-plane orientation at a lower fluence than for NiO. The temporal limits of the optically induced switching, the switching with single pulses and the influence of excitations above the bandgap of CoO should be explored. An additional promising material system is NiO(111), as we have observed an optical spin torque in NiO(111)/Pt thin films in THz emission experiments [343]. The study of THz emissions from AFMs is another research area for potential ultrafast devices, as the THz emission depends on the underlying domain structure [342, 343]. One could use patterning or current-induced switching to control the domain structure. Thus, allowing for the potential tailoring of the signal shape and amplitude of the THz emission. Furthermore, the generation of additional domain walls by laser-irradiation could influence the coupling between the low and high frequency modes of NiO [99]. Thus, allowing one to tailor the THz emission of insulating AFMs.
The integration of spin-transport and ultrafast phenomena is vital for realizing ultrafast and energy-efficient spintronic devices. One example illustrating the joint potential is the laser-irradiation of FM/AFM/Pt multilayers, such as MgO(001)/Pt/CoO/FeCoB multilayers [376]. Laser-irradiation of the FeCoB layer excites a spin current which is transported via THz magnons through the antiferromagnetic CoO layer (up to 5 nm) and results in a THz emission in the heavy metal. The combination of energy efficient spin-transport and ultrafast magnetization dynamics make insulating AFMs an attractive material platform.
From the materials class of insulating antiferromagnets, both NiO and CoO are often used for the exploration of fundamental effects. However, there is no single AFM that can be perfectly integrated into all future antiferromagnetic spintronic devices. NiO and CoO may have disadvantages over other AFMs for some applications due to their magnetoelastic coupling and sensitivity to strain. However, their advantage is that the antiferromagnetic properties of both materials have been well studied for over 60 years [144], and they are well understood. In addition, NiO and CoO have an accessible Néel temperature, a well studied spin structure, and we now have several tools to write and read their magnetic order [25, 106]. Thus, both materials serve as prototypical AFMs for considerations on how AFMs could be integrated into future technologies, like artificial neural networks based on AFMs [198, 377, 378], and also as platforms for the exploration of novel fundamental spintronic effects.
A fundamental research area that is currently emerging is the field of orbitronics, which aims at harnessing orbital currents [379]. Insulating antiferromagnets, like NiO or CoO, are attractive candidates to explore orbital effects in AFMs, due to their sizeable orbital moment [380–382].

Overall, NiO and CoO will continue to serve as prototypical insulating antiferromagnets for the exploration of fundamental spintronic effects and as a platform for the development of concepts for novel spintronic devices. The findings presented in this thesis contribute to this research by providing valuable tools to control and manipulate the magnetic domain structure of insulating antiferromagnets.

Bibliography

[1] J. E. Dittmar, "Information Technology and Economic Change: The Impact of The Printing Press," *Q. J. Econ.*, vol. 126, pp. 1133–1172, 2011.

[2] W. J. Boot, "The Transfer of Learning: The Import of Chinese and Dutch Books in Togukawa Japan," *Itinerario*, vol. 37, pp. 188–206, 2013.

[3] B. Basu, "Black Holes: From Concept to Reality," *Sci. Report.*, pp. 14–19, 2019.

[4] S. Kaisler, F. Armour, J. A. Espinosa, and W. Money, "Big Data: Issues and Challenges Moving Forward," in *2013 46th Hawaii Int. Conf. Syst. Sci.*, pp. 995–1004, IEEE, 2013.

[5] M. I. Jordan and T. M. Mitchell, "Machine learning: Trends, perspectives, and prospects," *Science*, vol. 349, pp. 255–260, 2015.

[6] D. Silver, A. Huang, C. J. Maddison, A. Guez, L. Sifre, G. Van Den Driessche, J. Schrittwieser, I. Antonoglou, V. Panneershelvam, M. Lanctot, S. Dieleman, D. Grewe, J. Nham, N. Kalchbrenner, I. Sutskever, T. Lillicrap, M. Leach, K. Kavukcuoglu, T. Graepel, and D. Hassabis, "Mastering the game of Go with deep neural networks and tree search," *Nature*, vol. 529, pp. 484–489, 2016.

[7] T. Wu, S. He, J. Liu, S. Sun, K. Liu, Q.-L. Han, and Y. Tang, "A Brief Overview of ChatGPT: The History, Status Quo and Potential Future Development," *IEEE/CAA J. Autom. Sin.*, vol. 10, pp. 1122–1136, 2023.

[8] A. Jain, J. Mao, and K. Mohiuddin, "Artificial neural networks: a tutorial," *IEEE Computer*, vol. 29, pp. 31–44, 1996.

[9] E. Strubell, A. Ganesh, and A. McCallum, "Energy and Policy Considerations for Modern Deep Learning Research," *Proc. AAAI Conf. Artif. Intell.*, vol. 34, pp. 13693–13696, 2020.

[10] W. B. Levy and V. G. Calvert, "Communication consumes 35 times more energy than computation in the human cortex, but both costs are needed to predict synapse number," *Proc. Natl. Acad. Sci.*, vol. 118, 2021.

[11] S. Chopra and S. Subramaniam, "A Review on Challenges for MOSFET Scaling," *Int. J. Innov. Sci. Eng. Technol.*, vol. 2, pp. 1055–1057, 2015.

[12] N. Z. Haron and S. Hamdioui, "Why is CMOS scaling coming to an END?," in *2008 3rd Int. Des. Test Work.*, pp. 98–103, IEEE, 2008.

[13] M. Dayarathna, Y. Wen, and R. Fan, "Data Center Energy Consumption Modeling: A Survey," *IEEE Commun. Surv. Tutorials*, vol. 18, pp. 732–794, 2016.

[14] I. Žutić, J. Fabian, and S. Das Sarma, "Spintronics: Fundamentals and applications," *Rev. Mod. Phys.*, vol. 76, pp. 323–410, 2004.

[15] M. Julliere, "Tunneling between ferromagnetic films," *Phys. Lett. A*, vol. 54, pp. 225–226, 1975.

[16] G. Binasch, P. Grünberg, F. Saurenbach, and W. Zinn, "Enhanced magnetoresistance in layered magnetic structures with antiferromagnetic interlayer exchange," *Phys. Rev. B*, vol. 39, pp. 4828–4830, 1989.

[17] M. N. Baibich, J. M. Broto, A. Fert, F. N. Van Dau, F. Petroff, P. Etienne, G. Creuzet, A. Friederich, and J. Chazelas, "Giant Magnetoresistance of (001)Fe/(001)Cr Magnetic Superlattices," *Phys. Rev. Lett.*, vol. 61, pp. 2472–2475, 1988.

[18] J. Katine and E. E. Fullerton, "Device implications of spin-transfer torques," *J. Magn. Magn. Mater.*, vol. 320, pp. 1217–1226, 2008.

[19] J. Sun and D. Ralph, "Magnetoresistance and spin-transfer torque in magnetic tunnel junctions," *J. Magn. Magn. Mater.*, vol. 320, pp. 1227–1237, 2008.

[20] S. Bader and S. Parkin, "Spintronics," *Annu. Rev. Condens. Matter Phys.*, vol. 1, pp. 71–88, 2010.

[21] C. Chappert, A. Fert, and F. N. Van Dau, "The emergence of spin electronics in data storage," *Nat. Mater.*, vol. 6, pp. 813–823, 2007.

[22] D. Xiong, Y. Jiang, K. Shi, A. Du, Y. Yao, Z. Guo, D. Zhu, K. Cao, S. Peng, W. Cai, D. Zhu, and W. Zhao, "Antiferromagnetic spintronics: An overview and outlook," *Fundam. Res.*, vol. 2, pp. 522–534, 2022.

[23] L. Néel, "Magnetism and Local Molecular Field," *Science*, vol. 174, pp. 985–992, 1971.

[24] W. H. Meiklejohn and C. P. Bean, "New Magnetic Anisotropy," *Phys. Rev.*, vol. 105, pp. 904–913, 1957.

[25] V. Baltz, A. Manchon, M. Tsoi, T. Moriyama, T. Ono, and Y. Tserkovnyak, "Antiferromagnetic spintronics," *Rev. Mod. Phys.*, vol. 90, p. 015005, 2018.

[26] S. Loth, S. Baumann, C. P. Lutz, D. M. Eigler, and A. J. Heinrich, "Bistability in Atomic-Scale Antiferromagnets," *Science*, vol. 335, pp. 196–199, 2012.

[27] T. Kampfrath, A. Sell, G. Klatt, A. Pashkin, S. Mährlein, T. Dekorsy, M. Wolf, M. Fiebig, A. Leitenstorfer, and R. Huber, "Coherent terahertz control of antiferromagnetic spin waves," *Nat. Photonics*, vol. 5, pp. 31–34, 2011.

[28] A. Brataas, B. van Wees, O. Klein, G. de Loubens, and M. Viret, "Spin insulatronics," *Phys. Rep.*, vol. 885, pp. 1–27, 2020.

[29] R. Lebrun, A. Ross, S. A. Bender, A. Qaiumzadeh, L. Baldrati, J. Cramer, A. Brataas, R. A. Duine, and M. Kläui, "Tunable long-distance spin transport in a crystalline antiferromagnetic iron oxide," *Nature*, vol. 561, pp. 222–225, 2018.

[30] S. Das, A. Ross, X. X. Ma, S. Becker, C. Schmitt, F. van Duijn, E. F. Galindez-Ruales, F. Fuhrmann, M.-A. Syskaki, U. Ebels, V. Baltz, A.-L. Barra, H. Y. Chen, G. Jakob, S. X. Cao, J. Sinova, O. Gomonay, R. Lebrun, and M. Kläui, "Anisotropic long-range spin transport in canted antiferromagnetic orthoferrite $YFeO_3$," *Nat. Commun.*, vol. 13, p. 6140, 2022.

[31] W. L. Roth, "Neutron and Optical Studies of Domains in NiO," *J. Appl. Phys.*, vol. 31, pp. 2000–2011, 1960.

[32] J. Xu, C. Zhou, M. Jia, D. Shi, C. Liu, H. Chen, G. Chen, G. Zhang, Y. Liang, J. Li, W. Zhang, and Y. Wu, "Imaging antiferromagnetic domains in nickel oxide thin films by optical birefringence effect," *Phys. Rev. B*, vol. 100, p. 134413, 2019.

[33] H. Nakayama, M. Althammer, Y.-T. Chen, K. Uchida, Y. Kajiwara, D. Kikuchi, T. Ohtani, S. Geprägs, M. Opel, S. Takahashi, R. Gross, G. E. W. Bauer, S. T. B. Goennenwein, and E. Saitoh, "Spin Hall Magnetoresistance Induced by a Nonequilibrium Proximity Effect," *Phys. Rev. Lett.*, vol. 110, p. 206601, 2013.

[34] G. R. Hoogeboom, A. Aqeel, T. Kuschel, T. T. M. Palstra, and B. J. van Wees, "Negative spin Hall magnetoresistance of Pt on the bulk easy-plane antiferromagnet NiO," *Appl. Phys. Lett.*, vol. 111, p. 052409, 2017.

[35] J. Sinova, S. O. Valenzuela, J. Wunderlich, C. H. Back, and T. Jungwirth, "Spin Hall effects," *Rev. Mod. Phys.*, vol. 87, pp. 1213–1260, 2015.

[36] D. Ralph and M. Stiles, "Spin transfer torques," *J. Magn. Magn. Mater.*, vol. 320, pp. 1190–1216, 2008.

[37] C. L. Dennis, R. P. Borges, L. D. Buda, U. Ebels, J. F. Gregg, M. Hehn, E. Jouguelet, K. Ounadjela, I. Petej, I. L. Prejbeanu, and M. J. Thornton, "The defining length scales of mesomagnetism: a review," *J. Phys. Condens. Matter*, vol. 14, pp. R1175–R1262, 2002.

[38] C. D. Stanciu, F. Hansteen, A. V. Kimel, A. Kirilyuk, A. Tsukamoto, A. Itoh, and T. Rasing, "All-Optical Magnetic Recording with Circularly Polarized Light," *Phys. Rev. Lett.*, vol. 99, p. 047601, 2007.

[39] S. Mangin, M. Gottwald, C.-H. Lambert, D. Steil, V. Uhlíř, L. Pang, M. Hehn, S. Alebrand, M. Cinchetti, G. Malinowski, Y. Fainman, M. Aeschlimann, and E. E. Fullerton, "Engineered materials for all-optical helicity-dependent magnetic switching," *Nat. Mater.*, vol. 13, pp. 286–292, 2014.

[40] T. Moriyama, K. Oda, T. Ohkochi, M. Kimata, and T. Ono, "Spin torque control of antiferromagnetic moments in NiO," *Sci. Rep.*, vol. 8, p. 14167, 2018.

[41] X. Z. Chen, R. Zarzuela, J. Zhang, C. Song, X. F. Zhou, G. Y. Shi, F. Li, H. A. Zhou, W. J. Jiang, F. Pan, and Y. Tserkovnyak, "Antidamping-Torque-Induced Switching in Biaxial Antiferromagnetic Insulators," *Phys. Rev. Lett.*, vol. 120, p. 207204, 2018.

[42] L. Baldrati, O. Gomonay, A. Ross, M. Filianina, R. Lebrun, R. Ramos, C. Leveille, F. Fuhrmann, T. R. Forrest, F. Maccherozzi, S. Valencia, F. Kronast, E. Saitoh, J. Sinova, and M. Kläui, "Mechanism of Néel Order Switching in Antiferromagnetic Thin Films Revealed by Magnetotransport and Direct Imaging," *Phys. Rev. Lett.*, vol. 123, p. 177201, 2019.

[43] E. V. Gomonay, "Mechanism of Formation of the Equilibrium Domain Structure in Crystals Undergoing Thermoelastic Phase Transitions," *Phys. Solid State*, vol. 47, p. 1755, 2005.

[44] H. V. Gomonay and V. M. Loktev, "Shape-induced phenomena in finite-size antiferromagnets," *Phys. Rev. B*, vol. 75, p. 174439, 2007.

[45] C. Tzschaschel, K. Otani, R. Iida, T. Shimura, H. Ueda, S. Günther, M. Fiebig, and T. Satoh, "Ultrafast optical excitation of coherent magnons in antiferromagnetic NiO," *Phys. Rev. B*, vol. 95, p. 174407, 2017.

[46] N. Kanda, T. Higuchi, H. Shimizu, K. Konishi, K. Yoshioka, and M. Kuwata-Gonokami, "The vectorial control of magnetization by light," *Nat. Commun.*, vol. 2, p. 362, 2011.

[47] P. Němec, M. Fiebig, T. Kampfrath, and A. V. Kimel, "Antiferromagnetic opto-spintronics," *Nat. Phys.*, vol. 14, pp. 229–241, 2018.

[48] A. V. Kimel, A. Kirilyuk, A. Tsvetkov, R. V. Pisarev, and T. Rasing, "Laser-induced ultrafast spin reorientation in the antiferromagnet $TmFeO_3$," *Nature*, vol. 429, pp. 850–853, 2004.

[49] H. Meer, F. Schreiber, C. Schmitt, R. Ramos, E. Saitoh, O. Gomonay, J. Sinova, L. Baldrati, and M. Kläui, "Direct Imaging of Current-Induced Antiferromagnetic Switching Revealing a Pure Thermomagnetoelastic Switching Mechanism in NiO," *Nano Lett.*, vol. 21, pp. 114–119, 2021.

[50] H. Meer, O. Gomonay, C. Schmitt, R. Ramos, L. Schnitzspan, F. Kronast, M.-A. Mawass, S. Valencia, E. Saitoh, J. Sinova, L. Baldrati, and M. Kläui, "Strain-induced shape anisotropy in antiferromagnetic structures," *Phys. Rev. B*, vol. 106, p. 094430, 2022.

[51] H. Meer, S. Wust, C. Schmitt, P. Herrgen, F. Fuhrmann, S. Hirtle, B. Bednarz, A. Rajan, R. Ramos, M. A. Niño, M. Foerster, F. Kronast,

A. Kleibert, B. Rethfeld, E. Saitoh, B. Stadtmüller, M. Aeschlimann, and M. Kläui, "Laser-Induced Creation of Antiferromagnetic 180-Degree Domains in NiO/Pt Bilayers," *Adv. Funct. Mater.*, p. 2213536, 2023.

[52] S. Blundell, *Magnetism in Condensed Matter*.
Oxford Master Series in Condensed Matter Physics, New York:Oxford University Press, 2001.

[53] J. M. D. Coey, *Magnetism and Magnetic Materials*.
Magnetism and Magnetic Materials, Cambridge University Press, 2010.

[54] M. Faraday, "On new magnetic actions, and on the magnetic condition of all matter," *J. Franklin Inst.*, vol. 42, pp. 66–69, 1846.

[55] M. P. Langevin, "Une formule fondamentale de théorie cinétique," in *Ann. Chim. Phys. Ser.*, vol. 5, pp. 245–288, 1905.

[56] P. Weiss, "La variation du ferromagnétisme avec la température," *Comptes Rendus*, vol. 143, pp. 1136–1139, 1906.

[57] J. A. Ewing, "VII. On the production of transient electric currents in iron and steel conductors by twisting them when magnetised or by magnetising them when twisted," *Proc. R. Soc. London*, vol. 33, pp. 21–23, 1882.

[58] L. Néel, "Influence des fluctuations du champ moléculaire sur les propriétés magnétiques des corps," in *Ann. Phys. (Paris).*, vol. 17, pp. 5–105, 1932.

[59] F. Bitter, "A Generalization of the Theory of Ferromagnetism," *Phys. Rev.*, vol. 54, pp. 79–86, 1938.

[60] B. Barbara, "Louis Néel: His multifaceted seminal work in magnetism," *Comptes Rendus Phys.*, vol. 20, pp. 631–649, 2019.

[61] J. P. Rodriguez, "Quantized topological point defects in two-dimensional antiferromagnets," *Phys. Rev. B*, vol. 39, pp. 2906–2909, 1989.

[62] B. Barbara and E. M. Chudnovsky, "Macroscopic quantum tunneling in antiferromagnets," *Phys. Lett. A*, vol. 145, pp. 205–208, 1990.

[63] M. L. Néel, "Propriétés magnétiques des ferrites ; ferrimagnétisme et antiferromagnétisme," in *Ann. Phys. (Paris).*, vol. 12, pp. 137–198, 1948.

[64] L. Landau and E. Lifshitz, "On the theory of the dispersion of magnetic permeability in ferromagnetic bodies," in *Perspect. Theor. Phys.*, vol. 169, pp. 51–65, Elsevier, 1992.

[65] A. Wittmann, O. Gomonay, K. Litzius, A. Kaczmarek, A. E. Kossak, D. Wolf, A. Lubk, T. N. Johnson, E. A. Tremsina, A. Churikova, F. Büttner,

S. Wintz, M.-A. Mawass, M. Weigand, F. Kronast, L. Scipioni, A. Shepard, T. Newhouse-Illig, J. A. Greer, G. Schütz, N. O. Birge, and G. S. D. Beach, "Role of substrate clamping on anisotropy and domain structure in the canted antiferromagnet α-Fe_2O_3," *Phys. Rev. B*, vol. 106, p. 224419, 2022.

[66] S. Reimers, O. Gomonay, O. J. Amin, F. Krizek, L. X. B. Y. Lytvynenko, S. Poole, R. P. Campion, V. Novák, F. Maccherozzi, D. Carbone, A. Björling, Y. Niu, E. Golias, D. Kriegner, J. Sinova, M. Kläui, M. Jourdan, S. S. Dhesi, K. W. Edmonds, and P. Wadley, "Magnetic domain engineering in antiferromagnetic CuMnAs and Mn_2Au devices," *arXiv, 2302.09550*, pp. 1–30, 2023.

[67] B. Karetta, *Antiferromagnetic Domains in presence of Magnetoelastic Interactions.*
Master thesis, Johannes Gutenberg University Mainz, 2021.

[68] W. Heisenberg, "Mehrkörperproblem und Resonanz in der Quantenmechanik," *Zeitschrift für Phys.*, vol. 38, pp. 411–426, 1926.

[69] P. Dirac, "On the theory of quantum mechanics," *Proc. R. Soc. London. Ser. A, Contain. Pap. a Math. Phys. Character*, vol. 112, pp. 661–677, 1926.

[70] J. H. Van Vleck, "A Survey of the Theory of Ferromagnetism," *Rev. Mod. Phys.*, vol. 17, pp. 27–47, 1945.

[71] J. Kanamori, "Theory of the Magnetic Properties of Ferrous and Cobaltous Oxides, I," *Prog. Theor. Phys.*, vol. 17, pp. 177–196, 1957.

[72] C. G. Shull, W. A. Strauser, and E. O. Wollan, "Neutron Diffraction by Paramagnetic and Antiferromagnetic Substances," *Phys. Rev.*, vol. 83, pp. 333–345, 1951.

[73] H. Kramers, "L'interaction Entre les Atomes Magnétogènes dans un Cristal Paramagnétique," *Physica*, vol. 1, pp. 182–192, 1934.

[74] P. W. Anderson, "Antiferromagnetism. Theory of Superexchange Interaction," *Phys. Rev.*, vol. 79, pp. 350–356, 1950.

[75] J. H. Van Vleck, "On the Anisotropy of Cubic Ferromagnetic Crystals," *Phys. Rev.*, vol. 52, pp. 1178–1198, 1937.

[76] J. Stöhr, "Exploring the microscopic origin of magnetic anisotropies with X-ray magnetic circular dichroism (XMCD) spectroscopy," *J. Magn. Magn. Mater.*, vol. 200, pp. 470–497, 1999.

[77] K. O'Grady, J. Sinclair, K. Elphick, R. Carpenter, G. Vallejo-Fernandez, M. I. Probert, and A. Hirohata, "Anisotropy in antiferromagnets," *J. Appl. Phys.*, vol. 128, no. 4, 2020.

[78] R. Rytov and N. Usov, "A shape visualization of a magnetic anisotropy energy density of single-domain magnetic nanoparticles," *Sci. Vis.*, vol. 12, no. 3, pp. 26–37, 2020.

[79] P. Vergallo, B. Karetta, G. Consolo, and O. Gomonay, "Domain-wall orientation in antiferromagnets controlled by magnetoelastic effects," *arXiv, 2301.12539*, 2023.

[80] A. Ross, *Probing Magnetostatic and Magnetotransport Properties of the Antiferromagnetic Iron Oxide Hematite*.
Dissertation, Johannes Gutenberg University Mainz, 2020.

[81] L. C. Bartel and B. Morosin, "Exchange Striction in NiO," *Phys. Rev. B*, vol. 3, pp. 1039–1043, 1971.

[82] A. Kohn, A. Kovács, R. Fan, G. J. McIntyre, R. C. C. Ward, and J. P. Goff, "The antiferromagnetic structures of IrMn3 and their influence on exchange-bias," *Sci. Rep.*, vol. 3, p. 2412, 2013.

[83] P. Weiss, "L'hypothèse du champ moléculaire et la propriété ferromagnétique," *J. Phys. Théorique Appliquée*, vol. 6, no. 1, pp. 661–690, 1907.

[84] L. Néel, "Propriétés magnétiques de l'état métallique et énergie d'interaction entre atomes magnétiques," *Ann. Phys. (Paris).*, vol. 11, pp. 232–279, 1936.

[85] L. Néel, "Théorie du paramagnétisme constant. Application au manganèse," *Comptes Rendus Hebd. Des Seances L Acad. Des Sci.*, vol. 203, pp. 304–306, 1936.

[86] F. Bloch, *Zur Theorie des Austauschproblems und der Remanenzerscheinung der Ferromagnetika*, vol. 74.
Berlin, Heidelberg: Springer Berlin Heidelberg, 1932.

[87] L. Néel, "Energie des parois de Bloch dans les couches minces," *Comptes Rendus Hebd. Des Seances L Acad. Des Sci.*, vol. 241, no. 6, pp. 533–537, 1955.

[88] A. Scholl, J. Stöhr, J. Lüning, J. W. Seo, J. Fompeyrine, H. Siegwart, J.-P. Locquet, F. Nolting, S. Anders, E. E. Fullerton, M. R. Scheinfein, and H. A. Padmore, "Observation of Antiferromagnetic Domains in Epitaxial Thin Films," *Science*, vol. 287, pp. 1014–1016, 2000.

[89] B. Náfrádi, T. Keller, F. Hardy, C. Meingast, A. Erb, and B. Keimer, "Magnetostriction and Magnetostructural Domains in Antiferromagnetic $YBa_2Cu_3O_6$," *Phys. Rev. Lett.*, vol. 116, p. 047001, 2016.

[90] W. J. Ince and A. Platzker, "Antiferromagnetic Domains in $RbMnF_3$," *Phys. Rev.*, vol. 175, pp. 650–653, 1968.

[91] A. V. Goltsev, R. V. Pisarev, T. Lottermoser, and M. Fiebig, "Structure and Interaction of Antiferromagnetic Domain Walls in Hexagonal $YMnO_3$," *Phys. Rev. Lett.*, vol. 90, p. 177204, 2003.

[92] F. J. Spooner and M. W. Vernon, "Growth, perfection and antiferromagnetic domain structure of epitaxial cobalt oxide," *J. Mater. Sci.*, vol. 4, pp. 734–742, 1969.

[93] A. S. Zimmermann, B. B. Van Aken, H. Schmid, J. P. Rivera, J. Li, D. Vaknin, and M. Fiebig, "Anisotropy of antiferromagnetic 180° domains in magnetoelectric $LiMPO_4$ (M = Fe, Co, Ni)," *Eur. Phys. J. B*, vol. 71, no. 3, pp. 355–360, 2009.

[94] H. Gomonay and V. M. Loktev, "Magnetostriction and magnetoelastic domains in antiferromagnets," *J. Phys. Condens. Matter*, vol. 14, pp. 3959–3971, 2002.

[95] Y. Y. Li, "Domain walls in antiferromagnets and the weak ferromagnetism of $\alpha-Fe_2O_3$," *Phys. Rev.*, vol. 101, pp. 1450–1454, 1956.

[96] E. V. Gomonay and V. M. Loktev, "On the theory of the formation of equilibrium domain structure in antiferromagnets," *Fiz. Nizk. Temp.*, vol. 30, no. 10, pp. 1071–1085, 2004.

[97] R. W. Balluffi, *Introduction to Elasticity Theory for Crystal Defects*. Cambridge University Press, 2012.

[98] O. Gomonay and D. Bossini, "Linear and nonlinear spin dynamics in multidomain magnetoelastic antiferromagnets," *J. Phys. D. Appl. Phys.*, vol. 54, p. 374004, 2021.

[99] D. Bossini, M. Pancaldi, L. Soumah, M. Basini, F. Mertens, M. Cinchetti, T. Satoh, O. Gomonay, and S. Bonetti, "Ultrafast Amplification and Nonlinear Magnetoelastic Coupling of Coherent Magnon Modes in an Antiferromagnet," *Phys. Rev. Lett.*, vol. 127, p. 077202, 2021.

[100] J. Joule, "XVII. On the effects of magnetism upon the dimensions of iron and steel bars," *London, Edinburgh, Dublin Philos. Mag. J. Sci.*, vol. 30, pp. 76–87, 1847.

[101] H. A. Pidgeon, "Magneto-Striction with Special Reference to Pure Cobalt," *Phys. Rev.*, vol. 13, pp. 209–237, 1919.

[102] E. W. Lee, "Magnetostriction and Magnetomechanical Effects," *Reports Prog. Phys.*, vol. 18, p. 305, 1955.

[103] G. A. Slack, "Crystallography and Domain Walls in Antiferromagnetic NiO Crystals," *J. Appl. Phys.*, vol. 31, pp. 1571–1582, 1960.

[104] E. Folven, T. Tybell, A. Scholl, A. Young, S. T. Retterer, Y. Takamura, and J. K. Grepstad, "Antiferromagnetic Domain Reconfiguration in Embedded $LaFeO_3$ Thin Film Nanostructures," *Nano Lett.*, vol. 10, pp. 4578–4583, 2010.

[105] L. Baldrati, C. Schmitt, O. Gomonay, R. Lebrun, R. Ramos, E. Saitoh, J. Sinova, and M. Kläui, "Efficient Spin Torques in Antiferromagnetic CoO/Pt Quantified by Comparing Field- and Current-Induced Switching," *Phys. Rev. Lett.*, vol. 125, p. 077201, 2020.

[106] H. Meer, O. Gomonay, A. Wittmann, and M. Kläui, "Antiferromagnetic insulatronics: Spintronics in insulating 3d metal oxides with antiferromagnetic coupling," *Appl. Phys. Lett.*, vol. 122, p. 080502, 2023.

[107] W. L. Roth, "Multispin Axis Structures for Antiferromagnets," *Phys. Rev.*, vol. 111, pp. 772–781, 1958.

[108] C. Henry La Blanchetais, "Contribution à l'étude de l'antiferromagnétisme. Etude thermomagnétique des protoxydes de cobalt et de nickel," *J. Phys. le Radium*, vol. 12, no. 8, pp. 765–771, 1951.

[109] D. Alders, L. H. Tjeng, F. C. Voogt, T. Hibma, G. A. Sawatzky, C. T. Chen, J. Vogel, M. Sacchi, and S. Iacobucci, "Temperature and thickness dependence of magnetic moments in NiO epitaxial films," *Phys. Rev. B*, vol. 57, pp. 11623–11631, 1998.

[110] F. Keffer and W. O'Sullivan, "Problem of Spin Arrangements in MnO and Similar Antiferromagnets," *Phys. Rev.*, vol. 108, pp. 637–644, 1957.

[111] M. T. Hutchings and E. J. Samuelsen, "Measurement of Spin-Wave Dispersion in NiO by Inelastic Neutron Scattering and Its Relation to Magnetic Properties," *Phys. Rev. B*, vol. 6, pp. 3447–3461, 1972.

[112] H. P. Rooksby, "A note on the structure of nickel oxide at subnormal and elevated temperatures," *Acta Crystallogr.*, vol. 1, pp. 226–226, 1948.

[113] W. L. Roth and G. A. Slack, "Antiferromagnetic Structure and Domains in Single Crystal NiO," *J. Appl. Phys.*, vol. 31, pp. S352–S353, 1960.

[114] J. S. Smart and S. Greenwald, "Crystal Structure Transitions in Antiferromagnetic Compounds at the Curie Temperature," *Phys. Rev.*, vol. 82, pp. 113–114, 1951.

[115] J. S. Smart, "Molecular Field Treatment of Ferromagnetism and Antiferromagnetism," *Phys. Rev.*, vol. 86, pp. 968–974, 1952.

[116] H. Kondoh and T. Takeda, "Observation of Antiferromagnetic Domains in Nickel Oxide," *J. Phys. Soc. Japan*, vol. 19, pp. 2041–2051, 1964.

[117] T. Yamada, "Antiferromagnetic Domain Walls in Nickel Oxide," *J. Phys. Soc. Japan*, vol. 18, pp. 520–530, 1963.

[118] T. Yamada, "Spin Configuration in Antiferromagnetic Domain Walls of the NiO-Type Crystals," *J. Phys. Soc. Japan*, vol. 21, pp. 650–664, 1966.

[119] T. Yamada, "Magnetic Anisotropy, Magnetostriction, and Magnetic Domain Walls in NiO. I. Theory," *J. Phys. Soc. Japan*, vol. 21, pp. 664–671, 1966.

[120] T. Yamada, S. Saito, and Y. Shimomura, "Magnetic Anisotropy, Magnetostriction, and Magnetic Domain Walls in NiO. II. Experiment," *J. Phys. Soc. Japan*, vol. 21, pp. 672–680, 1966.

[121] J. Baruchel, M. Schlenker, K. Kurosawa, and S. Saito, "Antiferromagnetic S-domains in NiO I. Neutron magnetic topographic investigation," *Philos. Mag. B*, vol. 43, pp. 853–860, 1981.

[122] W. Kleemann, F. J. Schäfer, and D. S. Tannhauser, "Linear birefringence in S-domains of NiO near the antiferromagnetic phase transition," *J. Magn. Magn. Mater.*, vol. 15-18, pp. 415–416, 1980.

[123] N. B. Weber, H. Ohldag, H. Gomonaj, and F. U. Hillebrecht, "Magnetostrictive Domain Walls in Antiferromagnetic NiO," *Phys. Rev. Lett.*, vol. 91, p. 237205, 2003.

[124] K. Arai, T. Okuda, A. Tanaka, M. Kotsugi, K. Fukumoto, T. Ohkochi, T. Nakamura, T. Matsushita, T. Muro, M. Oura, Y. Senba, H. Ohashi, A. Kakizaki, C. Mitsumata, and T. Kinoshita, "Three-dimensional spin orientation in antiferromagnetic domain walls of NiO studied by x-ray magnetic linear dichroism photoemission electron microscopy," *Phys. Rev. B*, vol. 85, p. 104418, 2012.

[125] R. Street and B. Lewis, "Anomalous Variation of Young's Modulus of Antiferromagnetics at the Neél Point," *Nature*, vol. 168, pp. 1036–1037, 1951.

[126] S. Mandal, K. S. R. Menon, F. Maccherozzi, and R. Belkhou, "Strain-induced nonequilibrium magnetoelastic domain structure and spin reorientation of NiO(100)," *Phys. Rev. B*, vol. 80, p. 184408, 2009.

[127] K. Kurosawa, S. Saito, and S. Takemoto, "Antiferromagnetic Domain Structures in Vapour-Grown NiO (111) Platelets Containing Growth Twins," *Jpn. J. Appl. Phys.*, vol. 13, pp. 804–811, 1974.

[128] V. Mandel, "Twin domains in nickel-oxide type crystals," *J. Cryst. Growth*, vol. 174, pp. 346–353, 1997.

[129] C. Giovanardi, A. di Bona, S. Altieri, P. Luches, M. Liberati, F. Rossi, and S. Valeri, "Structure and morphology of ultrathin NiO layers on Ag(001)," *Thin Solid Films*, vol. 428, pp. 195–200, 2003.

[130] Y. Z. Wu, Y. Zhao, E. Arenholz, A. T. Young, B. Sinkovic, C. Won, and Z. Q. Qiu, "Analysis of x-ray linear dichroism spectra for NiO thin films grown on vicinal Ag(001)," *Phys. Rev. B*, vol. 78, p. 064413, 2008.

[131] M. Lee, S. Seo, D. Seo, E. Jeong, and I. K. Yoo, "Properties of nickel oxide films by DC reactive sputtering," *Integr. Ferroelectr.*, vol. 68, pp. 19–25, 2004.

[132] M. Finazzi, L. Duò, and F. Ciccacci, "Magnetic properties of interfaces and multilayers based on thin antiferromagnetic oxide films," *Surf. Sci. Rep.*, vol. 64, pp. 139–167, 2009.

[133] M. James and T. Hibma, "Thickness-dependent relaxation of NiO(001) overlayers on MgO(001) studied by X-ray diffraction," *Surf. Sci.*, vol. 433-435, pp. 718–722, 1999.

[134] S. Altieri, M. Finazzi, H. H. Hsieh, H. J. Lin, C. T. Chen, T. Hibma, S. Valeri, and G. A. Sawatzky, "Magnetic Dichroism and Spin Structure of Antiferromagnetic NiO(001) Films," *Phys. Rev. Lett.*, vol. 91, p. 137201, 2003.

[135] M. Finazzi and S. Altieri, "Magnetic dipolar anisotropy in strained antiferromagnetic films," *Phys. Rev. B*, vol. 68, p. 054420, 2003.

[136] S. Saito, "X-Ray Diffraction Micrography on the Twin Structure of Antiferromagnetic Nickel Oxide," *J. Phys. Soc. Japan*, vol. 17, pp. 1287–1299, 1962.

[137] C. Schmitt, L. Baldrati, L. Sanchez-Tejerina, F. Schreiber, A. Ross, M. Filianina, S. Ding, F. Fuhrmann, R. Ramos, F. Maccherozzi, D. Backes, M.-A. Mawass, F. Kronast, S. Valencia, E. Saitoh, G. Finocchio, and M. Kläui, "Identification of Néel Vector Orientation in Antiferromagnetic Domains Switched by Currents in NiO/Pt Thin Films," *Phys. Rev. Appl.*, vol. 15, p. 034047, 2021.

[138] C. Schmitt, L. Sanchez-Tejerina, M. Filianina, F. Fuhrmann, H. Meer, R. Ramos, F. Maccherozzi, D. Backes, E. Saitoh, G. Finocchio, L. Baldrati, and M. Kläui, "Identifying the domain-wall spin structure in antiferromagnetic NiO/Pt," *Phys. Rev. B*, vol. 107, p. 184417, 2023.

[139] G. Ghiringhelli, G. Ghiringhelli, L. H. Tjeng, L. H. Tjeng, A. Tanaka, O. Tjernberg, O. Tjernberg, T. Mizokawa, T. Mizokawa, J. L. de Boer, and N. B. Brookes, "3d spin-orbit photoemission spectrum of nonferromagnetic materials: The test cases of CoO and Cu," *Phys. Rev. B*, vol. 66, p. 075101, 2002.

[140] N. C. Tombs and H. P. Rooksby, "Structure of Monoxides of some Transition Elements at Low Temperatures," *Nature*, vol. 165, pp. 442–443, 1950.

[141] S. Greenwald and J. S. Smart, "Deformations in the Crystal Structures of Antiferromagnetic Compounds," *Nature*, vol. 166, pp. 523–524, 1950.

[142] Y. Y. Li, "Magnetic moment arrangements and magnetocrystalline deformations in antiferromagnetic compounds," *Phys. Rev.*, vol. 100, pp. 627–631, 1955.

[143] W. Jauch, M. Reehuis, H. J. Bleif, F. Kubanek, and P. Pattison, "Crystallographic symmetry and magnetic structure of CoO," *Phys. Rev. B*, vol. 64, p. 052102, 2001.

[144] W. L. Roth, "Magnetic Structures of MnO, FeO, CoO, and NiO," *Phys. Rev.*, vol. 110, pp. 1333–1341, 1958.

[145] T. Nagamiya and K. Motizuki, "Theory of the Magnetic Scattering of Neutrons by CoO," *Rev. Mod. Phys.*, vol. 30, pp. 89–93, 1958.

[146] B. van Laar, "Multi-Spin-Axis Structure for CoO," *Phys. Rev.*, vol. 138, pp. A584–A587, 1965.

[147] B. van Laar, "A New Interpretation of Magnetic Anisotropy Measurement on CoO Single Crystals," *J. Phys. Soc. Japan*, vol. 20, pp. 1282–1283, 1965.

[148] B. van Laar, J. Schweizer, and R. Lemaire, "Neutron-Diffraction Investigation of CoO Single Crystals," *Phys. Rev.*, vol. 141, pp. 538–540, 1966.

[149] J. Kanamori, "Theory of the Magnetic Properties of Ferrous and Cobaltous Oxides, II," *Prog. Theor. Phys.*, vol. 17, pp. 197–222, 1957.

[150] S. Saito, K. Nakahigashi, and Y. Shimomura, "X-Ray Diffraction Study on CoO," *J. Phys. Soc. Japan*, vol. 21, pp. 850–860, 1966.

[151] T. Nagamiya, S. Saito, Y. Shimomura, and E. Uchida, "Magnetic Structure of CoO," *J. Phys. Soc. Japan*, vol. 20, pp. 1285–1286, 1965.

[152] D. Herrmann-Ronzaud, P. Burlet, and J. Rossat-Mignod, "Equivalent type-II magnetic structures: CoO, a collinear antiferromagnet," *J. Phys. C Solid State Phys.*, vol. 11, pp. 2123–2137, 1978.

[153] K. H. Germann, K. Maier, and E. Strauss, "Linear Magnetic Birefringence in Transition Metal Oxides: CoO," *Phys. status solidi*, vol. 61, pp. 449–454, 1974.

[154] O. Nakanishi and T. Yamada, "Magnetic Anisotropy from Exchange Interaction and Magnetic Structure of CoO," *J. Phys. Soc. Japan*, vol. 36, pp. 1315–1321, 1974.

[155] K. Tomiyasu, T. Inami, and N. Ikeda, "Magnetic structure of CoO studied by neutron and synchrotron x-ray diffraction," *Phys. Rev. B*, vol. 70, p. 184411, 2004.

[156] E. Krüger, "Magnetic Structure of CoO," *Symmetry*, vol. 13, p. 1513, 2021.

[157] E. Krüger, "Magnetic Bands Producing a Monoclinic Magnetic Structure in NiO, FeO, MnO, and a Tetragonal One in CoO," *Symmetry*, vol. 14, p. 1285, 2022.

[158] E. Uchida, N. Fukuoka, H. Kondoh, T. Takeda, Y. Nakazumi, and T. Nagamiya, "Magnetic Anisotropy Measurements of CoO Single Crystal," *J. Phys. Soc. Japan*, vol. 19, pp. 2088–2095, 1964.

[159] M. D. Rechtin and B. L. Averbach, "Tetragonal elongation in CoO near the Néel point," *Phys. Rev. Lett.*, vol. 26, pp. 1483–1485, 1971.

[160] Q. Li, T. Gu, J. Zhu, Z. Ding, J. X. Li, J. H. Liang, Y. M. Luo, Z. Hu, C. Y. Hua, H.-J. Lin, T. W. Pi, C. Won, and Y. Z. Wu, "Multiple in-plane spin reorientation transitions in Fe/CoO bilayers grown on vicinal MgO(001)," *Phys. Rev. B*, vol. 91, p. 104424, 2015.

[161] S. I. Csiszar, M. W. Haverkort, Z. Hu, A. Tanaka, H. H. Hsieh, H.-J. Lin, C. T. Chen, T. Hibma, and L. H. Tjeng, "Controlling Orbital Moment and Spin Orientation in CoO Layers by Strain," *Phys. Rev. Lett.*, vol. 95, p. 187205, 2005.

[162] J. Zhu, Q. Li, J. X. Li, Z. Ding, C. Y. Hua, M. J. Huang, H.-J. Lin, Z. Hu, C. Won, and Y. Z. Wu, "Strain-modulated antiferromagnetic spin orientation and exchange coupling in Fe/CoO(001)," *J. Appl. Phys.*, vol. 115, p. 193903, 2014.

[163] J. Zhu, Q. Li, J. X. Li, Z. Ding, J. H. Liang, X. Xiao, Y. M. Luo, C. Y. Hua, H.-J. Lin, T. W. Pi, Z. Hu, C. Won, and Y. Z. Wu, "Antiferromagnetic spin reorientation transition in epitaxial NiO/CoO/MgO(001) systems," *Phys. Rev. B*, vol. 90, p. 054403, 2014.

[164] W. N. Cao, J. Li, G. Chen, J. Zhu, C. R. Hu, and Y. Z. Wu, "Temperature-dependent magnetic anisotropies in epitaxial Fe/CoO/MgO(001) system studied by the planar Hall effect," *Appl. Phys. Lett.*, vol. 98, p. 262506, 2011.

[165] J. Xu, H. Chen, C. Zhou, D. Shi, G. Chen, and Y. Wu, "Optical imaging of antiferromagnetic domains in ultrathin CoO(001) films," *New J. Phys.*, vol. 22, p. 083033, 2020.

[166] J. Xu, J. Xia, X. Zhang, C. Zhou, D. Shi, H. Chen, T. Wu, Q. Li, H. Ding, Y. Zhou, and Y. Wu, "Exchange-Torque-Triggered Fast Switching of Antiferromagnetic Domains," *Phys. Rev. Lett.*, vol. 128, p. 137201, 2022.

[167] Z. Zheng, J. Y. Shi, Q. Li, T. Gu, H. Xia, L. Q. Shen, F. Jin, H. C. Yuan, Y. Z. Wu, L. Y. Chen, and H. B. Zhao, "Magneto-optical probe of ultrafast spin dynamics in antiferromagnetic CoO thin films," *Phys. Rev. B*, vol. 98, p. 134409, 2018.

[168] M. J. Grzybowski, C. F. Schippers, M. E. Bal, K. Rubi, U. Zeitler, M. Foltyn, B. Koopmans, and H. J. M. Swagten, "Electrical switching of antiferromagnetic CoO — Pt across the Néel temperature," *Appl. Phys. Lett.*, vol. 120, p. 122405, 2022.

[169] P. M. Sarte, S. D. Wilson, J. P. Attfield, and C. Stock, "Magnetic Fluctuations and the Spin-Orbit Interaction in Mott Insulating CoO," *J. Phys. Condens. Matter*, vol. 32, pp. 958–959, 2020.

[170] E. H. Hall, "On a New Action of the Magnet on Electric Currents," *Am. J. Math.*, vol. 2, p. 287, 1879.

[171] E. Hall, "XVIII. On the "Rotational Coefficient" in nickel and cobalt," *London, Edinburgh, Dublin Philos. Mag. J. Sci.*, vol. 12, pp. 157–172, 1881.

[172] Y. K. Kato, R. C. Myers, A. C. Gossard, and D. D. Awschalom, "Observation of the Spin Hall Effect in Semiconductors," *Science*, vol. 306, pp. 1910–1913, 2004.

[173] J. Sinova, D. Culcer, Q. Niu, N. A. Sinitsyn, T. Jungwirth, and A. H. MacDonald, "Universal Intrinsic Spin Hall Effect," *Phys. Rev. Lett.*, vol. 92, p. 126603, 2004.

[174] J. E. Hirsch, "Spin Hall Effect," *Phys. Rev. Lett.*, vol. 83, pp. 1834–1837, 1999.

[175] N. Nagaosa, J. Sinova, S. Onoda, A. H. MacDonald, and N. P. Ong, "Anomalous Hall effect," *Rev. Mod. Phys.*, vol. 82, pp. 1539–1592, 2010.

[176] E. Saitoh, M. Ueda, H. Miyajima, and G. Tatara, "Conversion of spin current into charge current at room temperature: Inverse spin-Hall effect," *Appl. Phys. Lett.*, vol. 88, p. 182509, 2006.

[177] N. Vlietstra, J. Shan, V. Castel, J. Ben Youssef, G. E. W. Bauer, and B. J. van Wees, "Exchange magnetic field torques in YIG/Pt bilayers observed by the spin-Hall magnetoresistance," *Appl. Phys. Lett.*, vol. 103, p. 032401, 2013.

[178] Y.-T. Chen, S. Takahashi, H. Nakayama, M. Althammer, S. T. B. Goennenwein, E. Saitoh, and G. E. W. Bauer, "Theory of spin Hall magnetoresistance," *Phys. Rev. B*, vol. 87, p. 144411, 2013.

[179] J. Fischer, O. Gomonay, R. Schlitz, K. Ganzhorn, N. Vlietstra, M. Althammer, H. Huebl, M. Opel, R. Gross, S. T. B. Goennenwein, and S. Geprägs, "Spin Hall magnetoresistance in antiferromagnet/heavy-metal heterostructures," *Phys. Rev. B*, vol. 97, p. 014417, 2018.

[180] L. Baldrati, A. Ross, T. Niizeki, C. Schneider, R. Ramos, J. Cramer, O. Gomonay, M. Filianina, T. Savchenko, D. Heinze, A. Kleibert, E. Saitoh,

J. Sinova, and M. Kläui, "Full angular dependence of the spin Hall and ordinary magnetoresistance in epitaxial antiferromagnetic NiO(001)/Pt thin films," *Phys. Rev. B*, vol. 98, p. 024422, 2018.

[181] L. Baldrati, O. Gomonay, A. Ross, M. Filianina, R. Lebrun, R. Ramos, C. Leveille, F. Fuhrmann, T. R. Forrest, F. Maccherozzi, S. Valencia, F. Kronast, E. Saitoh, J. Sinova, and M. Kläui, "Mechanism of Néel Order Switching in Antiferromagnetic Thin Films Revealed by Magnetotransport and Direct Imaging," *Phys. Rev. Lett.*, vol. 123, p. 177201, 2019.

[182] F. Schreiber, L. Baldrati, C. Schmitt, R. Ramos, E. Saitoh, R. Lebrun, and M. Kläui, "Concurrent magneto-optical imaging and magneto-transport readout of electrical switching of insulating antiferromagnetic thin films," *Appl. Phys. Lett.*, vol. 117, p. 082401, 2020.

[183] T. Kawahara, K. Ito, R. Takemura, and H. Ohno, "Spin-transfer torque RAM technology: Review and prospect," *Microelectron. Reliab.*, vol. 52, pp. 613–627, 2012.

[184] L. Berger, "Emission of spin waves by a magnetic multilayer traversed by a current," *Phys. Rev. B*, vol. 54, pp. 9353–9358, 1996.

[185] J. Slonczewski, "Current-driven excitation of magnetic multilayers," *J. Magn. Magn. Mater.*, vol. 159, pp. L1–L7, 1996.

[186] A. Manchon, J. Železný, I. M. Miron, T. Jungwirth, J. Sinova, A. Thiaville, K. Garello, and P. Gambardella, "Current-induced spin-orbit torques in ferromagnetic and antiferromagnetic systems," *Rev. Mod. Phys.*, vol. 91, p. 035004, 2019.

[187] I. M. Miron, K. Garello, G. Gaudin, P. J. Zermatten, M. V. Costache, S. Auffret, S. Bandiera, B. Rodmacq, A. Schuhl, and P. Gambardella, "Perpendicular switching of a single ferromagnetic layer induced by in-plane current injection," *Nature*, vol. 476, pp. 189–193, 2011.

[188] L. Liu, C.-F. Pai, Y. Li, H. W. Tseng, D. C. Ralph, and R. A. Buhrman, "Spin-Torque Switching with the Giant Spin Hall Effect of Tantalum," *Science*, vol. 336, pp. 555–558, 2012.

[189] S. D. Ganichev, E. L. Ivchenko, V. V. Bel'kov, S. A. Tarasenko, M. Sollinger, D. Weiss, W. Wegscheider, and W. Prettl, "Spin-galvanic effect," *Nature*, vol. 417, pp. 153–156, 2002.

[190] J. Železný, H. Gao, K. Výborný, J. Zemen, J. Mašek, A. Manchon, J. Wunderlich, J. Sinova, and T. Jungwirth, "Relativistic Néel-Order Fields Induced by Electrical Current in Antiferromagnets," *Phys. Rev. Lett.*, vol. 113, p. 157201, 2014.

[191] P. Wadley, B. Howells, J. Železný, C. Andrews, V. Hills, R. P. Campion, V. Novák, K. Olejník, F. Maccherozzi, S. S. Dhesi, S. Y. Martin, T. Wagner, J. Wunderlich, F. Freimuth, Y. Mokrousov, J. Kuneš, J. S. Chauhan, M. J. Grzybowski, A. W. Rushforth, K. W. Edmonds, B. L. Gallagher, and T. Jungwirth, "Electrical switching of an antiferromagnet," *Science*, vol. 351, pp. 587–590, 2016.

[192] S. Y. Bodnar, L. Šmejkal, I. Turek, T. Jungwirth, O. Gomonay, J. Sinova, A. A. Sapozhnik, H.-J. Elmers, M. Kläui, and M. Jourdan, "Writing and reading antiferromagnetic Mn_2Au by Néel spin-orbit torques and large anisotropic magnetoresistance," *Nat. Commun.*, vol. 9, p. 348, 2018.

[193] T. Shiino, S.-H. Oh, P. M. Haney, S.-W. Lee, G. Go, B.-G. Park, and K.-J. Lee, "Antiferromagnetic Domain Wall Motion Driven by Spin-Orbit Torques," *Phys. Rev. Lett.*, vol. 117, p. 087203, 2016.

[194] N. L. Schryer and L. R. Walker, "The motion of 180° domain walls in uniform dc magnetic fields," *J. Appl. Phys.*, vol. 45, pp. 5406–5421, 1974.

[195] O. Gomonay, T. Jungwirth, and J. Sinova, "High Antiferromagnetic Domain Wall Velocity Induced by Néel Spin-Orbit Torques," *Phys. Rev. Lett.*, vol. 117, p. 017202, 2016.

[196] S. Baierl, J. H. Mentink, M. Hohenleutner, L. Braun, T.-M. Do, C. Lange, A. Sell, M. Fiebig, G. Woltersdorf, T. Kampfrath, and R. Huber, "Terahertz-Driven Nonlinear Spin Response of Antiferromagnetic Nickel Oxide," *Phys. Rev. Lett.*, vol. 117, p. 197201, 2016.

[197] T. Moriyama, K. Hayashi, K. Yamada, M. Shima, Y. Ohya, and T. Ono, "Intrinsic and extrinsic antiferromagnetic damping in NiO," *Phys. Rev. Mater.*, vol. 3, p. 051402, 2019.

[198] H. Bradley, S. Louis, C. Trevillian, L. Quach, E. Bankowski, A. Slavin, and V. Tyberkevych, "Artificial neurons based on antiferromagnetic auto-oscillators as a platform for neuromorphic computing," *AIP Adv.*, vol. 13, p. 015206, 2023.

[199] D. Hou, Z. Qiu, and E. Saitoh, "Spin transport in antiferromagnetic insulators: progress and challenges," *NPG Asia Mater.*, vol. 11, p. 35, 2019.

[200] I. Gray, T. Moriyama, N. Sivadas, G. M. Stiehl, J. T. Heron, R. Need, B. J. Kirby, D. H. Low, K. C. Nowack, D. G. Schlom, D. C. Ralph, T. Ono, and G. D. Fuchs, "Spin Seebeck Imaging of Spin-Torque Switching in Antiferromagnetic Pt/NiO Heterostructures," *Phys. Rev. X*, vol. 9, p. 041016, 2019.

[201] C. Schmitt, A. Rajan, G. Beneke, A. Kumar, T. Sparmann, H. Meer, B. Bednarz, R. Ramos, M. A. Nino, M. Foerster, E. Saitoh, and M. Kläui, "Mechanism of electrical switching of ultra-thin CoO/Pt bilayers," *arXiv, 2303.13308*, 2023.

[202] T. Matalla-Wagner, J.-M. Schmalhorst, G. Reiss, N. Tamura, and M. Meinert, "Resistive contribution in electrical-switching experiments with antiferromagnets," *Phys. Rev. Res.*, vol. 2, p. 033077, 2020.

[203] B. J. Jacot, G. Krishnaswamy, G. Sala, C. O. Avci, S. Vélez, P. Gambardella, and C.-H. Lambert, "Systematic study of nonmagnetic resistance changes due to electrical pulsing in single metal layers and metal/antiferromagnet bilayers," *J. Appl. Phys.*, vol. 128, p. 173902, 2020.

[204] P. Zhang, J. Finley, T. Safi, and L. Liu, "Quantitative Study on Current-Induced Effect in an Antiferromagnet Insulator/Pt Bilayer Film," *Phys. Rev. Lett.*, vol. 123, p. 247206, 2019.

[205] M. Meinert, D. Graulich, and T. Matalla-Wagner, "Electrical switching of antiferromagnetic Mn_2Au and the role of thermal activation," *Phys. Rev. Appl.*, vol. 9, p. 064040, 2018.

[206] P. S. Ho and T. Kwok, "Electromigration in metals," *Reports Prog. Phys.*, vol. 52, pp. 301–348, 1989.

[207] A. Churikova, D. Bono, B. Neltner, A. Wittmann, L. Scipioni, A. Shepard, T. Newhouse-Illige, J. Greer, and G. S. D. Beach, "Non-magnetic origin of spin Hall magnetoresistance-like signals in Pt films and epitaxial NiO/Pt bilayers," *Appl. Phys. Lett.*, vol. 116, p. 022410, 2020.

[208] Y. Cheng, S. Yu, M. Zhu, J. Hwang, and F. Yang, "Electrical Switching of Tristate Antiferromagnetic Néel Order in α-Fe_2O_3 Epitaxial Films," *Phys. Rev. Lett.*, vol. 124, p. 027202, 2020.

[209] F. Schreiber, H. Meer, C. Schmitt, R. Ramos, E. Saitoh, L. Baldrati, and M. Kläui, "Magnetic Sensitivity Distribution of Hall Devices in Antiferromagnetic Switching Experiments," *Phys. Rev. Appl.*, vol. 16, p. 064023, 2021.

[210] S. Arpaci, V. Lopez-Dominguez, J. Shi, L. Sánchez-Tejerina, F. Garesci, C. Wang, X. Yan, V. K. Sangwan, M. A. Grayson, M. C. Hersam, G. Finocchio, and P. Khalili Amiri, "Observation of current-induced switching in non-collinear antiferromagnetic $IrMn_3$ by differential voltage measurements," *Nat. Commun.*, vol. 12, p. 3828, 2021.

[211] A. Barra, A. Ross, O. Gomonay, L. Baldrati, A. Chavez, R. Lebrun, J. D. Schneider, P. Shirazi, Q. Wang, J. Sinova, G. P. Carman, and M. Kläui, "Effective strain manipulation of the antiferromagnetic state of polycrystalline NiO," *Appl. Phys. Lett.*, vol. 118, p. 172408, 2021.

[212] W. Grove, "VII. On the electro-chemical polarity of gases," *Phil. Trans. R. Soc.*, vol. 142, pp. 87–101, 1852.

[213] W. Grove, "XXXIII. On some anomalous cases of electrical decomposition," *Lond. Edinb. Dublin philos. mag. j. sci.*, vol. 5, pp. 203–209, 1853.

[214] V. S. Smentkowski, "Trends in sputtering," *Prog. Surf. Sci.*, vol. 64, pp. 1–58, 2000.

[215] P. Kelly and R. Arnell, "Magnetron sputtering: a review of recent developments and applications," *Vacuum*, vol. 56, pp. 159–172, 2000.

[216] G. Bräuer, "Magnetron Sputtering," in *Comprehensive Materials Processing*, vol. 4, pp. 57–73, Elsevier, 2014.

[217] F. Schreiber, *Imaging and electrical characterization of current-induced switching in antiferromagnetic materials*.
Master thesis, Johannes Gutenberg University Mainz, 2021.

[218] G. West and P. Kelly, "Influence of inert gas species on the growth of silver and molybdenum films via a magnetron discharge," *Surf. Coatings Technol.*, vol. 206, pp. 1648–1652, 2011.

[219] R. Hippler, M. Cada, V. Stranak, and Z. Hubicka, "Time-resolved optical emission spectroscopy of a unipolar and a bipolar pulsed magnetron sputtering discharge in an argon/oxygen gas mixture with a cobalt target," *Plasma Sources Sci. Technol.*, vol. 28, p. 115020, 2019.

[220] P. Sigmund, "Theory of Sputtering. I. Sputtering Yield of Amorphous and Polycrystalline Targets," *Phys. Rev.*, vol. 184, pp. 383–416, 1969.

[221] K. Wasa, "2 - Sputtering Phenomena," in *Handb. Sputtering Technol. (Second Ed.* (K. Wasa, I. Kanno, and H. Kotera, eds.), pp. 41–75, Oxford: William Andrew Publishing, second edi ed., 2012.

[222] K. Wasa, "3 - Sputtering Systems," in *Handb. Sputtering Technol. (Second Ed.* (K. Wasa, I. Kanno, and H. Kotera, eds.), pp. 77–139, Oxford: William Andrew Publishing, second edi ed., 2012.

[223] T. H. Kim and G. Y. Yeom, "A Review of Inductively Coupled Plasma-Assisted Magnetron Sputter System," *Appl. Sci. Converg. Technol.*, vol. 28, no. 5, pp. 131–138, 2019.

[224] J. Hopwood, "Review of inductively coupled plasmas for plasma processing," *Plasma Sources Sci. Technol.*, vol. 1, pp. 109–116, 1992.

[225] J. Hopwood and F. Qian, "Mechanisms for highly ionized magnetron sputtering," *J. Appl. Phys.*, vol. 78, pp. 758–765, 1995.

[226] M. Yamashita, "Fundamental characteristics of built-in high-frequency coil-type sputtering apparatus," *J. Vac. Sci. Technol. A: Vac. Surf. Films*, vol. 7, pp. 151–158, 1989.

[227] D. A. L. Loch, Y. A. Gonzalvo, and A. P. Ehiasarian, "Plasma analysis of inductively coupled impulse sputtering of Cu, Ti and Ni," *Plasma Sources Sci. Technol.*, vol. 26, p. 065012, 2017.

[228] K. Pedersen, J. Bøttiger, M. Sridharan, M. Sillassen, and P. Eklund, "Texture and microstructure of Cr_2O_3 and $(Cr,Al)_2O_3$ thin films deposited by reactive inductively coupled plasma magnetron sputtering," *Thin Solid Films*, vol. 518, pp. 4294–4298, 2010.

[229] Sales - ULVAC Equipment www.ulvac-es.co.jp/products/qam-series/, "QAM4 ULVAC Data Sheet," 2014.

[230] W. Sproul, D. Christie, and D. Carter, "Control of reactive sputtering processes," *Thin Solid Films*, vol. 491, pp. 1–17, 2005.

[231] H. Adachi, T. Hata, and K. Wasa, "5 - Basic Process of Sputtering Deposition," in *Handb. Sputtering Technol. (Second Ed.* (K. Wasa, I. Kanno, and H. Kotera, eds.), pp. 295–359, Oxford: William Andrew Publishing, second edi ed., 2012.

[232] T. Motohiro, "4 - Computer Simulation," in *Handb. Sputtering Technol. (Second Ed.* (K. Wasa, I. Kanno, and H. Kotera, eds.), pp. 143–294, Oxford: William Andrew Publishing, second edi ed., 2012.

[233] M. Ohring, "Chapter 14 - Emerging Thin-Film Materials and Applications," in *The Materials Science of Thin Films* (M. Ohring, ed.), pp. 629–683, San Diego: Academic Press, 1992.

[234] S.-W. Cheong, M. Fiebig, W. Wu, L. Chapon, and V. Kiryukhin, "Seeing is believing: visualization of antiferromagnetic domains," *npj Quantum Materials*, vol. 5, p. 3, 2020.

[235] J. F. Dillon, "Observation of Domains in the Ferrimagnetic Garnets by Transmitted Light," *J. Appl. Phys.*, vol. 29, pp. 1286–1291, 1958.

[236] W. Gebhardt, "What can be learned from magnetooptic measurements?," *J. Magn. Magn. Mater.*, vol. 3, pp. 129–142, 1976.

[237] G. A. Smolenskiĭ, R. V. Pisarev, and I. G. Siniĭ, "Birefringence of light in magnetically ordered crystals," *Sov. Phys. - Uspekhi*, vol. 18, pp. 410–429, 1975.

[238] G. A. Gehring, "Magnetic birefringence," *J. Appl. Phys.*, vol. 53, pp. 8152–8156, 1982.

[239] J. F. Dillon, "Magnetooptics and its uses," *J. Magn. Magn. Mater.*, vol. 31-34, no. PART 1, pp. 1–9, 1983.

[240] J. Ferre and G. A. Gehring, "Linear optical birefringence of magnetic crystals," *Reports Prog. Phys.*, vol. 47, pp. 513–611, 1984.

[241] J. Kerr, "XLIII. On rotation of the plane of polarization by reflection from the pole of a magnet," *London, Edinburgh, Dublin Philos. Mag. J. Sci.*, vol. 3, pp. 321–343, 1877.

[242] P. N. Schatz and A. J. McCaffery, "The Faraday effect," *Quarterly Reviews, Chemical Society*, vol. 23, no. 4, p. 552, 1969.

[243] W. Feng, G.-Y. Guo, J. Zhou, Y. Yao, and Q. Niu, "Large magneto-optical Kerr effect in noncollinear antiferromagnets Mn_3X (X =Rh, Ir, Pt)," *Phys. Rev. B*, vol. 92, p. 144426, 2015.

[244] V. Saidl, P. Němec, P. Wadley, V. Hills, R. P. Campion, V. Novák, K. W. Edmonds, F. Maccherozzi, S. S. Dhesi, B. L. Gallagher, F. Trojánek, J. Kuneš, J. Železný, P. Malý, and T. Jungwirth, "Optical determination of the Néel vector in a CuMnAs thin-film antiferromagnet," *Nat. Photonics*, vol. 11, pp. 91–96, 2017.

[245] S. A. Siddiqui, J. Sklenar, K. Kang, M. J. Gilbert, A. Schleife, N. Mason, and A. Hoffmann, "Metallic antiferromagnets," *J. Appl. Phys.*, vol. 128, p. 040904, 2020.

[246] H. Dachs, H. C. Wolfe, C. D. Graham, and J. J. Rhyne, "Linear Magnetic Birefringence Associated With Phase Transitions," in *AIP Conf. Proc.*, vol. 854, pp. 854–863, AIP, 1973.

[247] G. A. Gehring, "On the observation of critical indices of primary and secondary order parameters using birefringence," *J. Phys. C Solid State Phys.*, vol. 10, pp. 531–542, 1977.

[248] S. Saito and Y. Shimomura, "Back-Reflection X-Ray Micrography," *J. Phys. Soc. Japan*, vol. 16, pp. 2351–2351, 1961.

[249] T. Takeda and H. Kondoh, "Thermal Pits of NiO Crystals," *J. Phys. Soc. Japan*, vol. 17, pp. 1317–1318, 1962.

[250] H. Kondoh, "A New Birefringence Pattern of Antiferromagnetic NiO Crystal," *J. Phys. Soc. Japan*, vol. 18, pp. 595–596, 1963.

[251] A. Treindl and K. H. Germann, "Linear optical anisotropy investigations of the antiferromagnetic phase transition in MnO," *Phys. Status Solidi*, vol. 80, pp. 159–166, 1977.

[252] R. V. Pisarev, I. G. Sinii, and G. A. Smolenskii, "Turning of Magnetic Sublattices and Anomalies of the Cottonmouton Effect in Terbium Iron Garnet and in Hematite," *ZhETF Pis. Red.*, vol. 9, pp. 294–298, 1969.

[253] I. Jahn and H. Dachs, "Change of the optical birefringence associated with the antiferromagnetic ordering of MnF_2, FeF_2, CoF_2, and NiF_2," *Solid State Commun.*, vol. 9, pp. 1617–1620, 1971.

[254] K. Germann, K. Maier, and E. Strauss, "Magnetic order induced birefringence and critical behaviour of the long range order parameter in NiO," *Solid State Commun.*, vol. 14, pp. 1309–1311, 1974.

[255] H. C. Mertins, P. M. Oppeneer, J. Kuneš, A. Gaupp, D. Abramsohn, and F. Schäfers, "Observation of the X-Ray Magneto-Optical Voigt Effect," *Phys. Rev. Lett.*, vol. 87, p. 047401, 2001.

[256] P. M. Oppeneer, H. C. Mertins, D. Abramsohn, A. Gaupp, W. Gudat, J. Kuneš, and C. M. Schneider, "Buried antiferromagnetic films investigated by x-ray magneto-optical reflection spectroscopy," *Phys. Rev. B*, vol. 67, p. 052401, 2003.

[257] S. Valencia, A. Kleibert, A. Gaupp, J. Rusz, D. Legut, J. Bansmann, W. Gudat, and P. M. Oppeneer, "Quadratic X-Ray Magneto-Optical Effect upon Reflection in a Near-Normal-Incidence Configuration at the M Edges of 3d-Transition Metals," *Phys. Rev. Lett.*, vol. 104, p. 187401, 2010.

[258] B. K. Tanner, "Antiferromagnetic domains," *Contemp. Phys.*, vol. 20, pp. 187–210, 1979.

[259] "Evico Magnetics, User Instruction for Standard Kerr Microscope and Magnetometer V10."

[260] I. V. Soldatov and R. Schäfer, "Selective sensitivity in Kerr microscopy," *Rev. Sci. Instrum.*, vol. 88, p. 073701, 2017.

[261] J. Maddox, "The sensational discovery of X-rays," *Nature*, vol. 375, pp. 183–183, 1995.

[262] R. Heintzmann and G. Ficz, "Breaking the resolution limit in light microscopy," *Brief. funct. genomics proteomics*, vol. 5, pp. 289–301, 2006.

[263] D. A. Shapiro, Y.-S. Yu, T. Tyliszczak, J. Cabana, R. Celestre, W. Chao, K. Kaznatcheev, A. L. D. Kilcoyne, F. Maia, S. Marchesini, Y. S. Meng, T. Warwick, L. L. Yang, and H. A. Padmore, "Chemical composition mapping with nanometre resolution by soft X-ray microscopy," *Nat. Photonics*, vol. 8, pp. 765–769, 2014.

[264] P. Willmott, *An Introduction to Synchrotron Radiation: Techniques and Applications.*
Wiley, 2019.

[265] J. Stöhr and H. Siegmann, *Magnetism: From Fundamentals to Nanoscale Dynamics.*
Springer Series in Solid-State Sciences, Springer, 2006.

[266] E. D. Smit, J. F. Creemer, H. W. Zandbergen, B. M. Weckhuysen, and F. M. F. de Groot, "In-situ Scanning Transmission X-ray Microscopy of catalytic materials under reaction conditions," *J. Phys. Conf. Ser.*, vol. 190, p. 012161, 2009.

[267] M. Ghidini, F. Maccherozzi, S. S. Dhesi, and N. D. Mathur, "XPEEM and MFM Imaging of Ferroic Materials," *Adv. Electron. Mater.*, vol. 8, p. 2200162, 2022.

[268] S. M. Czekaj, *Ferromagnetic and Antiferromagnetic Domain Configurations in Thin Films and Multilayers – Towards a Patterned Exchange Bias System.* Doctoral thesis, ETH, 2007.

[269] R. Nakajima, J. Stöhr, and Y. U. Idzerda, "Electron-yield saturation effects in L -edge x-ray magnetic circular dichroism spectra of Fe, Co, and Ni," *Phys. Rev. B*, vol. 59, pp. 6421–6429, 1999.

[270] J. Stöhr and S. Anders, "X-ray spectro-microscopy of complex materials and surfaces," *IBM J. Res. Dev.*, vol. 44, pp. 535–551, 2000.

[271] H. Ebert, J. Stöhr, S. S. P. Parkin, M. Samant, and A. Nilsson, "L -edge x-ray absorption in fcc and bcc Cu metal: Comparison of experimental and first-principles theoretical results," *Phys. Rev. B*, vol. 53, pp. 16067–16073, 1996.

[272] G. van der Laan, J. Zaanen, G. A. Sawatzky, R. Karnatak, and J.-M. Esteva, "Comparison of x-ray absorption with x-ray photoemission of nickel dihalides and NiO," *Phys. Rev. B*, vol. 33, pp. 4253–4263, 1986.

[273] J. Stöhr, K. Baberschke, R. Jaeger, R. Treichler, and S. Brennan, "Orientation of Chemisorbed Molecules from Surface-Absorption Fine-Structure Measurements: CO and NO on Ni(100)," *Phys. Rev. Lett.*, vol. 47, pp. 381–384, 1981.

[274] B. T. Thole, G. van der Laan, and G. A. Sawatzky, "Strong Magnetic Dichroism Predicted in the M4,5 X-Ray Absorption Spectra of Magnetic Rare-Earth Materials," *Phys. Rev. Lett.*, vol. 55, pp. 2086–2088, 1985.

[275] G. van der Laan, B. T. Thole, G. A. Sawatzky, J. B. Goedkoop, J. C. Fuggle, J.-M. Esteva, R. Karnatak, J. P. Remeika, and H. A. Dabkowska, "Experimental proof of magnetic x-ray dichroism," *Phys. Rev. B*, vol. 34, pp. 6529–6531, 1986.

[276] J. Goulon, C. Goulon-Ginet, A. Rogalev, V. Gotte, C. Malgrange, C. Brouder, and C. R. Natoli, "X-ray natural circular dichroism in a uniaxial gyrotropic single crystal of LiIO3," *J. Chem. Phys.*, vol. 108, pp. 6394–6403, 1998.

[277] G. Schütz, W. Wagner, W. Wilhelm, P. Kienle, R. Zeller, R. Frahm, and G. Materlik, "Absorption of circularly polarized x rays in iron," *Phys. Rev. Lett.*, vol. 58, pp. 737–740, 1987.

[278] C. Schmitz-Antoniak, "X-ray absorption spectroscopy on magnetic nanoscale systems for modern applications," *Reports Prog. Phys.*, vol. 78, no. 6, p. 62501, 2015.

[279] I. P. Krug, *Magnetic Proximity Effects in Highly-ordered Transition Metal Oxide Heterosystems - A Study by Soft X-Ray.*
Forschungszentrum Juelich GmbH Zentralbibliothek Verlag, 2008.

[280] M. W. Haverkort, S. I. Csiszar, Z. Hu, S. Altieri, A. Tanaka, H. H. Hsieh, H.-J. Lin, C. T. Chen, T. Hibma, and L. H. Tjeng, "Magnetic versus crystal-field linear dichroism in NiO thin films," *Phys. Rev. B*, vol. 69, p. 020408, 2004.

[281] E. Arenholz, G. Van Der Laan, R. V. Chopdekar, and Y. Suzuki, "Angle-dependent Ni2+ X-ray magnetic linear dichroism: Interfacial coupling revisited," *Phys. Rev. Lett.*, vol. 98, p. 197201, 2007.

[282] Y. Z. Wu, B. Sinkovic, C. Won, J. Zhu, Y. Zhao, and Z. Q. Qiu, "Experimental study of the x-ray linear dichroism of NiO films grown on Fe(001)," *Phys. Rev. B - Condens. Matter Mater. Phys.*, vol. 85, p. 134436, 2012.

[283] P. Kuiper, B. G. Searle, P. Rudolf, L. H. Tjeng, and C. T. Chen, "X-ray magnetic dichroism of antiferromagnet Fe_2O_3: The Orientation of Magnetic Moments Observed by Fe 2p x-ray absorption spectroscopy," *Phys. Rev. Lett.*, vol. 70, pp. 1549–1552, 1993.

[284] M. M. Schwickert, G. Y. Guo, M. A. Tomaz, W. L. O'Brien, and G. R. Harp, "X-ray magnetic linear dichroism in absorption at the L edge of metallic Co, Fe, Cr, and V," *Phys. Rev. B*, vol. 58, pp. R4289–R4292, 1998.

[285] F. P. Chmiel, N. Waterfield Price, A. D. Johnson, R. D .and Lamirand, J. Schad, G. van der Laan, D. T. Harris, J. Irwin, M. S. Rzchowski, C.-B. Eom, and P. G. Radaelli, "Observation of magnetic vortex pairs at room temperature in a planar α-Fe_2O_3/Co heterostructure," *Nat. Mater.*, vol. 17, pp. 581–585, 2018.

[286] S. Czekaj, F. Nolting, L. J. Heyderman, P. R. Willmott, and G. van der Laan, "Sign dependence of the x-ray magnetic linear dichroism on the antiferromagnetic spin axis in $LaFeo_3$ thin films," *Phys. Rev. B*, vol. 73, p. 020401, 2006.

[287] S. Finizio, *Field-free Control of Magnetism in Nanostructured Materials Probed with High Resolution X-ray Microscopy.*
Dissertation, Johannes Gutenberg-Universität Mainz, 2015.

[288] M. Hand, H. Wang, F. Maccherozzi, M. Apollonio, J. Zhu, S. S. Dhesi, and K. Sawhney, "Quantitative investigation of linear arbitrary polarization in an APPLE-II undulator," *J. Synchrotron Radiat.*, vol. 25, pp. 378–384, 2018.

[289] E. C. Longhi, P. Bencok, A. Dobrynin, E. C. M. Rial, A. Rose, P. Steadman, C. Thompson, A. Thomson, and H. Wang, "Developments in Polarization and Energy Control of APPLE-II Undulators at Diamond Light Source," *J. Phys. Conf. Ser.*, vol. 425, p. 032011, 2013.

[290] S. Anders, H. A. Padmore, R. M. Duarte, T. Renner, T. Stammler, A. Scholl, M. R. Scheinfein, J. Stöhr, L. Séve, and B. Sinkovic, "Photoemission electron microscope for the study of magnetic materials," *Rev. Sci. Instrum.*, vol. 70, pp. 3973–3981, 1999.

[291] L. Aballe, M. Foerster, E. Pellegrin, J. Nicolas, and S. Ferrer, "The ALBA spectroscopic LEEM-PEEM experimental station: layout and performance," *J. Synchrotron Radiat.*, vol. 22, pp. 745–752, 2015.

[292] F. Kronast, J. Schlichting, F. Radu, S. Mishra, T. Noll, and H. Dürr, "Spin-resolved photoemission microscopy and magnetic imaging in applied magnetic fields," *Surf. Interface Anal.*, vol. 42, pp. 1532–1536, 2010.

[293] U. Flechsig, F. Nolting, A. Fraile Rodriguez, J. Krempaskỳ, C. Quitmann, T. Schmidt, S. Spielmann, and D. Zimoch, "Performance measurements at the sls sim beamline," in *AIP Conf. Proc.*, vol. 1234, pp. 319–322, American Institute of Physics, 2010.

[294] L. Le Guyader, A. Kleibert, A. Fraile Rodríguez, S. El Moussaoui, A. Balan, M. Buzzi, J. Raabe, and F. Nolting, "Studying nanomagnets and magnetic heterostructures with X-ray PEEM at the Swiss Light Source," *J. Electron Spectros. Relat. Phenomena*, vol. 185, pp. 371–380, 2012.

[295] A. Locatelli and E. Bauer, "Recent advances in chemical and magnetic imaging of surfaces and interfaces by XPEEM," *J. Phys. Condens. Matter*, vol. 20, p. 093002, 2008.

[296] M. J. Grzybowski, P. Wadley, K. W. Edmonds, R. Beardsley, V. Hills, R. P. Campion, B. L. Gallagher, J. S. Chauhan, V. Novak, T. Jungwirth, F. Maccherozzi, and S. S. Dhesi, "Imaging Current-Induced Switching of Antiferromagnetic Domains in CuMnAs," *Phys. Rev. Lett.*, vol. 118, p. 057701, 2017.

[297] S. Y. Bodnar, M. Filianina, S. P. Bommanaboyena, T. Forrest, F. Maccherozzi, A. A. Sapozhnik, Y. Skourski, M. Kläui, and M. Jourdan, "Imaging of current induced Néel vector switching in antiferromagnetic Mn_2Au," *Phys. Rev. B*, vol. 99, p. 140409, 2019.

[298] B. Dieny, I. L. Prejbeanu, K. Garello, P. Gambardella, P. Freitas, R. Lehndorff, W. Raberg, U. Ebels, S. O. Demokritov, J. Akerman, A. Deac, P. Pirro, C. Adelmann, A. Anane, A. V. Chumak, A. Hirohata, S. Mangin, S. O. Valenzuela, M. C. Onbaşlı, M. D'Aquino, G. Prenat, G. Finocchio, L. Lopez-Diaz, R. Chantrell, O. Chubykalo-Fesenko, and P. Bortolotti, "Opportunities

and challenges for spintronics in the microelectronics industry," *Nat. Electron.*, vol. 3, pp. 446–459, 2020.

[299] Q. Shao, P. Li, L. Liu, H. Yang, S. Fukami, A. Razavi, H. Wu, K. Wang, F. Freimuth, Y. Mokrousov, M. D. Stiles, S. Emori, A. Hoffmann, J. Akerman, K. Roy, J.-P. Wang, S.-H. Yang, K. Garello, and W. Zhang, "Roadmap of Spin–Orbit Torques," *IEEE Trans. Magn.*, vol. 57, pp. 1–39, 2021.

[300] P. Zhang, C.-T. Chou, H. Yun, B. C. McGoldrick, J. T. Hou, K. A. Mkhoyan, and L. Liu, "Control of Néel Vector with Spin-Orbit Torques in an Antiferromagnetic Insulator with Tilted Easy Plane," *Phys. Rev. Lett.*, vol. 129, p. 017203, 2022.

[301] C. F. Schippers, M. J. Grzybowski, K. Rubi, M. E. Bal, T. J. Kools, R. A. Duine, U. Zeitler, and H. J. M. Swagten, "Disentangling electrical switching of antiferromagnetic NiO using high magnetic fields," *Phys. Rev. B*, vol. 106, p. 174434, 2022.

[302] M. Yang, Q. Li, T. Wang, B. Hong, C. Klewe, Z. Li, X. Huang, P. Shafer, F. Zhang, C. Hwang, W. S. Yan, R. Ramesh, W. S. Zhao, Y. Z. Wu, X. Zhang, and Z. Q. Qiu, "Current switching of the antiferromagnetic Néel vector in Pd/CoO/MgO(001)," *Phys. Rev. B*, vol. 106, p. 214405, 2022.

[303] C. C. Chiang, S. Y. Huang, D. Qu, P. H. Wu, and C. L. Chien, "Absence of Evidence of Electrical Switching of the Antiferromagnetic Néel Vector," *Phys. Rev. Lett.*, vol. 123, p. 227203, 2019.

[304] P. Wadley, B. Howells, J. Železný, C. Andrews, V. Hills, R. P. Campion, V. Novák, K. Olejník, F. Maccherozzi, S. S. Dhesi, S. Y. Martin, T. Wagner, J. Wunderlich, F. Freimuth, Y. Mokrousov, J. Kuneš, J. S. Chauhan, M. J. Grzybowski, A. W. Rushforth, K. Edmond, B. L. Gallagher, and T. Jungwirth, "Spintronics: Electrical switching of an antiferromagnet," *Science*, vol. 351, no. 6273, pp. 587–590, 2016.

[305] E. Aytan, B. Debnath, F. Kargar, Y. Barlas, M. M. Lacerda, J. X. Li, R. K. Lake, J. Shi, and A. A. Balandin, "Spin-phonon coupling in antiferromagnetic nickel oxide," *Appl. Phys. Lett.*, vol. 111, p. 252402, 2017.

[306] L. Mihalceanu, S. Keller, J. Greser, D. Karfaridis, K. Simeonidis, G. Vourlias, T. Kehagias, A. Conca, B. Hillebrands, and E. T. Papaioannou, "Spin-pumping through a varying-thickness MgO interlayer in Fe/Pt system," *Appl. Phys. Lett.*, vol. 110, p. 252406, 2017.

[307] Y. Zhou, C. Guo, C. Wan, X. Chen, X. Zhou, R. Zhang, Y. Gu, R. Chen, H. Wu, X. Han, F. Pan, and C. Song, "Current-Induced In-Plane Magnetization Switching in a Biaxial Ferrimagnetic Insulator," *Phys. Rev. Appl.*, vol. 13, p. 064051, 2020.

[308] Q. Guo, A. D'Addario, Y. Cheng, J. Kline, I. Gray, H. F. H. Cheung, F. Yang, K. C. Nowack, and G. D. Fuchs, "Current-induced switching of thin film α-Fe_2O_3 devices imaged using a scanning single-spin microscope," *arXiv, 2210.06233*, 2022.

[309] J. J. Michel, J. Flores, and F. Yang, "Sub-Nanosecond Electrical Pulse Switching of an Easy Plane Antiferromagnetic Insulator," *arXiv, 2211.07589*, 2022.

[310] Y. Cheng, E. Cogulu, R. D. Resnick, J. J. Michel, N. N. Statuto, A. D. Kent, and F. Yang, "Third harmonic characterization of antiferromagnetic heterostructures," *Nat. Commun.*, vol. 13, p. 3659, 2022.

[311] E. Cogulu, H. Zhang, N. N. Statuto, Y. Cheng, F. Yang, R. Cheng, and A. D. Kent, "Quantifying Spin-Orbit Torques in Antiferromagnet–Heavy-Metal Heterostructures," *Phys. Rev. Lett.*, vol. 128, p. 247204, 2022.

[312] P. Zhang, *Current-induced Dynamics of Easy-Plane Antiferromagnets.* Dissertation, MIT, 2023.

[313] M. Schwager, *Current-induced switching of antiferromagnetic NiO/Pt thin films probed electrically and by magneto-optical imaging.* Bachelor thesis, Johannes Gutenberg University Mainz, 2021.

[314] P. Sheng, Z. Zhao, O. J. Benally, D. Zhang, and J.-P. Wang, "Thermal contribution in the electrical switching experiments with heavy metal/antiferromagnet structures," *J. Appl. Phys.*, vol. 132, p. 073902, 2022.

[315] H. Bai, X. Zhou, Y. Zhou, X. Chen, Y. You, F. Pan, and C. Song, "Functional antiferromagnets for potential applications on high-density storage and high frequency," *J. Appl. Phys.*, vol. 128, p. 210901, 2020.

[316] Y. Takeuchi, Y. Yamane, J.-y. Yoon, R. Itoh, B. Jinnai, S. Kanai, J. Ieda, S. Fukami, and H. Ohno, "Chiral-spin rotation of non-collinear antiferromagnet by spin–orbit torque," *Nat. Mater.*, vol. 20, pp. 1364–1370, 2021.

[317] E. Cogulu, N. N. Statuto, Y. Cheng, F. Yang, R. V. Chopdekar, H. Ohldag, and A. D. Kent, "Direct imaging of electrical switching of antiferromagnetic Néel order in α-Fe_2O_3 epitaxial films," *Phys. Rev. B*, vol. 103, p. L100405, 2021.

[318] V. Grigorev, M. Filianina, S. Y. Bodnar, S. Sobolev, N. Bhattacharjee, S. Bommanaboyena, Y. Lytvynenko, Y. Skourski, D. Fuchs, M. Kläui, M. Jourdan, and J. Demsar, "Optical Readout of the Néel Vector in the Metallic Antiferromagnet Mn_2Au," *Phys. Rev. Appl.*, vol. 16, p. 014037, 2021.

[319] S. Reimers, Y. Lytvynenko, Y. R. Niu, E. Golias, B. Sarpi, L. S. I. Veiga, T. Denneulin, A. Kovács, R. E. Dunin-Borkowski, J. Bläßer, M. Kläui, and M. Jourdan, "Current-driven writing process in antiferromagnetic Mn_2Au for memory applications," *Nat. Commun.*, vol. 14, p. 1861, 2023.

[320] J. Miltat and A. Thiaville, "Lattice-compliant simulations of antiferromagnetic textures and their response to spin-orbit torques," *Phys. Rev. B*, vol. 105, p. 014401, 2022.

[321] G. P. Zhang, Y. H. Bai, T. Jenkins, and T. F. George, "Laser-induced ultrafast transport and demagnetization at the earliest time: first-principles and real-time investigation," *J. Phys. Condens. Matter*, vol. 30, p. 465801, 2018.

[322] O. Gomonay, S. Kondovych, and V. Loktev, "Shape-induced anisotropy in antiferromagnetic nanoparticles," *J. Magn. Magn. Mater.*, vol. 354, pp. 125–135, 2014.

[323] S. Czekaj, F. Nolting, L. J. Heyderman, K. Kunze, and M. Krüger, "Antiferromagnetic domain configurations in patterned $LaFeO_3$ thin films," *J. Phys. Condens. Matter*, vol. 19, p. 386214, 2007.

[324] M. S. Lee, P. Lyu, R. V. Chopdekar, A. Scholl, S. T. Retterer, and Y. Takamura, "Controlling antiferromagnetic domains in patterned La 0.7 Sr 0.3 FeO 3 thin films," *J. Appl. Phys.*, vol. 127, p. 203901, 2020.

[325] E. Folven, A. Scholl, A. Young, S. T. Retterer, J. E. Boschker, T. Tybell, Y. Takamura, and J. K. Grepstad, "Effects of nanostructuring and substrate symmetry on antiferromagnetic domain structure in $LaFeO_3$ thin films," *Phys. Rev. B*, vol. 84, p. 220410, 2011.

[326] E. Folven, Y. Takamura, and J. K. Grepstad, "X-PEEM study of antiferromagnetic domain patterns in $LaFeO_3$ thin films and embedded nanostructures," *J. Electron Spectros. Relat. Phenomena*, vol. 185, pp. 381–388, 2012.

[327] E. Folven, J. Linder, O. V. Gomonay, A. Scholl, A. Doran, A. T. Young, S. T. Retterer, V. K. Malik, T. Tybell, Y. Takamura, and J. K. Grepstad, "Controlling the switching field in nanomagnets by means of domain-engineered antiferromagnets," *Phys. Rev. B*, vol. 92, p. 094421, 2015.

[328] T. Moriyama, K. Hayashi, K. Yamada, M. Shima, Y. Ohya, and T. Ono, "Tailoring THz antiferromagnetic resonance of NiO by cation substitution," *Phys. Rev. Mater.*, vol. 4, p. 074402, 2020.

[329] A. Kozioł-Rachwał, M. Ślęzak, M. Zając, P. Dróżdż, W. Janus, M. Szpytma, H. Nayyef, and T. Ślęzak, "Control of spin orientation in antiferromagnetic NiO by epitaxial strain and spin–flop coupling," *APL Mater.*, vol. 8, p. 061107, 2020.

[330] H. Qiu, L. Zhou, C. Zhang, J. Wu, Y. Tian, S. Cheng, S. Mi, H. Zhao, Q. Zhang, D. Wu, B. Jin, J. Chen, and P. Wu, "Ultrafast spin current generated from an antiferromagnet," *Nat. Phys.*, vol. 17, pp. 388–394, 2021.

[331] J. Stöhr, A. Scholl, T. J. Regan, S. Anders, J. Lüning, M. R. Scheinfein, H. A. Padmore, and R. L. White, "Images of the Antiferromagnetic Structure of a NiO(100) Surface by Means of X-Ray Magnetic Linear Dichroism Spectromicroscopy," *Phys. Rev. Lett.*, vol. 83, pp. 1862–1865, 1999.

[332] F. Kronast and S. Valencia Molina, "SPEEM: The photoemission microscope at the dedicated microfocus PGM beamline UE49-PGMa at BESSY II," *J. large-scale Res. Facil. JLSRF*, vol. 2, p. A90, 2016.

[333] K. Nakahigashi, N. Fukuoka, and Y. Shimomura, "Crystal Structure of Antiferromagnetic NiO Determined by X-Ray Topography," *J. Phys. Soc. Japan*, vol. 38, pp. 1634–1640, 1975.

[334] C. Teodosiu, *Elastic Models of Crystal Defects*.
Berlin, Heidelberg: Springer Berlin Heidelberg, 1982.

[335] M. Kléman and M. Schlenker, "The Use of Dislocation Theory in Magnetoelasticity," *J. Appl. Phys.*, vol. 43, pp. 3184–3190, 1972.

[336] J. D. Eshelby, "The Continuum Theory of Lattice Defects," *Solid State Physics - Advances in Research and Applications*, vol. 3, pp. 79–144, 1956.

[337] C. Kittel, "Physical Theory of Ferromagnetic Domains," *Rev. Mod. Phys.*, vol. 21, pp. 541–583, 1949.

[338] J. Simmons, R. De Wit, and R. Bullough, *Fundamental Aspects of Dislocation Theory*, vol. 1.
U.S. National Bureau of Standards, 1970.

[339] K.-E. Kim, S. Jeong, K. Chu, J. H. Lee, G.-Y. Kim, F. Xue, T. Y. Koo, L.-Q. Chen, S.-Y. Choi, R. Ramesh, and C.-H. Yang, "Configurable topological textures in strain graded ferroelectric nanoplates," *Nat. Commun.*, vol. 9, p. 403, 2018.

[340] R. White, R. Newt, and R. Pease, "Patterned media: a viable route to 50 Gbit/in^2 and up for magnetic recording?," *IEEE Trans. Magn.*, vol. 33, pp. 990–995, 1997.

[341] E. Folven, A. Scholl, A. Young, S. T. Retterer, J. E. Boschker, T. Tybell, Y. Takamura, and J. K. Grepstad, "Crossover from Spin-Flop Coupling to Collinear Spin Alignment in Antiferromagnetic/Ferromagnetic Nanostructures," *Nano Lett.*, vol. 12, pp. 2386–2390, 2012.

[342] H. Qiu, L. Zhou, C. Zhang, J. Wu, Y. Tian, S. Cheng, S. Mi, H. Zhao, Q. Zhang, D. Wu, B. Jin, J. Chen, and P. Wu, "Ultrafast spin current generated from an antiferromagnet," *Nat. Phys.*, vol. 17, pp. 388–394, 2021.

[343] E. Rongione, O. Gueckstock, M. Mattern, O. Gomonay, H. Meer, C. Schmitt, R. Ramos, T. Kikkawa, M. Mičica, E. Saitoh, J. Sinova, H. Jaffrès, J. Mangeney, S. T. B. Goennenwein, S. Geprägs, T. Kampfrath, M. Kläui, M. Bargheer, T. S. Seifert, S. Dhillon, and R. Lebrun, "Emission of coherent THz magnons in an antiferromagnetic insulator triggered by ultrafast spin–phonon interactions," *Nat. Commun.*, vol. 14, p. 1818, 2023.

[344] T. Satoh, S.-J. Cho, R. Iida, T. Shimura, K. Kuroda, H. Ueda, Y. Ueda, B. A. Ivanov, F. Nori, and M. Fiebig, "Spin Oscillations in Antiferromagnetic NiO Triggered by Circularly Polarized Light," *Phys. Rev. Lett.*, vol. 105, p. 077402, 2010.

[345] S. Wust, C. Seibel, H. Meer, P. Herrgen, C. Schmitt, L. Baldrati, R. Ramos, T. Kikkawa, E. Saitoh, O. Gomonay, J. Sinova, Y. Mokrousov, H. C. Schneider, M. Kläui, B. Rethfeld, B. Stadtmüller, and M. Aeschlimann, "Indirect optical manipulation of the antiferromagnetic order of insulating NiO by ultrafast interfacial energy transfer," *arXiv, 2205.02686*, 2022.

[346] M. S. El Hadri, M. Hehn, G. Malinowski, and S. Mangin, "Materials and devices for all-optical helicity-dependent switching," *J. Phys. D. Appl. Phys.*, vol. 50, p. 133002, 2017.

[347] S. Alebrand, A. Hassdenteufel, D. Steil, M. Cinchetti, and M. Aeschlimann, "Interplay of heating and helicity in all-optical magnetization switching," *Phys. Rev. B*, vol. 85, p. 092401, 2012.

[348] A. V. Kimel and M. Li, "Writing magnetic memory with ultrashort light pulses," *Nat. Rev. Mater.*, vol. 4, pp. 189–200, 2019.

[349] I. Radu, K. Vahaplar, C. Stamm, T. Kachel, N. Pontius, H. A. Dürr, T. A. Ostler, J. Barker, R. F. Evans, R. W. Chantrell, A. Tsukamoto, A. Itoh, A. Kirilyuk, T. Rasing, and A. V. Kimel, "Transient ferromagnetic-like state mediating ultrafast reversal of antiferromagnetically coupled spins," *Nature*, vol. 472, pp. 205–209, 2011.

[350] S. Manz, M. Matsubara, T. Lottermoser, J. Büchi, A. Iyama, T. Kimura, D. Meier, and M. Fiebig, "Reversible optical switching of antiferromagnetism in TbMnO3," *Nat. Photonics*, vol. 10, pp. 653–656, 2016.

[351] G. Lefkidis and W. Hübner, "First-principles study of ultrafast magneto-optical switching in NiO," *Phys. Rev. B*, vol. 76, p. 014418, 2007.

[352] G. Lefkidis and W. Hübner, "Ultrafast laser-driven magnetic-switching scenario in NiO: Role of phonons," *J. Magn. Magn. Mater.*, vol. 321, pp. 979–983, 2009.

[353] T. Chirac, J.-Y. Chauleau, P. Thibaudeau, O. Gomonay, and M. Viret, "Ultrafast antiferromagnetic switching in NiO induced by spin transfer torques," *Phys. Rev. B*, vol. 102, p. 134415, 2020.

[354] T. Dannegger, M. Berritta, K. Carva, S. Selzer, U. Ritzmann, P. M. Oppeneer, and U. Nowak, "Ultrafast coherent all-optical switching of an antiferromagnet with the inverse Faraday effect," *Phys. Rev. B*, vol. 104, p. L060413, 2021.

[355] P. Stremoukhov, D. Carl S, A. Safin, S. Nikitov, and A. Kirilyuk, "Phononic manipulation of antiferromagnetic domains in NiO," *New J. Phys.*, vol. 24, p. 023009, 2022.

[356] T. Higuchi, N. Kanda, H. Tamaru, and M. Kuwata-Gonokami, "Selection Rules for Light-Induced Magnetization of a Crystal with Threefold Symmetry: The Case of Antiferromagnetic NiO," *Phys. Rev. Lett.*, vol. 106, p. 047401, 2011.

[357] A. Stupakiewicz, C. S. Davies, K. Szerenos, D. Afanasiev, K. S. Rabinovich, A. V. Boris, A. Caviglia, A. V. Kimel, and A. Kirilyuk, "Ultrafast phononic switching of magnetization," *Nat. Phys.*, vol. 17, pp. 489–492, 2021.

[358] K. Venkatakrishnan, B. Tan, P. Stanley, and N. R. Sivakumar, "The effect of polarization on ultrashort pulsed laser ablation of thin metal films," *J. Appl. Phys.*, vol. 92, pp. 1604–1607, 2002.

[359] J. N. Armstrong, M. R. Sullivan, and H. D. Chopra, "Antiferromagnetic spin and twin domain walls govern hysteretic expressions of exchange anisotropy," *Phys. Rev. B*, vol. 80, p. 104429, 2009.

[360] F. Krizek, S. Reimers, Z. Kašpar, A. Marmodoro, J. Michalička, O. Man, A. Edström, O. J. Amin, K. W. Edmonds, R. P. Campion, F. Maccherozzi, S. S. Dhesi, J. Zubáč, D. Kriegner, D. Carbone, J. Železný, K. Výborný, K. Olejník, V. Novák, J. Rusz, J.-C. Idrobo, P. Wadley, and T. Jungwirth, "Atomically sharp domain walls in an antiferromagnet," *Sci. Adv.*, vol. 8, pp. 1–11, 2022.

[361] A. Pohm, C. Sie, R. Uttecht, V. Kao, and O. Agrawal, "Chalcogenide glass bistable resistivity (Ovonic) memories," *IEEE Trans. Magn.*, vol. 6, pp. 592–592, 1970.

[362] K. Olejník, T. Seifert, Z. Kašpar, V. Novák, P. Wadley, R. P. Campion, M. Baumgartner, P. Gambardella, P. Němec, J. Wunderlich, J. Sinova, P. Kužel, M. Müller, T. Kampfrath, and T. Jungwirth, "Terahertz electrical writing speed in an antiferromagnetic memory," *Sci. Adv.*, vol. 4, pp. 1–9, 2018.

[363] V. Grigorev, M. Filianina, Y. Lytvynenko, S. Sobolev, A. R. Pokharel, A. P. Lanz, A. Sapozhnik, A. Kleibert, S. Bodnar, P. Grigorev, Y. Skourski, M. Kläui, H.-J. Elmers, M. Jourdan, and J. Demsar, "Optically Triggered Néel Vector Manipulation of a Metallic Antiferromagnet Mn_2Au under Strain," *ACS Nano*, vol. 16, pp. 20589–20597, 2022.

[364] E. Rongione, *Ultrafast spin-currents mediated by spin-orbit coupling : towards new concepts for THz emitters.*
Dissertation, Université Paris-Saclay, 2022.

[365] T. Satoh, R. Iida, T. Higuchi, Y. Fujii, A. Koreeda, H. Ueda, T. Shimura, K. Kuroda, V. I. Butrim, and B. A. Ivanov, "Excitation of coupled spin–orbit dynamics in cobalt oxide by femtosecond laser pulses," *Nat. Commun.*, vol. 8, p. 638, 2017.

[366] H.-h. Chou and H. Y. Fan, "Light scattering by magnons in CoO, MnO, and $\alpha-$MnS," *Phys. Rev. B*, vol. 13, pp. 3924–3938, 1976.

[367] D. Xiong, Y. Jiang, K. Shi, A. Du, Y. Yao, Z. Guo, D. Zhu, K. Cao, S. Peng, W. Cai, D. Zhu, and W. Zhao, "Antiferromagnetic spintronics: An overview and outlook," *Fundam. Res.*, vol. 2, pp. 522–534, 2022.

[368] L. Pellegrino, M. Biasotti, E. Bellingeri, C. Bernini, A. S. Siri, and D. Marré, "All-Oxide Crystalline Microelectromechanical Systems: Bending the Functionalities of Transition-Metal Oxide Thin Films," *Adv. Mater.*, vol. 21, pp. 2377–2381, 2009.

[369] A. Bukharaev, A. K. Zvezdin, A. P. Pyatakov, and Y. K. Fetisov, "Straintronics: a new trend in micro- and nanoelectronics and material science," *Uspekhi Fiz. Nauk*, vol. 188, pp. 1288–1330, 2018.

[370] H. Wang, C. Du, P. C. Hammel, and F. Yang, "Antiferromagnonic Spin Transport from $Y_3Fe_5O_{12}$ into NiO," *Phys. Rev. Lett.*, vol. 113, p. 097202, 2014.

[371] Z. Qiu, J. Li, D. Hou, E. Arenholz, A. T. N'Diaye, A. Tan, K.-i. Uchida, K. Sato, S. Okamoto, Y. Tserkovnyak, Z. Q. Qiu, and E. Saitoh, "Spin-current probe for phase transition in an insulator," *Nat. Commun.*, vol. 7, p. 12670, 2016.

[372] G. R. Hoogeboom, G.-J. N. S. Nicolaas, A. Alexander, O. Kuschel, J. Wollschläger, I. Ennen, B. J. van Wees, and T. Kuschel, "Role of NiO in the nonlocal spin transport through thin NiO films on $Y_3Fe_5O_{12}$," *Phys. Rev. B*, vol. 103, p. 144406, 2021.

[373] T. Ikebuchi, Y. Kobayashi, I. Sugiura, Y. Shiota, T. Ono, and T. Moriyama, "Long-distance spin current transmission in single-crystalline NiO thin films," *Appl. Phys. Express*, vol. 14, p. 123001, 2021.

[374] A. Ross, R. Lebrun, O. Gomonay, D. A. Grave, A. Kay, L. Baldrati, S. Becker, A. Qaiumzadeh, C. Ulloa, G. Jakob, F. Kronast, J. Sinova, R. Duine, A. Brataas, A. Rothschild, and M. Kläui, "Propagation Length of Antiferromagnetic Magnons Governed by Domain Configurations," *Nano Lett.*, vol. 20, pp. 306–313, 2020.

[375] A. V. Chumak, V. I. Vasyuchka, A. A. Serga, and B. Hillebrands, "Magnon spintronics," *Nat. Phys.*, vol. 11, pp. 453–461, 2015.

[376] Y. Sasaki, G. Li, T. Moriyama, T. Ono, R. V. Mikhaylovskiy, A. V. Kimel, and S. Mizukami, "Laser stimulated THz emission from Pt/CoO/FeCoB," *Appl. Phys. Lett.*, vol. 117, 2020.

[377] A. Mitrofanova, A. Safin, O. Kravchenko, S. Nikitov, and A. Kirilyuk, "Optically initialized and current-controlled logical element based on antiferromagnetic-heavy metal heterostructures for neuromorphic computing," *Appl. Phys. Lett.*, vol. 120, p. 072402, 2022.

[378] A. Kurenkov, S. Fukami, and H. Ohno, "Neuromorphic computing with antiferromagnetic spintronics," *J. Appl. Phys.*, vol. 128, p. 010902, 2020.

[379] D. Go, D. Jo, H.-W. Lee, M. Kläui, and Y. Mokrousov, "Orbitronics: Orbital currents in solids," *EPL (Europhysics Lett.)*, vol. 135, p. 37001, 2021.

[380] V. Fernandez, C. Vettier, F. de Bergevin, C. Giles, and W. Neubeck, "Observation of orbital moment in NiO," *Phys. Rev. B*, vol. 57, pp. 7870–7876, 1998.

[381] W. Neubeck, C. Vettier, F. de Bergevin, F. Yakhou, D. Mannix, L. Ranno, and T. Chatterji, "Orbital moment determination of simple transition metal oxides using magnetic X-ray diffraction," *J. Phys. Chem. Solids*, vol. 62, pp. 2173–2180, 2001.

[382] R. Radwanski and Z. Ropka, "Orbital moment in CoO and in NiO," *Phys. B Condens. Matter*, vol. 345, pp. 107–110, 2004.

[383] COMSOL Multiphysics® v. 5.4. www.comsol.com. COMSOL AB, "Heating-Circuit."

[384] H. Watanabe, "Thermal constants for Ni, NiO, MgO, MnO and CoO at low temperatures," *Thermochimica Acta*, vol. 218, pp. 365–372, 1993.

[385] G. A. Slack, "Platinum as a Thermal Conductivity Standard," *J. Appl. Phys.*, vol. 35, pp. 339–344, 1964.

[386] M. Mori, T. Yamamoto, H. Itoh, H. Inaba, and H. Tagawa, "Thermal Expansion of Nickel-Zirconia Anodes in Solid Oxide Fuel Cells during Fabrication and Operation," *J. Electrochem. Soc.*, vol. 145, pp. 1374–1381, 1998.

[387] D. Jia, A. Zhou, Y. Ling, K. An, A. Stoica, and X. Wang, "Effect of porosity on the mechanical properties of YSZ/NiO composite anode materials," *World J. Eng.*, vol. 7, no. 3, p. 489, 2011.

[388] A. S. Madhusudhan Rao and K. Narender, "Studies on thermophysical properties of CaO and MgO by γ -ray attenuation," *J. Thermodyn.*, pp. 1–8, 2014.

[389] A. M. Ezhil, M. Jayachandran, and C. Sanjeeviraja, "Fabrication techniques and material properties of dielectric MgO thin films — A status review," *CIRP J. Manuf. Sci*, vol. 2, no. 2, pp. 92–113, 2010.

[390] C. Schmitt, *Imaging of current-induced domain walls and characterisation of switching mechanism in insulating antiferromagnetic thin films.* Master thesis, Johannes Gutenberg University Mainz, 2021.

[391] J. M. Liu, "Simple technique for measurements of pulsed Gaussian-beam spot sizes," *Opt. Lett.*, vol. 7, p. 196, 1982.

[392] F. Ruffino and M. G. Grimaldi, "Nanostructuration of Thin Metal Films by Pulsed Laser Irradiations: A Review," *Nanomaterials*, vol. 9, p. 1133, 2019.

[393] M. Olbrich, E. Punzel, P. Lickschat, S. Weißmantel, and A. Horn, "Investigation on the Ablation of thin Metal Films with Femtosecond to Picosecond-pulsed Laser Radiation," *Phys. Procedia*, vol. 83, pp. 93–103, 2016.

[394] Y. S. Touloukian, *Thermal Conductivity-Metallic Elements and Alloys*, vol. 1. Springer New York, NY, 1 ed., 1970.

[395] D. L. Windt, W. C. Cash, M. Scott, P. Arendt, B. Newnam, R. F. Fisher, and A. B. Swartzlander, "Optical constants for thin films of Ti, Zr, Nb, Mo, Ru, Rh, Pd, Ag, Hf, Ta, W, Re, Ir, Os, Pt, and Au from 24 Å to 1216 Å," *Appl. Opt.*, vol. 27, p. 246, 1988.

[396] J. Lombard, F. Detcheverry, and S. Merabia, "Influence of the electron–phonon interfacial conductance on the thermal transport at metal/dielectric interfaces," *J. Phys. Condens. Matter*, vol. 27, p. 015007, 2014.

[397] J. Arblaster, "The thermodynamic properties of platinum on ITS-90," *Platin. Met. Rev.*, vol. 38, no. 3, pp. 119–125, 1994.

[398] J. Schindelin, I. Arganda-Carreras, E. Frise, V. Kaynig, M. Longair, T. Pietzsch, S. Preibisch, C. Rueden, S. Saalfeld, B. Schmid, J.-Y. Tinevez, D. J. White, V. Hartenstein, K. Eliceiri, P. Tomancak, and A. Cardona, "Fiji: an open-source platform for biological-image analysis," *Nature Methods*, vol. 9, pp. 676–682, 2012.

A | Sample Preparation

A.1 | Sample Growth

Reactive magnetron sputtering has been used to grow the epitaxial MgO(001)/NiO/Pt and MgO(001)/CoO/Pt thin films used in this thesis, similar to previous studies [42, 105, 137, 182]. Here, we briefly describe the growth of AFM samples at the QAM4 chamber [229] in the Saitoh Laboratory via an automatic sputtering process. We outline the key steps for the sputtering at the example of NiO thin films.
To achieve high-quality film growth, new MgO substrates are used, which have been stored in an argon glove box before usage. We minimize the air exposure time of the MgO substrates and place them face down in the sample holder, blowing them with nitrogen before insertion into the loading chamber. Once the pressure in the loading chamber reaches $p_{\mathrm{Load}} < 5 \times 10^{-4}$ Pa, the sample can be transferred to a central chamber that connects the load chamber, chamber 1 (for sputtering non-magnetic materials), chamber 2 (for sputtering magnetic materials), and chamber 4.

AFM Deposition

NiO and CoO are deposited by reactive magnetron sputtering at elevated temperatures. We discuss the individual steps by following the temperature evolution in chamber 2, as shown in Fig. A.1. The base pressure of chamber 2 was $p_2 < 1.2 \times 10^{-5}$ Pa.

I To pre-anneal the MgO substrates the chamber temperature is first raised to about T_{Ch}=970°C and then kept there for 50 minutes. At the holder position this is equivalent to an annealing of the MgO substrates at $T_{\mathrm{MgO}} \approx 770$°C.

II After annealing the substrates, the temperature is stabilized at the deposition temperature T_{Ch2}=573°C, $T_{\mathrm{MgO}} \approx 430$°C.

III The deposition process consists of multiple steps to avoid possible errors in the automatic sputtering process. The sample holder rotates with 10 rpm.

- i DC:20 W, Ar=15 sccm - sputtering for 10 s with shutter closed.
- ii RF:150 W, Ar=15 sccm - sputtering for 300 s with shutter closed.
- iii RF:150 W [HC:20 W for NiO], Ar=15 sccm, $O_2 \neq 0$ sccm - deposition after pre-sputtering.

IV When the deposition is finished, the heater turns off and the sample cools down. Once the chamber temperature is below $T_{\mathrm{Ch2}} < 500°\mathrm{C}$ the sample holder is transferred to chamber 4 for a faster cooling. The sample cools down ideally overnight or until temperature in chamber 2 is $T_{\mathrm{Ch2}} < 100°\mathrm{C}$ before further depositions.

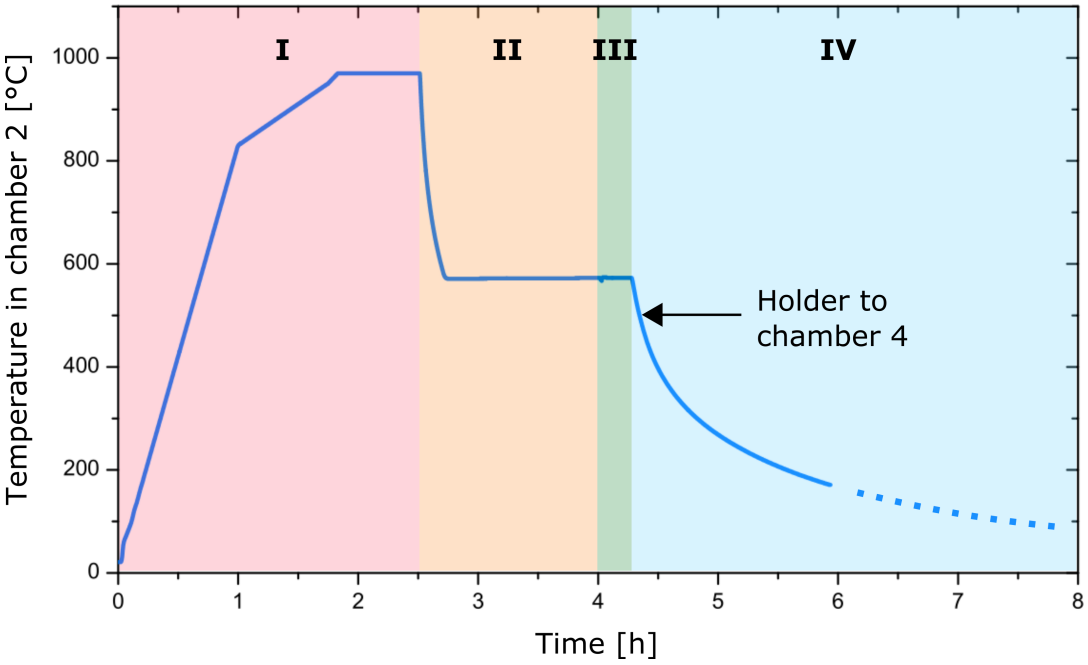

Figure A.1: Temperature evolution in chamber 2 during the automatic deposition procedure.

Machine errors in the automatic deposition can occur after step II during the initialization of the sputtering plasma in step III. It is likely that the deposition of material over time in the chamber, such as the accumulation of excess material on the helical coil (HC), can alter the optimal parameters for plasma ignition. If the plasma fails to ignite, the deposition process is automatically aborted, and the heater is turned off. In such cases, one can switch to manual operation mode of the sputtering system, restart the heater, and, after the temperature is stabilized, initiate manual sputtering. The samples used in this work have been grown by automatic sputtering deposition. However, the samples grown by the author have mostly been grown with manual deposition due to machine errors. Ongoing investigations by C. Schmitt indicate a lower quality of the manually deposited thin films, which might be attributed to the extended heating of the substrates and less stable deposition temperature.

Growth Rates

The following growth rates have been used during sample deposition by the author. The sputtering recipes for NiO and CoO have been developed by Dr. Rafael Ramos. The author was supported by Dr. Takashi Kikkawa in the sample growth who also provided guidance on the parameters for the non-magnetic materials.

Material	Power	Gas	Temperature	Growth Rate
NiO	RF:150 W, HC:20 W	Ar:15 sccm, O_2:3 sccm	430°C	0.020 nm/s
CoO	RF:150 W	Ar:15 sccm, O_2:2 sccm	430°C	0.046 nm/s
Pt	DC:20 W	Ar:15 sccm	21°C	0.023 nm/s
Al	DC:27 W	Ar:15 sccm	21°C	0.039 nm/s
Cu	DC:20 W	Ar:15 sccm	21°C	0.027 nm/s
W	DC:20 W	Ar:15 sccm	21°C	0.010 nm/s

A.2 | Lithography Recipes

In the following, we outline the lithography steps used to pattern the devices used in this thesis.

A.2.1 Sample Cleaning

The following procedure was used by the author for sample cleaning:

i Immerse sample in acetone beaker number for 180 s in an ultrasonic bath.

ii Immerse sample in another acetone beaker for 180 s in an ultrasonic bath.

iii Immerse sample in isopropyl alcohol (IPA) for 120 s in an ultrasonic bath.

iv Blow dry with nitrogen.

A.2.2 Optical Lithography

Spin Coating

The negative resist AR-N7520.17 was used for spin coating. After the placement of a drop of resist on the sample, the rotation should be directly started.

Step	Time	Speed	Acceleration
Prespin	2 s	500 rpm	500 rpm/s
Main	60 s	6000 rpm	4000 rpm/s

i 60 s softbake at $T = 85°C$ on the hotplate

ii 60 s cooldown of the sample

Exposure

iii Adjust pressure until fringes appear on the optical mask

iv 10 s exposure with UV light

Development

v 100 s puddle development in AR300-47 developer

vi 20 s development break in high purity water

vii Blow dry with nitrogen

Check the development under an optical microscope and increase development in steps of 5-15 s by repeating steps v-vii with adjusted development time.

A.2.3 Electron Beam Lithography

The positive resist polymethyl methacrylate (PMMA) A11 has been used for spin coating. After the placement of a drop of resist on the sample the rotation should be directly started.

Step	Time	Speed	Acceleration
Main	60 s	4000 rpm	4000 rpm/s

i Softbake for 180°C on the hotplate

ii 90 s cooldown

For better conductivity insulating samples have additionally been coated with a conductive e-spacer for PMMA. The conductive e-spacer minimizes charging effects during focusing.

Step	Time	Speed	Acceleration
Main	60 s	3000 rpm	3000 rpm/s

Exposure

iii EHT voltage 20 kV, Aperture 30(60) µm

iv Dose: 335 uC/cm^2, for smaller structures with proximity effects 64 % of dose can be used

Development

v 30 s immersion in purified water to remove e-spacer

vi 45 s immersion in methyl isobutyl ketone:iso-2-propanol (IPA) (MIBK:IPA with 1:3 ratio) for development

vii 30 s immersion in IPA alcohol to stop development

viii Blow dry with nitrogen

Check the development under an optical microscope and increase development in steps of 5-15 s by repeating steps vi-ix with adjusted development time.

A.2.4 Etching

Ion beam etching has been performed in an Ionsys500 ion etcher with an argon plasma. The dosage has been 356 µA/cm^2 at 90° angle. For longer etch times, the etching should be conducted in 30 s steps to avoid heating effects. The etching time depends on the desired depth, which can be measured with an atomic force microscope. Here are two examples for MgO(001)/NiO(10)/Pt(2 nm) bilayers:

1. 65 s etching removes approx. 6 nm, device with hole in Ref. [49].
2. 240 s etching removes approx. 20 nm, shape pattern in Ref. [50].

After etching ruthenium (ca. 1 nm) can be deposited into the trenches for better visibility of patterns or markers in XMLD-PEEM. The resist can then be removed via the above described cleaning process.

B | Results

B.1 | Current-Induced Switching

The following section reproduces part of the supplementary of Ref. [49].

B.1.1 COMSOL Simulations

We use COMSOL Multiphysics for 3D finite element modelling of the temperature and strain profiles to study the current-induced heating and resulting strain contributions in our different device and pulsing geometries. To set up the model we follow the steps outlined in the tutorial model *Heating-Circuit* [383].
The device and substrate dimensions correspond to the actual experimental environment, we consider the platinum layer to be etched and the contact pads are simplified to reduce computational efforts, see Fig. B.1 (a). We model the electrically generated heat in the Pt layer using the Electric Currents, Layered Shell interface from the AC/DC Module. To model the heat transfer in the thin conductive layer we use the Thin Layer feature from the Heat Transfer in Solids interface. The current-induced heat can dissipate on the top of the platinum layer and on the bottom side into the NiO layer. As boundary condition for the temperature distribution we assume that the top and bottom of our sample are in contact with a 300 K environment and that the heat transfer coefficients are $10\,\mathrm{W/(m^2K)}$ between device and air and $500\,\mathrm{W/(m^2K)}$ between the device and a sample holder [204]. We use the Structural Mechanics Module to simulates the thermal expansion of the layers. The stresses are zero at 293.15 K and the boundary conditions are determined by the Rigid Motion Suppression of COMSOL.
We apply 0.1 ms pulses with varying current densities across the platinum layers (2 nm). We modeled the end of the current pulse with a step function and displayed here the strain and heat distributions at the surface of the NiO layer after 0.1 ms, see Fig. B.1 (a,b) for the example of a cross shaped horizontal pulse.
We model the current induced heating by the current flowing through the platinum layer. The subsequent current-induced temperature profile inside the NiO (and MgO) leads to inhomogeneous thermal expansion, thus resulting in inhomogeneous strain.
Our approach here is similar to the one presented in Ref. [204] and we neglect the shear strains u_{xy}, which are significantly smaller in the switched regions of our devices compared to normal strains, see Fig. B.1 (c-d).

For the resistance of our platinum layer we use a measured resistivity of $2.8(3)\cdot10^{-7}$ Ohm·m. We use the temperature dependent heat capacities and thermal conductivities for our materials reported in Ref. [384, 385]. For the temperature-induced strain in the NiO and MgO layers, we use the following thermal expansion coefficients α, Youngs moduli E and Poisson ratios ν: NiO $\alpha = 14.1 \cdot 10^{-6}\,\mathrm{K}^{-1}$ from Ref. [386], $E = 171.8\,\mathrm{GPa}$ and $\nu = 0.384$ from Ref. [387], MgO $\alpha = 10.42 \cdot 10^{-6}\,\mathrm{K}^{-1}$ from Ref. [388], $E = 249\,\mathrm{GPa}$ and $\nu = 0.18$ from Ref. [389].

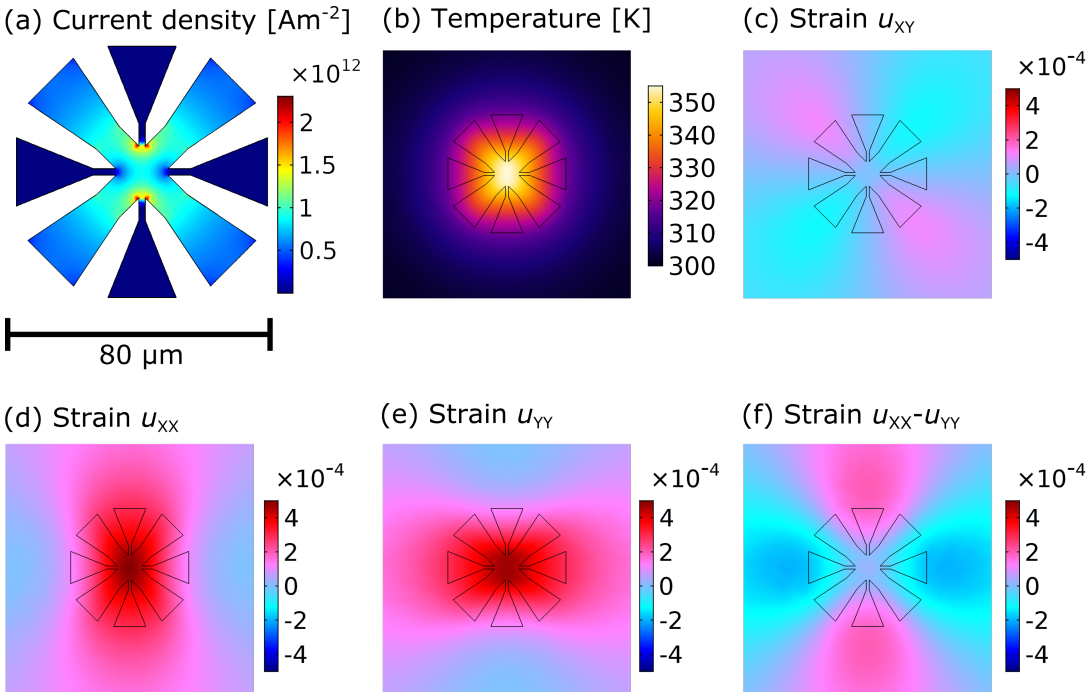

Figure B.1: COMSOL simulations of the current distribution for a horizontal X-shaped current pulse ($j = 1.95 \cdot 10^{12}\,\mathrm{A/m^2}$, $\Delta t = 0.1\,\mathrm{ms}$) (a), the temperature (b) and the strain (c-f) in an Mgo(001)/NiO(10 nm)/Pt(2 nm) thin film.

B.2 | Antiferromagnetic Shape Anisotropy

In the following sections we reproduce and expand part of the supplementary information from Ref. [50].

B.2.1 XMLD Analysis

For our MgO(001)/NiO(10 nm)/Pt(2 nm) sample, we have observed X-ray magnetic linear dichroism (XMLD) in Fig. B.2 (a), calculated as I_{LH}-I_{LV}, and an absence of circular magnetic dichroism (XMCD) in Fig. B.2 (b), indicating purely antiferromagnetic ordering of our films. For subsequent XMLD imaging we have utilized the inversion of the XMLD contrast at the Ni L_2 edge at the energies E_1=868.3 eV, E_2=870.1 eV and calculated the XMLD image by $[I(E_1)\text{-}I(E_2)]/[I(E_1)+I(E_2)]$. By studying the XMLD contrast dependence on the azimuthal angle γ and angle of the beam-polarization ω we can identify in Fig. B.3 (a) four different antiferromagnetic domains to be present in a rectangular element of 10×5 µm whose long axis is oriented along the [110] direction.

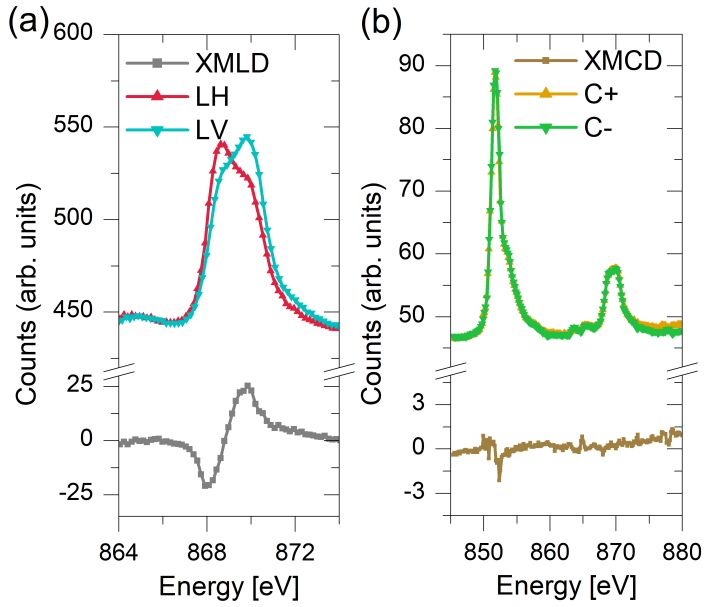

Figure B.2: (a) X-ray absorption spectrum and XMLD for linear polarized X-rays in the vicinity of the Ni L_2 edge of our MgO(001)/NiO(10 nm)/Pt(2 nm) bilayer . (b) X-ray absorption spectrum and XMCD for circular polarized X-rays. Adapted with permission from Ref. [50]. Copyright 2022 American Physical Society.

NiO is a compensated collinear antiferromagnet with two magnetic sublattices whose magnetic structure is uniquely described by the Néel vector $\boldsymbol{n}$. In bulk NiO crystals the exchange-striction leads to a rhombohedral contraction along the $\langle 111 \rangle$ axes. Thus, four T-domains can be formed with the spins being ferromagnetically coupled inside the $\{111\}$ planes and antiferromagnetically between the $\{111\}$ planes, due to the superexchange interaction. Within such a T-domain the spins can be oriented along three possible easy axes $\langle 11\bar{2} \rangle$, leading to three different S-domains per T-domain. There are a total of 12 possible domains in bulk NiO crystals [31, 103, 113]. However, in NiO thin films the growth induced strain from the substrate mismatch can lead to a preferential stabilization of S-domains parallel or perpendicular to the sample plane [109, 134]. In a previous study on similarly grown MgO(001)/NiO(10 nm)/Pt(2 nm) thin films, it has been observed that the epitaxial growth of NiO on MgO substrates results in compressive strain, which lead to a preferential out-of-plane component of the Néel vector [109, 134, 137]. By analyzing the contrast changes among the domains with varying azimuthal angle γ and orientation of the linear beam polarization ω one can determine the orientation of the Néel vector.
We use here the same code and procedure that Christin Schmitt has used previously to determine the domain structure in our NiO thin films [137], the details of such a fitting procedure are outlined in her Master thesis [390], here we only give a brief overview. We can express the XMLD intensity I as a function of the experimental parameters [286]

$$I = I_0 + \cos^2(\alpha), \tag{B.1}$$

with I_0 and I_1 as constants and α as angle between the the E-field of the X-rays $\boldsymbol{E}$ and the Néel vector $\boldsymbol{n}$. Using the angles θ, ω and the incidence angle $\chi = 16°$, as defined in Fig. 5.2, we can express the E-field as:

$$\cos(\alpha) = \boldsymbol{E} \cdot \boldsymbol{n} = \begin{pmatrix} \sin(\omega) \cdot \sin(\chi) \cdot \cos(\gamma) - \cos(\omega) \cdot \sin(\gamma) \\ \sin(\omega) \cdot \sin(\chi) \cdot \sin(\gamma) + \cos(\omega) \cdot \cos(\gamma) \\ \sin(\omega) \cdot \cos(\chi) \end{pmatrix} \cdot \boldsymbol{n}, \tag{B.2}$$

In addition to XMLD also XNLD contributes to the observed signal. The additional contribution arises from the growth on MgO(001) and the induced out-of-plane strain. It depends on the angle β between the $\boldsymbol{E}$ field and the out-of-plane axes

$$\cos(\beta) = \boldsymbol{E} \cdot \begin{pmatrix} 0 \\ 0 \\ 1 \end{pmatrix}. \tag{B.3}$$

Thus, the total angle dependent X-ray intensity can be expressed as

$$I = I_0 + I_1 \cos^2(\alpha) + I_2 \cos^2(\beta), \tag{B.4}$$

with I_2 as additional constant. We can identify the orientation of the Néel vector of our domains to be along $[\pm 5 \pm 5\, 19]$ by extracting their angle dependent contrast and

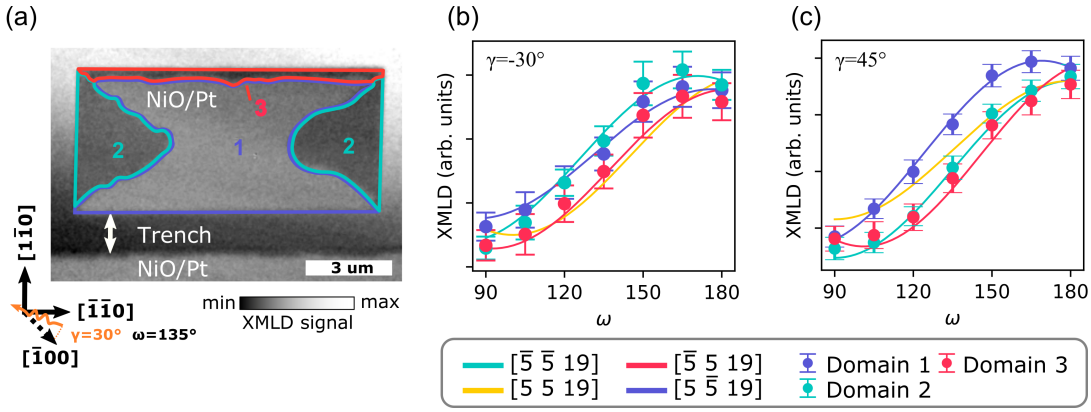

Figure B.3: Observed domain structure in patterned devices (a). Simulated and experimental contrast of the different domains dependent on the beam polarization for (a) $\gamma = -30°$ and (b) $\gamma = 45°$. Adapted with permission from Ref. [50]. Copyright 2022 American Physical Society.

comparing their contrast changes with the expected contrast for the different domains according to Eq. B.4, see Fig. B.3 (b,c).
Further details on the determination of the Néel vector orientation from the angle dependent contrast variations can be found in Refs. [137, 268, 286, 390].

B.3 | Optical Domain Creation in AFM/Pt Bilayers

In the following sections we reproduce parts of the supplementary of Ref. [51] with permission.

B.3.1 Irradiation with Laser Light

Irradiation has been performed by S. Wust and P. Herrgen (TU Kaiserslautern).

The irradiation of the NiO/Pt bilayer thin films has been performed ex-situ with an ultrafast amplified laser system, Astrella (from Coherent), with a central wavelength of 800 nm and with a pulse repetition rate of 1 kHz. The pulse lengths have been determined by employing auto-correlation methods. The laser has been focused down to 40 µm ± 2 µm in diameter with an x50 objective, while the irradiation time has been controlled using a electrical shutter system. We have determined the spot size and calculated the fluences via the $1/e^2$ width of the spot [391]. The intensity distribution of the laser spot with respect to a typical domain image is depicted in Fig. B.4, more details on the methods can be found in the supplementary of Ref. [345].

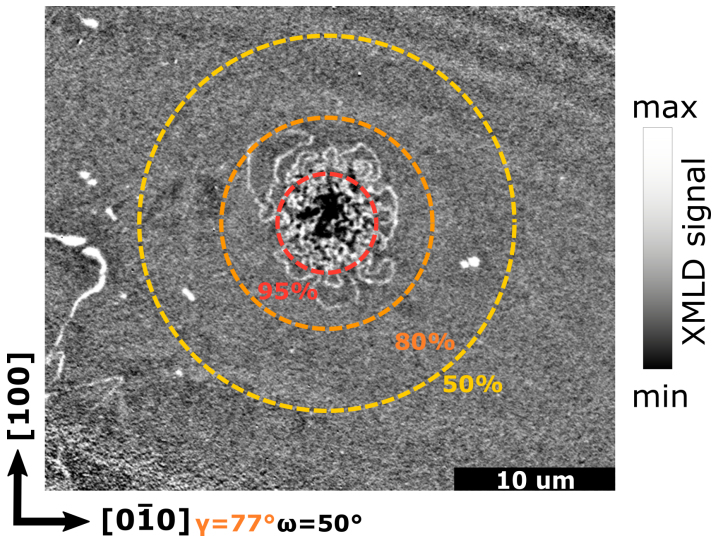

Figure B.4: XMLD-PEEM image of the AFM domain structure of a MgO(001)/NiO(10 nm)/Pt(2 nm) sample after irradiation with an overlay of the intensity profile for a Gaussian beam with an $1/e^2$ width of 40 µm. Adapted with permission from the supplementary of Ref. [51] with enhanced contrast, see Appendix B.3.4.

B.3.2 Effects of Ablation

In addition to the antiferromagnetic contrast of the domain walls, we can observe contrast at the center of the laser dot due to laser ablation of the platinum layer. In the case of Fig. B.4, we used a pulse length of 6.7 ps, a laser fluence of $12\pm2\,\mathrm{mJ/cm^2}$ for 2 second long irradiation. Considering the 1 kHz repetition rate of our laser, we illuminated the spot with a total of 2000 laser pulses. Ablation starts to occur when the accumulated heat from the laser irradiation leads to an increase of the Pt temperature higher than its melting point, causing structural changes of the Pt layer [392]. If we increase the fluence to $16\pm2\,\mathrm{mJ/cm^2}$, the damaged area becomes more homogeneous as can be seen in Fig. B.5 (a). Although the Pt layer has been structurally changed, the conductive layer is still intact and we can observe the underlying optically induced domain structure in the NiO. Thus, the underlying NiO is not damaged and the dark contrast in B.5 (b) is a result of the damaged capping layer and the high surface sensitivity of X-PEEM imaging. For higher fluences of $20\pm3\,\mathrm{mJ/cm^2}$, we can observe in Fig. B.5 (b) the results of a two-step ablation process that is characteristic for metal thin films [393]. In the outer part of the spot, the Pt layer is heated above its melting temperature and similar deformations occur as for lower fluences. However, in the center of the laser spot the accumulated heat reaches the boiling point of Pt and the Pt layer evaporates. The absence of the platinum layer in the center of the dot leads to charging during the X-PEEM imaging, as can be seen in Fig. B.5 (b).

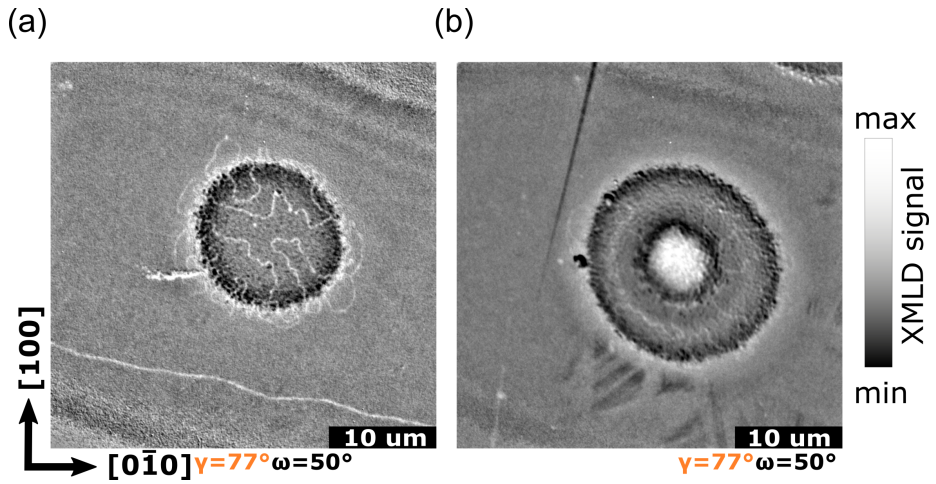

Figure B.5: XMLD-PEEM image of the AFM domain structure, of areas on a MgO(001)/NiO(10 nm)/Pt(2 nm) thin film that have been illuminated with 2000 pulses of circular right polarized laser light with a pulse length of 6.7 ps and a fluence of 16±2 mJ/cm^2 (a) and 20±3 mJ/cm^2 (b). Adapted with permission from the supplementary of Ref. [51] with enhanced contrast, see Appendix B.3.4.

Annealing of Films

In order to validate the antiferromagnetic origin of the domain walls, we annealed our MgO(001)/NiO(10 nm)/Pt(2) sample above the Néel temperature of NiO. The sample has been annealed at around 550 K under vacuum without the application of a magnetic field for 15 minutes, before cooling down. The sample temperature during this annealing process is plotted in Fig. B.6 (a). We have previously observed that such an annealing procedure allows the reconfiguration of the domain structure, for example by antiferromagnetic shape anisotropy [50]. To ensure that the sample is sufficiently heated, we patterned differently oriented geometrical elements onto our sample. We imaged the domain structure of these elements before Fig. B.6 (b) and after Fig. B.6 (c) the annealing process by birefringence imaging and observed a reorientation of antiferromagnetic domains due to the annealing process. Confirming the sufficient heating of our sample to allow for a reconfiguration of the domain structure. By conducting a linear fit of the temperature decrease between 550 K and 500 K we can estimate 3.0±0.2 K/min as an upper estimate for the cooling rate through the Néel temperature of our film.

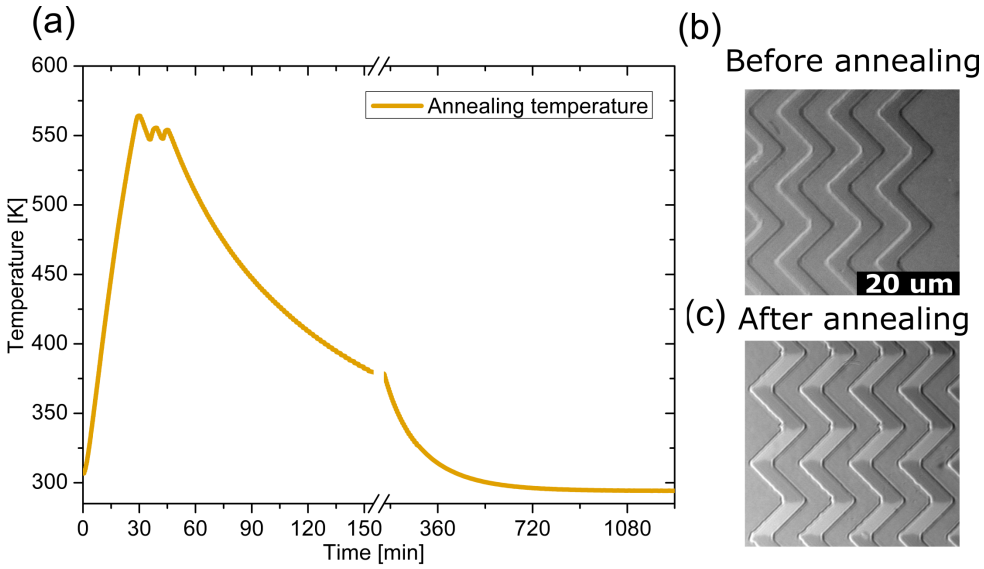

Figure B.6: (a) The temperature evolution during the annealing of the sample. (b) Birefringence image of the antiferromagnetic domain structure of a patterned MgO(001)/NiO(10 nm)/Pt(2 nm) element before the annealing procedure. (c) Birefringence image of the same patterned element after the annealing process, dark and bright contrast indicates an orthogonal in-plane projection of the Néel vector. Adapted with permission from the supplementary of Ref. [51].

B.3.3 Laser-Induced Heating

The calculations have been performed by S. Hirtle (TU Kaiserslautern).

In the following, we investigate the laser-induced heating of our NiO layer. With our simulation we intend to calculate a lower bound for the maximum temperature, which is reached in the NiO layer and to show that this lower bound is higher than the Néel temperature.
To estimate the timescale on which the energy dissipates in the Pt layer (the NiO layer is neglected at first), we solve the heat transport equation

$$c_{\mathrm{Pt}} \frac{\partial T(r,t)}{\partial t} = \kappa \Delta T(r,t), \tag{B.5}$$

to obtain the evolution of the temperature in time and space. Here, we take $\kappa = 100\,\mathrm{Wm^{-1}K^{-1}}$ as an upper bound for the heat transport coefficient of Pt at high temperatures [394] and $c_{\mathrm{Pt}} = 2.74 \cdot 10^6\,\mathrm{Jm^{-3}K^{-1}}$ as the heat capacity of Pt obtained by the Petit-Dulong law. By overestimating the heat transport coefficient κ and underestimating the heat capacity c_{Pt} for the temperature range between room temperature $T_{\mathrm{room}} = 300\,\mathrm{K}$ and melting temperature $T_{\mathrm{melt}} = 2041\,\mathrm{K}$, we obtain a lower bound for the transport timescale. Due to the small thickness of the Pt layer

of 2 nm compared to the laser penetration depth of approx. 10 nm [395] for a laser wavelength of 800 nm, we assume homogeneous heating of this layer. Therefore, we only have to solve the heat transport equation laterally in two dimensions. As a starting point we choose a Gaussian distribution with the $1/e^2$-radius $r_0 = 20$ µm, as it is present in the Pt layer shortly after laser excitation, that is

$$T(\boldsymbol{r}, t = 0) = T_{\text{room}} + (T_{\text{peak}} - T_{\text{room}}) \exp(-\frac{2\boldsymbol{r}^2}{r_0^2}) \,. \tag{B.6}$$

The solution to the heat equation (B.5) with starting condition (B.6) is given by

$$T(\boldsymbol{r}, t) = T_{\text{room}} + (T_{\text{peak}} - T_{\text{room}}) \frac{\frac{1}{2}\pi r_0^2}{\frac{1}{2}\pi r_0^2 + 4\pi \frac{\kappa}{c_{\text{Pt}}} t} \exp(-\frac{r^2}{\frac{1}{2} r_0^2 + 4 \frac{\kappa}{c_{\text{Pt}}} t}) \,. \tag{B.7}$$

As the peak temperature T_{peak} the melting temperature $T_{\text{melt}} = 2041$ K of Pt is chosen as a lower bound for the temperature if ablation occurs. The obtained temperature profile for different times is shown in Fig. B.7.

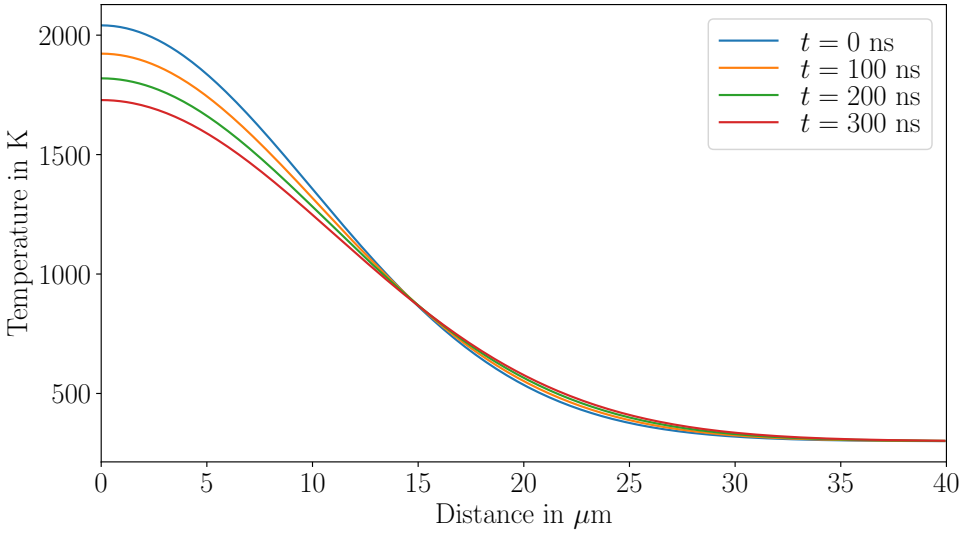

Figure B.7: Simulated temperature profile of the Pt layer at different times. Adapted with permission from the supplementary of Ref. [51].

It can be seen that the heat transport in the Pt layer takes place on a timescale > 100 ns. Based on the calculations of Ref. [396] for the conductance at Pt/insulator interfaces and the calculated relaxation times, we expect relaxation times < 1 ns for the temperature equilibration at the Pt/NiO interface. The above estimations show that heat transport from the laser-excited Pt layer to NiO takes place before any other dissipation mechanisms are active. To estimate a lower bound of the temperature in NiO, we assume therefore that Pt and NiO reach a joint temperature which can be estimated by solving

$$d_{\mathrm{Pt}} \int_{T_{\mathrm{room}}}^{T_{\mathrm{melt}}} c_{\mathrm{Pt}}(T')\, dT' = d_{\mathrm{Pt}} \int_{T_{\mathrm{room}}}^{T} c_{\mathrm{Pt}}(T')\, dT' + d_{\mathrm{NiO}} \int_{T_{\mathrm{room}}}^{T} c_{\mathrm{NiO}}(T')\, dT' \qquad \text{(B.8)}$$

for T with the thicknesses $d_{\mathrm{Pt}} = 2\,\mathrm{nm}$ and $d_{\mathrm{NiO}} = 10\,\mathrm{nm}$ for the Pt and NiO layer. Here, we use experimentally obtained, temperature-dependent heat capacities for Pt [397] and NiO [384] with linear inter- and extrapolation. By applying a root-finding algorithm, we find $T = 519\,\mathrm{K}$.

This temperature estimate is slightly below the bulk Néel temperature $T_{(\mathrm{N,Bulk})} = 523\,\mathrm{K}$ of NiO. However, in NiO thin films the Néel temperature is reduced with decreasing thickness [109]. We conducted XMLD-PEEM imaging of our thin films at 400 K, see Fig. B.8 (a), and at 460 K, see Fig. B.8 (b). We observed an absence of contrast at 460 K indicating that the Néel temperature of our thin films is between 400 K and 460 K.

Therefore, we deem it realistic that the laser-irradiation of our thin films can lead to a local increase of the temperature of the NiO thin film above its Néel temperature and to a reordering of the antiferromagnetic spins.

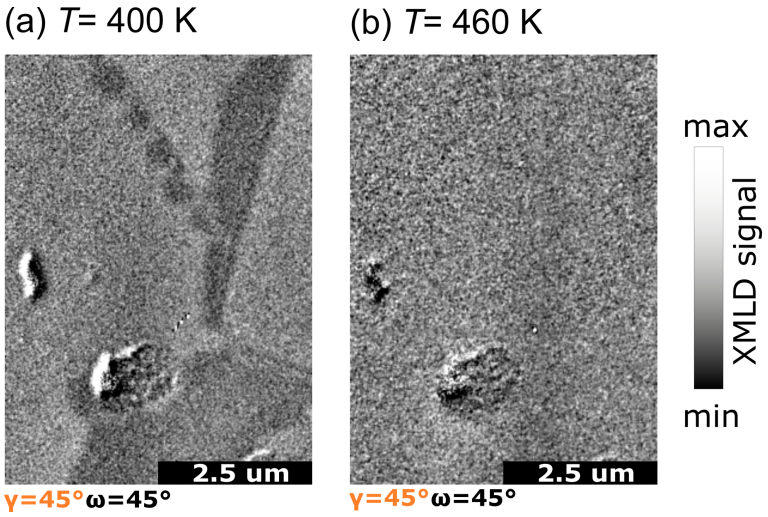

Figure B.8: Temperature dependent antiferromagnetic contrast in XMLD-PEEM of a MgO(001)/NiO(10 nm)/Pt(2 nm) film at 400 K (a) and at 460 K (b). Adapted with permission from the supplementary of Ref. [51] with enhanced contrast, see Appendix B.3.4.

B.3.4 Image Processing

The contrast of the XMLD-PEEM images can be enhanced by using an image processing software, such as Fiji [398]. Usually, the combination of a linear background subtraction and brightness/contrast adjustment is sufficient for contrast enhancement. However, reducing the dynamic range for contrast enhancement can result in a loss of detail. This is particularly an issue in images where there are additional defects or structures that appear very bright or dark in the XMLD-PEEM images and are close to the domain structure, such as the areas where the platinum capping has been altered by laser irradiation, see Fig. B.9 (a).

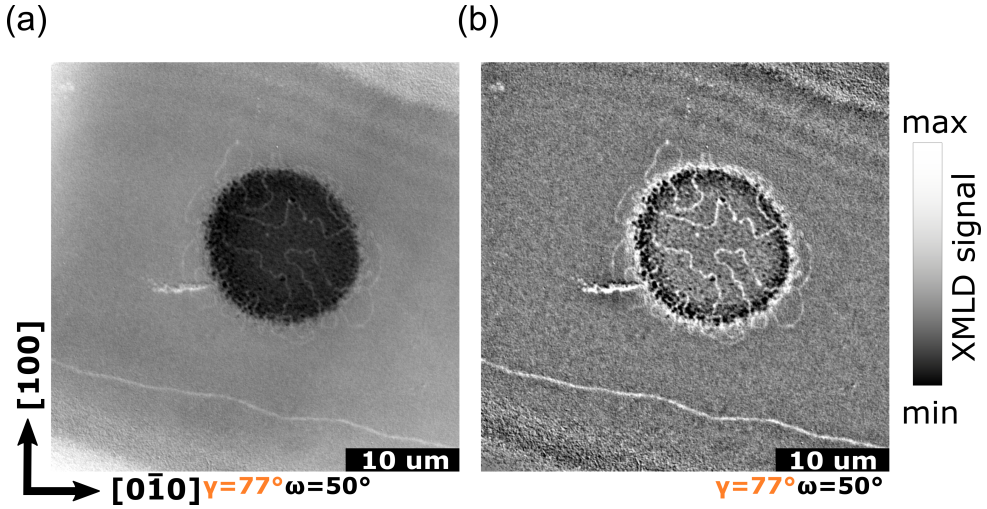

Figure B.9: (a) XMLD-PEEM image of the AFM domain structure, of areas on a MgO(001)/NiO(10 nm)/Pt(2 nm) thin film that have been illuminated with 2000 pulses of circular right polarized laser light with a pulse length of 6.7 ps and a fluence of 16±2 mJ/cm^2. (b) The same XMLD-PEEM image after using a FTT band-pass filter (1-30 px) and subtraction of the same image with a Gaussian blur (30 px).

To further enhance the visibility of the narrow domain walls, we use a combination of a fast Fourier transformation (FFT) band-pass filter and a background subtraction of the same image blurred with the Gaussian blur filter. Fiji's FFT band-pass filtering allows it to filter out features that are much larger than the narrow domain walls we are interested in, and background subtraction with a Gaussian blur increases the contrast. However, near the edges of patterned elements or areas of ablation, subtraction can introduce image artifacts. In Fig. B.9 (b) the subtraction results in a white border around the laser ablated area which is not of magnetic origin but a result of image processing. Such effects must be taken into account when interpreting the contrast. However, these effects can be minimized by performing the Gaussian blur and subtraction only in the region of interest. For example only in the non-etched areas of a patterned shape, as has been done for Fig. 5.11.

C | Other Information

C.1 | Contributions

This section details the contributions of the author and co-workers (from JGU Mainz if not noted otherwise) to the results presented in this work.

Current-induced switching of AFM/Pt bilayers

i Imaging of the domain structures by the author and F. Schreiber.

ii Electrical measurements by F. Schreiber, supported by the author.

iii Sample growth by C. Schmitt, Dr. R. Ramos (Tohoku University at the time) and A. Rajan under the supervision of Prof. Dr. E. Saitoh (Tohoku University).

iv Data evaluation by the author, supported by Dr. L. Baldrati, Prof. Dr. O. Gomonay and F. Schreiber.

v Sample fabrication and design by Dr. L. Baldrati and the author, supported by T. Reimer.

vi Manuscript writing by the author, Dr. L. Baldrati, F.Schreiber and Prof. Dr. M. Kläui with input from the co-authors.

Own contributions: See above and COMSOL simulations.

vii Pulselength dependent studies by M. Schwager, supported by the author, for details see Ref. [313].

viii Device sensitivity studies by F. Schreiber, supported by the author, for details see Ref. [217].

Antiferromagnetic shape anisotropy

i Imaging during beamtimes was led by the author, supported by C. Schmitt, F. Fuhrmann, B. Bednarz, A. Rajan and the beamline scientists: Dr. F. Kronast, Dr. M.-A. Mawass, Dr. S. Valencia (at BESSY) and Dr. M. A. Niño and Dr. M. Foerster (at ALBA).

ii Sample growth by C. Schmitt, Dr. R. Ramos (Tohoku University at the time) and A. Rajan under the supervision of Prof. Dr. E. Saitoh (Tohoku University). Additional Ru deposition by L. Schnitzspan.

iii Data evaluation by the author, supported by C. Schmitt.

iv Sample annealing by the author and L. Schnitzspan.

v Sample fabrication and design by the author supported by T. Reimer.

vi Theory and magnetoelastic simulations by Prof. Dr. O. Gomonay.

vii Manuscript writing by the author, Prof. Dr. O. Gomonay and Prof. Dr. M. Kläui with input from the co-authors.

Own contributions: See above and birefringence imaging.

Optically induced switching in AFM/Pt bilayers

i Imaging during beamtimes was lead by the author, supported by C. Schmitt, F. Fuhrmann, B. Bednarz, A. Rajan and the beamline scientists: Dr. M. A. Niño, Dr. M. Foerster (at ALBA), Dr. F. Kronast (at BESSY), and Dr. A. Kleibert (at SLS).

ii Sample growth by C. Schmitt, Dr. R. Ramos (Tohoku University at the time) and A. Rajan under the supervision of Prof. Dr. E. Saitoh (Tohoku University). Additional Ru depositions by L. Schnitzspan, M. Syskaki and F. Kammerbauer.

iii Sample fabrication and design by the author supported by T. Reimer.

iv Laser irradiation at TU Kaiserslautern by S. Wust and P. Herrgen supported by the author under the guidance of Dr. B. Stadtmüller and Prof. Dr. M. Aeschlimann (all TU Kaiserslautern at the time, except the author).

v Simulation of temperature increase by S. Hirtle and Prof. Dr. B. Rethfeld (both TU Kaiserslautern).

vi Manuscript writing by the author and Prof. Dr. M. Kläui with input from the co-authors.

Own contributions: See above, data evaluation, annealing and birefringence imaging.

List of Publications

- H. Meer, F. Schreiber, C. Schmitt, R. Ramos, E. Saitoh, O. Gomonay, J. Sinova, L. Baldrati, and M. Kläui, "Direct Imaging of Current-Induced Antiferromagnetic Switching Revealing a Pure Thermomagnetoelastic Switching Mechanism in NiO," *Nano Lett.*, vol. 21, pp. 114–119, 2021.

- F. Schreiber, H. Meer, C. Schmitt, R. Ramos, E. Saitoh, L. Baldrati, and M. Kläui, "Magnetic Sensitivity Distribution of Hall Devices in Antiferromagnetic Switching Experiments," *Phys. Rev. Appl.*, vol. 16, p. 064023, 2021.

- H. Meer, O. Gomonay, C. Schmitt, R. Ramos, L. Schnitzspan, F. Kronast, M.-A. Mawass, S. Valencia, E. Saitoh, J. Sinova, L. Baldrati, and M. Kläui, "Strain-induced shape anisotropy in antiferromagnetic structures," *Phys. Rev. B*, vol. 106, p. 094430, 2022.

- C. Schmitt, L. Sanchez-Tejerina, M. Filianina, F. Fuhrmann, H. Meer, R. Ramos, F. Maccherozzi, D. Backes, E. Saitoh, G. Finocchio, L. Baldrati, and M. Kläui, "Identifiying the domain wall spin structure in current-induced switching of antiferromagnetic NiO/Pt," *Phys. Rev. B*, vol. 107, p. 184417, 2023.

- H. Meer, O. Gomonay, A. Wittmann, and M. Kläui, "Antiferromagnetic insulatronics: Spintronics in insulating 3d metal oxides with antiferromagnetic coupling," *Appl. Phys. Lett.*, vol. 122, p. 080502, 2023.

- H. Meer, S. Wust, C. Schmitt, P. Herrgen, F. Fuhrmann, S. Hirtle, B. Bednarz, A. Rajan, R. Ramos, M. A. Niño, M. Foerster, F. Kronast, A. Kleibert, B. Rethfeld, E. Saitoh, B. Stadtmüller, M. Aeschlimann, and M. Kläui, "Laser-Induced Creation of Antiferromagnetic 180-Degree Domains in NiO/Pt Bilayers," *Adv. Funct. Mater.*, p. 2213536, 2023.

- E. Rongione, O. Gueckstock, M. Mattern, O. Gomonay, H. Meer, C. Schmitt, R. Ramos, T. Kikkawa, M. Mičica, E. Saitoh, J. Sinova, H. Jaffrès, J. Mangeney, S. T. B. Goennenwein, S. Geprägs, T. Kampfrath, M. Kläui, M. Bargheer, T. S. Seifert, S. Dhillon, and R. Lebrun, "Emission of coherent THz magnons in an antiferromagnetic insulator triggered by ultrafast spin–phonon interactions," *Nat. Commun.*, vol. 14, p. 1818, 2023.

- S. Wust, C. Seibel, H. Meer, P. Herrgen, C. Schmitt, L. Baldrati, R. Ramos, T. Kikkawa, E. Saitoh, O. Gomonay, J. Sinova, Y. Mokrousov, H. C. Schneider, M. Kläui, B. Rethfeld, B. Stadtmüller, and M. Aeschlimann, "Indirect optical manipulation of the antiferromagnetic order of insulating NiO by ultrafast interfacial energy transfer," *arXiv, 2205.02686*, 2022.

- C. Schmitt, A. Rajan, G. Beneke, A. Kumar, T. Sparmann, H. Meer, B. Bednarz, R. Ramos, M. A. Nino, M. Foerster, E. Saitoh, and M. Kläui, "Mechanism of electrical switching of ultra-thin CoO/Pt bilayers," *arXiv, 2303.13308*, 2023.

Acknowledgements

Removed due to data privacy

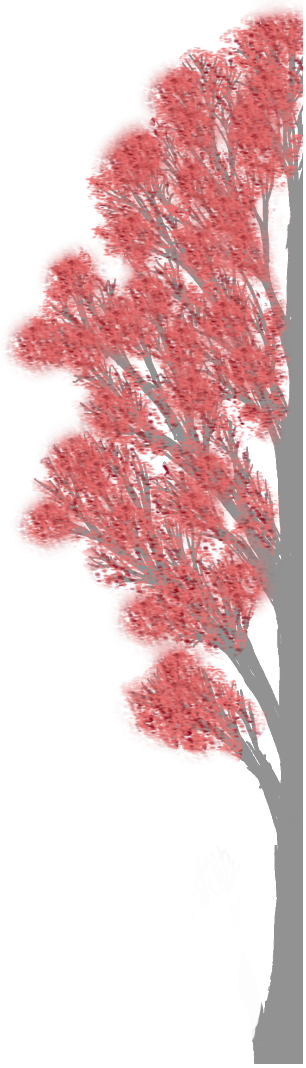

Acknowledgements

Removed due to data privacy

Removed due to data privacy